

Model-based optimal treatment schedules for acute leukemia

Der Fakultät für Mathematik
der Otto-von-Guericke-Universität Magdeburg
zur Erlangung des akademischen Grades

**doctor rerum naturalium
(Dr. rer. nat.)**

am 04.07.2020 vorgelegte Dissertation

von

Felix Jost (M. Sc.)

Abstract

During intensive chemotherapy of acute myeloid leukemia (AML) and acute lymphoblastic leukemia (ALL), leukopenia and neutropenia are commonly arising adverse events. These forms of white blood cell (WBC) suppression in the bone marrow (myelosuppression) are responsible for a higher risk of infectious complications during chemotherapy and consequently for delayed, dose-reduced or stopped treatments, longer hospitalization periods, and overall higher mortality as the worst case.

The objective of the present thesis was to apply mathematical methods, meaning mathematical modeling, simulation and optimization, to describe and predict myelosuppression during chemotherapy of adult AML and pediatric ALL patients and determine the interaction between different biomarkers and clinical outcome. Furthermore, the developed mathematical models for myelosuppression were applied to investigate adapted treatment schedules via simulation and optimization processes aiming at improving clinically relevant outcomes.

More precisely, we developed population pharmacokinetic(s) (PK)/pharmacodynamic(s) (PD) models describing the dynamics of WBCs, granulocyte-colony stimulating factor (G-CSF) and leukemic blasts during consolidation treatment using intermediate or high-dose cytarabine (Ara-C) and exogenous G-CSF (lenograstim) in AML. For the maintenance therapy of childhood ALL patients with oral 6-mercaptopurine (6MP) and methotrexate (MTX), we investigated population PK/PD models describing the neutrophils over a treatment period of up to two years.

The models were developed from and evaluated on three different datasets containing measurements from 23 and 44 AML patients as well as 116 pediatric ALL patients. Parameter estimations were performed using the first order conditional estimation approximation method for nonlinear mixed-effects models. After model calibration and evaluation, we used the personalized models to simulate and analyze myelosuppression and short-term disease progression for different standard treatment schedules. To date, even the standard treatments still involve several decisions to be made by the treating physician on a case-by-case basis (i.e. what dose to start with, when and how to increase or decrease chemotherapy, when to start the next treatment cycle or what impact does the co-medication have on therapy), for which no international consensus exist. Therefore, the *in silico* studies are further steps along the path to support physicians making model-informed decisions. In addition to treatment simulations, we also formulated an optimal control problem to optimize treatment schedules with respect to short-term disease progression, WBC nadirs, and the amount of Ara-C and G-CSF. The results of the present work provide new insights into the timing and the number of treatment cycles, the administration of lenograstim and its beneficial influence on the eradication of leukemic blasts.

Regarding methodological investigations, we proposed a feedback optimal control algorithm with optimal measurement time points from optimal experimental designs and applied the algorithm to the Lotka-Volterra fishing example. Finally, we inves-

tigated Fisher's scoring method in the context of parameter estimation for nonlinear mixed-effect models. For two examples, differing in their model complexity and number of measurements, we compared Fisher's method with state-of-the-art methods.

Overall, the present thesis contributed to a better understanding of chemotherapy and related myelosuppression during consolidation therapy of [AML](#) patients and maintenance therapy of childhood [ALL](#) patients. Future clinical studies are warranted to investigate the proposed treatment schedules.

Zusammenfassung

Leukopenie und Neutropenie sind zwei häufig auftretende unerwünschte Arzneimittelwirkungen während der intensiven Chemotherapie von akuter myeloischer und lymphatischer Leukämie (AML/ALL). Diese Formen der Suppression von Leukozyten (weiße Blutkörperchen) im Knochenmark (auch Myelosuppression genannt) sind verantwortlich für ein erhöhtes Risiko an infektiösen Komplikationen während der Chemotherapie und folglich für eine verzögerte, dosisreduzierte oder abgebrochene Behandlung, längere Krankenhausaufenthalte und im äußersten Fall eine erhöhte Sterblichkeit. Das Ziel dieser Arbeit war die Anwendung mathematischer Methoden, darunter mathematische Modellierung, Simulation und Optimierung, zur Beschreibung und Vorhersage von Myelosuppression während der Chemotherapie von AML bei Erwachsenen und ALL bei Kindern und die gleichzeitige Untersuchung von Interaktionen zwischen Biomarkern und Behandlungsergebnissen. Des Weiteren wurden die entwickelten mathematischen Modelle zur Beschreibung von Myelosuppression verwendet, um mittels Simulation und Optimierung angepasste Behandlungspläne auf Verbesserungen in der Erzielung klinisch relevanter Ergebnisse zu untersuchen.

Präziser formuliert wurden populationsbasierte pharmakokinetische/pharmakodynamische (PK/PD) Modelle entwickelt, die die Dynamik von Leukozyten, Granulozyten-Kolonie-stimulierenden Faktoren (G-CSF) und leukämischen Blasten während der Konsolidierungstherapie bei AML unter Verwendung von mittel- und hochdosiertem Cytarabin (Ara-C) beschreiben. Für die Erhaltungstherapie von ALL bei Kindern mit oralem 6-Mercaptopurin (6MP) und Methotrexat (MTX) wurden verschiedene populationsbasierte PK/PD Modelle untersucht, die die Dynamik von Neutrophilen über einen Behandlungszeitraum von bis zu zwei Jahren beschreiben.

Für die Entwicklung und Evaluation der Modelle wurden drei unterschiedliche Datensätze verwendet. Die Datensätze enthalten Messinformationen von 23, beziehungsweise 44 AML Patienten und 116 pädiatrischen ALL Patienten. Parameterschätzungen für nichtlineare Modelle mit gemischten Effekten wurden unter Verwendung der *first order conditional estimation* Approximationsmethode durchgeführt. Nach Modellkalibrierung und Auswertung wurden die personalisierten Modelle verwendet, um Myelosuppression und das kurzzeitige Fortschreiten der Krankheit bei verschiedenen etablierten Behandlungsplänen zu simulieren und zu analysieren. Bis heute müssen auch bei den etablierten Therapien wichtige Entscheidungen von den behandelnden Ärzten für jeden Patienten einzeln getroffen werden, für die es keine internationalen Übereinstimmungen gibt. Wichtige Entscheidungen sind hierbei mit welcher Dosis die Behandlung begonnen wird, wann und in welcher Menge die Dosis erhöht oder verringert werden muss, wann mit dem nächsten Therapiezyklus begonnen wird und welchen Einfluss eine Komedikation auf die Behandlung hat. Daher sind unsere *in silico* Studien weitere Schritte auf dem Weg zur Unterstützung der Ärzte bei ihrer Entscheidungsfindung durch modellbasierte Ergebnisse. Neben der Simulation von Behandlungsplänen wurde ein Optimalsteuerungsproblem formuliert, welches Be-

handlungspläne hinsichtlich kurzzeitigem Krankheitsverlauf, Leukozyten-Nadir und der zu verabreichenden Menge an Ara-C und G-CSF optimiert. Die Ergebnisse der vorliegenden Arbeit liefern neue Einblicke über den Behandlungsstartpunkt und die Anzahl an Behandlungszyklen, die Verabreichung von Lenograstim und sein vorteilhafter Einfluss auf die Abtötung von leukämischen Blasten.

In Bezug auf methodische Untersuchungen wurde ein Feedback-Optimalsteuerungsalgorithmus mit optimalen Messzeitpunkten durch optimale Versuchsplanung vorgeschlagen und auf das *Lotka-Volterra fishing* Problem angewendet. Schließlich haben wir *Fisher's Scoring* Methode im Rahmen der Parameterschätzung für nichtlineare Modelle mit gemischten Effekten untersucht. Für zwei Beispiele, welche sich in ihrer Modellkomplexität und Anzahl an Messungen unterscheiden, wurde Fisher's Methode mit etablierten Standardmethoden verglichen. Insgesamt trägt die vorliegende Arbeit zu einem besseren Verständnis der Chemotherapie und resultierender Myelosuppression während der Konsolidierungstherapie bei AML Patienten und der Erhaltungstherapie von ALL bei Kindern bei. Zukünftige klinische Studien sind im nächsten Schritt notwendig, um die in dieser Arbeit vorgeschlagenen Behandlungspläne weiter zu untersuchen.

Acknowledgements

I would like to start thanking the European Research Council *Mathematical Optimization for clinical Decision Support and Training* under the European Union's Horizon 2020 research and innovation program for the financial support, the opportunity to present our novel contributions and results at international conferences and the endorsement of open-access publishing.

In this context, I would like to say *thank you* to my supervisor Prof. Sebastian Sager, head of MathOpt group at the Institute of Mathematical Optimization, Faculty of Mathematics, Otto-von-Guericke University Magdeburg, who placed his trust in me and offered me this exciting interdisciplinary dissertation topic within his group. I greatly value the fact that he always had an open door for helping and guiding me making critical decisions and discussing both detailed issues and broader scopes we were aiming for.

I had a great time at the Institute of Mathematical Optimization with its open-door philosophy, open-minded colleagues and perfectly organized administration department (Susanne Hess & Ines Brückner). Especially, I would like to thank the *MathOpt group* with whom I not only had a great time at university on campus, but also during spare time, conducting poker tournaments and whiskey tastings, playing soccer (Monday/Wednesday working group soccer), watching soccer (1. FC Magdeburg) and enjoying group retreats at nicely chosen places.

Next, I would also like to express my sincere gratitude to my collaboration partners Dr. Enrico Schalk and Prof. Thomas Fisher from the Department of Hematology and Oncology, University Hospital Magdeburg, Daniela Weber and Prof. Hartmut Döhner from the Department of Internal Medicine III, University Hospital Magdeburg and Dr. Jakob Zierk, Thomas Raupach, Prof. Manfred Rauh and Prof. Markus Metzler from the Department of Paediatrics and Adolescent Medicine, University Hospital Erlangen for sharing exciting clinical data, for fruitful discussions and their interest in our interdisciplinary research projects.

Another word of thanks is addressed to Anna Gebhard, Patrick Lilienthal and Robert Scholz for their careful proof-reading of this thesis and their valuable comments.

I would like to thank Prof. Stefan Körkel and his former research group *Optimum Experimental Design* at the Interdisciplinary Center for Scientific Computing, University of Heidelberg forming my interest on research topics such as optimal experimental design and modeling of dynamic systems. They gave me the opportunity to see how excellent research in an interdisciplinary environment can successfully be performed and encouraged me to start a dissertation.

Many thanks to the *Graduate Research Training Program PharMetrX: Pharmacometrics & Computational Disease Modelling*, chaired by Prof. Charlotte Kloft, Freie Universität Berlin, and Prof. Wilhelm Huisinga, Universität Potsdam, for enabling me to participate in this excellent international program forming the next generation of pharmacometricians.

I want to thank my family and friends who always supported my decisions and gave me the backbone I needed for achieving all my goals. Finally, I want to express my sincerest thanks to Franzi for her support during the finalization of my thesis, her encouraging words during challenging times, her trust in my abilities and the wonderful four years spending time together and many more to come.

Contents

Abbreviations	x
1 Introduction	1
1.1 Thematic classification	1
1.2 Motivation	3
1.3 Contributions	4
1.4 Thesis overview	5
I Background, concepts and data	8
2 Medical background	9
2.1 Hematopoiesis	9
2.2 Acute leukemia	10
2.2.1 Acute myeloid leukemia	10
2.2.2 Treatment of acute myeloid leukemia	11
2.2.3 Childhood acute lymphoblastic leukemia	13
2.2.4 Treatment of childhood acute lymphoblastic leukemia	13
3 Modeling of dynamic processes	15
3.1 Ordinary differential equations	15
3.2 Semi-mechanistic pharmacokinetic/pharmacodynamic modeling	16
3.2.1 Pharmacokinetic models	17
3.2.2 Pharmacodynamic functions	20
3.2.3 Transduction models	21
3.3 Models in the context of acute leukemia	21
3.3.1 Myelosuppression model	22
3.3.2 Myelosuppression model with endogenous G-CSF	24
3.3.3 Leukemic cells	25
3.3.4 Pharmacokinetic models of cytarabine	26
3.3.5 Pharmacokinetic model of lenograstim	27
3.3.6 Pharmacokinetic models of 6-mercaptopurine	29
3.3.7 Pharmacokinetic model of methotrexate	32

4	Optimization of dynamic processes	35
4.1	Theory	35
4.1.1	Optimality conditions	36
4.1.2	Nonlinear dynamic optimization problems	37
4.2	Problem formulations	38
4.2.1	Optimal control	38
4.2.2	Parameter estimation	38
4.2.3	Optimal experimental design	45
4.3	Methods for solving dynamic optimization problems	48
4.3.1	Methods for solving nonlinear optimization problems	51
4.4	Software	54
5	Clinical data	56
5.1	Clinical data from the university hospital in Magdeburg	56
5.2	Clinical data from the university hospital in Ulm	57
5.3	Clinical data from the university hospital in Erlangen	57
II	Developed models and numerical methods for myelosuppression	60
6.1	Mathematical models for consolidation therapies of AML patients	61
6.1.1	Pharmacokinetic model of cytarabine	61
6.1.2	Secondary pharmacodynamic effects of cytarabine	64
6.1.3	Initial conditions of the differential states	68
6.1.4	Cytarabine-derived and lenograstim-reduced myelosuppression	70
6.2	Mathematical model for maintenance therapy of pediatric ALL patients	75
6.3	Feedback optimal control algorithm with optimal measurement time points	79
III	Numerical results & discussions	85
7.1	Personalized mathematical models	86
7.1.1	PK/PD model with cytarabine (Data Magdeburg)	86
7.1.2	PK/PD model with cytarabine and lenograstim (Data Ulm)	108
7.1.3	PK/PD model with 6MP and MTX (Data Erlangen)	119
7.2	Optimal treatment schedules for acute leukemia	125
7.2.1	Influence of treatment starts on leukopenia	125
7.2.2	Consolidation therapy schedules for AML derived by optimizations	125
7.2.3	Maintenance therapy schedules for ALL derived by simulations	131
7.3	Feedback optimal control algorithm for the Lotka-Volterra fishing problem	136
7.4	Fisher's method for population parameter estimations	143
IV	Summary & future perspectives	148
	Bibliography	152

Abbreviations

6MP	6-mercaptopurine
6TGN	6-thioguanine nucleotide
ALL	acute lymphoblastic leukemia
AML	acute myeloid leukemia
ANC	absolute neutrophil count
Ara-C	cytarabine
Ara-CTP	arabinofuranosylcytosine triphosphate
AraU	arabinofuranosyl-uracil
BDF	backward differentiation formula
BFGS	Broyden, Fletcher, Goldfarb, and Shanno
BM	bone marrow
BSA	body surface area
CC	consolidation cycle
CR	complete remission
CT	consolidation therapy
dCK	deoxycytidine kinase
DNA	deoxyribonucleic acid
EM	expectation maximization
FIM	Fisher information matrix
FO	first order
FOCE	first order conditional estimation
FOCEi	first order conditional estimation with interaction
G-CSF	granulocyte-colony stimulating factor
GI	gastrointestinal
GN	Gauss-Newton
HAM	high-dose cytarabine and mitoxantrone
HGPRT	hypoxanthine-guanine phosphoribosyltransferase
HSC	hematopoietic stem cell
IIV	interindividual variability
IVP	initial value problem
KKT	Karush-Kuhn-Tucker
LICQ	linear independence constraint qualification
LM	Levenberg-Marquardt
MAE	mean absolute error

MAP	maximum a posteriori
MeMP	methyl-mercaptopurines
M-M	Michaelis-Menten
MMT	mean maturation time
MRD	minimal residual disease
MT	maintenance therapy
MTX	methotrexate
MTXPG	methotrexate polyglutamate
NLME	nonlinear mixed-effects
NLP	nonlinear optimization problem
OED	optimal experimental design
ODE	ordinary differential equation
PK	pharmacokinetic(s)
PD	pharmacodynamic(s)
PM	personalized model
QP	quadratic programming
RBC	red blood cell
RMSE	root mean squared error
SAEM	stochastic approximation expectation maximization
S-HAM	sequential high-dose cytarabine and mitoxantrone
SQP	sequential quadratic programming
RNA	ribonucleic acid
TPMT	thiopurine methyltransferase
VPC	visual predictive check
WBC	white blood cell

1 | Introduction

1.1 Thematic classification

The present thesis is located at the intersection of mathematics, control theory, systems biology, pharmacology, pharmacometrics and medicine. The principle objectives are the description and prediction of healthy and cancer cells during chemotherapy of acute leukemia and the simulation, optimization and analysis of individual treatment schedules using tailored mathematical models.

Leukemias are a group of malignant disorders of the blood and bone marrow (BM) [1]. In the UK, leukemia is the 13th most common cancer accounting for 3% of all new cancer cases in 2016. The U.S. National Cancer Institute reports a similar estimated number of 3.5% of all new cancer cases for 2019. In Germany, 2.7% of all diagnosed cancers of women and 3.1% of men are leukemia. Although leukemia is a relatively rare cancer disease in comparison to breast, lung or gut cancer, it is very heterogeneous with a low 5-year survival rate and a high death rate [2].

Pharmacometrics, the science of developing and applying mathematical and statistical methods (including modeling, simulation and optimization) in the fields of biology, pharmacology and diseases, is intended to help

- characterizing and understanding a drug's behavior and response in terms of its pharmacokinetic(s) (PK), pharmacodynamic(s) (PD) and biomarker/treatment outcomes,
- interpreting the interaction between biomarkers and clinical effects,
- identifying and predicting critical periods during treatment,
- identifying subpopulations with varying PK of an administered drug,
- evaluating dosing strategies *in silico* before studies are conducted and
- developing more individualized treatment schedules based on models tailored to the individual patient.

Based on the clinical questions and the available measurement information, specific modeling concepts are used, differing in their detailedness and physiological foundation of describing the dynamical processes.

The sophisticated description of complex systems using mechanistic modeling is defined as systems pharmacology which is emerged through the fusion of systems biology and PK/PD [3–5]. These models are often multiscale, multilevel, and physiologically based and are used to understand and analyze drug effects at whole-organism levels and extrapolate PK and PD properties. A complementary modeling approach is reflected by empirical models which describe the clinical data and dynamic processes through one or more empirical compartments representing the body with limited physiological interpretability and thus might not be suited for extrapolations or predictions. The mechanistic approach results in the most advanced and reliable mathematical models contributing to a better understanding of the biological process but often the available data is not sufficient to inform all parts of the model. A good compromise between these two categories are semi-mechanistic modeling approaches trying to find a balance between mechanistically modeling the most important dynamics supported by available experimental data and the agglomeration of physiological properties through empirical functions.

The mathematical models presented in this thesis contain values which characterize specific time profiles of biomarkers such as granulocyte-colony stimulating factor (G-CSF) and clinical outcomes like white blood cells (WBCs) and leukemic blasts. The values are either known and can be fixed to constants or they are not exactly known and defined as parameters whose values need to be identified via experiments. Appropriate values for these parameters can be determined by fitting the model to experimental/clinical data. Regarding an experimental study with several patients, different parameter estimation approaches exist to identify the optimal set of parameter values for each patient. The state-of-the art method nowadays is the population-based approach, or (non)linear mixed-effects approach, providing a set of estimated parameters describing the population and individual sets of parameters for each subject together with information of the interindividual variability (IIV) also called between-subject variability [6]. Other possibilities to handle data from several patients are the so called two-step and naïve pooling approach. The two-step method firstly estimates the parameters of each patient individually and afterwards descriptive statistics for the population are generated. In the naïve pooling approach, all individual datasets are pooled to one large dataset and the mathematical model is fitted simultaneously without an assignment of the measurements to the patients ignoring individual differences in exposure and response. Both approaches have been shown to estimate biased parameter values such that these methods are rarely used nowadays [7].

After model development and fitting, simulation and optimization methods can be applied to analyze and answer clinically relevant questions and support physicians in their decision making. Simulation studies with heuristically defined experimental designs and strategies are widely used to generate *what if* scenarios and investigate biological hypotheses. The heuristic part can be replaced with optimization-derived experimental strategies based on the objective of interest. The experimental control strategy as the solution of an optimization problem can highlight strategies which are optimal for the current problem and might be non-intuitive for the corresponding

experimenter.

The application of optimization methods becomes more and more a state-of-the-art method in the preparation and design of experimental or clinical studies. For example, the US Food and Drug Administration suggests in their guidance document for industry on *Population Pharmacokinetics* the usage of optimal experimental design (OED) methods for the computation of the most informative measurement time points in clinical studies [8]. Another example is the insulin administration derived by an adaptive optimization algorithm for patients with type-1 diabetes via an artificial pancreas, mimicking a patient's glucose regulating function through an insulin pump and continuous glucose monitor. The artificial pancreas was tested for six months in a randomized, multicenter trial [9]. Within simulation studies, the heuristic scenarios already consider constraints like limited amount of drug that can be administered (e.g. in oral dosing), practically feasible administration and measurement times or dosing regimens (e.g. maximal duration of infusions). Within the optimization problems all these aspects have to be considered such that the obtained results are clinically relevant. Further, the simulation and optimization results are grounded on the developed models. A profound model analysis and evaluation using clinical data should be performed such that the inter- and extrapolations of the model outcomes are reliable and applicable in real life.

1.2 Motivation

In this work we deal with adult acute myeloid leukemia (AML) and pediatric acute lymphoblastic leukemia (ALL).

In 1994, Mayer *et al.* [10] established intermediate/high-dose instead of low dose cytarabine (Ara-C) schedules to prevent relapses after complete remission (CR) of AML patients. Since then, Mayer's proposed treatment schedule is one of the most important treatments during consolidation therapy (CT) of AML. Still, knowledge on the PK and PD of Ara-C is limited and specific adverse events occur regularly after treatment. Novel treatment schedules are analyzed in clinical studies achieving reduced adverse events and higher survival rates [20]. Besides novel treatment schedules, co-medications such as G-CSF can be administered seeking to overcome the occurrence of adverse events. But also in this case, it is not known what the best timing of G-CSF administration should be and what impact G-CSF has on leukemic cells.

In pediatric acute lymphoblastic leukemia (ALL), 10-15% of the patients experience a relapse and event-free survival of patients with first relapse is just around 35 to 50% [11]. Thus, successful treatment requires initial high-intensity chemotherapy, followed by low-intensity oral maintenance therapy (MT) with oral 6-mercaptopurine (6MP) and methotrexate (MTX) until 2-3 years after disease onset. However, intra- and IIV in the PK and PD of 6MP and MTX make it challenging to balance the desired antileukemic effects with undesired excessive myelosuppression during MT.

We leverage pharmacometric approaches to investigate several aspects of the mentioned problems for the two types of leukemia. The investigated aspects are listed in the next section. We concentrate on semi-mechanistic modeling approaches partly driven

by the available data and applied different parameter estimation techniques (individual, naïve pooling and population approach) to fit the developed models to clinical data. With the developed models, we performed simulations and used direct optimal control methods to derive individualized treatment schedules.

1.3 Contributions

The contributions of this interdisciplinary work are threefold. Firstly, we determine several medical aspects which are of high clinical relevance and need further investigation:

- Recovery time of **WBC** counts after standard and dense **Ara-C** treatment schedules
- Relationship between timing of consolidation cycle (**CC**) start and **WBC** recovery time
- Effect of **G-CSF** administrations on **WBCs** and leukemic cells
- Optimal schedules of **Ara-C** and **G-CSF** regarding relapse and adverse events
- Optimal number of **CT** cycles
- Stratification of **AML** patients for optimal treatment timing
- Heterogeneity in pediatric **ALL** treatment efficacy and toxicity

Their analysis and understanding can help physicians to propose more tailored treatment schedules simultaneously reducing the occurrence of adverse events. Secondly, we investigate these questions with the development of mathematical models and their use in simulation and optimization studies:

- **PK** model of **Ara-C**
- **PK/PD** model for the **CT** of **AML** considering secondary effects of **Ara-C**
- **PK/PD** model for the **CT** of **AML** with **Ara-C** and lenograstim
- **PK/PD** model for the **MT** of pediatric **ALL** with **6MP** and **MTX**

As a third part, we investigate different numerical methods enhancing the population approaches:

- Investigation of Fisher's method in the context of parameter estimation for non-linear mixed-effect models
- Feedback optimal control algorithm with a focus on measurement times derived from **OED**

During the development of this thesis the following publications have been published:

References

- [A] **Jost, F.**, Schalk, E., Weber, D., Döhner, H., Fischer, T. & Sager, S. Model-based optimal AML consolidation treatment. *IEEE Transactions on Biomedical Engineering*. accepted (2020).
- [B] **Jost, F.**, Zierk, J., Le, T. T., Raupach, T., Rauh, M., Suttorp, M., Stanulla, M., Metzler, M., Sager, S. Model-based simulation of maintenance therapy of childhood acute lymphoblastic leukemia. *Frontiers in Physiology* **11**, 217 (2020).
- [C] **Jost, F.**, Schalk, E., Rinke, K., Fischer, T. & Sager, S. Mathematical models for cytarabine-derived myelosuppression in acute myeloid leukaemia. *PLoS One* **14**, e0204540 (2019).
- [D] Le, T. T., **Jost, F.**, Raupach, T., Zierk, J., Rauh, M., Suttorp, M., Stanulla, M., Metzler, M. & Sager, S. A mathematical model of white blood cell dynamics during maintenance therapy of childhood acute lymphoblastic leukemia. *Mathematical Medicine and Biology* **36**, 471–488 (Oct. 2018).
- [E] **Jost, F.**, Sager, S. & Le, T. A Feedback Optimal Control Algorithm with Optimal Measurement Time Points. *Processes* **5**, 1–19 (2017).
- [F] **Jost, F.**, Rinke, K., Fischer, T., Schalk, E. & Sager, S. Optimum experimental design for patient specific mathematical leukopenia models. *IFAC-PapersOnLine* **49**, 344–349 (2016).
- [G] Rinke, K., **Jost, F.**, Findeisen, R., Fischer, T., Bartsch, R., Schalk, E. & Sager, S. Parameter estimation for leukocyte dynamics after chemotherapy. *IFAC-PapersOnLine* **49**, 44–49 (2016).

Within this thesis, the results and their discussion of the publications [A], [B], [C] and [E] are presented in an altered form within the different sections. The conference papers [F] and [G] and the publication [D], out of which the follow-up publication [B] resulted, are not considered within the thesis. The next section gives an overview of the thesis, describes which chapters belong to which publication and explains the contributions of the authors of the considered publications [A], [B], [C] and [E].

1.4 Thesis overview

The first part of the thesis gives an introduction to hematopoiesis and blood cancers, especially acute myeloid and lymphoblastic leukemia, we are dealing with. Afterwards, we present different mathematical concepts to model, simulate and optimize drug induced and reduced myelosuppression and dynamics of cancer cells. Several mathematical models for myelosuppression and for the pharmacodynamics of various drugs are described. The chapter concludes with the description of three different datasets used for model fitting and cross-validation.

The subsequent part comprises novel mathematical models and numerical methods for drug induced myelosuppression. Next, we present the results of model fitting and validation to clinical data and interesting outcomes from state-of-the-art and optimized treatment schedules.

Finally, we summarize our findings in the last part and give an outlook for future perspectives.

From the perspective of the four presented publications [A], [B], [C] and [E], in the following we will describe in which sections the content of each publication can be found.

Publication [A]

The PK/PD model is presented in section 6.1.4, the model fitting in section 7.1.2 and the investigation of optimal treatment schedules in section 7.2.2.

Contributions: FJ developed the PK/PD models, proposed the study designs, performed the numerical computations and wrote the first draft of the manuscript. SS, ES and TF contributed to the model development, the study designs and the interpretation of the results. ES, TF, DW and HD provided the clinical data. All authors contributed to writing the final manuscript.

Publication [B]

The PK/PD model is presented in section 6.2, the model fitting in section 7.1.3 and the analysis of different available treatment schedules in section 7.2.3.

Contributions: FJ developed the PK/PD models, performed the numerical computations and wrote the first draft of the manuscript. JZ, TTTL, TR, MR, MM, and SS contributed to the model development, the study designs, and the interpretation of the results. MSu and MSt provided clinical data. All authors contributed to writing the final manuscript.

Publication [C]

The PK/PD modeling is presented in sections 6.1.1 to 6.1.3, the model fitting in section 7.1.1 and the analysis of the treatment start on nadir values in section 7.2.1.

Contributions: FJ extended and implemented the mathematical models and did all numerical computations. ES and TF contributed to modeling, study design and provided clinical data. KR contributed to data, mathematical modeling and developed the PK model for Ara-C. SS contributed to mathematical modeling, numerical approaches, and study design. All authors contributed to discussion of results and writing of the final paper.

Publication [D]

The feedback optimal control algorithm with optimal measurement time points is presented in section 6.3 and the related numerical results in section 7.3.

Contributions: FJ implemented the algorithm and did all numerical calculations and is the corresponding author of the article. LTT and SS contributed to the general idea, to the theoretical aspects, and to proof-reading of the manuscript.

Part I

Background, concepts and data

2 | Background, concepts and data: Medical background

In this chapter, we give an introduction to hematopoiesis, the hematopoietic disease *acute leukemia* and review the state-of-the-art chemotherapy treatments. For further information the interested reader is referred to [12] or [13].

2.1 Hematopoiesis

Hematopoiesis is defined as the formation of blood cells, specified in different cell lineages, predominantly taking place in the **BM**. All mature cells originate from multipotent hematopoietic stem cells (**HSCs**) located in the **BM** with multilineage developmental potential and are ultimately mandatory for the regeneration of hematopoiesis after hematopoietic disorder caused by e.g. stem cell transplantation or chemotherapy. Due to the limited lifespan of matured cells and the 10-fold lower amount of total **HSCs** compared to the daily human need for homeostasis (maintaining steady-state blood counts), **HSCs** perform regulated cell divisions. The stem cell division is intended to maintain the stem cell pool (ability of self-renewal) and to produce daughter stem cells which differentiate and mature until the cells are released from the **BM** to the circulating blood to carry out their specific functions. During this process, the cells pass several consecutive stages (compare figure 2.1) including the selection of a specific cell lineage at one point. Two main cell lineages are defined, the myeloid lineage from which erythrocytes, thrombocytes, granulocytes and monocytes result and the lymphoid lineage from which T- and B-lymphocytes and natural killer cells are formed. Figure 2.2 represents the hierarchical process of hematopoiesis with its cell line specification. Hematopoiesis and the release of matured cells from the **BM** into peripheral blood is controlled and regulated by intrinsic and extrinsic factors, such as cell-cell interactions, hematopoietic growth factors and cytokines. For example, the production of erythrocytes is mainly controlled by the hormone erythropoietin whereas neutrophils, one type of granulocytes, are mainly controlled by **G-CSF** [12]. Further differences exist regarding the mean maturation time (**MMT**), half-life and lifespan of the different cell types. Neutrophils have a **MMT** of a few days (3.9 days obtained by [14]) and a lifespan of several hours in contrast to erythrocytes with a **MMT** of 20 days and mean life expectancy in the blood stream of 120 days [12].



Figure 2.1: **Stages in hematopoiesis.** Figure adapted from [12].

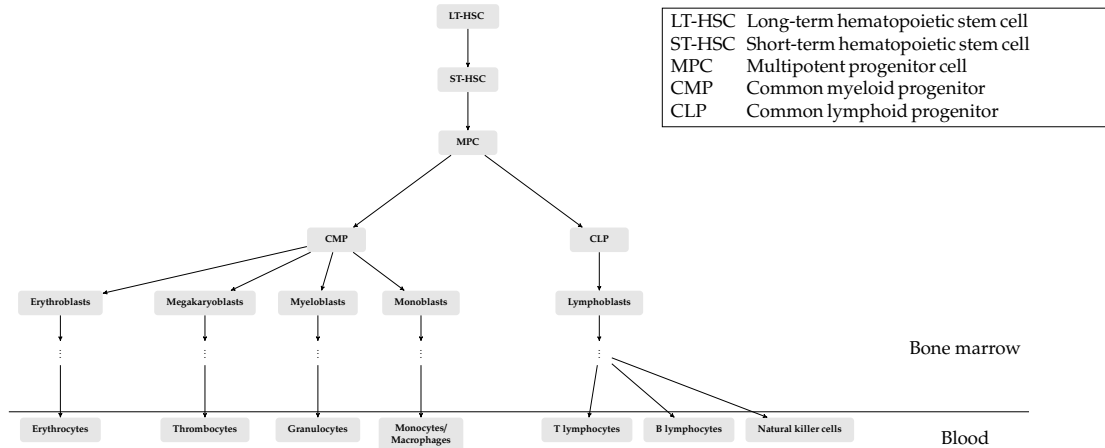


Figure 2.2: **Simplified representation of hematopoiesis.** Schematic visualization is adapted from [12, 15]. For a more detailed representation including additional stages symbolized by the arrows and dots, the interested reader is referred to [12, 13]

2.2 Acute leukemia

Leukemia is a cancer of blood cells, mainly of **WBCs** (leukocytes), divided into four subtypes, i.e. acute/chronic myeloid/lymphoblastic leukemia. A distinction between myeloid and lymphoblastic is made according to the affected cell lineage. Further, the disease is either defined as acute or chronic depending on its abrupt occurrence and short-lived outcome or its persistence. In the present thesis, we are focusing on acute leukemia, especially **AML** and childhood **ALL**. As references and further information see [12, 13, 16–18].

2.2.1 Acute myeloid leukemia

AML is a malignant clonal disorder of myeloid stem and progenitor cells (compare figure 2.3) primarily occurring in older adults with a median age at diagnosis of 70 years [2, 12, 17]. In untreated **AML**, immature neoplastic myeloid blasts proliferate rapidly and suppress the maturation of blood cells. Consequently, the disease is fatal for the majority of patients ($\approx 80\%$) with a 5-year survival of 40%, for patients younger than 55 to 60 years and 5% to 10% for patients older than 60 years [2].

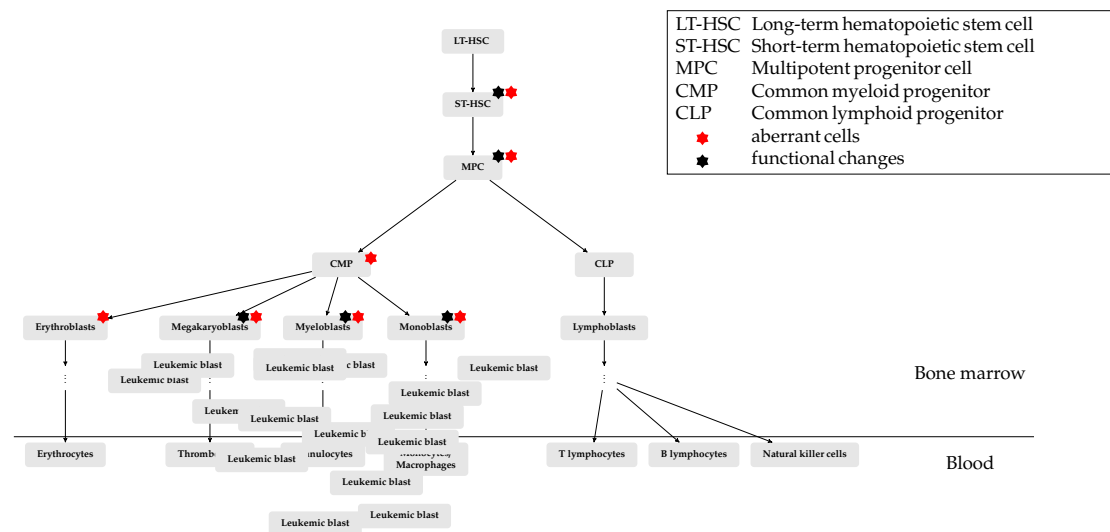


Figure 2.3: **Simplified representation of disorders in hematopoiesis arising from acute myeloid leukemia.** The immature neoplastic myeloid blasts occurring in acute myeloid leukemia are represented by the numerous leukemic blast boxes arranged in a chaotic manner. Schematic visualization is adapted from [17].

2.2.2 Treatment of acute myeloid leukemia

Chemotherapy treatment of AML is usually divided into an induction and a consolidation phase [19]. The goal of the induction phase is the eradication of blasts. By blasts, we refer to a combination of aberrant/leukemic and physiological blasts that are cytologically $\geq 20\%$ in the BM at the time of AML diagnosis [19]. The standard treatment consists of intensive chemotherapy with three days of anthracycline (idarubicin or daunorubicin) and seven days of Ara-C [19]. To monitor the relative numbers of blasts in each cycle, BM aspirations are collected and analyzed. After the induction phase, the relative number of blasts should be below 5% in the BM (assessed by cytology) and not measurable in the circulating blood.

In this work, we are focusing on the subsequent consolidation phase. Consolidation treatment is given once patients achieve CR and is considered the most important part of chemotherapy in preventing relapses. One standard AML consolidation treatment consists of Ara-C 3 g/m^2 (body surface area (BSA)-adjusted) intravenous infusion lasting 3 hours every 12 hours on days 1, 3 and 5 (D135) for patients aged 60 years and younger, which was investigated by Mayer *et al.* in 1994 [10] (compare figure 2.4). Older patients (> 60 years) receive an intermediate dosage of 1 g/m^2 Ara-C infusions in the same intervals (d135). In recent years, studies have proposed a dense treatment schedule at which high-dose Ara-C is administered on days 1, 2 and 3 (D123) to reduce the WBC recovery time and increase survival [20, 21].

While the goal to reduce the blasts as much as possible to prevent a relapse is identical

between the two phases, the conflicting objective to avoid complicating infections plays an important role in the consolidation phase. Neutropenia is characterized by decreased counts of neutrophil granulocytes in the peripheral blood. Equivalent, an extremely low WBC count is defined as leukopenia. These are serious and common adverse events arising during the treatment with cytotoxic chemotherapy of AML. The two forms of WBC suppression in the BM (myelosuppression) are responsible for a higher risk of infections and consequently for delayed, dose-reduced or stopped treatments, longer hospitalization periods, and mortality as the worst case [22].

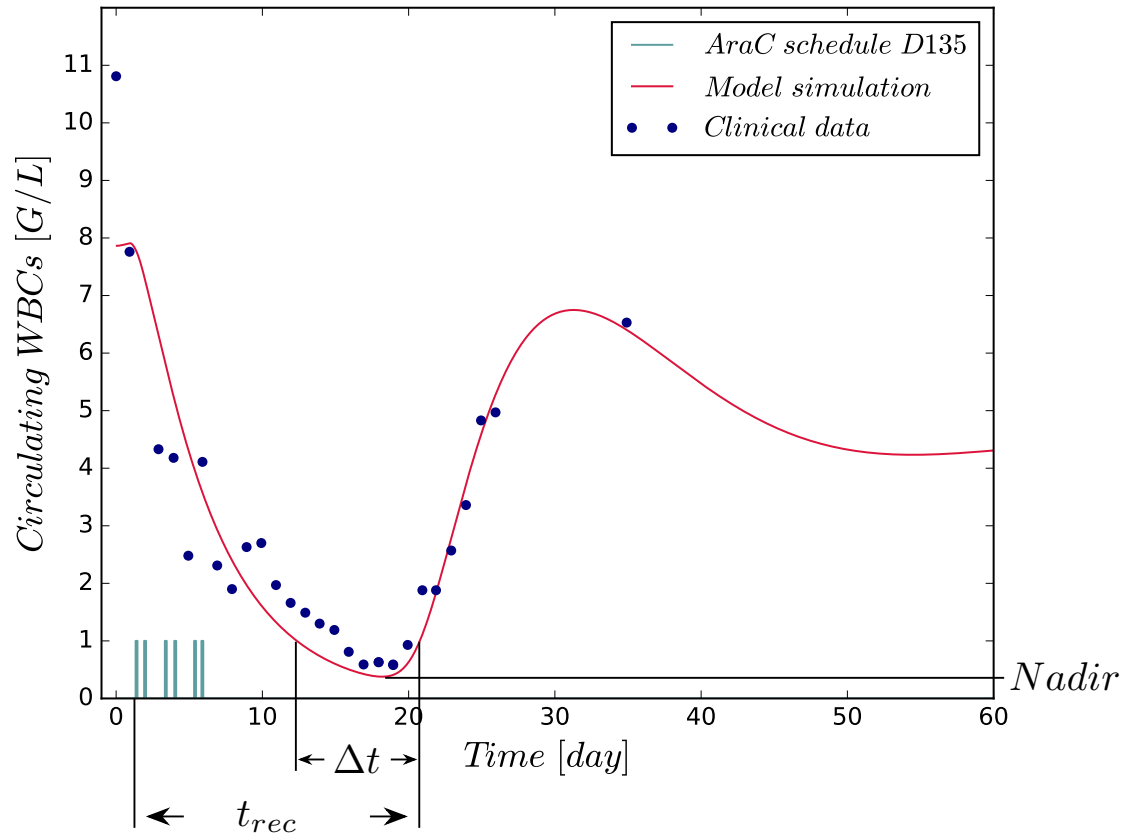


Figure 2.4: A typical progression of white blood cells after cytarabine administration during consolidation therapy of acute myeloid leukemia patients. The values of interest are the recovery time t_{rec} (time when white blood cells (WBCs) recover above 1 G/L after the start of the first cytarabine (Ara-C) administration), the myelosuppression interval Δt (the number of days with WBC count ≤ 1 G/L) and the minimal WBC concentration defined as *nadir*.

In addition to new treatment schedules, the administration of G-CSF can reduce the depth and duration of leukopenia [23]. Hematopoietic growth factors such as G-CSF regulate blood cell production, including survival, proliferation, and differentiation

of HSCs and stimulation of mature cell functions by activating signal transduction pathways [12]. The impact of G-CSF was enhanced by the clinical development of a recombinant human G-CSF, called filgrastim, in 1986 for the prevention of leukopenia and HSC mobilization before autologous or allogeneic HSC transplantation [24]. The European Society for Medical Oncology suggests daily filgrastim administration after the last day of chemotherapy until a sufficient postnadir absolute neutrophil count (ANC) recovery, for approximately 10 days [25]. On top of chemotherapy, the additional burden of daily filgrastim administration was reduced by the invention of pegfilgrastim, a pegylated form of filgrastim. The inclusion of filgrastim into a polyethyleneglycol polymer prolongs the half-life from 3.5 hours to 46-62 hours such that the permanence of pegfilgrastim in blood circulation is up to 16 days after a single administration [26], replacing the frequent filgrastim administrations. In addition to filgrastim, lenograstim was developed, which is a physicochemically, immunologically and biologically identical glycosylated recombinant G-CSF to human G-CSF [26].

Until 2017, no new drug beyond the previously mentioned treatment options had been approved for the treatment of AML, although the disease is clinically and genetically heterogeneous with a poor survival prognosis [2]. In their publication, Wats and Nimer together reviewed the latest advances in the understanding and treatment of AML discussing therapeutic advances such as genetic heterogeneity, promising drug targets, ongoing clinical trials (see also [27]) and four recently approved new drugs.

2.2.3 Childhood acute lymphoblastic leukemia

The most common cancer in children is ALL, comprising approximately 25% of all childhood malignancies. ALL is characterized by the overproduction and accumulation of immature, abnormal WBCs (lymphoblasts) and consecutive displacement of normal hematopoiesis [28].

2.2.4 Treatment of childhood acute lymphoblastic leukemia

Current treatment schedules for childhood ALL are based on combination chemotherapy and achieve long-term survival in >90% of children [28]. With some international variation, all major treatment protocols start with intensive, high-dose treatment for approximately 6 months (so-called induction and CT) followed by less-intensive, low-dose treatment (so-called MT) until 2–3 years after disease onset. While severe therapy-induced myelosuppression and frequent associated hospitalizations are acceptable up to a certain level during lymphoblast elimination in intensive treatment periods, MT aims to achieve sustained antileukemic activity against lymphoblasts below the limit of detection, with minimal impact on quality of life due to adverse effects.

The MT includes daily oral 6MP and weekly oral MTX administration to achieve WBC suppression without unintended myelotoxicity according to treatment protocol-specific target ranges. The treatment protocol AIEOP-BFM 2009 specifies a WBC target range of 1.5–3.0 G/L, ANC target range of 0.5–2.0 G/L, and recommends dose reduction for WBC counts < 1.5 G/L, neutrophils < 0.5 G/L, lymphocytes < 0.3 G/L and platelets

< 50 G/L [29, 30]. The starting dose of 6MP and MTX varies within the different protocols and doses are adjusted by the physicians if the drug-induced ANC steady-state is not within the target range due to high intra- and IIV in the PK and PD of 6MP and MTX [30] and other unexplained circumstances as infections.

3 | Background, concepts and data: Modeling of dynamic processes

In this work, we are examining mathematical models described by systems of ordinary differential equations (ODEs). They give a good tradeoff between covering the fundamentals of the representing dynamic processes and being applicable for optimization methods presented in later sections. Other modeling approaches as delay, stochastic or partial differential equations are not part of this work.

3.1 Ordinary differential equations

We assume that a dynamic process can be described as an initial value problem (IVP), consisting of a system of ODEs

$$\dot{x}(t) = f(x(t), u(t), \theta), \quad (3.1a)$$

$$x(t_0; \theta) = x_0(\theta) \quad (3.1b)$$

on a time interval $t \in [t_0, t_f] = \mathcal{T}$ with the differential state vector $x(t) : \mathcal{T} \rightarrow \mathbb{R}^{n_x}$, the time-constant process-specific parameters $\theta \in \mathbb{R}^{n_\theta}$ and the control function $u(t) : \mathcal{T} \rightarrow \mathcal{U}$, $\mathcal{U} \in \mathbb{R}^{n_u}$ affecting the state dynamics. The initial condition (3.1b) may depend on all or a subset of the parameters θ . The function $f : \mathbb{R}^{n_x} \times \mathcal{U} \times \mathbb{R}^{n_\theta} \rightarrow \mathbb{R}^{n_x}$ is assumed to be Lipschitz continuous, such that (3.1) has an unique solution on \mathcal{T} for a given control function u and parameters θ . The solution of (3.1), also called trajectory, is defined as $x^*(t) : \mathcal{T} \rightarrow \mathbb{R}^{n_x}$. Further, we assume that derivatives (also called sensitivities) of $x(\cdot)$ with respect to the different variables exist. These sensitivities are needed for the derivative-based optimization methods in the following sections. Different approaches exist to derive sensitivities, as numeric (finite differences and i-trick also called complex step derivative approximation or complex variable method), symbolic or algorithmic differentiation [31–33]. In problem formulations as OEDs or first order approximation methods for parameter estimation of nonlinear mixed-effects (NLME) models, sensitivities of $x(\cdot)$ with respect to the model parameters θ appear in the problem formulation. We are focusing on the computation of those sensitivities $G(\cdot) = \frac{dx(\cdot)}{d\theta} : \mathcal{T} \rightarrow \mathbb{R}^{n_x \times n_\theta}$ as the solution of the variational differential equations

$$\dot{G}(t) = f_x(x^*(t), u(t), \theta)G(t) + f_\theta(x^*(t), u(t), \theta), \quad G(t_0) = \frac{dx_0(\theta)}{d\theta} \quad (3.2)$$

with $x^*(t)$ the solution of (3.1) and the partial derivatives $f_x(\cdot) := \frac{\partial f}{\partial x}$ and $f_\theta(\cdot) := \frac{\partial f}{\partial \theta}$ often written in short form as subscripts within the work. Note that here and in the following matrix equations are to be understood component-wise. Again, we assume unique solutions for (3.2).

For the rest of this work, we define a function \mathcal{I}

$$\mathcal{I} : \mathbb{R}^{n_x} \times \mathbb{R}^{n_u} \times \mathbb{R}^{n_\theta} \rightarrow \mathbb{R}^{n_x}, \quad (x(t_0), u(t), \theta) \rightarrow x(t_f), \quad t \in [t_0, t_f] \quad (3.3)$$

which solves the IVP (3.1) on the time interval $t \in [t_0, t_f]$ with the end point $x(t_f)$. The software we use to solve the optimization problems internally calculate $x(\cdot)$ and its sensitivities numerically by appropriate methods as described, e.g., in [34]. The function \mathcal{I} serves as a symbolic representation of a numerical method which solves the IVP. Instead of the trajectory $x^*(t)$, which describes the solution of the IVP (3.1), function \mathcal{I} will be used within the numerical methods for solving dynamic optimization problems in section 4.3. In section 4.4 we will comment on the different numerical methods which are used in this work.

The interested reader is referred to [35, 36] for a comprehensive overview of the theory of ODEs, including existence, uniqueness and smoothness (existence and continuity of second derivatives) of its solution depending on properties of the function f and input variables. See [4, 37–39] in the context of biological and medical applications.

3.2 Semi-mechanistic pharmacokinetic/pharmacodynamic modeling

In this section, we give an introduction to semi-mechanistic PK/PD modeling. If the reader is interested in complementing the presented methods, we recommend the two textbooks [40, 41] giving a comprehensive overview and description of the fundamental mathematical concepts in the PK and PD field. From these two references and additionally selected publications, we present a collection of general mathematical concepts and formulas which are applicable to a wide range of drugs and biological processes and serve as a basis to understand and develop semi-mechanistic PK/PD models in the context of leukemia. Afterwards, in section 3.3 we introduce in detail the specific PK and PD models which we use to describe the dynamics of several cell lineages during cytotoxic treatment.

PK is the study of absorption, metabolism, distribution (through the whole body and to the site of drug action) and excretion of a drug after administration by any route, e.g. orally, as (intravenous/subcutaneous) infusion, as (intravenous/subcutaneous/intramuscular) injection or transdermally (i.e. what the body does to the drug). Whereas PD is defined as the study of the time course of the biological effects of a drug and the mechanisms of drug action (i.e. what the drug does to the body). The definition of and relation between PK and PD are illustrated in figure 3.1.

PK and PD models can be regarded as separate model blocks which are linked by special functions presented in the next section. Thus, we start introducing basic concepts

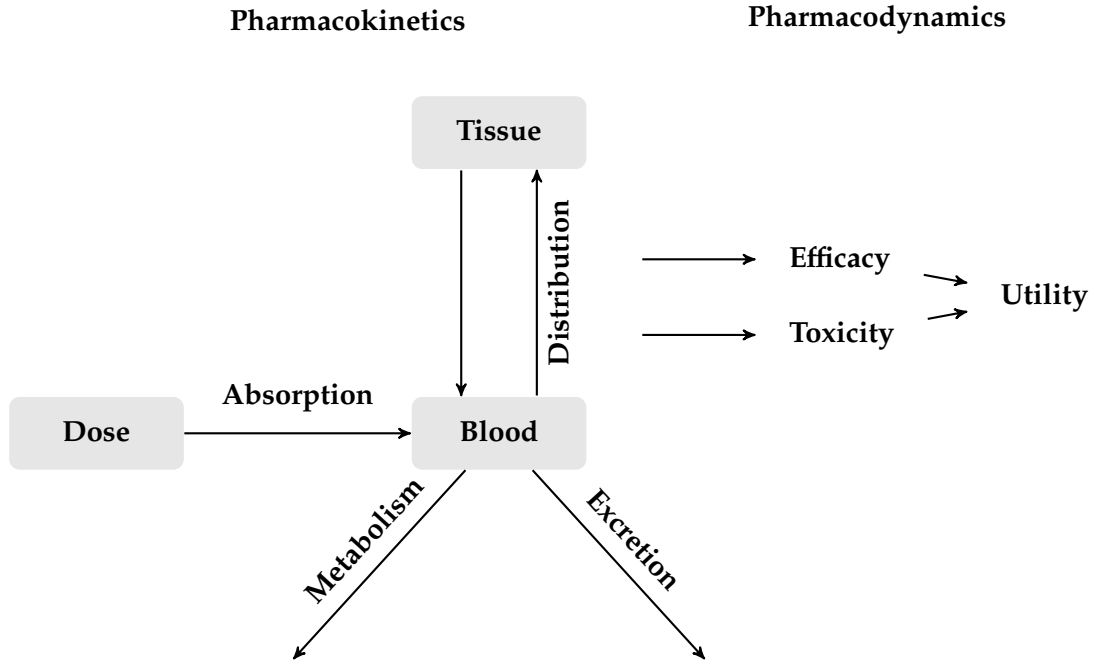


Figure 3.1: Schematic presentation of pharmacokinetic(s) and pharmacodynamic(s). The figure is adapted from [42].

of PK modeling, afterwards we present the three most common PD functions which are used to model the interaction between the PK models and arbitrary PD models, out of which we present one special model type (transduction models) in the subsequent section. In section 3.3, all presented PD model variations originate from this PD model type.

3.2.1 Pharmacokinetic models

In compartmental modeling, the PK of a drug can be described in the simplest way by a one-compartment model defined by the IVP

$$\dot{C}(t) = -K C(t) = -\frac{CL}{V} C(t), \quad t \in \mathcal{T} \quad (3.4)$$

$$C(t_0) = C_0 = \frac{D}{V} \quad (3.5)$$

or its analytical solution

$$C(t) = \frac{D}{V} \exp(-K t), \quad C_0 = \frac{D}{V}, \quad t \in \mathcal{T}. \quad (3.6)$$

Here, the whole body is defined as one single compartment in which at time point t_0 a drug D is administered in form of an intravenous infusion or injection. C_0 is the concentration of the compartment at time of administration t_0 governing by the drug amount D and the volume of distribution V . In this scenario, absorption can be neglected, such that the model captures only the disposition (distribution and elimination processes) of the drug. $\dot{C}(t)$ is the rate of change of the plasma concentration per unit time, $C(t)$ is the plasma concentration and K is the first order rate constant associated with the drug's elimination process. K can also be described by the clearance CL and the volume of distribution V , defined as the space or volume into which a drug is distributed. If the drug is administered by any other than the intravenous route, an absorption step is contained to the PK which results in adding a second compartment to the mathematical model. The second compartment, defined as absorption compartment modeling the absorption processes before the drug enters the central compartments, is connected to the central compartment via a first-order process with the absorption rate constant K_a . Now, the rate of drug change is controlled by the absorption and elimination rate. Bioavailability F , multiplied to the administered dose, is defined as the fraction of the dose that enters the central compartment. This parameter can only be determined if two different types of administrations are compared and assuming that the clearance is constant between the two occasions. Absolute bioavailability is observed when the comparing type is an intravenous infusion, otherwise we determine relative bioavailability. If the observed concentration-time profile shows more than one exponential (mono-exponential) decline, a one-compartment model may not be sufficient to describe the concentration-time profile. Then, multi-compartmental models are necessary to describe the distributional processes such as perfusion and diffusion into and out of the peripheral compartments, visible in concentration-time curves as distinct declines with different slopes. Either the compartments are characterized by means of a chain with uni- or bi-directional transition rates (catenary model) or the peripheral compartments are all connected to the central compartment with uni- or bidirectional transition rates (mamillary model). In both cases, drug administration and elimination only occur to and from the central compartment. Often, the central compartment represents blood or plasma and other rapidly equilibrating tissues, whereas the peripheral compartments symbolize more slowly equilibrating tissues as muscles or adipose tissue, which may be poorly perfused or enclosed by difficult-to-pass membranes.

For simplicity, we assume a two-compartment model with a central and peripheral compartment C_1 and C_2 parameterized by the transition rates k_{12} , k_{21} , the elimination rate k_{10} and the volume of distribution of the central compartment V_1 . At time point t_0 a drug amount D is administered which defines together with V_1 the initial drug concentration $C_1(t_0)$ in the central compartment C_1 . The peripheral compartment C_2 is set to zero at the start of treatment. The IVP for the two-compartment model is defined

as

$$\dot{C}_1(t) = -k_{12} C_1 + k_{21} C_2 - k_{10} C_1 \quad (3.7)$$

$$\dot{C}_2(t) = k_{12} C_1 - k_{21} C_2 \quad (3.8)$$

$$C_1(t_0) = D/V_1 \quad (3.9)$$

$$C_2(t_0) = 0 \quad (3.10)$$

with the variables k_{12} , k_{21} , k_{10} and V_1 defined as micro-constants. The two-compartment model can additionally be parameterized with more physiologically meaningful parameters clearance CL , intercompartmental clearance Q and the volumes of distribution V_1 and V_2 which are nowadays more often used. The IVP (3.7) is then reformulated to

$$\dot{C}_1(t) = -Q/V_1 C_1 + Q/V_2 C_2 - CL/V_1 C_1$$

$$\dot{C}_2(t) = Q/V_1 C_1 - Q/V_2 C_2$$

$$C_1(t_0) = D/V_1$$

$$C_2(t_0) = 0$$

with the relation

$$k_{12} = Q/V_1 \quad (3.11)$$

$$k_{21} = Q/V_2 \quad (3.12)$$

$$k_{10} = CL/V_1 \quad (3.13)$$

between the micro-constants and physiological parameters.

Not all drugs are already present in their activated form after entering the body or the site of action. Drugs might have to be transformed or metabolized before they become pharmacologically activate. If this is the case, additional compartments can be introduced and linked via linear or nonlinear functions to the central compartment representing the metabolized substrates (active metabolite). One possibility to describe the process of metabolism is to use Michaelis-Menten (M-M) kinetics. This type of function is presented in the next section as it is also used to describe the PD effects of drugs.

During the treatment of leukemia, the patients not only receive one drug administration but multiple administrations over a few days or also over 1-2 years. Depending on the half life of the drug and the time intervals of administrations, the idea of multiple dosing is the achievement of a constant concentration level over a longer time period (steady state). In other treatment regimens, multiple doses are needed for a treatment success but no accumulation of drug concentration is intended.

In this work, we use and discuss PK models of Ara-C, lenograstim, 6MP and MTX for the treatment of acute myeloid and lymphoblastic leukemia administered by different routes of administration:

- intravenous infusions (Ara-C),

- subcutaneous injections (lenograstim),
- oral dosing (6MP, MTX).

The route of administration impacts the PK and PD of the drug including tissue distributions, delays between administration and drug effect or first pass effects.

3.2.2 Pharmacodynamic functions

The content of the current and the following section is a summary of [7, 43].

The relationship between the concentration of the drug and the response of the system is defined by a PD function. A commonly used function is the E_{max} model

$$E(t) = E_0 \pm \frac{Emax C(t)^h}{EC50^h + C(t)^h}, \quad (3.14)$$

formulated by a baseline effect E_0 (if appropriate), the drug concentration $C(t)$, the maximum possible drug effect ($Emax$) and the drug concentration (potency) $EC50$ resulting in 50% of the maximal effect $Emax$. Here, we assume that h is equal to 1 but in the following we will also comment on h unequal to 1. The time-course of the drug effect $E(t)$ at the site of action is derived by drug-receptor interaction and several assumptions, including the law of mass action, listed below:

- linear relationship between drug effect (response) and receptor occupancy at a particular time
- one receptor has only one binding site forming binary complexes
- only occupied receptors have zero response $\rightarrow E(C(t) = 0) = 0$
- one receptor produces one type of response
- constant receptor number $Emax$

The sigmoidal E_{max} model, defined by a Hill exponent $h \neq 1$ yields variability in the steepness of the concentration-effect relationship. Higher values of h describe all-or-nothing effects whereas $h < 1$ results in flat concentration-effect curves.

If not the full range of concentration is obtained and only concentrations less than the $EC50$ are available (less than 20% of maximum drug effect is observed), equation (3.14) can be reduced to a linear PD function

$$E(t) = E_0 \pm slope C(t) \quad (3.15)$$

representing a drug effect which is proportional to drug concentration with the parameter *slope*.

When concentration-time profiles between 20% and 80% of maximal drug effect are available, the drug effect is proportionally related to the logarithmic drug concentration:

$$E(t) = E_0 + slope \log(1 + C(t)). \quad (3.16)$$

The PD functions (3.15) and (3.16) are not based on biological mechanism but have been successfully applied and commonly used in PK/PD modeling and are good approximations when the range of concentrations limits the ability to predict E_{max} . Extrapolations are not supposed to be done, since no information about E_{max} is available.

3.2.3 Transduction models

The PD functions from the previous section are one core element of the PD models but still a variety of different PD models (direct effect, link effect (effect compartment), indirect effect (turnover), tolerance compartment) describing drug-system interactions exist [7, 40]. The differences occur from various physiological mechanisms which result in different PD models, e.g. different sites of action and observable drug effects, leading to an immediate or delayed relationship between concentration and response. In this work, we are confronted with transduction models, also called transit PD compartment models, in which the PD effect is observable at the last compartment (effect compartment) whereas the site of action of the drug arises at the first transit compartment. A schematic presentation of the PD model with an arbitrary PK model and PD function is shown in figure 3.2. Between the first transit compartment and the effect compartment, a chain of compartments are connected via own transfer functions (here different first order rate constants k_{tr}^i) accounting for the delay between drug administration and observed response. The transfer functions represent the time it takes for the state entering and leaving the compartments. In our case, the transfer functions are either different or the same first order transition rate constants $k_{tr}^1, \dots, k_{tr}^n$. These models are used when long delays between the drug administration and the observed effect occur, e.g. in drug-induced myelosuppression [7] and ODEs are preferred to delay differential equations. We refer the interested reader to [44] for the presentation and discussion of two additional approaches (stochastic process and gamma distribution) and their equivalence for modeling delays. Regarding delay differential equations, in [45] a link between ODEs and gamma distributed discrete delay differential equations models describing delays was shown.

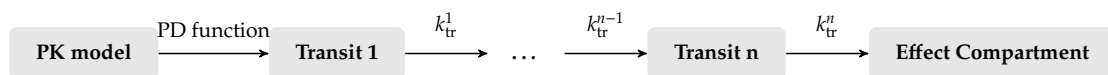


Figure 3.2: Pharmacodynamic transit compartment model with an arbitrary pharmacokinetic(s) model and pharmacodynamic(s) function.

3.3 Models in the context of acute leukemia

In this section, we present several published PK and PD models which we use, adapt, extend or modify to fit our medical applications and purpose. The PD models represent the dynamics of different biomarkers, especially leukocytes, neutrophils, leukemic cells

and endogenous **G-CSF**, which play an important role in the understanding of disease progression and adverse events of **AML** during **CT** and childhood **ALL** during **MT**. They are all based on models representing the hematopoiesis via transduction models.

There are many different levels on which hematopoiesis [46–48], granulopoiesis [49–51], myelosuppression [52–55] and dynamics of leukemic cells [48, 56–60] can be modelled [61, 62]. Further, several hematopoiesis models combining endogenous and exogenous **G-CSF** have been published for the prediction of myelosuppression of neutrophils [63–67] and leukocytes [68–70]. A comprehensive overview and summary of the various models is given in the recently published reviews [71, 72]. Depending on the medical question, the required outcome and the available biomarker information in the different projects, we analyze models that capture only the most important dynamics for (non-)leukemic cells and *agglomerate* different physiological effects into simplified expressions. Higher levels of detail in more sophisticated models, covering many physiological properties and thus providing a deeper understanding of biological phenomena, come at the price of needing more observed biomarker data and model parameters. Depending on the available information and desired research question, more complex models can be reformulated into minimalistic models that concentrate on the fundamental physiological mechanisms without a qualitative loss of the outcome [45, 73]. The developed **PK/PD** models in section 6.1 and 6.2 are based on the **PD** models from [48, 52, 53] and we will introduce these three models in the next sections. Afterwards, we describe in detail the **PK** models of the appropriate drugs which will be linked to the **PD** models.

3.3.1 Myelosuppression model

In 2002, Friberg *et al.* published a **PK/PD** model describing myelosuppression induced by different chemotherapeutic agents (docetaxel, paclitaxel, and etoposide) [52]. The well studied model showed a good trade-off between capturing the important aspects of the dynamics, containing a moderate number of identifiable model parameters, and being applicable for different cytostatic drugs. It has become the gold-standard model in pharmacometrics [72] with different **PK** and population-based modifications to topotecan [74], to daunorubicin [75], to a combination therapy of **Ara-C** (low-dose), etoposide and daunorubicin in the induction treatment for **AML** [76], to a physiologically based **PK** model for the induction therapy of **AML** patients with daunorubicin and **Ara-C** (low-dose) [77], to a combination therapy of carboplatin, etoposide and thiotepa [78], to paclitaxel [55], to an individual-based approach [79], and to drug specific optimizations [57].

As previously presented, **WBCs** derive from differentiated, matured **HSCs** which passed several intermediate stages during maturation (c.f. section 2.1). The chain of maturation is reflected in the mathematical model as a clustering of cells in several consecutive compartments with identical properties. Each compartment is described as a differential state. The $3 + n_{\text{tr}}$ differential states of the mathematical model are the amount or concentration of an arbitrary drug x_1 , the amounts x_{pr} of proliferating cells, $x_{\text{tr},1}, \dots, x_{\text{tr},n_{\text{tr}}}$ of differentiating cells in n_{tr} transient compartments, and x_{ma} of mature,

circulating WBCs per liter.

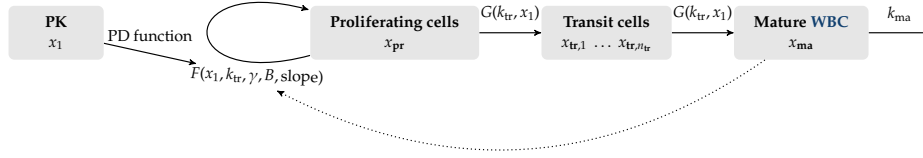


Figure 3.3: **Schematic presentation of chemotherapy induced myelosuppression of white blood cells.** The figure is adapted from [52].

The differential equations that correspond to figure 3.3 are

$$\dot{x}_1(t) = f_{PK}(\cdot) \quad (3.17a)$$

$$\dot{x}_{pr}(t) = -G(k_{tr}, x_1) x_{pr}(t) + F(x_1, k_{tr}, \gamma, B, \text{slope}) x_{pr}(t) \quad (3.17b)$$

$$\dot{x}_{tr,1}(t) = G(k_{tr}, x_1) x_{pr}(t) - G(k_{tr}, x_1) x_{tr,1}(t) \quad (3.17c)$$

$$\dot{x}_{tr,2}(t) = G(k_{tr}, x_1) (x_{tr,1}(t) - x_{tr,2}(t)) \quad (3.17d)$$

...

$$\dot{x}_{tr,n_{tr}}(t) = G(k_{tr}, x_1) (x_{tr,n_{tr}-1}(t) - x_{tr,n_{tr}}(t)) \quad (3.17e)$$

$$\dot{x}_{ma}(t) = G(k_{tr}, x_1) x_{tr,n_{tr}}(t) - k_{ma} x_{ma}(t) \quad (3.17f)$$

with a PK model f_{PK} and the functions F and G which will be chosen differently in section 6.1.2 and are defined as

$$G = k_{tr} \quad (3.18)$$

$$E = \text{slope} \log(1 + x_1(t)) \quad (3.19)$$

$$F = (1 - E) k_{tr} (B/x_{ma})^\gamma \quad (3.20)$$

in the standard model.

For fixed transition rate k_{tr} , the number of compartments can be used to model the delay between the proliferating and circulating cells (due to the MMT [80]). As there is no common consensus on the precise number of differentiation stages [47, 81] we compare $n_{tr} = 6$, as proposed by Nock [78], $n_{tr} = 3$, as proposed by Friberg *et al.* [52] and $n_{tr} = 1$, proposed in this work in which we comprise the whole maturation process into one transition compartment. The fusion of the differentiation steps into one compartment is justified by the MMT from proliferating stem cells to circulating mature WBCs, which we compare with published values and present in the section 7.1.1. Cells mature with a maturation rate constant $G = k_{tr}$ summarizing the fraction of cells performing self-renewal and differentiation into one parameter. This is a simplified assumption made by Friberg *et al.* providing homeostasis [45] and identifiability of the estimated parameters. Mature cells x_{ma} are dying by the process of apoptosis with a death rate constant k_{ma} .

From Monte Carlo simulations it could be concluded that k_{ma} is not very sensitive to the **WBC** dynamics during a **CC**, hence we fix k_{ma} to a constant value as previously proposed [82].

The function $F(x_1, k_{\text{tr}}, \gamma, B, \text{slope})$ is a general description of the proliferation rate of x_{pr} and incorporates the **PD** effect E on the proliferating cells (c.f. section 3.2.2), as discussed in Minami *et al.*[83], Derendorf *et al.*[84] and applied, e.g. in Hing *et al.*[85] and the effect of **G-CSF** on the system. The basic structure of the function F derived in [52], is $(1 - E) k_{\text{tr}}(B/x_{\text{ma}})^\gamma$ in which the mature cells influence the proliferation rate k_{tr} of x_{pr} with a feedback term $(B/x_{\text{ma}})^\gamma$ that leads to higher rates if the number of circulating cells x_{ma} is below the baseline **WBC** count B , and vice versa. It is motivated from studies showing that the proliferation rate can be affected by endogenous growth factors and cytokines [12] and that circulating neutrophil counts and the growth factor **G-CSF** levels are inversely related [86]. Including this term allows a temporary overshoot of **WBC** compared with the baseline value B . The proliferation exponent γ indicates the strength of this feedback. The estimation parameters are B , slope, k_{tr} , and γ plus a varying number of additional parameters depending on the initial condition approach, see section 6.1.3.

Apart from different **PK** models which are linked to the myelosuppression model, modifications of the structural model are also proposed [54, 55]. Both models have a more detailed description of the stem cell compartment. The model from Henrich *et al.* covers a consecutive decrease of the leukocyte's nadir in the treatment cycles achieved by a prior additional compartment mimicking the slow replication of pluripotent stem cells in the **BM**. Mangas-Sanjuan *et al.* describe a cell-cycle occurring in the **BM** compartment covering quiescent cells which do not enter the proliferation process and are not sensitive to the **PD** effect of the treatment.

3.3.2 Myelosuppression model with endogenous G-CSF

At the beginning of section 3.3 we reviewed several myelosuppression models considering endogenous **G-CSF**. Hemapoetic growth factors such as **G-CSF** regulate the blood cell production including survival, proliferation, differentiation of stem cells and stimulation of mature cell functions by activating signal transduction pathways [12]. Neutrophils, making up to 70% of the **WBCs**, and their precursor cells are predominantly regulated by **G-CSF** in an inverse manner [87–89]. In this work, we focus on one specific model published in [53] which serves as a starting point for the model development in section 6.1.4.

The **PK/PD** model by Quartino *et al.* [53] describes the proliferation and differentiation of stem cells to mature neutrophils, and its regulation by endogenous **G-CSF**. The model can be seen as an extended version of model (3.17) in which a further state $x_g(t)$ is introduced. The feedback term $F(\cdot)$, which indirectly models the effect of **G-CSF** on the proliferation, is replaced by the ratio of the current **G-CSF** concentration and its steady state level with the proliferation strength exponent γ . Additionally, the transition rate k_{tr} is multiplied by $(x_g/B_g)^\beta$ as **G-CSF** affects not only the proliferating cells but also influences the whole maturation process. Thus, two effects of **G-CSF**, especially the

control of the proliferation and the MMT with two separate parameters γ and β , are introduced. The dynamic of endogenous G-CSF itself is described as a turnover model [53] and we will use the estimated parameters of $\beta, B_g, k_{ANC}, k_{e,g}$ as constants listed in table 6.4, as no G-CSF concentration measurements are available to reestimate the parameters. The model is visualized in figure 3.4 and the model equations can be found in section 6.1.4.

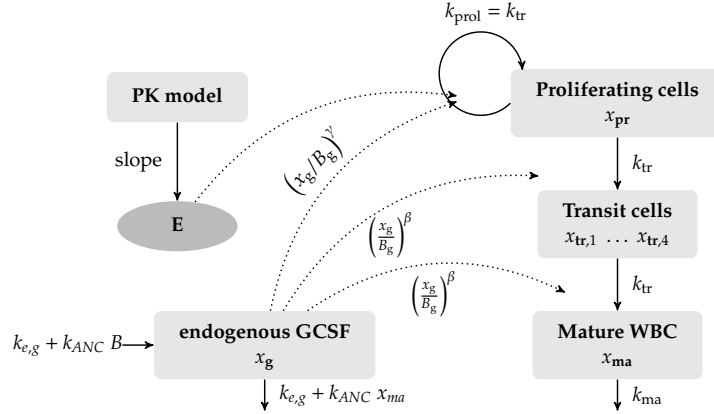


Figure 3.4: Schematic model from [53] describing the hematopoietic process of white blood cells (WBCs) and endogenous granulocyte-colony stimulating factor (G-CSF) affected by an arbitrary drug.

3.3.3 Leukemic cells

For the mathematical description of leukemic cells, we focus on the compartment models presented by Stiehl *et al.* in [48]. Therein, they present two models describing the proliferation and dynamics of leukemic cells distinguishing between cytokine-dependent and autonomous (cytokine-independent) leukemic cell proliferation. For simplicity and the analysis of the effect of G-CSF administration on the growth of leukemic cells, we concentrate on the cytokine-dependent proliferation model. The model is shown in figure 6.4 consisting of two compartments x_1 and x_2 which represent the leukemic blasts in the BM and circulating blood, respectively. The leukemic blasts in the BM grow and proliferate with the first order rate p_1 . During cell division, a leukemic blast divides into two daughter cells, so that the outflux from mitosis is $2p_1x_1$. The outflux is then separated into the process of self-renewal by the rate $2p_1a_1k_l$ with the fraction constant a_1 determining the fraction of daughter cells staying at the current differentiation stage and cell movement by the rate $2p_1(1-a_1)$ to the consecutive compartment. $k_l = \frac{1}{1+c_2x_2}$ models the cytokine-dependent proliferation of leukemic blasts. Leukemic cells are dying by the first order rate d_2 . The term has been derived from a quasi-steady-state assumption of the G-CSF dynamics [90]. The system of ODEs can be found in section 6.1.4.

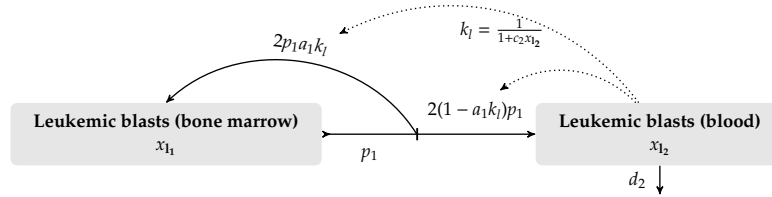


Figure 3.5: Schematic representation of the two-compartment model for leukemic blasts with cytokine-dependent proliferation from [48].

3.3.4 Pharmacokinetic models of cytarabine

The PK of Ara-C, one of the most important component in CT [19, 91] having the highest antileukemic efficacy of all currently used therapies in the treatment of AML [42], have been investigated [42, 92, 93] from low to high dosage and one, respectively two-compartment models have been developed describing concentration-time curves [76, 92–94].

Pharmacology of Ara-C is particularly difficult, as its exact mechanisms of action both on normal and leukemic cells are not fully understood. The main effect of Ara-C on normal and leukemic proliferating cells is the active uptake into the target cells and the subsequent inclusion of intracellular phosphorylated active metabolite arabinofuranosylcytosine triphosphate (Ara-CTP) into deoxyribonucleic acid (DNA) and ribonucleic acid (RNA) during the S phase of the cell cycle resulting in cell death [42]. A second effect mentioned in [95, 96] and references therein is the inhibition of DNA polymerase, surprisingly not mentioned by recently published works [42, 97].

In vitro experiments showed that high-dose Ara-C infusions result in plasma Ara-C concentrations that saturate the accumulation of Ara-CTP by circulating leukemic cells [98] due to the rate-limiting metabolic step in the activation of Ara-C into the monophosphorylated derivative Ara-C monophosphate by the enzyme deoxycytidine kinase (dCK) [95]. Saturation is already achieved with Ara-C concentrations higher than $10 \mu\text{M}$ ($10 \mu\text{mol/L} = 2.43 \mu\text{g/mL}$) [95], whereas high dosage exceeds this value 5- to 10 fold [98]. Thus, the clinical success of intermediate-/high-dose Ara-C is not well explained and understood [10, 42, 98]. Additional effects are the subject of ongoing research [42, 97].

One speculation could be that accumulated arabinofuranosyl-uracil (AraU) might influence the WBC recovery, as it has been reported that the deaminated form may delay cell progression through an increased activity of the anabolic key enzyme of Ara-C, dCK, enhancing the cytotoxicity of Ara-C [93, 99]. However, Burk *et al.* stated that they did not observe a dose- or concentration dependent cumulation of AraU after repetitive applications although AraU has a half-life of about 3 to 4 hours and Ara-C is administered twice daily by continuous 3 h infusions on day 1 to 3, respectively 1, 2, 8 and 9 during the high-dose cytarabine and mitoxantrone (HAM), respectively

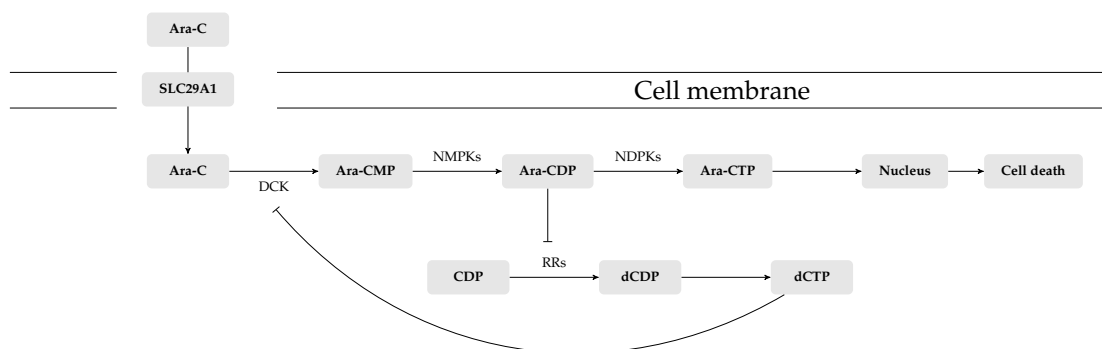


Figure 3.6: **Schematic presentation of the pharmacokinetic(s) and pharmacodynamic(s) of cytarabine.** The figure is adapted from [42].

sequential high-dose cytarabine and mitoxantrone (*S-HAM*), protocol.

Comparing the compartment models derived by low (subcutaneous injection twice daily [2×20 mg] on days 1–10 [94], $100 \text{ mg}/\text{m}^2$ twice a day i.v. push over 5 min on days 1–10 [76]) and intermediate/high-dose [92, 93] *Ara-C* administrations, it can be seen that throughout one dosing group the published *PK* parameters are more or less comparable. Comparing the derived values between the different dosing groups, a roughly 50% decreased clearance is observable.

Simulations for high-dose *Ara-C* infusions lasting 3 hours are performed using the compartment models derived by low dose *Ara-C* [76, 94]. Figure 3.7 compares the simulations with concentration-time profiles of high-dose *Ara-C* administrations collected from eight patients [92]. It is shown that the low-dose derived compartment models are not able to reproduce the higher concentrations.

We do not use the *PK* models from Krogh *et al.* and Solans *et al.*, because they are fitted to low-dose treatment schedules. Although *Ara-C* is reported to have a linear *PK* [92], simulations with these *PK* models do not coincide well with the concentration measurements from high-dose treatment schedules published in [92] as shown in figure 3.7. Thus, we decide not to use the *PK* models from Krogh *et al.* and Solans *et al.*, instead using our own model derived in section 6.1.1.

3.3.5 Pharmacokinetic model of lenograstim

During the last years, several *PK* models for exogenous *G-CSF* (filgrastim [100–103], pegfilgrastim [103–105] and lenograstim [106–109]) have been developed. Often *G-CSF* is administered subcutaneously. A review about *PK* modeling of the subcutaneous absorption of therapeutic proteins is given by Kagan [110].

In this work, we consider patients who are treated with subcutaneous lenograstim. As no *G-CSF* measurements are available and lenograstim is a physicochemically, immunologically and biologically identical glycosylated recombinant *G-CSF* to human

Table 3.1: Comparison of a published one- and two-compartment pharmacokinetic(s) model.

Compartments	Solans2018 [94]	Krogh2012 [76]
CL [L/h]	208.73	272.0
V_p [L]	-	75.4
Q [L/h]	-	13.7
V_c [L]	209.25	62.8
k_{10} [1/h]	1.0	4.3
k_{12} [1/h]	-	0.2
k_{21} [1/h]	-	0.2

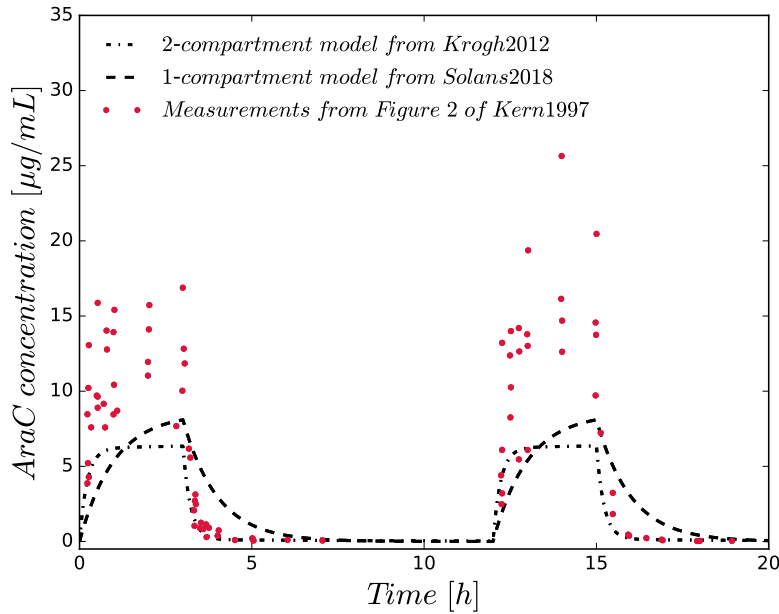


Figure 3.7: Plasma cytarabine measurements from figure 2 of [92] during high-dose cytarabine therapy with 1 g/m^2 or 3 g/m^2 over 3 hours. Simulations with published one- and two-compartment models using typical parameter values (see table 3.1) after high-dose cytarabine therapy with 3 g/m^2 over 3 hours from 0 h to 3 h and 12 h to 15 h and an assumed body surface area of 1.78 m^2 .

G-CSF, we describe the subcutaneous administration of lenograstim entering the central G-CSF compartment by transit compartments with varying number in section 6.1.4.

3.3.6 Pharmacokinetic models of 6-mercaptopurine

In this work, we use and compare two published PK models for 6MP [111–113]. In the following, we present both models.

Jayachandran2014

A simplified version of the compartment model in [112] is used to describe the PK of 6MP and 6-thioguanine nucleotide (6TGN). A diagram of the model is depicted in figure 3.8. In particular, 6MP is absorbed after oral intake at the rate k_a gastrointestinal (GI) tract into plasma. From plasma, it is partly excreted at the rate k_e and partly uptaken by red blood cells (RBCs). Here, it undergoes intracellular metabolism. 6MP is metabolized by the enzyme hypoxanthine-guanine phosphoribosyltransferase (HGPRT) and other enzymes at the rates k_{pt} and k_{pm} , respectively. Finally, the metabolite 6TGN is assumed to be eliminated from RBC at the rate k_{te} . Since the 6MP concentrations in RBCs are negligible [111], we assume that it is metabolized as soon as it enters RBC. Moreover, only the metabolic pathway leading to 6TGN by HGPRT is considered since 6TGN are the primary mediators of the cytotoxic effect of 6MP through their incorporation as a false nucleotides into DNA [114]. The second metabolic pathway is controlled by thiopurine methyltransferase (TPMT) competing with HGPRT and leading to the formation of various methyl-mercaptopurines (MeMP). This pathway is ignored, as we only consider the concentration of 6TGN within the PD function. Even so, the conversion rate constant of 6MP to MeMP is considered, thus, no modification of the published PK model in [112] is made.

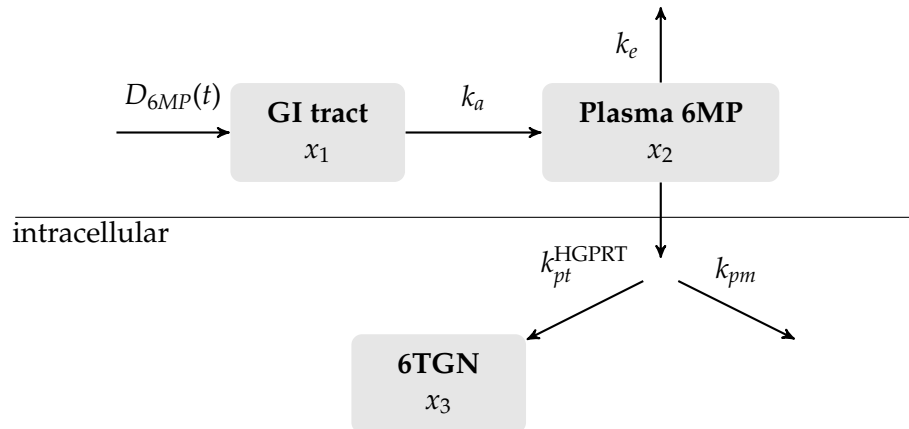


Figure 3.8: Schematic 6-mercaptopurine (6MP) and 6-thioguanine nucleotide (6TGN) model from [112] without the compartment of various methyl-mercaptopurines.

Table 3.2: State variables of the pharmacokinetic(s) model of 6-mercaptopurine (6MP) and its metabolite 6-thioguanine nucleotide (6TGN) from [112].

Variables	Units	Description
x_1	pmol	Amount of 6MP in gastrointestinal tract
x_2	pmol	Amount of 6MP in plasma
x_3	pmol/ 8×10^8 RBCs	Concentration of 6TGN in red blood cells

The mathematical model is

$$\begin{aligned}
 \dot{x}_1 &= -k_a x_1 + \frac{\alpha F D_{6MP}(t)}{T_{dur}}, \\
 \dot{x}_2 &= k_a x_1 - k_e x_2 - \frac{k_{pt}(1 - e_{rel})x_2}{K_t + x_2} - \frac{k_{pm}e_{rel}x_2}{K_m + x_2}, \\
 \dot{x}_3 &= \frac{v_{pt}k_{pt}(1 - e_{rel})x_2}{K_t + x_2} - k_{te}x_3
 \end{aligned} \tag{3.21}$$

with initial values

$$x_1(0) = x_2(0) = x_3(0) = 0. \tag{3.22}$$

The 6MP control function $D_{6MP}(t)$ is defined as

$$D_{6MP}(t) = \begin{cases} D_i, & t \in [t_i, t_i + T_{dur}] \text{ if an amount of 6-mercaptopurine dose } D_i \text{ was taken at time } t_i, \\ \text{otherwise } 0. \end{cases}$$

Notice that v_{pt} is used only for unit consistency. Since our clinical data does not contain concentration measurements of 6MP and 6TGN, most values of parameters appearing in the 6MP and 6TGN model (3.21) are taken from [112] and are used for all patients. Simulations show that T_{dur} does not have a strong effect on the concentration of 6TGN in RBCs. Moreover, due to large IIV in bioavailability of 6MP reported in [29, 115, 116], F and T_{dur} are assigned to 0.45 and 1/24, respectively. These values will be used for MTX as well for the same reason. All state variables and parameters of (3.21) are summarized in tables 3.2 and 3.3.

Hawwa2008

The compartment model from [111] has a comparable structure with the compartments representing the absorption via the GI tract, 6MP and 6TGN. But the metabolic transformations are described by first order instead of Michaelis-Menten kinetics and the elimination is described by an BSA-dependent clearance term. Similar to (3.21), the metabolite 6-methylmercaptopurine nucleotide is neglected without any model modification. Model constants are shown in table 3.4.

Table 3.3: Model constants of the pharmacokinetic(s) model of 6-mercaptopurine (6MP) and its metabolite 6-thioguanine nucleotide (6TGN) from [112].

Constant	Value	Unit	Description
k_a	4.8	1/day	6MP absorption rate from gastrointestinal tract
k_e	5.0	1/day	6MP elimination rate from plasma
k_{pt}	29.8	pmol 6MP/day	6MP to 6TGN conversion rate
k_{pm}	655.8	pmol 6MP/day	6MP to methyl-mercaptopurines conversion rate
K_t	4.04×10^5	pmol	Michaelis-Menten constant for 6TGN
k_{te}	0.0714	1/day	6TGN elimination rate from red blood cells
e_{rel}	0.5		thiopurine methyltransferase enzyme activity constant
v_{pt}	1	$\frac{\text{pmol 6TGN}}{\text{pmol 6MP}/8 \times 10^8 \text{ RBCs}}$	6TGN elimination rate from RBCs
F	0.45		Bioavailability factor
T_{dur}	1/24	day	Time duration for drug absorption
$D_{6MP}(t)$		mg	6MP control function
α	$10^{12}/152177$	pmol/mg	Unit consistency constant

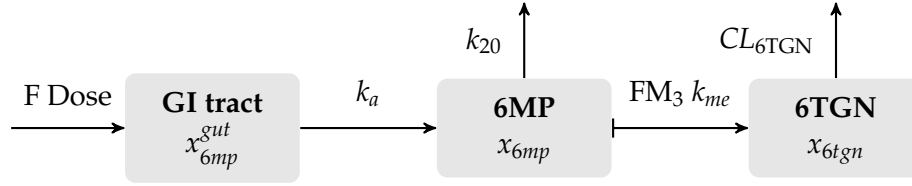


Figure 3.9: Visualization of pharmacokinetic(s) model from [111] without 6-methylmercaptopurine nucleotide compartment.

$$\dot{x}_{6mp}^{gut}(t) = -k_a x_{6mp}^{gut}(t) + F u(t_i), \quad (3.23a)$$

$$\dot{x}_{6mp}(t) = k_a x_{6mp}^{gut}(t) - k_{20} x_{6mp}(t), \quad (3.23b)$$

$$\dot{x}_{6tgn}(t) = FM_3 k_{me} x_{6mp}(t) - CL_{6tgn}(BSA) x_{6tgn}(t) \quad (3.23c)$$

with the BSA dependent clearance

$$CL_{6tgn} = 0.00914 (BSA)^{1.16} \quad (3.24)$$

and the patient-specific 6MP amount $u(t_i)$ administered at time point t_i .

Table 3.4: Model constants of the pharmacokinetic(s) model of 6-mercaptopurine (6MP) and its metabolite 6-thioguanine nucleotide (6TGN) from [111].

Constant	Value	Unit	Description
F	0.22	1/day	Bioavailability factor
k_a	31.2	1/day	Absorption rate constant of 6MP
k_{20}	12.72	1/day	Elimination rate constant of 6MP
FM_3	0.019		Fractional metabolic transformation into 6TGN
k_{me}	9.9216	1/day	Metabolic transformation rate constant of 6MP into either 6TGN or 6-methylmercaptopurine nucleotides
$CL_{6tgn}(BSA)$	$0.219 (BSA)^{1.16}$	L/day	body surface area dependent clearance of metabolite 6TGN

3.3.7 Pharmacokinetic model of methotrexate

Several PK models for MTX [117–123] have been published, but not all have been developed for ALL with low-dosage treatments and validated on pediatric populations. Here, we use the mathematical model from Panetta *et al.* [117, 118], where its detailed description and assumption can be found, describing the PK of MTX and its metabolites methotrexate polyglutamate (MTXPG) $_i$ ($i = 1, \dots, 7$ is the number of glutamates attached to each MTX molecule). A schematic illustration of the model is displayed in figure 3.10. The extracellular PK of MTX after oral intake to the GI tract is described by a two-compartment model in [117, 118]. In this work, it is simplified and comprehensively incorporated by a one-compartment model with first order absorption, see the upper part of figure 3.10 or mathematically the first two equations in (3.25). The mathematical model is the system of ODEs

$$\begin{aligned}
\dot{x}_4 &= -k_a x_4 + \frac{\beta F D_{MTX}(t)}{T_{dur} BSA}, \\
\dot{x}_5 &= k_a x_4 - k_e x_5, \\
\dot{x}_6 &= \frac{V_{ml} x_5 / V}{K_{ml} + x_5 / V} + \frac{k_p x_5}{V} - K_{eff} x_6 - \frac{V_{m-fpgs} x_6}{K_{m-fpgs} + x_6} + K_{ggh} x_7, \\
\dot{x}_7 &= \frac{V_{m-fpgs} x_6}{K_{m-fpgs} + x_6} - K_{ggh} x_7
\end{aligned} \tag{3.25}$$

with initial values

$$x_4(0) = x_5(0) = x_6(0) = x_7(0) = 0. \tag{3.26}$$

The definition of the drug control function $D_{MTX}(t)$ is similar to that of $D_{6MP}(t)$ and following [124], we calculate the BSA as $BSA = W^{0.425} H^{0.725} 71.84$ with patients' weight W and height H . The last term in the first equation of (3.25) is divided by BSA for unit consistency.

As in the 6MP case, measurements of MTX and MTXPG $_{1-7}$ are not available. We set most model parameters in (3.25) to values from the literature [118], (table 2). The values

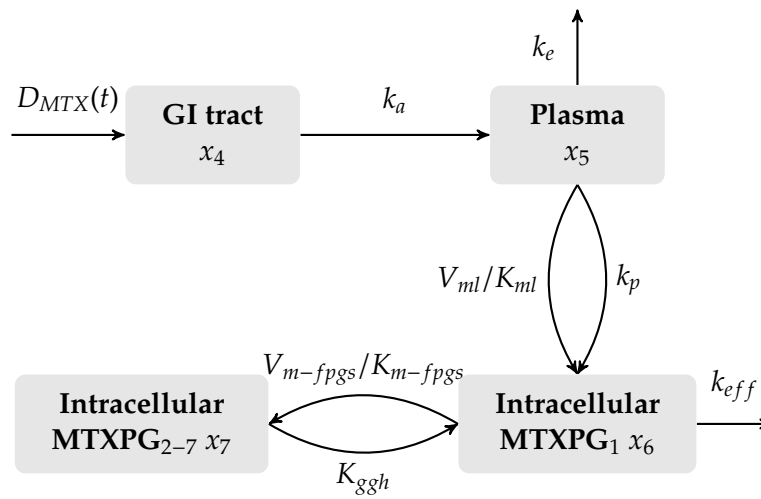


Figure 3.10: Schematic methotrexate (MTX) and methotrexate polyglutamate (MTXPG) model.

of k_a, k_e are obtained via parameter estimation based on measurements of MTX concentration reported in [125]. All state variables and parameters of (3.25) are summarized in tables 3.6 and 3.5.

Table 3.5: Model constants of the pharmacokinetic(s) model of methotrexate (MTX) and methotrexate polyglutamate (MTXPG) from [118].

Constant	Value	Unit	Description
k_a	26.64	1/day	MTX absorption rate from gastrointestinal tract
k_e	5.76	1/day	MTX elimination rate from plasma
k_p	9.6	1/day	Passive influx rate
V	11.606	L/m ²	Systematic volume
V_{ml}	2.3895×10^4	pmol/10 ⁹ cells/day	Michaelis-Menten (M-M) parameter for active (RFC) influx
K_{ml}	2.898	μ M	M-M parameter for active (RFC) influx
K_{eff}	179.76	1/day	first order efflux parameter
V_{m-fpgs}	7.0119×10^3	pmol/10 ⁹ cells/day	M-M parameter for FPGS activity
K_{m-fpgs}	35.262	pmol/10 ⁹ cells	M-M parameter for FPGS activity
K_{ggh}	4.992	1/day	first order GGH activity
F	0.45		Bioavailability factor
T_{dur}	1/24	day	Time duration for drug absorption
BSA		m ²	Body surface area
$D_{MTX}(t)$		mg	MTX control function
β	$10^6/454440$	μ mol/mg	Unit consistency constant

RFC: reduced folate carrier, GGH: gamma-glutamyl hydrolase, FPGS: folylpolyglutamate synthetase

Table 3.6: State variables of the pharmacokinetic(s) model of methotrexate (MTX) and methotrexate polyglutamate (MTXPG) from [118].

Variables	Units	Description
x_4	μ mol/m ²	Amount of MTX in gastrointestinal tract
x_5	μ mol/m ²	Amount of MTX in plasma
x_6	pmol/10 ⁹ cells	Intracellular concentration of MTXPG ₁
x_7	pmol/10 ⁹ cells	Intracellular concentration of MTXPG ₂₋₇

4 | Background, concepts and data: Optimization of dynamic processes

In this chapter, we give a brief introduction to the theory and concepts of nonlinear optimization. We start to formulate general infinite-dimensional constrained nonlinear optimization problems (NLPs) and review definitions and optimality conditions to characterize their optimal solutions. Next, we present specific problem formulations which we are confronted with throughout the medical applications. In the following section, we describe different discretization techniques to reformulate the infinite-dimensional problems to finite problems. Finally, we describe different algorithms to compute numerical solutions of the various discretized NLPs. The following sections summarize the content of [126, 127].

4.1 Theory

Let us consider NLPs

$$\min_{x \in \mathbb{R}^{n_x}} f(x) \quad (4.1a)$$

$$\text{s.t. } h_i(x) = 0, \quad i \in \mathcal{E}, \quad |\mathcal{E}| = n_{eq} \quad (4.1b)$$

$$g_i(x) \geq 0, \quad i \in \mathcal{I}, \quad |\mathcal{I}| = n_{ineq} \quad (4.1c)$$

with an objective function $f(x) : \mathbb{R}^{n_x} \rightarrow \mathbb{R}$, equality constraints $h(x) : \mathbb{R}^{n_x} \rightarrow \mathbb{R}^{n_{eq}}$ and inequality constraints $g(x) : \mathbb{R}^{n_x} \rightarrow \mathbb{R}^{n_{ineq}}$ and \mathcal{E} and \mathcal{I} two finite sets of indices. In our applications, the equality constraints $h_i(x)$ contain the dynamic process (3.1). The functions f, h_i and g_i are assumed to be at least twice differentiable.

Definition 4.1.1. (*Feasible set*)

The set

$$\mathcal{X} = \{x \in \mathbb{R}^{n_x} : g(x) \geq 0, h(x) = 0\} \quad (4.2)$$

is defined as the feasible set of the NLP (4.1) and $x \in \mathcal{X}$ is a feasible point.

Definition 4.1.2. (*Local and global solution*)

A vector x^* is a local solution of the NLP (4.1), if x^* is a feasible point and there exists an open neighborhood U of x^* (open set containing x^*) such that $f(x) \geq f(x^*)$ for $x \in U \cap \mathcal{X}$. A vector x^* is a global solution of (4.1), if x^* is feasible and $f(x) \geq f(x^*)$ holds for $x \in \mathcal{X}$.

Definition 4.1.3. (Active set)

For a feasible point x , we define the active set

$$\mathcal{A}(x) = \mathcal{E} \cup \{ i \in \mathcal{I} \mid g_i(x) = 0 \}. \quad (4.3)$$

Definition 4.1.4. (Lagrangian function)

The function $\mathcal{L} : \mathbb{R}^{n_x} \times \mathbb{R}^{n_\lambda} \times \mathbb{R}^{n_\mu} \rightarrow \mathbb{R}$,

$$\mathcal{L}(x, \lambda, \mu) = f(x) - \lambda g(x) - \mu h(x)$$

is called Lagrange-function of the NLP (4.1). The vectors λ and μ are called Lagrange multipliers.

Definition 4.1.5. (Linear independence constraint qualification)

Given a feasible point \bar{x} with its active set $\mathcal{A}(\bar{x})$, we say that the linear independence constraint qualification (LICQ) holds, if the set of active constraint gradients, i.e. the gradients $\nabla h(\bar{x})$ and the gradients $\nabla g_i(\bar{x})$ of all active inequality constraints $i \in \mathcal{I} \cap \mathcal{A}(\bar{x})$, is linearly independent.

Remark 4.1.6. There exist several other constraint qualifications, e.g. Abadie-, Guignard-, Mangasarian-Fromovitz-, and positive linear constraint qualifications to allow the formulation of optimality conditions. Their definitions and relationship to each other are stated and discussed e.g. in [126, 127].

4.1.1 Optimality conditions

Theorem 4.1.7. (First order necessary optimality conditions/Karush–Kuhn–Tucker conditions)

Let $x^* \in \mathbb{R}^{n_x}$ be a local solution of the NLP (4.1) and the LICQ holds at x^* . Then there exist unique Lagrange multiplier $\lambda^* \in \mathbb{R}^{n_{eq}}$ and $\mu^* \in \mathbb{R}^{n_{ieq}}$ such that the following conditions are satisfied at (x^*, λ^*, μ^*)

1. $\nabla_x \mathcal{L}(x^*, \lambda^*, \mu^*) = 0$ (stationary condition)
2. $h(x^*) = 0, g(x^*) \geq 0$ (primal feasibility)
3. $\lambda^* \geq 0$ (dual feasibility)
4. $\lambda^{*T} g(x^*) = 0$ (complementary condition)

Then, (x^*, λ^*, μ^*) is called a Karush-Kuhn-Tucker (KKT) point.

Proof: See [126].

Definition 4.1.8. (Nullspace matrix of active constraint gradients)

Let $A(x^*) \in \mathbb{R}^{m \times n_x}$ with $m = |\mathcal{A}(x^*)|$ be the matrix whose rows are the active constraint gradients of x^* , i.e. $A^T(x^*) = (\nabla h_1, \dots, \nabla h_{n_{eq}}, \nabla g_1, \dots, \nabla g_{|\mathcal{I} \cap \mathcal{A}(x^*)|})$. Then, we define $Z \in \mathbb{R}^{n_x \times (n_x - m)}$ as a matrix whose columns are a basis for the null space of $A(x^*)$:

$$Z \in \mathbb{R}^{n_x \times (n_x - m)}, \quad Z \text{ has full column rank,} \quad A(x^*)Z = 0. \quad (4.4)$$

Definition 4.1.9. (*Strict complementary*)

Given the *KKT* point (x^*, λ^*, μ^*) , strict complementary is defined if exactly one of λ_i^* and $g_i(x^*)$ is zero for each index $i \in \mathcal{I}$, respectively, $\lambda_i^* > 0$ for all $i \in \mathcal{I} \cap \mathcal{A}(x^*)$.

Theorem 4.1.10. (*Second-order necessary optimality conditions*)

Let (x^*, λ^*, μ^*) be a *KKT* point of the *NLP* (4.1) that satisfies the *LICQ* condition. Further, strict complementary is satisfied and let Z be a matrix whose columns form a basis of the null space of the strictly active constraints $A(x^*)$. Then, the Hessian of the Lagrangian is positive semidefinite on the nullspace of the active constraints, i.e.,

$$Z^T \nabla_{xx}^2 L(x^*, \lambda^*, \mu^*) Z \succeq 0. \quad (4.5)$$

Proof: See [126].

Theorem 4.1.11. (*Second-order sufficient optimality conditions*)

Let (x^*, λ^*, μ^*) be a *KKT* point of (4.1) and the Hessian of the Lagrangian is positive definite on the null space of active constraints, i.e.,

$$Z^T \nabla_{xx}^2 L(x^*, \lambda^*, \mu^*) Z > 0. \quad (4.6)$$

Then x^* is a strict local solution of the *NLP* (4.1).

Proof: See [126].

Remark 4.1.12. A *QR* factorization of A^T can be applied to determine the null space Z of the matrix of active constraint gradients [126].

4.1.2 Nonlinear dynamic optimization problems

In this work, we consider nonlinear dynamic optimization problems

$$\min_{u \in \mathbb{R}^{n_u}} \psi(x(t), u(t)) \quad (4.7a)$$

$$\text{s.t. } \dot{x}(t) = f(x(t), u(t), \theta), \quad t \in [t_0, t_f] \quad (4.7b)$$

$$x(t_0; \theta) = x_0(\theta) \quad (4.7c)$$

which are constrained by a system of *ODEs* (3.1a) describing the dynamical system of interest. Additionally, equality and inequality constraints comprising

- additional boundary conditions $r(x(t_0), x(t_f)) = 0_{n_r}$,
- combined control and state constraints $c(x(t), u(t)) \leq 0_{n_c} \quad \forall t \in [t_0, t_f]$,
- and state constraints $s(x(t)) \leq 0_{n_s} \quad \forall t \in [t_0, t_f]$.

can be added, depending on the practical relevance.

4.2 Problem formulations

Within this work, different dynamic optimization problems are formulated which fit all in the general nonlinear dynamic problem formulation (4.7). Depending on whether the objective function in (4.7) is of control, experimental design or estimation nature, we define the corresponding optimization problems as *optimal control*-, *optimal experimental design*- or *parameter estimation problem*. In the following sections, we present the special problem classes.

4.2.1 Optimal control

Mathematical models can be used to simulate scenarios before they are realized in real experiments. Despite these simulations with heuristically chosen control settings, the models can be used in the formulation of optimal control problems aiming for an optimal control strategy of the dynamic process to minimize (maximize) a desired performance index (quantitative measure of the performance), e.g. the amount of drug administration, the number of cancer cells or a desired steady state the system should target.

Here, we consider an optimal control problem of the following form

$$\begin{aligned}
 \min_{x(\cdot), u(\cdot)} \quad & \int_{t_0}^{t_f} L(x(\tau), u(\tau)) \, d\tau + M(x(t_f)) \\
 \text{s.t.} \quad & \dot{x}(t) = f(x(t), u(t), \theta) \quad \forall t \in [t_0, t_f] \\
 & x(t_0) = x_0 \\
 & x(t) \in \mathcal{X} \quad \forall t \in [t_0, t_f] \\
 & u(t) \in \mathcal{U} \quad \forall t \in [t_0, t_f]
 \end{aligned} \tag{4.8}$$

constrained by the IVP (3.1) and some bounded sets \mathcal{X} and \mathcal{U} for the states and controls and a Bolza term, consisting of a Mayer term $M(x(t_f))$ and Lagrange term $\int_{t_0}^{t_f} L(x(\tau), u(\tau)) \, d\tau$, as objective function.

4.2.2 Parameter estimation

In (3.1a) we described dynamic processes by systems of ODEs with time-constant process-specific parameters θ . In section 3.2 we presented a variety of mathematical models from biology and pharmacometrics in which patient-specific parameters like rate constants for drug absorption, distribution and elimination, cell proliferation, differentiation and apoptosis and steady-state values for different biomarkers and clinical effects were introduced. In real applications, those parameters θ might not exactly be known and initial guesses by the modeler from previous experiments, literature or other prior knowledge on the considered system are made. If experimental data is available, another possibility is the estimation of the unknown model parameters through model fitting (also called parameter identification or model calibration) as the

unknown parameters are one factor for a good match between model and real world data. Measurement and state/model uncertainty are further factors influencing the difference between model and experimental data [128]. Despite parameter and measurement uncertainty, we assume that our models reflect the corresponding processes correctly, thus we do not further discuss the consideration and handling of other errors. Suppose that longitudinal measurements $y_{ij} \in \mathbb{R}$ at time points $j = 1, \dots, n_i$ from $i = 1, \dots, N$ experiments are available with corresponding independently normally distributed additive measurement errors $\varepsilon_{ij} \sim \mathcal{N}(0, \sigma_{ij}^2)$ with the given variance σ_{ij}^2 and an appropriate measurement function

$$h_{ij}(x(t_{ij}; \theta); \theta) \in \mathbb{R}, \quad i = 1, \dots, N, \quad j = 1, \dots, n_i. \quad (4.9)$$

As we assume that the model has no structural errors and no process noise is present, the following relation holds

$$y_{ij} = h(x(t_{ij}; \theta^{true}); \theta^{true}) + \varepsilon_{ij} \quad (4.10)$$

with true but inaccessible parameter estimates θ^{true} . The difference between measurement and model response is called residual $r_{ij} = y_{ij} - h(\cdot)$. Then, following the assumptions above, we define the least-squares parameter estimation problem

$$\min_{x(t), \theta} \frac{1}{2} \sum_i^N \sum_j^{n_i} \omega_j^i \left(\frac{y_{ij} - h_{ij}(x(t_{ij}; \theta); \theta)}{\sigma_{ij}} \right)^2 \quad (4.11a)$$

$$s.t. \quad \dot{x} = f(x(t), u(t), \theta) \quad (4.11b)$$

$$x^i(t_0) = x_0^i(\theta) \quad (4.11c)$$

$$\theta \in [\theta_{lo}, \theta_{up}] \quad (4.11d)$$

constrained by the ODE system (4.11b), initial conditions and lower and upper bounds of the parameters θ . The least-squares criterion (4.11a) is solidly grounded in statistics, e.g. for independent and identically normally distributed measurement errors ε_{ij} , the maximum likelihood estimate is obtained by minimizing the sum of squares (4.11) (compare for [126, 128]). The sampling decision variables (so called weights) $\omega_j^i \in \mathbb{R}$ indicate whether measurement j of experiment i is performed or not. For the parameter estimation problems, we fix all weights ω_j^i to 1, thus at all time points t_{ij} measurements are considered with the same weight. In OED problems, the sampling decision variables are part of the optimization variables determining the optimal measurement time points (see section 4.2.3).

Parameter uncertainty, respectively the quality of the resulting parameter estimates $\hat{\theta}$ from solving (4.11), can be approximated via the covariance matrix

$$C(\hat{\theta}) = \begin{pmatrix} I & 0 \end{pmatrix} \begin{pmatrix} J_1^T J_1 & J_2^T \\ J_2 & 0 \end{pmatrix}^{-1} \begin{pmatrix} J_1^T J_1 & 0 \\ 0 & 0 \end{pmatrix} \begin{pmatrix} J_1^T J_1 & J_2^T \\ J_2 & 0 \end{pmatrix}^{-T} \begin{pmatrix} I \\ 0 \end{pmatrix} \quad (4.12)$$

with the Jacobian $J_1 = \frac{dF_1}{d\theta}$ and $F_1 := \Sigma^{-1}(y - h)$ the compact, vectorized formulation of the double sum of (4.11a) with $\Sigma = \text{diag}(\sigma_{1,1}, \dots, \sigma_{N,n_i})$. J_2 is the Jacobian of the constraints resulting from discretization (parameterization) of model dynamics (4.11b) and possible additional constraints. A detailed description of the structure of the Jacobians is presented in [129]. The square root of the i -th diagonal element of C (e.g. $\sqrt{c_{ii}}$) serves as an estimate of the standard error of the i -th parameter θ_i and $\sqrt{c_{ii}}/|\theta_i|$ is the corresponding relative standard error. Derivation of the covariance matrix of the parameters θ and its approximation through model linearization can be found in [128, 130].

Nonlinear mixed-effects modeling

This section gives an introduction to NLME modeling and the related parameter estimation problems. A detailed description is presented in the books [6, 131, 132] and publications [133–138]. In this work, the N experiments from the previous section do not result from the same dynamic process but correspond to experiments from N individuals for each we have n_i measurements. For this scenario, the setting of nonlinear least-squares problems from the previous section with the assumption that every individual has the same set of parameters θ may not be appropriate. The assumption that the mathematical model (3.1a) is the same for each individual still holds but we now assume that every individual has its own set of parameters θ_i

$$\theta_i = b(\theta, \eta_i), \quad i = 1, \dots, N. \quad (4.13)$$

The function $b(\cdot)$ describes the relation (e.g. additive: $\theta_i = \theta + \eta_i$ or exponential: $\theta_i = \theta \exp(\eta_i)$) between the typical/population parameters (fixed effects) θ and the IIV (between subject variability) represented by realizations (individual parameters) $\eta_i \in \mathcal{R}^{n_\eta}$ of the random effects $\eta \sim \mathcal{N}(0, \Omega)$ with mean zero and covariance matrix $\Omega \in \mathcal{R}^{n_\eta \times n_\eta}$. Function $b(\cdot)$ can be augmented with covariate a_i (e.g. weight, sex, disease stage, absorption type, renal disease, ...) explaining parts of the IIV [6]. In our analysis no covariates were identified during model development such that we omit a_i in the rest of the thesis. The IVP (3.1) is now reformulated to

$$\dot{x}(t) = f(t, x(t), b(\theta, \eta_i), u_i(t)) \quad \forall i = 1, \dots, N, \quad (4.14a)$$

$$x_i(t_{0,i}; \theta_i) = x_{0,i}(b(\theta, \eta_i)) \quad \forall i = 1, \dots, N \quad (4.14b)$$

where the structural model f is the same for every individual but with differing parameters θ_i , initial values $x_{0,i}(\theta_i)$ and control function u_i describing the drug administration schedule.

Now, the n_i measurements η_{ij} of subject i can be described with an appropriate (see following paragraph) error model

$$y_{ij} = F_{ij}(h(x_i(t_{ij}; b(\theta^{true}, \eta_i(\Omega^{true})), q_{ij})), \varepsilon_1, \varepsilon_2, \dots, \varepsilon_S) \quad (4.15)$$

with the measurement errors $\varepsilon_s \sim \mathcal{N}(0, \sigma_s^{2^{true}})$, $s = 1, \dots, S$, $S \in \mathbb{N}$ (often $S = 1$ or $S = 2$) and the model response $h(\cdot)$ where q_{ij} is the discretized control function $u_i(t)$ of subject

i at time point j . Here, we assume that model f has no structural errors, meaning that the model contains all aspects of the dynamic process, and that the model response $h(\cdot)$ with true, but inaccessible, parameters θ_{true} and Ω_{true} is equivalent to the measurement y_{ij} despite some white measurement noise ε_s with true variance $\sigma_{s true}^2$.

Despite the additive error model (4.10), other error models, representing the error of measurement devices, exist for which equality holds with true but inaccessible parameters:

- Proportional error (constant of variation error)

$$y_{ij} = h(x(t_{ij}), \theta^{true})(1 + \varepsilon_{1,ij})$$

- Combined additive and proportional error

$$y_{ij} = h(x(t_{ij}), \theta^{true})(1 + \varepsilon_{1,ij}) + \varepsilon_{2,ij}$$

- Exponential error

$$y_{ij} = h(x(t_{ij}), \theta^{true})\exp(\varepsilon_{1,ij})$$

Further residual error models, also considering logarithmic transformed data, are presented in [139]. For simplicity, we assume an error model with one measurement error ε_1 and that one entry of the state vector $x(t)$ is measured directly, which is often the case in pharmacometric applications. All the results for scalar observations can be generalized to multiple-output measurement situations.

Parameter estimation for NLME models (4.14) results in determining the parameters $(\hat{\theta}, \hat{\Omega}, \hat{\sigma})$ that maximize the marginal likelihood $L(\theta, \Omega, \sigma^2|y)$ which is defined as the product of the individual likelihoods

$$L(\theta, \Omega, \sigma^2|y) = \prod_{i=1}^N L_i(\theta, \Omega, \sigma^2|y_i) = \prod_{i=1}^N \int P(y_i, \eta_i|\theta, \Omega, \sigma^2)d\eta_i \quad (4.16a)$$

$$= \prod_{i=1}^N \int P(y_i|\eta_i, \theta, \Omega, \sigma^2) P(\eta_i|\theta, \Omega, \sigma^2)d\eta_i \quad (4.16b)$$

$$= \prod_{i=1}^N \int P(y_i|\eta_i, \theta, \sigma^2) P(\eta_i|\Omega)d\eta_i \quad (4.16c)$$

with $P(y_i|\eta_i, \theta, \sigma^2)$ the conditional density of y_i given the random effect η_i , fixed effect θ and variance σ^2 and $P(\eta_i|\Omega)$ the density of η_i [135]. The last equation in (4.16) holds since $P(y_i|\eta_i, \theta, \sigma^2)$ does not involve any parameters in Ω and $P(\eta_i|\Omega)$ does not involve any parameters θ and σ^2 .

Analytical solutions of the marginal likelihood (4.16) are difficult to compute exactly due to the nonlinear occurrence of some, or all, fixed and random effects in the function

f. Several approximation techniques can be applied to (4.16) divided into methods using the exact likelihood (expectation maximization (EM), Monte-Carlo-EM or stochastic approximation expectation maximization (SAEM) algorithm) or likelihood approximations [6, 131, 140]. In the following, we focus on likelihood approximations derived by the first order (FO) approximation and the first order conditional estimation (FOCE) approximation with and without η - ε interaction. If no interaction is assumed (assuming that η and ε are independent, $COV(\eta, \varepsilon) = 0$), applying Laplace approximation or model linearization (Taylor approximation) results in the same approximated objective functions of the FO and FOCE method (see [135]). If the interaction between η and ε is assumed, both approximation methods result in different objective functions. We present the objective functions with their resulting parameter estimation problems for the FO and FOCE method derived by model linearizations and for the FOCE method with interaction via the Laplace approximation. We refer the interested reader to [135] for a comprehensive derivation in case of an additive or proportional error model and to [138] for a generalization. Further information can be found in [133, 134, 136, 137]. The approximation techniques are not applied to (4.16) but to the logarithmized likelihood $\log(L(\theta, \Omega, \sigma^2|y_i))$.

First order approximation

A FO Taylor series approximation of (4.15) at $\tilde{\eta} = 0$ and $\tilde{\varepsilon} = 0$ is performed, yielding

$$\begin{aligned} \bar{F}_{ij}(x_i(t_{ij}; b(\theta, 0)), 0) \approx \\ F_{ij}(x_i(t_{ij}; b(\theta, 0)), 0) + \left. \frac{\partial F_{ij}(\cdot)}{\partial \eta} \right|_{\tilde{\eta}=0, \tilde{\varepsilon}=0} (\eta - 0) + \left. \frac{\partial F_{ij}(\cdot)}{\partial \varepsilon} \right|_{\tilde{\eta}=0, \tilde{\varepsilon}=0} (\varepsilon - 0) \end{aligned}$$

with the mean

$$E(\bar{F}_{ij}(x_i(t_{ij}; b(\theta, 0)), 0)) = F_{ij}(x_i(t_{ij}; b(\theta, 0)), 0) = h(x_i(t_{ij}; g(\theta, 0), q_{ij})) \quad (4.17)$$

and the covariance matrix

$$V_{ij}(\bar{F}_{ij}(x_i(t_{ij}; b(\theta, 0)), 0)) = \frac{\partial F_{ij}(\cdot)}{\partial \eta} \Omega \frac{\partial F_{ij}^T(\cdot)}{\partial \eta} + \text{diag} \left(\frac{\partial F_{ij}(\cdot)}{\partial \varepsilon} \sigma^2 \frac{\partial F_{ij}^T(\cdot)}{\partial \varepsilon} \right) \quad (4.18)$$

resulting in

$$y_{ij} = \mathcal{N} \left(E \left(\bar{F}_{ij}(x_i(t_{ij}; b(\theta, 0)), 0) \right), V_{ij} \left(\bar{F}_{ij}(x_i(t_{ij}; b(\theta, 0)), 0) \right) \right). \quad (4.19)$$

Two times the negative log likelihood for (4.19) with respect to the parameters $\lambda = (\theta, \text{vec}(\Omega), \sigma^2)$ is

$$L = \sum_{i=1}^N -2 \log \left(\prod_{j=1}^{n_i} \frac{1}{\sqrt{2\pi V_{ij}(\lambda)}} \exp \left(-\frac{1}{2} V_{ij}^{-1}(\lambda) (y_{ij} - E(\bar{F}_{ij}(\theta)))^2 \right) \right) \quad (4.20)$$

resulting in the parameter estimation problem

$$\begin{aligned}
 \min_{x(t), \lambda} \quad & \sum_{i=1}^N \overbrace{\log(|V_i(\lambda)|) + \|V_i(\lambda)^{-1/2}(y_i - h_i(\theta))\|_2^2}^{L_i} \\
 \text{s.t.} \quad & \dot{x}_i(t) = f(t, x(t, b(\theta, 0), u_i(t))) \quad \forall t \in [t_0, t_f], \quad \forall i = 1, \dots, N \\
 & \lambda \in [\lambda_l, \lambda_u] \\
 & u_i(t) \in \mathcal{U} \quad \forall t \in [t_0, t_f], \quad \forall i = 1, \dots, N
 \end{aligned} \tag{4.21}$$

First order conditional estimation approximation

In the FOCE approximation the Taylor series of (4.15) is performed around (the mode of the posterior distribution) $\tilde{\eta} = \eta^t$, respectively $\tilde{\eta} = 0$ and $\tilde{\varepsilon} = 0$ resulting in

$$\bar{F}_{ij}(x_i(t_{ij}; b(\theta, \eta_t), 0)) = F_{ij}(x_i(t_{ij}; b(\theta, \eta_t), 0)) + \left. \frac{\partial F_{ij}(\cdot)}{\partial \eta} \right|_{\tilde{\eta}=\eta_t, \tilde{\varepsilon}=0} (\eta - \eta_t) + \left. \frac{\partial F_{ij}(\cdot)}{\partial \varepsilon} \right|_{\tilde{\eta}=0, \tilde{\varepsilon}=0} (\varepsilon - 0) \tag{4.22}$$

with the mean

$$E(\bar{F}_{ij}(x_i(t_{ij}; b(\theta, \eta_t), 0))) = F_{ij}(x_i(t_{ij}; g(\theta, \eta_t), 0)) - \left. \frac{\partial F_{ij}(\cdot)}{\partial \eta} \right|_{\tilde{\eta}=\eta_t, \tilde{\varepsilon}=0} \eta_t \tag{4.23}$$

and the covariance matrix (assuming $COV(\eta, \varepsilon) = 0$)

$$V_{ij}(\bar{F}_{ij}(x_i(t_{ij}; b(\theta, \eta_t), 0))) = \left. \frac{\partial F_{ij}(\cdot)}{\partial \eta} \right|_{\tilde{\eta}=\eta_t, \tilde{\varepsilon}=0} \Omega \left. \frac{\partial F_{ij}^T(\cdot)}{\partial \eta} \right|_{\tilde{\eta}=\eta_t, \tilde{\varepsilon}=0} + \text{diag} \left(\left. \frac{\partial F_{ij}(\cdot)}{\partial \varepsilon} \right|_{\tilde{\eta}=0, \tilde{\varepsilon}=0}, \sigma^2 \left. \frac{\partial F_{ij}^T(\cdot)}{\partial \varepsilon} \right|_{\tilde{\eta}=0, \tilde{\varepsilon}=0} \right) \tag{4.24}$$

The approximated log likelihood function is then

$$L_{outer}^{FOCE} = \sum_{i=1}^N -2 \log \left(\prod_{j=1}^{n_i} \frac{1}{\sqrt{2\pi V_{ij}(\lambda)}} \exp \left(-\frac{1}{2} V_{ij}^{-1}(\lambda) (y_{ij} - E(\bar{F}_{ij}(\theta)))^2 \right) \right). \tag{4.25}$$

Remark 4.2.1. For the FOCE method two different points are used around which the Taylor series approximation of (4.15) is performed, either $\left. \frac{\partial F_{ij}(\cdot)}{\partial \varepsilon} \right|_{\tilde{\eta}=0, \tilde{\varepsilon}=0}$ or $\left. \frac{\partial F_{ij}(\cdot)}{\partial \varepsilon} \right|_{\tilde{\eta}=\eta_t, \tilde{\varepsilon}=0}$. They are presented and briefly discussed in [137].

The likelihood for the maximum a posteriori (MAP) estimate of η for patient i is

$$L_{MAP}^{FOCE} = \log(|V_i^{MAP}|) + \left\| V_i^{MAP}(\lambda)^{-1/2}(y_i - F_i(\theta, \eta)) \right\|_2^2 + \eta_i \Omega^{-1} \eta_i^T \quad (4.26)$$

$$\text{with } V_{ij}^{MAP} = \text{diag} \left(\left. \frac{\partial F_{ij}(\cdot)}{\partial \varepsilon} \right|_{\hat{\eta}=0, \hat{\varepsilon}=0} \sigma^2 \left. \frac{\partial F_{ij}^T(\cdot)}{\partial \varepsilon} \right|_{\hat{\eta}=0, \hat{\varepsilon}=0} \right).$$

Parameter estimation for FOCE approximated error models results in two parameter estimation problems (estimating $\lambda = (\theta, \text{vec}(\Omega), \sigma^2)$ with fixed η and vice versa) which are iteratively solved until some convergence criterion is fulfilled.

$$\begin{aligned} \min_{x(t), \lambda} \quad & L_{outer}^{FOCE}(x(t), u(t), (\eta_1^*, \dots, \eta_N^*), \lambda) \\ \text{s.t.} \quad & \eta_i^* = \underset{\eta_i}{\text{argmin}} L_{MAP}^{FOCE}(x(t), u(t), \theta_i^*, \text{vec}(\Omega^*), \sigma^{*2}) \quad \forall i \in [1, \dots, N] \\ & \text{s.t.} \quad \dot{x}_i(t) = f(t, x_i(t), u_i(t), \theta_i) \quad \forall t \in [t_0, t_f] \\ & \quad \quad x_i(t_{0,i}; \theta_i) = x_{0,i}(\theta_i) \quad \forall i = 1, \dots, N \\ & \quad \quad \theta_i = g(\theta, \eta_i) \quad \forall i = 1, \dots, N \\ & \quad \quad u^i(t) \in \mathcal{U} \quad \forall t \in [t_0, t_f] \end{aligned} \quad (4.27)$$

The optimization problem can be interpreted as a bilevel optimization problem which is not further discussed in this work.

First order conditional estimation approximation with η - ε interaction

The two previous approximations assume $\text{COV}(\eta, \varepsilon) = 0$. Often, not an additive but a proportional, combined or power function error model is more suitable and used together with the FOCE method for parameter estimation [136]. In this scenario, the consideration of the interaction $\text{COV}(\eta, \varepsilon) \neq 0$ between η and ε provides more accurate parameter estimates. For the estimation of the unknown parameters in our derived models, we also apply proportional error models and the first order conditional estimation with interaction (FOCEi) algorithm. Thus, we want to conclude this section with the FOCEi approximation also resulting in a bilevel optimization problem such as (4.27) but with an altered objective function. For the derivation of the objective function for the FOCEi approximation, the Laplace method is applied to (4.16c) resulting in

$$\begin{aligned} \mathcal{L}_{outer}^{FOCEi} = & \log(2\pi) + \log \left(\left. \frac{\partial F(\cdot)}{\partial \varepsilon} \right|_{\hat{\eta}=\eta_i, \hat{\varepsilon}=0} \sigma^2 \left. \frac{\partial F^T(\cdot)}{\partial \varepsilon} \right|_{\hat{\eta}=\eta_i, \hat{\varepsilon}=0} + \left. \frac{\partial F(\cdot)}{\partial \eta} \right|_{\hat{\eta}=\eta_i, \hat{\varepsilon}=0} \Omega \left. \frac{\partial F^T(\cdot)}{\partial \eta} \right|_{\hat{\eta}=\eta_i, \hat{\varepsilon}=0} \right) \\ & + 2\sigma^2 \left. \frac{\partial F(\cdot)}{\partial \eta} \right|_{\hat{\eta}=\eta_i, \hat{\varepsilon}=0} \Omega \left. \frac{\partial F^T(\cdot)}{\partial \eta} \right|_{\hat{\eta}=\eta_i, \hat{\varepsilon}=0} + (y_i - f(\hat{\eta}_i, \theta))(f(\hat{\eta}_i, \theta)\sigma^2 f(\hat{\eta}_i, \theta)^T)(y_i - f(\hat{\eta}_i, \theta))^T + \hat{\eta}_i \Omega \hat{\eta}_i^T \end{aligned} \quad (4.28)$$

A derivative of the likelihood function can be found in [135].

Comment on parameter uncertainty for nonlinear mixed-effects models

Different approaches exist approximating the parameter uncertainties via the covariance matrix of the fixed effects θ , the variance of the measurement error σ^2 and the entries of the covariance matrix Ω . Similar to nonlinear least squares problems, the parameter uncertainties can be quantified via the inverse of the Fisher information matrix (FIM) of the maximum likelihood estimates. We comment on the computation of the FIM for NLME models in the following section. Other possibilities, which are implemented in the NLME modeling software NONMEM (ICON Plc., Dublin, Ireland) [141], are the computation of the inverse of the Hessian H of the log-likelihood functions from the previous section, the sum of the cross products of the gradient vectors S of the individual likelihoods or a combination of both matrices $H^{-1} S H^{-1}$ (see NONMEM Users Guide, Part IV and [142, 143]).

4.2.3 Optimal experimental design

We consider the OED problem as an optimal control problem with a particular structure, as suggested in [144]. The degrees of freedom in experimental design are the control functions u and the sampling decisions (or weights) w , which have been assumed to be fixed in section 4.2.2. The control can be used to excite the system dynamics, and hence also the sensitivities. The sampling chooses time points or intervals with much information on the sensitivity of the model response with respect to the model parameters. We assume u to be fixed on the level of the experimental design problem for reasons to be discussed later, therefore we concentrate from now on on w as the only degree of freedom.

For a self-contained presentation, we repeat the parameter estimation problem (4.11) and complement a version with continuous measurements. Following a maximum-likelihood approach, we estimate initial values and model parameters by solving the state and parameter estimation problem in the form of a nonlinear weighted least squares problem

$$\min_{x(t), \theta} \frac{1}{2} \sum_{\omega=1}^{n_\omega} \sum_{i=1}^N w_i^\omega \frac{(\eta_i^\omega - h^\omega(x(t_i)))^2}{\sigma_{\omega,i}^2} \quad \text{s.t. (4.11b)-(4.11d)} \quad (4.29)$$

for given and fixed controls $u : \mathcal{T} \mapsto \mathcal{U}$ and weights $w_i^\omega \in \mathcal{W}$. As the measurement times t_i may be a priori unknown, we will in our analysis in section 6.3 also look at the continuous analogue to (4.29). This is given by

$$\min_{x(t), \theta} \frac{1}{2} \sum_{\omega=1}^{n_\omega} \int_{t_0}^{t_f} w^\omega(t) \frac{(\eta^\omega(t) - h^\omega(x(t)))^2}{\sigma_\omega^2(t)} dt \quad \text{s.t. (4.11b)-(4.11d)}$$

By choosing the function space for $w^\omega : \mathcal{T} \mapsto \mathcal{W}$ such that we allow Borel measures $\xi^\omega(\mathcal{T})$ on $\mathcal{T} = [t_0, t_f]$ as solutions, we can define designs ξ^ω via $d\xi^\omega = w^\omega(t)dt$ and work

with

$$\min_{x(t), \theta} \frac{1}{2} \sum_{\omega=1}^{n_\omega} \int_{t_0}^{t_f} \frac{(\eta^\omega(t) - h^\omega(x(t)))^2}{\sigma_\omega^2(t)} d\xi^\omega \quad \text{s.t. (4.11b)-(4.11d)} \quad (4.30)$$

The objective of experimental design is maximizing information gain. With the sensitivities (3.2), we can define the FIM as

$$F_d(t_f) = \sum_{\omega=1}^{n_\omega} \sum_{i=1}^N w_i^\omega (h_x^\omega(x(t_i))G(t_i))^T (h_x^\omega(x(t_i))G(t_i)) \in \mathbb{R}^{n_p \times n_p} \quad (4.31)$$

for the discrete setting of (4.29) and as $F(\xi)$ via the Borel measure

$$F(\xi) = \sum_{\omega=1}^{n_\omega} \int_{t_0}^{t_f} (h_x^\omega(x(t))G(t))^T (h_x^\omega(x(t))G(t)) d\xi^\omega \in \mathbb{R}^{n_p \times n_p} \quad (4.32)$$

for the continuous measurement setting of (4.30).

Minimizing the uncertainty of state and parameter estimates, or maximizing information gain, can now be quantified via a scalar function $\phi(\cdot)$ of the FIM or its inverse, the covariance matrix. A list of different objective functions (criteria), such as trace, determinant or maximum eigenvalue of the respective matrix can be found, e.g., in [145]. To limit the amount of measurements, either an economic penalty in the objective as suggested in [144] can be used, or a normalization via constraints, e.g.,

$$1 = \sum_{i=1}^N w_i^\omega \quad (4.33)$$

for all ω and the discrete setting of (4.29) and as

$$1 = \int_{t_0}^{t_f} d\xi^\omega \quad (4.34)$$

for all ω and the continuous measurement setting of (4.30). Based on our assumptions and considerations, we define the OED problem with fixed u as

$$\min_{x(t), G(t), F_d(t_f), w \in \mathcal{W}^{n_\omega N}} \phi(F_d(t_f)) \quad \text{s.t. (3.1, 3.2, 4.31, 4.33)} \quad (4.35)$$

for the case of a discrete measurement grid and as

$$\min_{x(t), G(t), F(\xi), \xi} \phi(F(\xi)) \quad \text{s.t. (3.1, 3.2, 4.32, 4.34)} \quad (4.36)$$

for the continuous measurement flow. Problems (4.35) and (4.36) can be solved numerically with the same methods as general optimal control problems, and with specialized ones that take the structure of the derivatives and sensitivities into account, [129]. Our assumption of a fixed u and the specific way w enters the right hand side allow an

Algorithm 1 OED

Input: Fixed θ and u , initial values $x(t_0), G(t_0)$, possible measurement times $\{t_1, \dots, t_N\} \subset [t_0, t_f]$

- 1: Solve IVP (3.1,3.2) to obtain $x(\cdot)$ and $G(\cdot)$
- 2: Solve $\min_{F_d(t), w \in \mathcal{W}^{n_\omega N}} \phi(F_d(t_f))$ s.t. (4.31,4.33)

even more efficient approach, in which the expensive calculation of the states x and G is decoupled from the optimization over x and F_d , see Algorithm 1. This decoupling is not the main motivation for our approach to optimize sequentially over u and w , but it should be exploited and might be an argument for time-critical processes.

Algorithm 1 operates with a (fine) time grid of possible time points that can be chosen to take a measurement. If one wants to leave the exact timings $t_i \in \mathbb{R}$ as degrees of freedom, one can apply a time transformation (switching time optimization), as suggested and discussed in the context of mixed-integer optimal control, e.g., in [146–148] with stage lengths $T_i := t_{i+1} - t_i$. The variables T_i become additional optimization variables, integration of x and G is performed on the interval $[0, 1]$ and the dynamics (3.1 and 3.2) are scaled according to

$$\dot{x}(t) = T_i f(x(t), u(t), \theta), \quad x(t_0) = x_0(\theta), \quad (4.37)$$

$$\dot{G}(t) = T_i (f_x(\hat{x}(t), u(t), \theta)G(t) + f_p(\hat{x}(t), u(t), \theta)), \quad G(t_0) = \frac{dx_0(p)}{d\theta}. \quad (4.38)$$

Also continuity conditions at times t_i need to be included, and a constraint like $\sum_{i=0}^N T_i = t_f$ for fixed t_f . The advantage of using (4.37-4.38) is the independence of an a priori grid. However, this comes at the price of not being able to decouple the calculation of x and G from w and F any more, of higher computational costs due to the extra variables, an increased nonconvexity of the dynamics, and possibly not practically realizable (e.g., irrational) measurement times $t_i \in \mathbb{R}$. Therefore we prefer to use Algorithm 1 with a fine grid of possible measurement times.

Comment on Fisher information matrix matrix and optimal experimental design problems for nonlinear mixed-effects models

Computing population OEDs using the FIM was firstly elaborated by Mentré and Retout [149] for a specific NLME setting and the FO method and sequentially generalized in the last years [150–153]. An overview of existing software tools for optimal design problems is given in [154]. Bayesian and robust population optimal designs can be found in [155] and [156, 157]. Bazzoli *et al.* [152] showed that the uncertainty received from the inverse of the FIM for the FO method is in the same range as the standard errors computed by NONMEM’s FOCE method or Monolix’s SAEM algorithm. For the numerical testing of parameter estimation methods based on the FO approximation of

the likelihood function for NLME models, we also applied the Fisher's scoring method which can be understood as the counterpart of the Gauss-Newton (GN) method for (non-)linear regressions but for NLME models. Meaning, that we approximate the Hessian of parameter estimation problem (4.21) via the FIM

$$\begin{aligned}
 FIM^{FO} &= \sum_{i=1}^N E\left(\frac{\partial^2}{\partial(\theta, \Omega, \sigma)^2} L_i^{FO}\right) \\
 &= \sum_{i=1}^N FIM_i = \sum_{i=1}^N \overbrace{\begin{pmatrix} M_{1i} & 0 \\ M_{2i} & M_{3i} \end{pmatrix}^T}_{\mathbb{R}^{n_\lambda \times (n_i + n_i^2)}} \overbrace{\begin{pmatrix} V_i^{-1} & 0 \\ 0 & M_{4i}^{-1} \end{pmatrix}}_{\mathbb{R}^{(n_i + n_i^2) \times (n_i + n_i^2)}} \overbrace{\begin{pmatrix} M_{1i} & 0 \\ M_{2i} & M_{3i} \end{pmatrix}}_{\mathbb{R}^{(n_i + n_i^2) \times n_\lambda}} \\
 &= \sum_{i=1}^N \underbrace{\begin{pmatrix} M_{1i}^T V_i^{-1} M_{1i} + M_{2i}^T M_{4i}^{-1} M_{2i} & M_{2i}^T M_{4i}^{-1} M_{3i} \\ M_{3i}^T M_{4i}^{-1} M_{2i} & M_{3i}^T M_{4i}^{-1} M_{3i} \end{pmatrix}}_{\mathbb{R}^{n_\lambda \times n_\lambda}}
 \end{aligned}$$

with

$$\begin{aligned}
 M_{1i} &= \frac{\partial f(t_i, x_i(t_i), g(\theta, 0), q_i)}{\partial \theta} & M_{2i} &= \frac{\partial \text{vec}(V_i)}{\partial \theta} \\
 M_{3i} &= \left(\frac{\partial \text{vec}(V_i)}{\partial \text{vec}(\Omega)}, \frac{\partial \text{vec}(V_i)}{\partial \sigma^2} \right) & M_{4i} &= 2 V_i \otimes V_i \\
 n_\lambda &= n_\theta + n_{\text{vec}(\Omega)} + n_{\text{vec}(\Sigma)}
 \end{aligned}$$

and V_i the approximated covariance matrix (4.18) from the FO approximation. For a detailed description and more information we refer to [158].

4.3 Methods for solving dynamic optimization problems

In comparison to the general NLP (4.1), the dynamic optimization problem (4.7) is an infinite-dimensional optimization problem as the differential state $x(t)$ lives in function space. Thus, there exist a variety of approaches for solving the problems, comprehending dynamic programming based on Bellman's principle of optimality [159], indirect methods related to Pontryagin's maximum principle [160] or direct methods [161]. We focus on direct methods with a short comment on the indirect method based on *Pontryagin's maximum principle* which is useful for theoretical analysis of dynamical optimization problems. Applying direct methods results in finite-dimensional optimization problems of the form (4.1) for which different iterative procedures, tailored to the particular type and structure of the problem, can be used to numerically calculate optimal solutions.

Indirect method (Pontryagin's maximum principle)

Indirect methods solving optimal control problems are based on Pontryagin's maximum principle. The idea of this concept (so called *first optimize, then discretize*) is to apply FO

necessary conditions for optimality to the dynamic optimization formulation (4.7) in function space. We start with defining the Hamiltonian, which is used in the subsequent theorem.

Definition 4.3.1. (*Hamiltonian*)

For $x \in \mathbb{R}^{n_x}$, $u \in \mathbb{R}^{n_u}$, $\lambda_0 \in \mathbb{R}$ and $\lambda \in \mathbb{R}^{n_x}$ the Hamiltonian of the dynamic optimization problem (4.7) is given by

$$\mathcal{H}(x(t), u(t), \lambda_0, \lambda(t), \theta) := -\lambda_0 \psi(x(t), u(t), \theta) + \lambda^T f(x(t), u(t), \theta)$$

with adjoint variables λ_0 and λ .

Now, we can formulate the maximum principle in which the optimization problem is reformulated into a boundary value problem which then can be solved by numerical methods.

Theorem 4.3.2. (Maximum principle)

We assume problem (4.7) has a feasible optimal solution (x^*, u^*) . Then there exist $\lambda_0^* \in \mathbb{R}$ and adjoint variables $\lambda^*(\cdot)$, with $(\lambda_0^*, \lambda^*(\cdot)) \neq 0$ such that

$$\dot{x}^*(t) = \frac{\partial \mathcal{H}}{\partial \lambda}(x^*(t), u^*(t), \lambda_0^*, \lambda^*(t), \theta) = f(x^*(t), u^*(t), \theta), \quad (4.39a)$$

$$\dot{\lambda}^{*T}(t) = -\frac{\partial \mathcal{H}}{\partial x}(x^*(t), u^*(t), \lambda_0^*, \lambda^*(t), \theta), \quad (4.39b)$$

$$x^*(t_0; \theta) = x_{t_0}(\theta), \quad (4.39c)$$

$$\lambda(t_f) = 0, \quad (4.39d)$$

$$u^*(t) \in \arg \min_{u \in \mathcal{U}} \mathcal{H}(x^*(t), u, \lambda_0^*, \lambda^*(t), \theta), \quad (4.39e)$$

for $t \in \mathcal{T}$ almost everywhere.

For a proof of the maximum principle and a thorough introduction see [160, 162] and the references in [163]. For the application of Pontryagin's maximum principle to delay differential equations we refer the interested reader to the recent publications [164, 165].

Direct methods

In direct methods (*first discretize, then optimize*), the control function and states are first discretized such that the infinite-dimensional dynamic NLP (4.7) becomes a finite-dimensional NLP. Often, the discretized dynamic optimization problems have special structures which can be exploited for efficient solving.

For a fixed end time $t_f = T$, we partition the time interval $[t_0, t_f]$ into M smaller intervals at time points

$$t_0 < t_1 < \dots < t_M = T \quad (4.40)$$

and parameterize the control function $u(t)$. For simplicity, we use M piecewise constant controls:

$$u(t) := u_k \quad \forall t \in [t_k, t_{k+1}), \quad k = 0, \dots, M-1. \quad (4.41)$$

Introducing a further ODE $\dot{x}^L(t) = L(x(t), u(t))$ for the first term of the objective function of (4.8), the state trajectories $x(t)$ and $x^L(t)$ can be determined by integrating the ODE system forward in time using function \mathcal{I} (3.3) and time grid (4.40) resulting in

$$\begin{aligned} x_k &= \mathcal{I}(x_{k-1}, u_{k-1}, \theta) \quad \forall k \in 1, \dots, M \\ x_k^L &= \mathcal{I}(x_{k-1}^L, u_{k-1}, \theta) \quad \forall k \in 1, \dots, M. \end{aligned}$$

Now, we can apply the so called *single shooting* method to problem (4.8) resulting in a NLP of the form (4.1):

$$\begin{aligned} \min_{u_0, \dots, u_{M-1}} \quad & \sum_{k=1}^M x_k^L + M(x_M) \\ \text{s.t.} \quad & x_0 = x_0^{ini} \\ & x_0^L = 0 \\ & x_k \in [s^{lo}, s^{up}] \quad \forall k \in 1, \dots, M \\ & u_k \in [u^{lo}, u^{up}] \quad \forall k \in 1, \dots, M \end{aligned} \quad (4.42)$$

where the function and derivative evaluations are based on an integration of the ODE system on the time horizon $[t_0, t_f]$ and x_0^{ini} is a given initial condition. The recursive integration of the differential equations eliminates the state variables from the optimization variables such that they become dependent variables of the objective and constraint functions.

Another approach are *collocation methods* (simultaneous approach) in which the control function *and* the differential states are simultaneously discretized by low order polynomials [166]. The resulting NLP is large scale due to the introduction of additional optimization variables and constraints, but highly structured.

The extension of the single shooting method, eliminating some drawbacks and being a hybrid method between the previous two approaches, is defined as the *multiple shooting method*. Similar to collocation methods, additional variables and constraints are introduced but the differential states are not simultaneously discretized, instead, the differential equations are solved via embedded ODE solvers represented by the function \mathcal{I} as in the single shooting scenario. The introduction of M new variables s_k , $k = 1, \dots, M$ allows a parallel instead of sequential integration of the ODEs on the subintervals. If prior knowledge about the states at discretization time points $1, \dots, M$ is available, this information can be used to initialize the optimization problem. The inclusion of continuity (matching) constraints

$$s_k - \mathcal{I}(s_{k-1}, u_{k-1}, \theta) = 0, \quad k = 1, \dots, M$$

guarantees a continuous state trajectory. Additionally, the solution of the differential equations on smaller intervals tackles nonlinearity better, leading to a faster convergence to the NLP solution due to a lifting effect [167].

The resulting NLP reads as follows

$$\begin{aligned}
 \min_{\substack{s_1, \dots, s_M, \\ u_0, \dots, u_{M-1}}} & \sum_{k=1}^M s_k^L + M(s_M) \\
 \text{s.t.} & \quad s_k = \mathcal{I}(s_{k-1}, u_{k-1}, \theta) \quad \forall k \in 1, \dots, M \\
 & \quad s_k^L = \mathcal{I}(s_{k-1}^L, u_{k-1}, \theta) \quad \forall k \in 1, \dots, M \\
 & \quad s_0 = x_0^{ini} \\
 & \quad s_0^L = 0 \\
 & \quad s_k \in [x^{lo}, x^{up}] \quad \forall k \in 1, \dots, M \\
 & \quad u_k \in [u^{lo}, u^{up}] \quad \forall k \in 1, \dots, M
 \end{aligned} \tag{4.43}$$

with a special structure, which should be exploited while problem solving.

4.3.1 Methods for solving nonlinear optimization problems

After applying one of the presented direct methods, the discretized dynamic optimization problem can be solved with iterative procedures for NLPs, which are often tailored to the particular type and structure of the problem. We start with introducing methods for unconstrained optimization problems

$$\min_x f(x) \tag{4.44a}$$

with $x \in \mathbb{R}^{n_x}$ and $f : \mathbb{R}^{n_x} \rightarrow \mathbb{R}$ being a smooth function, as constrained NLPs can be solved with the same procedures if a reformulation to an unconstrained problem is performed.

Beginning with an initial guess x_0 of the optimal variable values, the algorithms calculate a sequence $\{x_{k+1}\}_{k=0}^K$ of improved estimates and terminate at the K -th iteration when a stopping criterion is fulfilled, either identifying a solution or further progress seems to be impossible. The algorithms differ in their strategy making progress to the optimal solution of the optimization problem, i.e. moving from one iterate to the next. A lot of algorithms are based on one of the two fundamental strategies *line search* and *trust region*. In line search strategies, the consecutive iterate x_{k+1} is derived by the previous iterate x_k plus a search direction d_k . The algorithm searches for a new iterate with a lower function value along the search direction d_k :

$$x_{k+1} = x_k + \alpha_k d_k. \tag{4.45}$$

The distance α_k can be determined by approximately solving the minimization problem $\min_{\alpha > 0} f(x_k + \alpha d_k)$. The appropriate choice of step length α_k defined via different conditions (e.g. (strong) Wolfe conditions, Armijo condition, Goldstein condition, sufficient

decrease and backtracking) ensures that for any initial guess x_0 the numerical method globally converges to a stationary (KKT-) point [126]. The search direction is defined as

$$d_k = -B_k^{-1} \nabla f(x_k) \quad (4.46)$$

with the selected Hessian matrix

$$B_k = \begin{cases} I & \text{(Steepest descent method)} \\ \nabla^2 f(x_k) & \text{(Newton's method)} \\ M_k & \text{(Quasi-Newton's method)} \\ \frac{\partial f_k}{\partial x}^T \frac{\partial f_k}{\partial x} & \text{(Gauss-Newton's method)} \\ FIM^{FO} & \text{(Fisher's method with FO approximation)} \end{cases} \quad (4.47)$$

of function $f(x)$ where I is the identity matrix with suitable dimension and M_k is an approximation of the exact Hessian $\nabla^2 f(x_k)$ which is updated each iteration by means of a low-rank formula. The choice of the matrix B_k is related to the choice of the solution method, i.e. steepest descent, Newton's, quasi-Newton's or GN's method [126]. The fifth option will be used during the parameter estimation of NLME models applying the FO method.

In comparison to line search strategies, the trust region method chooses the direction and length of each step simultaneously. A region of the current iterate x_k is defined within we trust an approximated function m_k (usually defined to be a quadratic function of the form $m_k(x_k + p) = f_k + p^T \nabla f_k + \frac{1}{2} p^T B_k p$) to be an adequate representation of $f(x_k)$. Then, we choose a step with a descent direction within this region by solving

$$\min_p m_k(x_k + p) \quad \text{s.t.} \quad \|p\|_2 \leq \Delta \quad (4.48)$$

with the trust-region radius $\Delta > 0$. The computation of the trust region Δ_k in each iterate and the description of methods for solving (4.48) (such as dogleg method, two-dimensional subspace minimization or Steihaug's approach) can be found in [126].

Comment on Gauss-Newton method

The GN method plays a major role in l_2 -norm optimization problems including parameter estimation problems. For these problems, the Hessian of the objective function $f(x_k)$ is approximated via neglecting the second derivative terms. In theory, the Hessian is a good approximation close to the solution as it is assumed that the omitted residual-dependent terms are considerable small [168]. The Hessian can also be derived performing a linearization of F_1 (not the objective function) such that (4.11) becomes a linear least squares problem with respect to the parameters. The GN method has several advantages related to parameter estimation problems:

- Hessian consists of gradient such that no computational expensive second derivatives have to be computed

- GN may have similar convergence speed as Newton's method: if assumption of small residuals is true, this leads to a quadratically (local) convergent rate while only calculating first derivatives. If assumption is violated only linear rate of convergence [166])
- GN direction is a descent direction (if Jacobian has full rank and gradient is nonzero)
- GN only converges to local minima, not affected by residuals [129]
- Last Hessian of GN algorithm serves as approximation for parameter uncertainties

For a profound analysis see [168].

Fisher's method

As already mentioned in the section about the FIM for NLME models, Fisher's method for NLME models is the counterpart of the GN method for (non-)linear least squares problems. Here, the FIM of the FO approximation method is used as an approximated Hessian B_k for the optimization procedures [169].

In the following, we give a brief summary of the most widespread numerical concepts for solving constrained NLPs. A more thorough introduction, description and analysis of nonlinear (dynamic) optimization and numerical algorithms can be found in [126, 127, 161, 166, 170, 171].

Interior-point method

The idea of interior-point (barrier) methods is the reformulation of the original constrained problem to a sequence of unconstrained problems by a penalty function $B(x; \mu)$ that consists of the original objective function of the constrained NLP (4.1) *plus* one additional term for each constraint. The resulting log-barrier/quadratic penalty function reads as

$$B(x; \mu) = f(x) - \mu \sum_{i \in \mathcal{I}} \log(g_i(x)) + \frac{1}{2\mu} \sum_{i \in \mathcal{E}} h_i^2(x) \quad (4.49)$$

combining the introduction of logarithmic barrier functions for the inequality constraints and quadratic penalty terms for equality constraints. Within the sequence of solving the unconstrained problems, the coefficient μ is iteratively decreased bringing the minimizer $x(\mu)$ of the penalty function (4.49) closer to the minimizer of the original constrained problem (4.1) [126].

Sequential quadratic programming

The second well-established method is sequential quadratic programming (SQP). In contrast to interior-point methods, the constraints are not integrated into the objective function. Instead, the NLP (4.1) is approximated in each iteration by a quadratic subproblem

$$\min_d \frac{1}{2}d^T B_k d + \nabla f(x_k)^T d \quad (4.50a)$$

$$s.t. \quad g_i(x_k) + \nabla g_i(x_k)^T d = 0, \quad i \in \mathcal{E} \quad (4.50b)$$

$$h_i(x_k) + \nabla h_i(x_k)^T d \geq 0, \quad i \in \mathcal{I} \quad (4.50c)$$

with linearized constraints and B_k being the exact Hessian or low rank approximations of the Lagrange function. The solution d^* of (4.50) at iteration k serves as search direction along which the new iterate x_{k+1} is obtained decreasing a certain merit function [126]. Active set methods are most widely used and most effective for solving problem (4.50) in which the set of inequalities is limited to the active ones in each iteration resulting in an equality-constrained quadratic programming (QP). The KKT system of the constrained QP can then be solved e.g. with a range space or null space method. The main challenge in each iteration is the determination of the working set including all equality constraints and a subset, but not necessarily all, of the active constraints. We refer the interested reader to [126] for a more comprehensive discussion of SQP methods and to two recent research papers dealing with non-smoothness [172] and combining SR1 and Broyden, Fletcher, Goldfarb, and Shanno (BFGS) updates in the context of optimal control problems in which the Hessian has a special block-diagonal structure [173].

4.4 Software

In this section, we give an overview of the different software packages which were used to numerically integrate the system of ODEs and solve the optimization problem.

The parameter estimation problems (4.11) were solved with a multiple shooting based GN algorithm coded in the PAREMERA software and an adaptive, error-controlled backward differentiation formula (BDF) method for integration coded in the software DAESOL, both included in the experimental design package VPLAN [130] developed at the Heidelberg University. The same integrator was used for all individual predictions (simulations) in this paper.

The population parameter estimation problems (4.21) and (4.27) with either likelihood (4.25) or likelihood (4.28) were solved with the gold-standard NLME modeling tool NONMEM using a variable metric (BFGS) optimization method [169]. This variable metric method, also called secant method, is a special form of the line search method with $\alpha_k = 1$ and specific quasi-Newton updates for B_k . The ODE systems are solved by CVODES, a solver for stiff and non-stiff ODEs using variable-order and variable-step multistep methods (Adams-Moulton and BDF), implemented in Sundials [174]. The

same ODE solvers are interfaced to CasADi which we also used for simulations and optimizations. Additionally, direct collocation with Lagrange polynomials with Legendre collocation points of order 3 was used for ODE discretization. The discretized optimal control (4.8) and experimental design problems (4.36) were formulated in CasADi and solved with the interior point method IPOPT [175] and the SQP method blocksqp [173].

Comment on software for population parameter estimation

There exist several other software packages for parameter estimation of NLME models. Several algorithms are provided in R. The software Monolix and Diffmem (see <https://bitbucket.org/tomhaber/diffmem/src/master/>, [176]) are based on SAEM algorithms and the recently published package Pumas (based on Julia, see <https://pumas.ai/>) contains several deterministic and stochastic algorithms.

5 | Background, concepts and data: Clinical data

The developed mathematical PK/PD models, which we present in the next chapter, are fitted and (cross-)validated to three clinical datasets provided by the university hospitals in Magdeburg, Ulm and Erlangen.

5.1 Clinical data from the university hospital in Magdeburg

AML patients who had received induction therapy (commonly defined as anthracycline- and Ara-C-based 7+3 regimen [19]) resulting in CR and who did not receive G-CSF during the post-remission consolidation therapy were eligible for data analysis. We focused on patients who did not receive growth factor support, as such effects were not yet accounted for in our mathematical models. Almost daily WBC counts from 42 CCs with Ara-C administrations of 23 AML patients (median 62 years, 14 male, mostly *de novo* AML (19/23), mostly AML FAB-M2 (9/19), mostly intermediate cytogenetic risk (12/20)) from 2008 to 2015 were analyzed from clinical charts provided by the Department of Hematology and Oncology, Magdeburg University Hospital, Magdeburg, Germany. The data were retrospectively collected and pseudonymized from records of the clinical routine. Interventions were not performed for this work. All clinical procedures were performed in accordance with the general ethical principles outlined in the Declaration of Helsinki. For this reason no patients' agreements were required. The CCs were partitioned in one, two, and three consecutive CCs from nine, nine, and five patients, respectively. Four different schedules D135, d135, D123, or D12, in which the numbers correspond to treatment days 1, 2, 3, and 5, respectively, d to intermediate-dose Ara-C (i.e. 1 g/m^2 per BSA twice a day over three hours) and D to high-dose Ara-C (i.e. 3 g/m^2 twice a day), were administered 24, 14, two, and two times. Patient P_{D123} (62 years, male) received two cycles of D123. Patient P_{D12} (64 years, female) received two cycles of D12. The 21 other patients received 1-3 D135 cycles (median 57 years, 8 male, 4 female) or d135 cycles (median 68 years, 5 male, 4 female). The cycle- and patientwise datasets can be found in form of NONMEM-specific datasets under <https://journals.plos.org/plosone/article?id=10.1371/journal.pone.0204540#sec021>.

5.2 Clinical data from the university hospital in Ulm

Data from the AMLSG 12-09 randomized controlled clinical phase II trial [21] were provided by the Department of Internal Medicine III, University Hospital Ulm, Ulm, Germany and used for model development, fitting, validation, and calibration. The dataset included WBC count measurements (6-16 per cycle) from 86 Ara-C CCs, partitioned into one, two, and three consecutive CCs from 20, 6, and 18 AML patients (median 65 years, 19 [43%] male), respectively, from 2010 and 2012, which were treated with D123 (31 out of 86 CCs) or d123 (55 out of 86 CCs) schedules of Ara-C. Additionally, in most cycles before Ara-C treatment (76 measurements), the relative number of blasts in the BM and the category of BM cellularity (punctio sicca, hypo-, normo- or hypercellular) were determined by cytology via BM aspiration. 13 BM measurements were below the limit of quantification and consequently excluded from the analysis. The treatment schedule included 263 μg of lenograstim administrations starting nine days after the start of Ara-C treatment until hematological recovery, i.e., neutrophil count $> 0.5 \text{ G/L}$, was achieved. Nine of the patients (1 only in the first cycle and 7 CCs each for d123 and D123) did not receive lenograstim.

For the analysis in *Secondary pharmacodynamic effect of Ara-C* of section 7.1.2, the dataset, (denoted by MD in figure 7.18) presented in the previous section, is combined with nine patients from the current dataset who did not receive lenograstim.

For the analysis in the consecutive section called *Modeling exogenous G-CSF*, the patientwise cycles of the current dataset are treated independently (although several cycles belong to the same patient) and combined with the cycles from the previous section.

In the section titled *Modeling leukemic blasts* the current dataset is used for model fitting. In the following section *Model predictions and optimal treatment schedules*, a subset of 24 patients, for whom at least two CCs are available, are used to perform model predictions. For the computation of optimized treatment schedules, this subset is further reduced to 14 patients for whom relative blast counts are available in the last CC. The different subsets used in each section are visualized as a diagram in figure 5.1.

5.3 Clinical data from the university hospital in Erlangen

The data used in this study were obtained retrospectively from 116 children who were diagnosed with *de novo* ALL at university hospitals in Erlangen and Dresden and treated according to the AIEOP-BFM 2000 and 2009 protocols. A subset of this data set (WBC counts from 9 patients) was used and described similarly in a previous study [177]. Patients were eligible if they were diagnosed with precursor B-cell or T-cell ALL, negative for the BCR-ABL- and MLL-AF4 translocations, and started MT (i.e., did not experience relapse before the end of CT and did not undergo stem cell transplantation). During MT administered according to the AIEOP-BFM 2000 and 2009 protocols, patients received oral chemotherapy with daily 6MP and once-weekly MTX until 2 years after ALL diagnosis. During MT, chemotherapy was applied to achieve antileukemic activ-

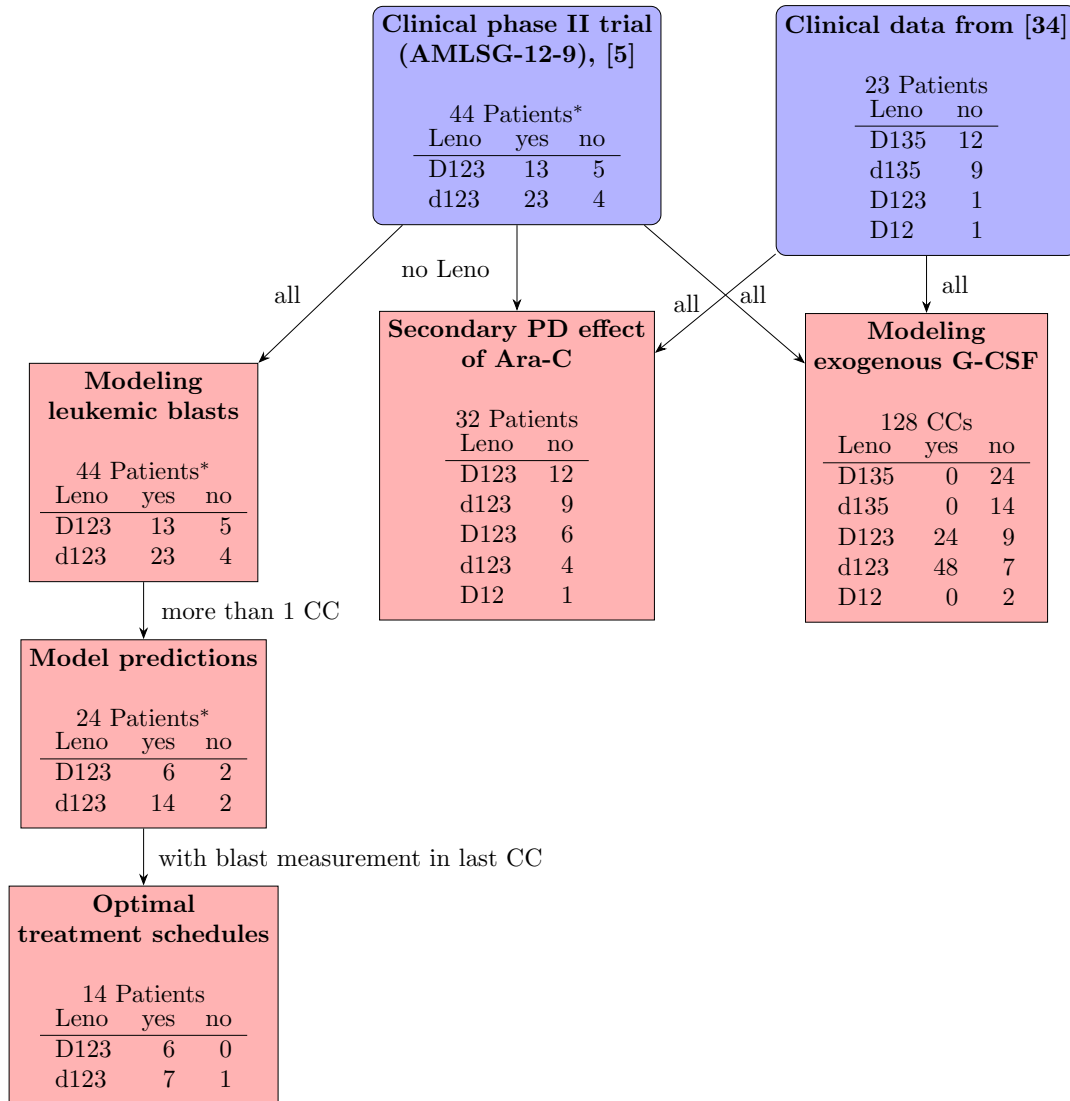


Figure 5.1: **Diagram of the two datasets and their subsets used in the different sections and for the pharmacodynamic(s) modeling.** Choices of subsets were based upon data availability, e.g., administration of lenograstim (Leno), granulocyte-colony stimulating factor (G-CSF), and numbers of consolidation cycles (CCs). One patient * received 1 CC without and 2 CCs with Leno, the data were split.

ity against lymphoblasts below the limit of detection. As a surrogate for antileukemic activity, **WBC** and **ANC** were measured regularly, with **ANC** <2 G/L, being correlated to a significantly better relapse-free survival [30], and **ANC** <0.5 G/L being an indicator of excessive myelosuppression. The target range for the **WBC** count was 1.5–3 G/L. The chemotherapeutic dose was reduced when cell counts fell below the lower limits (**WBC** count <1.5 G/L, **ANC** <0.5 G/L, lymphocyte count <0.3 G/L, and platelet count <0.05 G/L) or liver toxicity was suspected. For each patient included in the analysis, data regarding the following variables were recorded: gender, age, weight, height, **BSA**, prescribed **6MP** and **MTX** dosages (absolute and per **BSA**), **WBC** count, platelet count, lymphocyte and neutrophil counts, and therapy interruptions.

In this study, we focus on 5897 **ANCs** and 6640 **WBC** counts, disregarding measurements of other cell types. We use both **WBC** counts and **ANC** separately and compare the accuracy of the resulting mathematical models. In all, 1150 **ANC** and 1289 **WBC** count measurements are excluded due to corresponding high C-reactive protein levels indicating periods in which patients probably suffered from an infection. More precisely, we exclude measurements in the interval from two weeks before until two weeks after C-reactive protein levels of >5 mg/L were recorded. Among the remaining 4747 **ANC** measurements 56% are below the **ANC** threshold of 2 G/L, only 2% are below 0.5 G/L, and 54% are in the **ANC** target range 0.5–2 G/L. The demographic and clinical characteristics of the pediatric **ALL** population are shown in table 5.1. The dataset which is used for the final model presented in section 7.1.3 can be found in form of a NONMEM-specific dataset under <https://www.frontiersin.org/articles/10.3389/fphys.2020.00217/full#supplementary-material>.

Table 5.1: **Characteristics (median and range) of the pediatric acute lymphoblastic leukemia population consisting of 116 (64 male and 52 female) patients.** The body surface area was calculated using the Mosteller formula.

Characteristic	Unit	Median	Range
Age	year	4.75	1.1–17.1
Weight	kg	22	10–90
Height	cm	112.45	80–182.7
Body surface area	m ²	0.82	0.47–1.98
6MP daily dose	mg	40	5–150
MTX weekly dose	mg	15	1.25–60
ANC	G/L	1.8	0.0–19.9

Part II

Developed models and numerical methods for myelosuppression

6 | Developed models and numerical methods for myelosuppression:

6.1 Mathematical models for consolidation therapies of AML patients

In this section, we consecutively develop two PK/PD models for WBC count dynamics during consolidation treatment using intermediate or high-dose Ara-C in AML.

Firstly, we extend a mathematical model of myelosuppression and a PK model of Ara-C with different hypotheses of Ara-C's PD effects resulting in 12 model variations M1–M12. All model variations are based on the myelosuppression model developed by Friberg *et al.* [52] (c.f. section 3.3.1) and are tailored to the special case of Ara-C via a parameterized two-compartment PK model. The general modeling goals are the inclusion of possible secondary effects of Ara-C and to obtain a good balance between modeling detail, prediction accuracy, and the number of patient-specific parameters.

Secondly, we develop a population PK/PD model combining a myelosuppression model considering endogenous G-CSF a PK model for Ara-C and exogenous G-CSF, and a two-compartment model for leukemic blasts. We use the mathematical model to explore the impact of different treatment schedules and the administration of lenograstim on WBCs and leukemic blasts.

6.1.1 Pharmacokinetic model of cytarabine

We develop a two-compartment PK model for intravenous high-dose Ara-C infusions, which are administered in the consolidation phase, and compare it with two previously published PK models [76, 94]. 86 Ara-C concentration measurements ($\mu\text{g}/\text{mL} = \text{mg}/\text{L}$) from 11 patients are collected from figure 2 of Kern *et al.*[92] and presented in figure 6.2.

As figure 2 in [92] is our only source of data, no IIV analysis can be performed. The patients received high-dose ($3 \text{ g}/\text{m}^2$) Ara-C infusions over 3 hours every 12 hours on days 1, 2, 8 and 9. The measurements we are using have been collected at day 1 and 8 and we assume $\text{BSA} = 1.78 \text{ m}^2$. The resulting model with unknown parameters k_{10}, k_{12}, k_{21} and V_c denoting the elimination rate, distribution rates and the volume of the central compartment, is formulated as

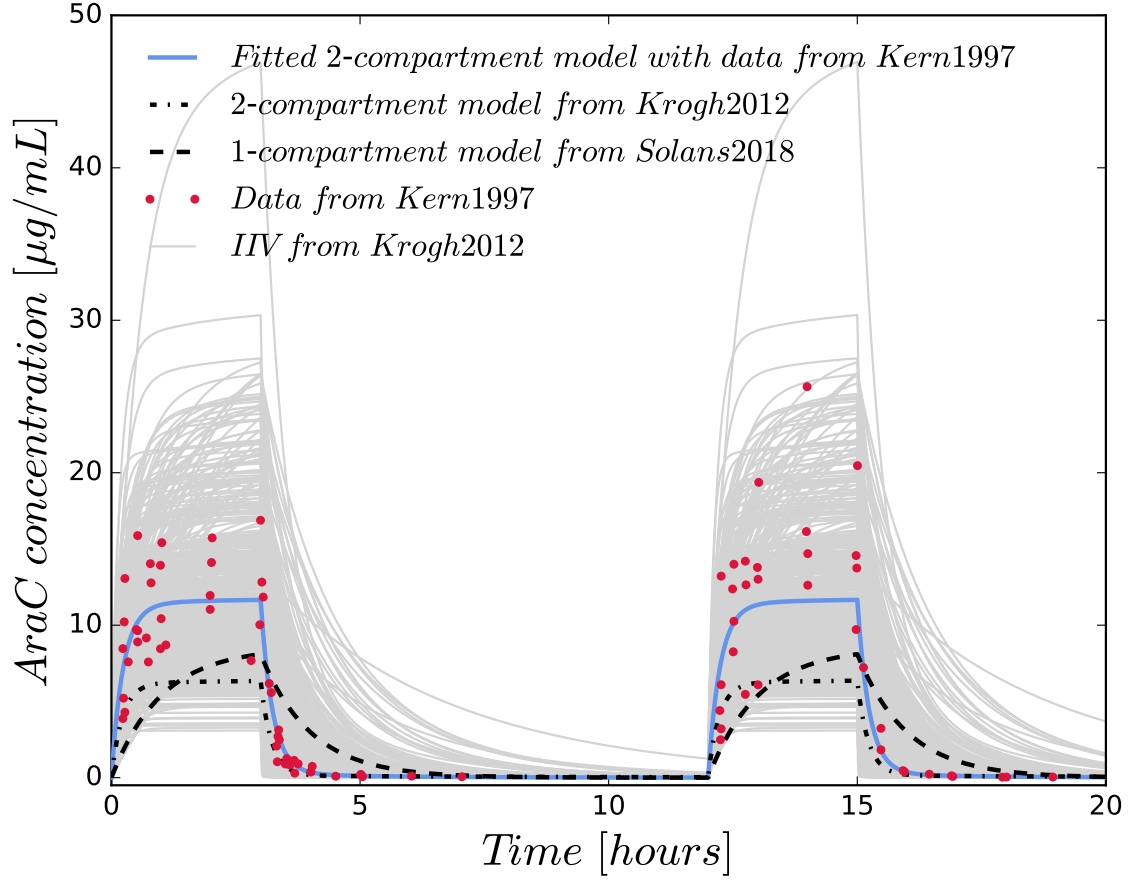


Figure 6.2: As figure 3.7, but with 500 simulations of our fitted two-compartment pharmacokinetic(s) model with interindividual variability (IIV) on the clearance and the central volume.

$$\dot{x}_1(t) = -(k_{10} + k_{12}) x_1(t) + k_{21} x_2(t) + \frac{u(t)BSA}{3} \quad (6.1a)$$

$$\dot{x}_2(t) = k_{12} x_1(t) - k_{21} x_2(t). \quad (6.1b)$$

We estimate the unknown parameters using a naïve pooling approach with exponential error model $\eta_{ij} = \frac{x_1(t_{ij})}{V_c} e^{\varepsilon_{ij}}$ where $\varepsilon_{ij} \sim \mathcal{N}(0, 1)$. The naïve pooling approach is used as the collected Ara-C measurements can not be assigned to the corresponding patients. The error model is transformed to $\log(\eta_{ij}) = \log\left(\frac{x_1(t_{ij})}{V_c}\right) + \varepsilon_{ij}$ and the following parameter estimation problem

$$\min_{k_{10}, k_{12}, k_{21}, V_c, x} \frac{1}{2} \sum_{i=1}^m \sum_{j=1}^{n_i} (\log(\eta_{ij}) - \log(x_1(t_{ij})/V_c))^2 \quad (6.2a)$$

$$\text{s.t.} \quad \dot{x}(t) = f(x(t), u(t), k_{10}, k_{12}, k_{21}, V_1), \quad x(t_0) = (0., 0.)^T \quad (6.2b)$$

is solved with a **GN** algorithm implemented in CasADi[178] with single shooting (CVODES). The estimated parameters and their relative standard deviations are presented in Table 6.2 together with the parameter values from Solans *et al.* [94] and Krogh *et al.* [76].

Table 6.2: Comparison of our derived pharmacokinetic(s) model with a published one- and two-compartment model. Final parameter estimates and relative standard errors (in brackets) are shown. Comparing our model with a published two-compartment model for low-dose **Ara-C** [76], we have estimated a smaller central volume leading to a reduced clearance activity derived from an almost equivalently estimated elimination rate constant value. The distribution rate constants differ by a factor of 2 to 2.5 and the peripheral volume by a factor of almost 10. The parameter values and the visual assessment of the one-compartment model [94] in figure 7.12 indicate, that the one- and two-compartment models describe **Ara-C** concentrations with qualitatively different dynamics.

	Solans2018 [94]	Krogh2012 [76]	Ours
CL [L/h]	208.73	272.0	154.225
V_p [L]	-	75.4	7.7825
Q [L/h]	-	13.7	4.1761
V_c [L]	209.25	62.8	37.6571 (21.30%)
k_{10} [1/h]	1.0	4.3	4.0955 (15.09%)
k_{12} [1/h]	-	0.2	0.1109 (67.64%)
k_{21} [1/h]	-	0.2	0.5366 (69.50%)

The two-compartment **PK** model representing a central and peripheral compartment, see figure 6.3, adequately describes the concentration-time data and coincides with the derived values for clearance and the elimination rate constant k_{10} from Table 6 in [92]. We use our derived two-compartment model with the given estimated parameter values in all calculations. We do not use the **PK** models from Krogh *et al.* and Solans *et al.*, because they were fitted to low-dose treatment schedules. Although **Ara-C** is reported to have a linear **PK** [92], simulations with these **PK** models do not coincide well with the concentration measurements from high-dose treatment schedules published in [92] as shown in figure 6.2.

During the model development process, we also have tested a kinetics-**PD** approach [179] which resulted in non-identifiability of the elimination rate constant of the virtual compartment during the individual parameter estimations.

As stated above, the PK model is fixed in the consecutive model development process of the PK/PD model. In one of the simulation studies we analyze the effect of the PK variability on the different modeling hypotheses. We present and discuss the results in figure 7.12.

6.1.2 Secondary pharmacodynamic effects of cytarabine

In this project with the underlying dataset, the current lack of clinical measurements of endogenous G-CSF concentrations and leukemic cell counts (as no relapse events occurred) leads to identifiability issues with the related dynamics. Due to these issues and our main focus on myelosuppression and WBC recovery, we concentrate on agglomerating effects of Ara-C on proliferation and maturation rates and do not consider models including G-CSF or leukemic cell dynamics.

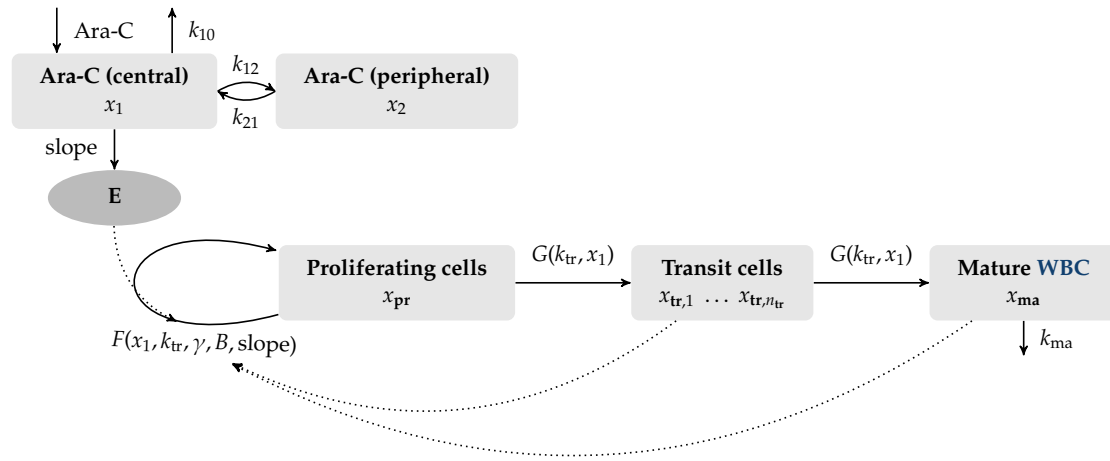


Figure 6.3: **Schematic model from which all mathematical models are derived.** We assume clustering of cells and Ara-C concentrations in compartments with identical properties. The white blood cell (WBC) differentiation is represented by a proliferating compartment x_{pr} , a number n_{tr} of transit compartments x_{tr} with different levels of maturation, and a compartment x_{ma} with mature, circulating WBCs. Cells mature with a maturation rate G . Mature cells x_{ma} are dying by the process of apoptosis with a death rate of k_{ma} . The pharmacodynamic effect of Ara-C is described as a log-linear function E targeting the proliferating cells in the bone marrow. It depends on the concentration x_1 of Ara-C in an assumed central compartment including the circulating blood. The proliferation rate F of x_{pr} models the replication rate of proliferating progenitor cells. Modelling assumptions are incorporated by choosing different functions F and G . The estimated model parameters used for personalization are $B, \text{slope}, k_{tr}, \gamma$, and initial conditions.

Figure 6.3 illustrates the basic assumptions from which we derive twelve model vari-

ations of the original Friberg model which we denote by M1–M12 from now on. They differ concerning the number of transition compartments (M1–M3), initial conditions for the differential equations (M3–M5), and model assumptions for the possible effects of *Ara-C* on proliferation and maturation rates (M5–M12) (compare table 6.3). In this designation, the original Friberg model is denoted by M2. The ordering of the first three models is chosen with respect to the decending number of transition compartments. Quartino *et al.* [82] propose a model with six instead of three transition compartments and is thus denoted as M1. After intermediate evaluations of accuracies we concentrate on the most promising choice of scaling, transition compartments, and initial conditions, and include different modeling assumptions in the models M6–M12 which are alternatives to M5, our reference myelosuppression model extended to *Ara-C*.

During the modeling and parameter estimation process we analyze a model considering separate parameters for the fraction of self-renewal and for differentiation in each compartment. The model has a similarly high accuracy but more challenging identifiability properties. Our findings are summarized in table 7.11.

Table 6.3: **Overview of all investigated mathematical models M1–M12.** For each mathematical model the number of transition compartments n_{tr} , the initial condition (IC) strategy, and the two functions F for proliferation rate and G for maturation rate are specified, compare figure 6.3, respectively. The models M1–M5 are used mainly to determine the best number of transition compartments and IC strategy, which are kept fixed from M5 onward. Different modeling assumptions are incorporated via different functions F and G in the models M5–M12.

Model	n_{tr}	IC	Proliferation rate F	G	Parameters
M1	6	I1	$(1 - E) k_{tr}(B/x_{ma})^\gamma$	k_{tr}	$B, k_{tr}, \gamma, \text{slope}$
Myelosuppression model with $n_{tr} = 6$, proposed in [82].					
M2	3	I1	$(1 - E) k_{tr}(B/x_{ma})^\gamma$	k_{tr}	$B, k_{tr}, \gamma, \text{slope}$
Original Friberg model [52] with $n_{tr} = 3$ transition compartments.					
M3	1	I1	$(1 - E) k_{tr}(B/x_{ma})^\gamma$	k_{tr}	$B, k_{tr}, \gamma, \text{slope}$
As M1, with $n_{tr} = 1$ transition compartments.					
M4	1	I2	$(1 - E) k_{tr}(B/x_{ma})^\gamma$	k_{tr}	B_0
As M3, but with IC approach I2 resulting in 1 additional parameter.					
M5	1	I3	$(1 - E) k_{tr}(B/x_{ma})^\gamma$	k_{tr}	$x_{pr}(t_0), x_{tr}(t_0), B_0$
As M3, but with IC approach I2 resulting in 3 additional parameters.					
M6	1	I3	$k_{tr}(B/x_{ma})^\gamma - E$	k_{tr}	$x_{pr}(t_0), x_{tr}(t_0), B_0$
As M5, but assuming a direct killing effect of Ara-C on the prol. cells.					
M7	1	I3	$(1 - E) k_{tr}/S(x_1)(B/x_{ma})^\gamma$	$\frac{k_{tr}}{S(x_1)}$	$x_{pr}(t_0), x_{tr}(t_0), B_0$
As M5, but replacing k_{tr} by $k_{tr}/S(x_1)$ throughout.					
M8	1	I3	$(1 - E) k_{tr}/S(x_1)(B/x_{ma})^\gamma$	k_{tr}	$x_{pr}(t_0), x_{tr}(t_0), B_0$
As M5, but replacing F by $F/S(x_1)$.					
M9	1	I3	$(1 - E) k_{tr}/S(x_1)(B/x_{ma})^{\gamma S(x_1)}$	k_{tr}	$x_{pr}(t_0), x_{tr}(t_0), B_0$
As M8, but also multiplying γ with $S(x_1)$.					
M10	1	I3	$(1 - E) k_{tr}(B/x_{ma})^{\gamma S(x_1)}$	k_{tr}	$x_{pr}(t_0), x_{tr}(t_0), B_0$
As M5, but multiplying γ with $S(x_1)$					
M11	1	I3	$(1 - E) k_{tr}(B_{bm}/(0.01 * x_{pr} + 0.99 * x_{tr}))^\gamma$	k_{tr}	$x_{pr}(t_0), x_{tr}(t_0), B_0$
As M5, but feedback depends on BM precursor WBC instead of WBC .					
M12	1	I3	$(1 - E) k_{tr}(B_{bm}/(0.01 * x_{pr} + 0.99 * x_{tr}))^{\gamma S(x_1)}$	k_{tr}	$x_{pr}(t_0), x_{tr}(t_0), B_0$
Combining both modeling assumptions of M10 and M11.					

M6: Modeling a direct killing effect of cytarabine on the proliferating cells. In the model M6, we choose the proliferation rate as discussed in previous works [57, 77, 84] as $F = k_{tr}(B/x_{ma})^\gamma - E$. The main difference to all other models is that the **PD** effect E is directly multiplied with x_{pr} and not with $k_{tr}(B/x_{ma})^\gamma x_{pr}$. Multiplying with x_{pr} can be seen as a direct (killing) impact of **Ara-C** on the amount of proliferating cells,

whereas the more plausible mechanism-based rationale is the induced reduction of the proliferation rate constant k_{tr} used in all models except in M6.

M7–M12: Extending the effects of cytarabine. The root mean squared error (RMSE) values indicate that model M5 with one transition compartment and initial condition approach I3 (described in the next section) provides the highest accuracy after model personalization compared to M1–M4.

The indirect effect of Ara-C with an impaired proliferation (M5) is more plausible than a direct killing effect (M6), because Ara-CTP is incorporated into DNA and RNA and impairs cell replication [180]. Therefore, M5 becomes the reference model for all further analysis. We extend the proliferation rate $F(\cdot)$ and/or the transition rate $G(\cdot)$ in M5 to capture potential secondary effects of Ara-C. To understand the implications of the extensions, we observe that the proliferation rate $F = (1 - E) k_{tr} (B/x_{ma})^\gamma$ is negative when $1 < E$. This is the case for

$$c_V x_1 > e^{\text{slope}^{-1}} - 1. \quad (6.3)$$

This corresponds to more proliferating cells being in the process of apoptosis than being in the process of cell division. It is important that the feedback term $(B/x_{ma})^\gamma$ increases the absolute value of F for $B > x_{ma}$, and decreases it for $B < x_{ma}$. Therefore, an analysis of F always has to consider all four cases related to the signs of $1 - E$ and of $B - x_{ma}$. Inspired by the log-linear behavior of the PD effect E , we choose

$$S(x_1) := 1 + \ln(1 + c_V x_1).$$

This monotonously increasing function is applied to different expressions in M5.

In M7, we replace the transition rate k_{tr} by $k_{tr}/S(x_1)$ throughout M5. This results in an Ara-C induced reduction of the transition rate.

In M8 we replace the complete feedback function F in M5 by $F/S(x_1)$. This models an Ara-C induced decreased auto-feedback of the proliferating cells. For high values of x_1 , i.e. when (6.3) holds, this results in a decreased killing of proliferative cells. For values $x_1 > 0$ below that boundary, we get a decreased positive proliferation rate.

In M9 we replace both the complete feedback function F by $F/S(x_1)$ and the proliferation exponent γ by $\gamma S(x_1)$. Again, depending on x_1 either the killing or the proliferation rate of x_{pr} are decreased by $F/S(x_1)$. In addition, the impact depends on whether the WBC count is below or above the baseline: for $x_{ma} < B$ we have an increased killing/proliferation rate $(B/x_{ma})^{\gamma S(x_1)} > (B/x_{ma})^\gamma$ and vice versa.

In M10 we replace the proliferation exponent γ in M5 by $\gamma S(x_1)$. This is motivated by the observation that the feedback term with exponent γ is related to the endogenous G-CSF [52]. In contrast to M9, the function F itself is not scaled. Like in M9, the $\gamma S(x_1)$ scaling results in an increase of killing/proliferation rates for WBC counts below the baseline, and a decrease else.

In M11, we replace the quotient B/x_{ma} by a comparison between cells in the BM and their baseline value. Based on the statement in [47] and the references therein, we assume that about 1 % of the WBC precursor cells in the BM are in the proliferating compartment x_{pr} , and 99 % in the transition compartment x_{tr} . In M12, we combine the

extensions from M10 and M11. The parameter vector contains also initial values, which we discuss next.

6.1.3 Initial conditions of the differential states

The initial values of the PK are chosen to be zero, $x_1(t_0) = x_2(t_0) = 0$, due to the fact that the considered time horizons start before administration of chemotherapy. Further, it is known that previous Ara-C treatments have no impact on the PK of subsequent treatments [92] which is supported by simulation studies showing that the values of $x_1(t)$ and $x_2(t)$ are below 10^{-6} after 16.35 days of the 1 Ara-C infusion. The remaining initial conditions are chosen using one of the following three strategies.

Initial condition approach I1. The WBC count $x_{\text{ma}}(t_0)$ is set to the long term WBC baseline (steady state) count B . With this particular choice all feedback terms simplify to

$$k_{\text{tr}}(B/x_{\text{ma}}(t_0))^{\gamma} = k_{\text{tr}}.$$

Assuming $x_1 = 0$, also $E = 0$, $S(x_1) = 1$, and hence $F = G = k_{\text{tr}}$ for all models at time t_0 , which simplifies the analysis. As initial conditions for the cell counts in the BM we choose the BM baseline cell count $B_{\text{bm}} := \frac{B k_{\text{ma}}}{k_{\text{tr}}}$,

$$x_{\text{pr}}(t_0) = B_{\text{bm}} \quad (6.4)$$

$$x_{\text{tr},1}(t_0) = \dots = x_{\text{tr},n_{\text{tr}}}(t_0) = B_{\text{bm}}, \quad (6.5)$$

which guarantees that inserting (6.4) into (3.17) leads to a right hand side of zero.

The advantage of this approach is the identifiability of the estimation problem, as no additional degrees of freedom in the estimation problem need to be introduced for the initial conditions. However, simulations show that both, the assumption of $x_{\text{ma}}(t_0) = B$ and the steady state assumption, are typically violated at the beginning of a new CC.

Initial condition approach I2. One additional parameter B_0 is introduced and estimated, as suggested by Nock [78]. It is used for the initialization as

$$x_{\text{ma}}(t_0) = B_0, \quad (6.6)$$

together with (6.5). The time derivative (3.17) at time t_0 is given by

$$\dot{x}_{\text{pr}}(t_0) = \left(k_{\text{tr}} \left(\frac{B}{B_0} \right)^{\gamma} - G(k_{\text{tr}}, x_1) \right) B_{\text{bm}}, \quad (6.7)$$

$$\dot{x}_{\text{tr},1}(t_0) = \dots = \dot{x}_{\text{tr},n_{\text{tr}}}(t_0) = 0 \quad (6.8)$$

$$\dot{x}_{\text{ma}}(t_0) = G(k_{\text{tr}}, x_1) B k_{\text{ma}}/k_{\text{tr}} - k_{\text{ma}}B_0, \quad (6.9)$$

which is not zero for $B_0 \neq B$. The advantage of this approach is that also increasing or decreasing WBC counts at t_0 can be captured, depending on the sign of (6.9).

Initial condition approach I3. The initial conditions $x_{\text{pr}}(t_0)$, $x_{\text{tr},1}(t_0)$, \dots , $x_{\text{tr},n_{\text{tr}}}(t_0)$, and, as in I2, also $x_{\text{ma}}(t_0) = B_0$ are introduced as additional estimation parameters. As this

leads to unidentifiability of the estimation problem, a term penalizing deviations from (6.4),

$$\alpha (x_{\text{pr}}(t_0) - B_{\text{bm}})^2 + \alpha \sum_{i=1}^{n_{\text{tr}}} (x_{\text{tr},i}(t_0) - B_{\text{bm}})^2$$

with $\alpha = 1/2500$ is added to the objective function of the least squares estimation problem. The regularization parameter α is chosen with respect to the tradeoff between identifiability of $x_{\text{pr}}(t_0)$ and $x_{\text{tr},i}(t_0)$ and the violation degree of the steady state assumption. Larger values of α result in similar parameter estimates compared to the initial condition approach I1, as more attention is drawn to the penalizing terms guaranteeing a solution close to the steady state assumption after parameter estimation. Smaller values of α weaken the steady state assumption but also increase the uncertainty of parameter estimates for $x_{\text{pr}}(t_0)$ and $x_{\text{tr},i}(t_0)$ resulting in large standard deviations. A good tradeoff is achieved with $\alpha = 1/2500$. For more information about the regularization approach see [130] and the references therein. Note that $B - B_0$ is not penalized. This approach is the most flexible with respect to the possibly transient initial dynamics resulting, e.g. from previous treatments.

6.1.4 Cytarabine-derived and lenograstim-reduced myelosuppression

Model development

The aim is to develop a population PK/PD model describing WBC counts and blasts of AML patients treated with Ara-C and lenograstim during CT. The model development is guided by previously published models and available WBC counts and blast measurements. The PK/PD model by Quartino *et al.* [53] describes the proliferation and differentiation of stem cells to mature neutrophils, and its regulation by endogenous G-CSF is used as a starting point. In the first step, we adapt the myelosuppression model to the PK of Ara-C and analyze the prediction accuracy of the model without considering exogenous G-CSF administrations. In the previous study, it is shown that the Ara-C version of the model from Friberg *et al.* [52] with one PD term on the proliferation rate is not sufficient to describe the WBC recovery times after applying different Ara-C treatment schedules for AML patients. Therefore, different assumptions and combinations of secondary PD effects of Ara-C are analyzed by multiplying $(1+\text{Effect})$ by the proliferation rate and strength. It is demonstrated that Ara-C has a further PD effect on the proliferation strength, leading to a significant decrease in the recovery time when dense schedules are applied. The dataset of the previous study only contains one patient with two cycles in which the novel schedule D123 is administered. Here, we try to underline the secondary PD effect by extending the previous study. We perform parameter estimations for three PK/PD models on a dataset including a variety of Ara-C treatment schedules (D12, D123, d123, d135 and D135) for CT in which no G-CSF is administered. Model Q14 is the Ara-C-induced version of the model from Quartino and colleagues [53] with one transition compartment. In model Q14 γ AraC, we add a PD effect on γ equivalent to our previous model [181]. Model Q14 $\hat{\gamma}$ AraC is the parameterized version of the previous model with one additional fixed effects parameter slopeG.

In a next step, the Ara-C version of Quartino's myelosuppression model is extended through absorption models with varying transit compartments describing the subcutaneous administration of lenograstim [110] and a bioavailability of 30% determined in [182]. The models are fitted to a variety of different CCs to determine the absorption model which described the hematopoietic effects of lenograstim administration best. The final model contains two absorption rate constants k_{a1} and k_{a2} and a bioavailability of 100% similar to subcutaneous modeling approaches presented in [110]. A bioavailability of 30% and one absorption rate constant resulted in non-identifiability issues. As no concentration measurements of G-CSF are collected and the global sensitivity analysis (compare for section 7.24) reveals that the G-CSF related constants do not significantly contribute to the model outcomes, we move forward with the best possible model. As two distinct absorption rate constants are not identifiable [110], we assume a linear relation between k_{a1} and k_{a2} and test several factors until we defined the relation $k_{a2} = \frac{10}{3}k_{a1}$.

Finally, a cytokine-dependent two-compartment model describing the dynamics of leukemic blasts is incorporated and the complete PK/PD model is fitted to the dataset of

the **Ara-C** consolidation arm of the AMLSG 12-09 trial. We include the leukemic blasts as a separate cell line. As the **BM** information consists of relative blast counts without distinguishing by cytology between physiological and leukemic blasts, we test several measurement functions as a fraction and combination of x_{l1} , x_{pr} and x_{tr} . In comparison, the **WBC** count measurements are directly matched to the state x_{ma} . As no endogenous **G-CSF** measurements are available, several parameters are fixed to values from publications, and the modeling process, especially the endogenous **G-CSF** concentrations after lenograstim administration, is guided by the observed **G-CSF** concentrations presented in figures 1 and 2 of [106] and [53], respectively. For the analysis of the influence of the leukemic blast lineage on the **WBC** lineage, we perform two parameter estimations with and without consideration of leukemic blasts.

Final pharmacokinetic(s)/pharmacodynamic(s) model

The developed **PK/PD** model is shown in figure 6.4.

The two-compartment **PK** model (x_1, x_2) for **Ara-C** is taken from [181] as our clinical data do not contain **Ara-C** measurements. The **PK** model describes the **PK** and biphasic elimination of **Ara-C** after high-dose infusions [92]. The hematopoiesis of **WBCs** is modeled by a chain of three compartments representing the proliferating stem cells x_{pr} and differentiating cells x_{tr} in the **BM** released to the blood stream after maturation to **WBCs**. Matured cells x_{ma} die by apoptosis with a death rate constant k_{ma} . **Ara-C** is incorporated into the **DNA** leading to cell death, such that a log-linear **PD** term as a first order kinetics negatively influences the proliferation of stem cells, equivalent to [181]. We assume that the plasma concentration is an adequate surrogate for the **PD** effect of **Ara-C** in the **BM**, as no **PK** model for high-dose **Ara-C** is available which considers the **BM** as an additional compartment. We take up this assumption in the discussion. Two modifications of the myelosuppression model are implemented for our purposes. Instead of three, we use one transit compartment x_{tr} , still guaranteeing a reliable interpretation of the **MMT** and no loss of model accuracy. A detailed discussion is given in [181]. Furthermore, the subcutaneous administration of lenograstim is modeled by a chain of three compartments describing the effect of enhanced proliferation and maturation. The first compartment is a depot compartment with the constant F representing the bioavailability of subcutaneous administration of lenograstim which was determined to be 30% [182]. As lenograstim has an equivalent chemical structure as endogenous **G-CSF** and they bind to the same receptors [26], lenograstim is released to compartment x_g via the first order absorption rate constant k_a positively affecting the production of **WBCs**. As no endogenous **G-CSF** measurements are available, several parameters are fixed to values from publications (see table 6.4). The leukemic blasts are included as a separate cell line. The sequential hierarchy [183, 184] of leukemic blasts (similar to **WBC**) is described by the two compartments x_{l1} and x_{l2} which represent the leukemic blasts in the **BM**, respectively circulating blood and was published in [48]. The leukemic blasts in the **BM** grow and proliferate with the first order rate p_1 . During cell division a leukemic blast divides into two daughter cells, so that the outflux from mitosis is $2p_1x_{l1}$. The outflux is then separated into the process of self-renewal by the rate $2p_1a_1k_l$ with the fraction

one and a half years after the start of the first CC. For each patient, the validated model drives into a purely leukemic steady state ($x_{pr} = x_{tr} = x_{ma} = 0$ and $x_{l1}, x_{l2} > 0$) after five months on average.

Values for a_1 and d_2 are taken from [48] and p_1 is chosen as a half of the WBC proliferation similar to [48] characterizing slow growing leukemic cells [185] resulting in a duration of remission in the range of 4.1 to 8.1 months reported by [186].

To formulate the mathematical model as a system of ODEs in a compact form, we use the following definitions, i.e., for the PD effect E on k_{tr} , the zero-order production rate k_{in} and first order elimination rate k_{out} of G-CSF, and the G-CSF quasi-steady-state term k_{lc} for the leukemic blasts, we define

$$E = \text{slope} \log\left(\frac{x_1}{V_c MM_{AraC}} + 1\right)$$

$$k_{in} = (k_{e,g} + k_{ANC} B) B_g + k_{a2} x_{exo1}$$

$$k_{out} = (k_{e,g} + k_{ANC} (x_{ma} + x_{l2}))$$

$$k_{lc} = \frac{1}{1 + c_1 x_{ma} + c_2 x_{l2}}.$$

All constants, control functions defining the administration of Ara-C and lenograstim, parameters, and initial conditions are specified in table 6.4. The time derivatives of all states are given by

$$\dot{x}_1 = -(k_{10} + k_{12}) x_1 + k_{21} x_2 + \frac{u_{AraC}(t) BSA}{\text{duration}} \quad (6.10a)$$

$$\dot{x}_2 = k_{12} x_1 - k_{21} x_2 \quad (6.10b)$$

$$\dot{x}_{prol} = -\left(\frac{x_g}{B_g}\right)^\beta k_{tr} x_{pr} + \left(x_g/B_g\right)^\gamma k_{tr}(1 - E) x_{pr} \quad (6.10c)$$

$$\dot{x}_{tr} = \left(\frac{x_g}{B_g}\right)^\beta k_{tr} x_{pr} - \left(\frac{x_g}{B_g}\right)^\beta k_{tr} x_{tr} \quad (6.10d)$$

$$\dot{x}_{wbc} = \left(\frac{x_g}{B_g}\right)^\beta k_{tr} x_{tr} - k_{ma} x_{ma} \quad (6.10e)$$

$$\dot{x}_g = k_{in} - k_{out} x_g \quad (6.10f)$$

$$\dot{x}_D = -k_{a1} x_D + \frac{u_l 1000}{V_g \text{dur}_l} \quad (6.10g)$$

$$\dot{x}_{exo1} = k_{a1} x_D - k_{a2} x_{exo1} \quad (6.10h)$$

$$\dot{x}_{exo2} = k_{a2} x_{exo1} - k_{a2} x_{exo2} \quad (6.10i)$$

$$\dot{x}_{l1} = (2a_1 k_{lc} - 1) p_1 x_{l1} - p_1 E x_{l1} \quad (6.10j)$$

$$\dot{x}_{l2} = 2(1 - a_1 k_{lc}) p_1 x_{l1} - d_2 x_{l2}. \quad (6.10k)$$

Table 6.4: Model constants, patient-specific constants, model parameters, and initial values with their units and descriptions.

Constant	Unit	Value	Description
PK model of Ara-C			
k_{10}	1/day	98.2920	Elimination rate of Ara-C from [181]
k_{12}	1/day	2.6616	Distribution rate of Ara-C from [181]
k_{21}	1/day	12.8784	Distribution rate of Ara-C from [181]
V_c	L	37.33	Volume of central compartment from [181]
MM_{AraC}	g/mol	243.217	Molecular mass of Ara-C
dur_c	day	1/8	Infusion time
PD model of WBC and leukemic blasts			
k_{ma}	1/day	2.3765	Death rate of circulating WBCs from [53]
B_g	ng/L	24.4	Endogenous G-CSF steady state from [53]
$k_{e,g}$	1/day	0.592×24	Non-specific elimination rate constant from [53]
k_{ANC}	1/day	5.64×24	Neutrophil-dependent elimination rate from [53]
β	-	0.234	Feedback regulation of G-CSF on WBCs
a_1	-	0.875	Probability of self-renewal from [48]
p_1	1/day	0.1	Leukemic cell proliferation rate from [48]
d_2	1/day	2.3	Leukemic cell death rate from [48]
c_1	L/ 10^9	0.01	G-CSF quasi steady-state feedback scaling factor
c_2	L/ 10^9	0.01	G-CSF quasi steady-state feedback scaling factor
PK model of lenograstim			
k_{a2}	-	$\frac{10}{3}k_{a1}$	2. absorption rate of lenograstim
V_g	L	14.5	Volume of distribution from [106]
dur_l	day	0.0007	Infusion time
BSA	m^2	[1.61, 2.07]	Body surface area (patient-specific)
$u_c(t)$	g/ m^2	[1, 3]	Ara-C dosage (patient-specific)
$u_l(t)$	μg	{263, 324}	Lenograstim dosage (patient-specific)
Parameter	Unit		Description
k_{a1}	1/day		1. absorption rate of lenograstim
k_{tr}	1/day		Transition rate
γ	-		Feedback regulation of G-CSF on WBC proliferation
slope	L/ μmol		PD effect of Ara-C on WBCs
B	$10^9/L$		Baseline of WBC count
x_{blasts}^0	$10^9/L$		Relative number of blasts at start of CT
State initial value	Value	State	Value
$x_1, x_2, x_{exo1}, x_{exo2}, x_D$	0	x_g	B_g
x_{pr}, x_{tr}	$(B k_{ma})/k_{tr}$	x_{l1}	$x_{blasts}^0 (DB CR) - 0.005(B k_{ma})/k_{tr}$
x_{ma}	B	x_{l2}	$B/99$

Measurement functions

The observed cell type measurements are WBC counts in the circulating blood and relative blast counts in the BM. The WBC count measurements are directly matched to the state x_{ma} resulting in the corresponding measurement function

$$h_{wbc}(t) = x_{ma}(t). \quad (6.11)$$

The measurement function of the relative blast count is used from previous publications [57, 187]:

$$h_{blasts}(t) = 100 \frac{x_{l1}(t) + 0.005 x_{tr}(t)}{CR_{ij} DB} \quad (6.12)$$

with the cellularity factor of patient i in the j -th CC

$$CR_{ij} = \begin{cases} 0.2 & \text{if hypocellular} \\ 0.4 & \text{if normocellular, years} > 65 \\ 0.5 & \text{if normocellular, years} \leq 65 \\ 0.95 & \text{if hypercellular} \end{cases} \quad (6.13)$$

and $DB = 10^{12}$ being the approximated maximal tumor cell burden in acute leukemia [13]. As the measurement method for determining the relative blast counts in the BM does not differentiate between physiological and leukemic blasts, the original function is extended with 0.5% cells of the transit compartment. Nombella and Manz [188] examined the range of the relative number of common myeloid progenitors in the BM to be 0.2-0.8% represented in the function by 0.5% cells of the transit compartment.

6.2 Mathematical model for maintenance therapy of pediatric ALL patients

Nonlinear mixed-effects modeling and parameter estimation

The $NLME$ modeling [6] is based on the PK/PD model of [177]. It describes the absorption of both drugs through the GI tract into the plasma after oral administration and their metabolization to their active forms. The MTX metabolites $MTXPG_2$ to $MTXPG_7$ inhibit several enzymes responsible for DNA synthesis [117]. The active form of $6MP$, $6TGNs$, is incorporated into the DNA [111]. Thus, both drugs negatively affect the hematopoiesis of neutrophils, which is described by a chain of five compartments. The first compartment represents the proliferating stem cells. It is negatively affected by $6MP$ and MTX via a linear PD term with one joint PD parameter. The next three transit compartments describe the maturation process until mature neutrophils are released into the circulating blood (last compartment). Further details about this model have been described [177].

During the model development, we have replaced the $6MP$ PK model of [112] with the PK model described by [111] in hopes of obtaining a better response to $6MP$ dosage. The model contains the BSA as a covariate in the clearance and thus provides individualized PK profiles. The PK model of [112] is validated on concentration data of 8 patients (adults) from [189]. However, the simulated $6TGN$ concentrations coincide with data from pediatric patients reported by [111]; hence, it is a priori unclear which would give better results. We also test the influence of weekly MTX administration by either ignoring or considering the administrations and their resulting concentrations through the MTX PK model with a second PD parameter during model fitting. We also test the myelosuppression model from [112], which contains a different feedback term for ANC recovery, but the accuracy has decreased and this line of research has not been further investigated.

The steady state of neutrophils Base, the transition rate k_{tr} , the feedback term γ , and the PD effect slope are defined as parameters. IIV is assumed as log-normally distributed for all four parameters, and the residual variability is estimated using a proportional error model. A linear residual variability model is tested, but results in a reduced model accuracy.

Population PK/PD analysis is performed with the NLME modeling program NONMEM 7.4 (ICON Plc., Dublin, Ireland) [141]. The parameters are estimated using the first order conditional estimation method with interaction. Standard errors are computed with the \$COVARIANCE step in NONMEM.

The final PK/PD model, which describes the clinical data best, is formulated by the system of ODEs

$$\begin{aligned}
 \dot{x}_{6mp}^{gut}(t) &= -k_a x_{6mp}^{gut}(t) + F u(t), \\
 \dot{x}_{6mp}(t) &= k_a x_{6mp}^{gut}(t) - k_{20} x_{6mp}(t), \\
 \dot{x}_{6tgn}(t) &= FM_3 k_{me} x_{6mp}(t) - CL_{6tgn}(BSA) x_{6tgn}(t) \\
 \dot{x}_{pr}(t) &= k_{prol} x_{pr}(t) (1 - E_{drug}) \left(\frac{Base}{x_{ma}(t)} \right)^\gamma - k_{tr} x_{pr}(t), \\
 \dot{x}_{tr1}(t) &= k_{tr} (x_{pr}(t) - x_{tr1}(t)), \\
 \dot{x}_{tr2}(t) &= k_{tr} (x_{tr1}(t) - x_{tr2}(t)), \\
 \dot{x}_{tr3}(t) &= k_{tr} (x_{tr2}(t) - x_{tr3}(t)), \\
 \dot{x}_{ma}(t) &= k_{tr} x_{tr3}(t) - k_{ma} x_{ma}(t)
 \end{aligned} \tag{6.14}$$

with the BSA-dependent clearance

$$CL_{6tgn} = 0.00914 (BSA)^{1.16} \tag{6.15}$$

and the linear PD effect

$$E_{drug} = \text{slope } x_{6tgn}, \tag{6.16}$$

and the patient-specific bioavailable 6MP amount $F u(t)$ of 6MP (implemented as point administration in NONMEM). The PK of 6MP is described by a three compartment model altered from [111]. A fraction of the orally administered 6MP dosage enters the GI tract where bioavailable 6MP is absorbed to the central compartment with the first order rate k_a . In the central compartment, 6MP is eliminated by k_{20} . The elimination also comprises metabolization of 6MP with the rate k_{me} out of which a fraction FM_3 is metabolized to the active form 6TGN. 6TGN is then cleared by the BSA-dependent clearance term CL_{6tgn} . The hematopoiesis of neutrophils is described via a chain of five compartments with equivalent transition rates k_{tr} representing the MMT of the neutrophils [45]. The proliferation rate of HSCs k_{prol} is equivalent to the transition rate k_{tr} guaranteeing homeostasis [45]. Deviations from the neutrophil baseline B are compensated by the feedback regulation $(B/x_{ma})^\gamma$ reflecting the G-CSF controlled proliferation of neutrophils [52, 55, 82, 181]. Negative deviations are induced by the MT modelled

through the linear PD term E_{drug} . As the active forms of both drugs affect the proliferation process, the PD effect is modelled via a linear term with one joint parameter slope multiplied to the feedback-regulated first order proliferation rate constant. Other modeling approaches for the incorporation of the PD effect previously showed worst results in model fitting such that we focused on the described term which is additionally more plausible regarding the PD effect, i.e. an impaired proliferation through the incorporation of the metabolized drug into the DNA [181]. Matured neutrophils die by the process of apoptosis with the rate k_{ma} . A schematic representation of the model is shown in figure 3.9 and model constants are listed in table 6.5. As no PK biomarkers have been measured in the examined dataset, we rely on published PK models and individualized the PD models with respect to individual sets of PD parameters.

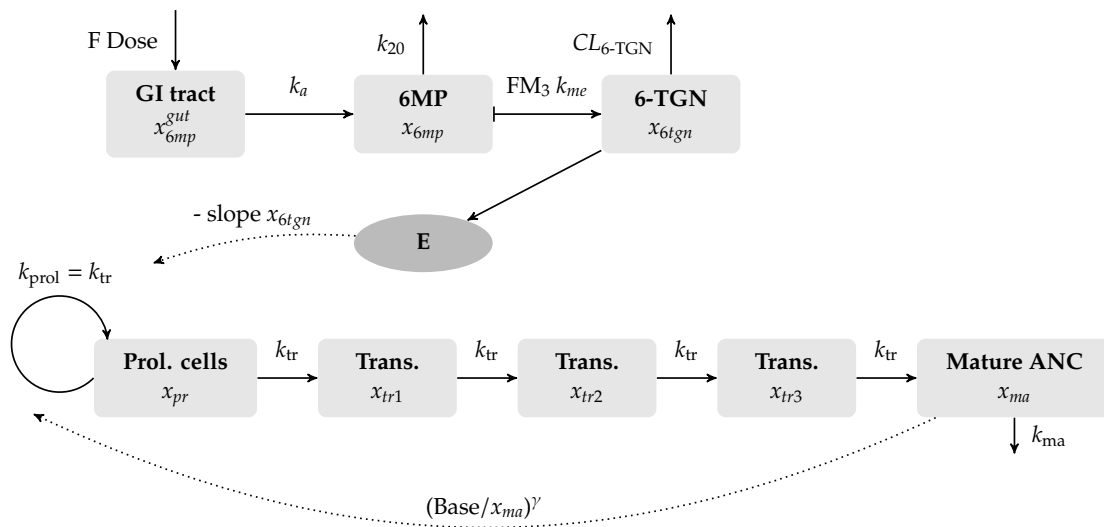


Figure 6.5: Visualization of the final compartment model used for the population pharmacokinetic(s)/pharmacodynamic(s) analysis. The pharmacokinetic(s) model was published by [111] and the myelosuppression model by [177].

Table 6.5: Model constants of the pharmacokinetic(s) model of 6-mercaptopurine (6MP) and its metabolite 6-thioguanine nucleotide (6TGN) from [111], death rate constant of matured neutrophils, and initial conditions of the model (6.14).

Constant	Value	Unit	Description / Comment
F	0.22		Bioavailability factor
k_a	31.2	1/day	Absorption rate constant of 6MP
k_{20}	12.72	1/day	Elimination rate constant of 6MP
FM_3	0.019		Fractional metabolic transformation into 6TGN
k_{me}	9.9216	1/day	Metabolic transformation rate constant of 6MP into either 6TGN or 6-methylmercaptopurine nucleotides
$CL_{6tgn}(BSA)$	$0.219 (BSA)^{1.16}$	L/day	BSA dependent clearance of metabolite 6TGN
k_{ma}	2.3765	1/day	Death rate of matured neutrophils/leukocytes
$u(t_i)$		mg	6MP amount at time point t_i
$x_{6mp}^{gut}(0)$	0	mg	Same initial value for $x_{6mp}(0)$
$x_{6tgn}(0)$	0	mg/L	
$x_{pr}(0)$	$(\text{Base } k_{ma})/k_{tr}$	G/L	Same initial value for $x_{tr1}(0) = x_{tr2}(0) = x_{tr3}(0)$
x_{ma}	Base	G/L	

6.3 Feedback optimal control algorithm with optimal measurement time points

We start by formulating the main algorithm, before we have a closer look at the role of optimal measurement times and one possible extension, the consideration of robustness.

As an alternative to a dual control approach which incorporates the system excitement, an optimizing control with respect to the control objective, and possibly also the choice of optimal measurement times into one single optimization problem, we propose a decoupled dual control approach. We formulate it for a shrinking horizon $[\tau, t_f]$ with respect to the control and experimental design tasks, and an expanding horizon $[t_0, \tau]$ with respect to state and parameter estimation, which can be easily adapted to a moving horizon setting if appropriate.

Algorithm 2 FOCOed

Input: Initial guess \hat{p} , initial values $x(t_0), G(t_0)$, possible measurement times $\{t_1, \dots, t_N\} \subset [t_0, t_f]$

Initialize sampling counter $i = 0$, measurement grid counter $k = 0$ and “current time” $\tau_0 = t_0$

while stopping criterion not fulfilled **do**

- 1: Solve optimal control problem (4.8) on the horizon $[\tau_i, t_f]$, obtain $u^*(\cdot), \hat{x}^*(\cdot)$
 - 2: Solve OED problem (4.35) on the horizon $[\tau_i, t_f]$, obtain $w^* \in \mathcal{W}^{n_\omega, N-k}$
 - 3: Set $i = i + 1, k^{\text{new}}$ such that $w_{k^{\text{new}}}^{\omega, *} > 0$ and $w_j^{\omega, *} = 0 \forall k < j < k^{\text{new}}$. Set $k = k^{\text{new}}$ and $\tau_i = t_k$
 - 4: Apply u^* on $[\tau_{i-1}, \tau_i]$, measure function ω at τ_i
 - 5: Solve state and parameter estimation problem ((4.11)) (4.29) on the horizon $[t_0, \tau_i]$, obtain $\hat{p}, \hat{x}(t)$
- end while**
- 6: Solve optimal control problem (4.8) on the horizon $[\tau_i, t_f]$
-

The algorithm iterates over time with a “current time” τ_i . It solves three subproblems that have been introduced in section 4.2. The solution of the optimal control problem (4.8) provides a control $u^*(\cdot)$ which optimizes with respect to the main control objective. This control is applied until the next update at time τ_{i+1} . This time point τ_{i+1} is calculated by means of an OED problem (4.35) as the first time point from a given fine grid of possible measurement points on which the calculated measurement weight $w_{k^{\text{new}}}^{\omega, *}$ is strictly positive. At this time a new measurement is performed, with a subsequent estimation of states and parameters. Based on the modified parameters, a new optimal

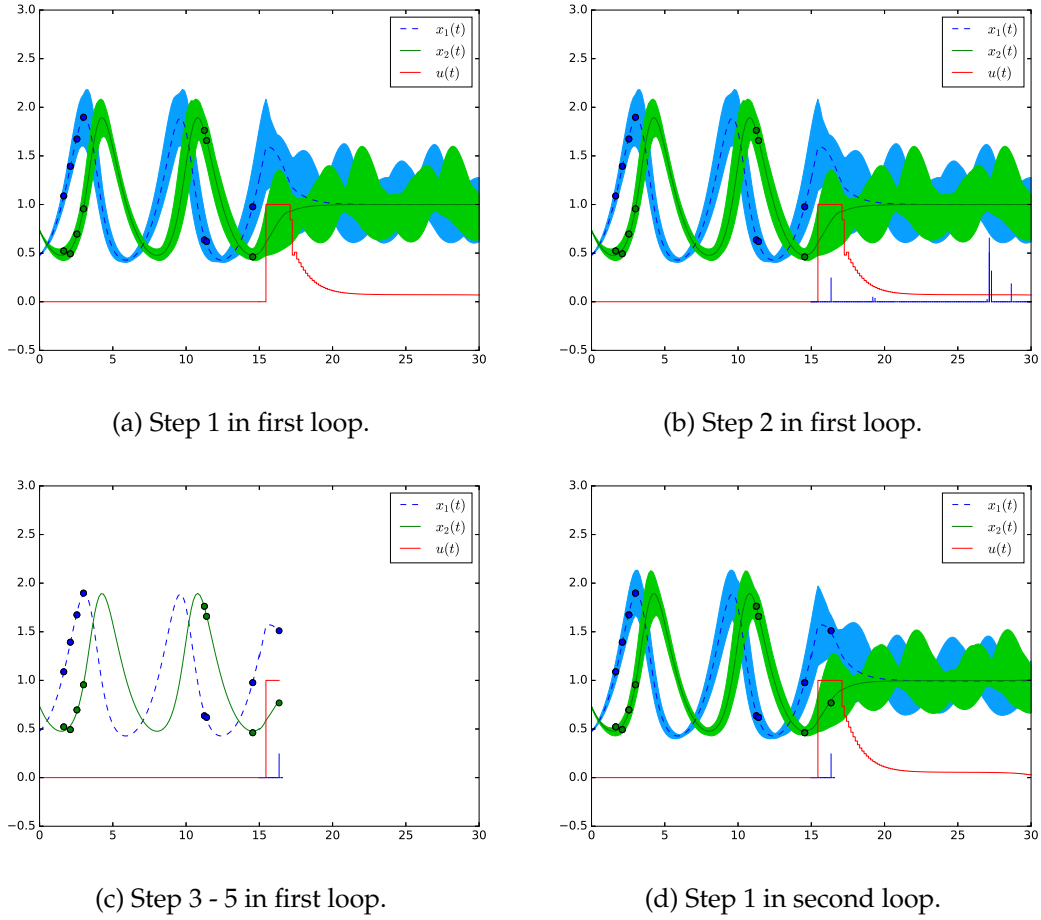


Figure 6.6: **Visualization of algorithm 2 performing one loop applied to the Lotka-Volterra fishing example.** In figure 6.6a the first step, solving an optimal control problem, of algorithm 2 is performed on the time interval $[15, 30]$ with initial values from a parameter and state estimation on the interval $[0, 15]$ with measurements from an optimal experimental design (OED) problem. The uncertainty tubes are computed from 100 simulations with parameter samples from a normal distribution with the estimated parameters and uncertainties as mean and variance. In figure 6.6b an OED is computed on $t \in [15, 30]$ with the optimal control strategy. The strictly positive optimal sampling weights are visualized as vertical lines. Next, the optimal control strategy is performed until time point t_i at which the first sampling weight is strictly positive and a measurement is taken. Afterwards a state and parameter estimation is performed (figure 6.6c). The loop starts again with solving an optimal control problem on $[t_i, 30]$ with the estimated values. The new optimal control strategy is shown in figure 6.6d with uncertainty tubes computed from 100 simulations with updated mean and variance.

control is calculated, based on the modified parameters and control, new measurement weights are calculated and so forth. Naturally, previous solutions can and should be used as initialization to speed up the calculations. Depending on the time scales of the process and the calculation times, there usually is a small time gap in which the old controls need to be applied. See, e.g., [190], for details on how to deal with this situation.

Figure 6.6 visualizes the start of one loop to the start of the next loop of algorithm 2 applied to the Lotka-Volterra fishing example which is described and discussed in detail in Section 7.3. In figure 6.6a an optimal control problem is solved with the initial values $\hat{x}(15)$ and \hat{p} on the interval $[15, 30]$. The initial values are obtained from a state and parameter estimation performed on the interval $[0, 15]$ with measurement time points derived from an OED problem. The uncertainty tubes around the two trajectories are created by 100 simulations with parameter values randomly chosen from a normal distribution with the estimated parameters and corresponding uncertainties as mean and variance. Next, an OED problem is solved for the optimal control strategy $u^*(t)$ and the associated solution $\hat{x}^*(t)$ obtaining optimal measurement time points on the interval $[15, 30]$ (see figure 6.6b). From the optimal design w^* the time point τ_1 is chosen for which the corresponding entry $w_j^* > 0$ is the first strictly positive one. In figure 6.6c the optimal control u^* is applied to the real system until time point τ_1 at which a measurement is performed and the parameters and the initial states are re-estimated with the additional measurements. With the updated values we are back at the start of the algorithm's loop and a new optimal control problem is solved with the updated values on the receding time horizon $[\tau_1, 30]$ shown in figure 6.6d. For the uncertainty tubes again 100 simulations with parameter values sampled from a normal distribution with updated values for the mean and the variance were used.

The stopping criterion is formulated in a general way as it usually depends on the experimenter's choice. Possible criteria are a minimum amount of uncertainty reduction, a fixed number of measurements, or an economic penalization term as proposed in [144].

Finite support designs

We look at the role of finite support for OEDs in more detail, as this will allow us to choose measurement points (and hence the sampling grid) in an optimal way. It is an interesting question how optimal solutions of the discrete OED problem (4.35) and of the continuous analogue (4.36) relate to one another. The answer is given by the following theorem, which states that to every optimal design there is a discrete design with finitely many measurement points resulting in the same FIM. This is obviously a justification for our iterative approach in Algorithm 2, using a finite number of measurements. Theorem 6.3.1 presents a property of optimal designs for the FIM.

Theorem 6.3.1. *Let $n_\omega = 1$. For any optimal design ξ of the OED problem (4.36) resulting in a nonsingular FIM of the state and parameter estimation problem (4.30) there exist a finite number N of measurement time points $\{t_1, t_2, \dots, t_N\} \subset \mathcal{T}$ and positive real numbers w_1, w_2, \dots, w_N*

with $\sum_{i=1}^N w_i = 1$ such that

$$F(\xi) = F_d(t_f) = \sum_{i=1}^N w_i (h_x(x(t_i))G(t_i))^T h_x(x(t_i))G(t_i)$$

with the bounds

$$\left\lfloor \frac{n_p}{n_\eta} \right\rfloor \leq N \leq \frac{n_p(n_p + 1)}{2}. \quad (6.17)$$

n_p is the number of parameters and n_η is the dimension of the model response $h(x)$.

A proof can be found in [191, 192]. It is based on the set of all matrices of the form (4.32) being a compact, convex set. The upper bound results from the Theorem of Carathéodory [145, 193] and the solution of the dual problem which is located at the boundary of the convex set [194]. The lower bound is based on the assumption of $F_d(t_f)$ having full rank n_p , and every update $w_i (h_x(x(t_i))G(t_i))^T h_x(x(t_i))G(t_i)$ having rank n_η . Our setting is slightly more general, as we allow n_ω different measurement functions. However, the result carries over.

Corollary 6.3.2. For any $n_\omega \geq 1$ Theorem 6.3.1 applies with $n_\eta = \sum_{\omega=1}^{n_\omega} n_\eta^\omega$.

Proof. The Minkowski sum of convex, compact sets is again a convex, compact set, and hence the argument for the representability due to the Theorem of Carathéodory and the upper bound are still valid. The maximum rank of the matrix update $\sum_{\omega=1}^{n_\omega} w_i^\omega (h_x^\omega(x(t_i))G(t_i))^T h_x^\omega(x(t_i))G(t_i)$ at time t_i is $\sum_{\omega=1}^{n_\omega} n_\eta^\omega$. The lower bound on N is the quotient of the assumed full rank n_p and this sum. \square

This corollary directly implies that to every optimal solution of the continuous OED problem (4.36) there is an equivalent solution of the discrete OED problem (4.35).

We are further interested in (a posteriori) characterizing the optimal measurement times t_i with corresponding $w_i^\omega > 0$. We make the following assumptions. Let an optimal solution (x^*, G^*, w^*, μ^*) of the optimization problem (4.36) with $\mathcal{W} = [w^{\min}, w^{\max}]$ be given. Here μ^* is the Lagrange multiplier of the constraint (4.33). Let $F^{*-1}(t_f)$ exist. We call

$$\Pi^\omega(t) := F^{*-1}(t_f) (h_x^\omega(x(t))G(t))^T h_x^\omega(x(t))G(t) F^{*-1}(t_f) \in \mathbb{R}^{n_p \times n_p} \quad (6.18)$$

the *global information gain matrix*. Let $\phi(F(t_f)^{-1}) = \text{trace}(F^{-1}(t_f))$ be the objective function of the OED problem (4.36) (for other objectives similar expressions can be found in [144]).

Under the above assumptions in [144] it is shown that

$$w^{\omega,*}(t) = \begin{cases} w^{\min} & \text{if } \text{trace}(\Pi^\omega(t)) < \mu^{\omega,*}, \\ w^{\max} & \text{if } \text{trace}(\Pi^\omega(t)) > \mu^{\omega,*}. \end{cases} \quad (6.19)$$

The proof is based on the application of Pontryagin's maximum principle, exploiting constant adjoint variables, and matrix calculus.

We want to join theorem 6.3.1 with this insight, and look at the special case of $w^{\min} = 0, w^{\max} = 1$. One particular case may arise when the lower bound on the number of support points in theorem 6.3.1, i.e., $\left\lfloor \frac{n_p}{n_\eta} \right\rfloor$ is equal to one. For one single measurement it can happen that $w_i^\omega = 1$ for one index, while otherwise the normalization constraint (4.33) ensures that all $w_i^\omega \in [0, 1)$. For this particular case we define $v^{\omega,*}$ to be the maximum of $\mu^{\omega,*}$ (the Lagrange multiplier of the normalization constraint) and of the upper bound constraint $w_i^\omega \leq 1$. In most cases, however, $v^* = \mu^{\omega,*}$.

Lemma 6.3.3. *For any optimal design ξ of the OED problem (4.36) resulting in a nonsingular FIM of the state and parameter estimation problem (4.30) there exist a finite number N of measurement time points $\{t_1, t_2, \dots, t_N\} \subset \mathcal{T}$ and positive real numbers $w_1^\omega, w_2^\omega, \dots, w_N^\omega$ with $\sum_{i=1}^N w_i^\omega = 1$ for all $\omega \in 1, \dots, n_\omega$ such that*

$$\text{trace}(\Pi^\omega(t)) \leq v^{\omega,*} \quad \forall t \in [t_0, t_f]. \quad (6.20)$$

Proof. Corollary 6.3.2 states the existence and optimality of such a design. Assuming there exists $t_i \in \mathcal{T}$ with $\text{trace}(\Pi^\omega(t_i)) > v^{\omega,*}$, it directly follows $w_i^\omega = w^{\max} = 1$ and with the normalization (4.33) that $w_j^\omega = 0 \quad \forall j \neq i$. The local impact on the optimal objective value is given by $\text{trace}(\Pi^\omega(t_i))$, the assumption of this value being strictly larger than both multipliers is hence a contradiction to optimization theory which states that the Lagrange multiplier of the active constraints give a local estimate for the change in the optimal objective function value. \square

Robustification

As mentioned in the introduction, there are many possible extensions to algorithm 2. Highlighting its flexibility, we exemplarily look at a possible robustification of the optimal control and of the OED problem.

The optimization problems (4.8) and (4.36) depend on given values of the model parameters and the computed control and measurement strategies are only optimal for the specific parameter values. If the true parameter values are known or the estimated parameter values are equal to the true values the optimal strategies can be applied to the real process without loss of optimality. But, in most cases the true parameter values are not exactly known. Then, the uncertainty of parameters in the spirit of confidence regions should be included into the optimization formulations to robustify the computed optimal control and measurement strategies. We apply a robustification approach suggested in [195–197]. The idea is to formulate a min-max optimization problem in which the maximal value of the objective function over the parameters' confidence region is minimized. Applying Taylor expansion with respect to the parameters, a computationally feasible approximation based on first derivatives is used. It aims at preferring solutions with a "flat objective function", i.e., which is not too sensitive with respect to the parameter value p .

Again, we assume that the parameters are normally distributed random variables with mean \hat{p} and variance $\Sigma_{\hat{p}}$. The confidence region of \hat{p} with confidence quantile γ is defined as the set

$$\{p : \|p - \hat{p}\|_{2, \Sigma^{-1}} \leq \gamma\} \quad (6.21)$$

where the positive definite matrix Σ^{-1} induces the norm $\|p\|_{2, \Sigma^{-1}} := (p^T \Sigma^{-1} p)^{\frac{1}{2}}$. Now, the OED objective function in (4.36) is augmented to

$$\phi(F(\xi; \hat{p})) + \gamma \left\| \frac{d}{dp} \phi(F(\xi; \hat{p})) \right\|_{2, \Sigma} \quad (6.22)$$

and similarly the robust optimal control objective function is defined as

$$M(x(t_f); \hat{p}) + \gamma \left\| \frac{d}{dp} M(x(t_f); \hat{p}) \right\|_{2, \Sigma}. \quad (6.23)$$

No further modifications to algorithm 2 are necessary. Note that the norms are evaluated pointwise, as Mayer term and the FIM in problems (4.8) and (4.36) are evaluated at time t_f . However, the analysis of section 6.3 can not be applied in a straightforward way due to the derivative term in the objective function (6.22), as the weights may jump as \hat{p} changes locally. Intuition and numerical results hint into the direction that also for the robust case discrete designs are optimal, probably with the same bounds on the number of support points. But we only conjecture this and do not have a proof.

Part III

Numerical results & discussions

7 | Numerical results & discussions:

7.1 Personalized mathematical models

In this section, we investigate the personalization and prediction accuracy of the mathematical models developed in the previous section. We cross-validate the 12 model variations M1–M12 using dense WBC count measurements from 23 AML patients. Surprisingly, the prediction accuracy remains satisfactory in each of the models despite different modeling hypotheses. Therefore, we compare average clinical and calculated WBC recovery times for different Ara-C schedules as a successful methodology for model discrimination. As a result, a new hypothesis of a secondary PD effect on the proliferation rate seems plausible.

Next, the Ara-C-derived and lenograstim-reduced PK/PD myelosuppression model considering leukemic cells is fitted to data of 44 AML patients during CT with a novel Ara-C plus G-CSF schedule from a phase II controlled clinical trial. The model provides good prediction accuracy and an interpretation of the interaction between WBCs, G-CSF, and leukemic blasts.

Finally, the developed PK/PD model for MT of childhood ALL is fitted to clinical data from 116 pediatric patients.

7.1.1 PK/PD model with cytarabine (Data Magdeburg)

Personalization/Accuracy of PMs with fixed Ara-C schedule

We use all 42 CCs to personalize our mathematical models M1–M12 performing point estimations (individual approach). The point estimates are used to analyze the different modeling assumptions. Additionally, we personalize the most relevant models M3, M10 (with I1), the model from Henrich *et al.*[55], the model from Mangas-Sanjuan *et al.*[54] and the model from Stiehl *et al.*[48] applying NLME modeling (population approach). The population approach is used on the one hand to qualitatively confirm our proposed model variation based on the set of population parameters. On the other hand, we want to compare our set of population parameter values with recently published models and give a reason why the Friberg model serves as our basic model and not recently published models which are similar to the Friberg model, but with several extensions. Once the model parameters have particular values, the model is

called personalized model (PM).

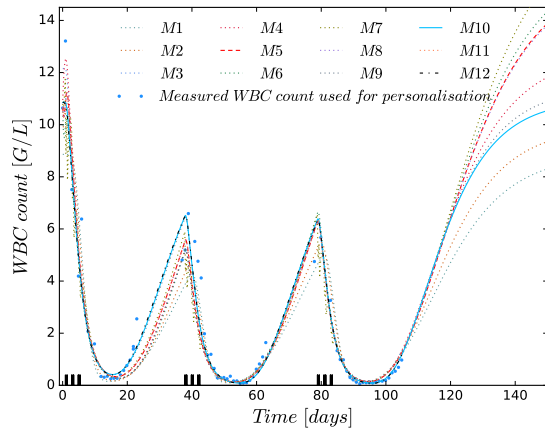
Table 7.6 shows statistics about the accuracies of the PMs describing the clinical data, for a pure estimation (using all available WBC counts to personalize the model) and for a cross-validation (using all but the last CC for personalization).

Table 7.6: **Calculated root mean squared error values for the models M1–M12.** Measured and calculated white blood cell counts are compared. The estimations and predictions use personalized models that are calculated based on the twelve different mathematical models M1–M12. The first row refers to a personalization for all 42 consolidation cycles. The second row shows results for personalizations using all available cycles per patient (Pat). For predictions (Pred) all but one cycle are used for personalization and the last cycle for cross-validation. Four more rows show the predictions separated into the different schedules (D135, d135, D123 and D12). The root mean squared error (RMSE) values decrease from cycles to patients and from personalization towards prediction, as expected. Comparing the mathematical models, the accuracy increases with a reduced number of compartments from M1 to M3. The initial condition strategies I2 in M4 and I3 in M5 decrease RMSE values further. M5–M12 all use $n_{tr} = 1$ and I3 and perform equally well, with the slight exception of M7. Note that in particular there is no significant difference between the established gold-standard model M5 and our newly proposed extended model M10.

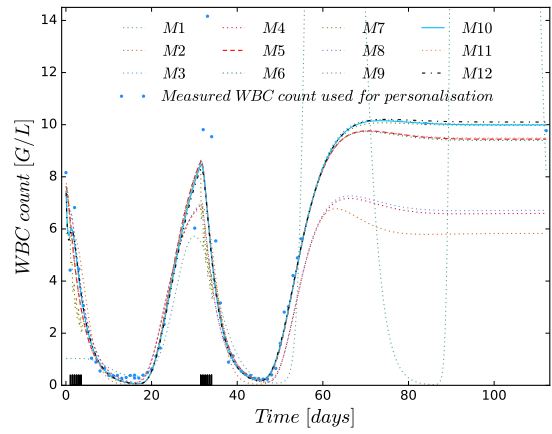
RMSE	M1	M2	M3	M4	M5	M6	M7	M8	M9	M10	M11	M12
42 CCs	0.911	0.836	0.742	0.636	0.579	0.595	0.639	0.576	0.574	0.574	0.577	0.587
23 Pat	1.154	1.011	0.892	0.825	0.741	0.758	0.785	0.753	0.738	0.740	0.740	0.741
14 Pred	1.269	1.128	1.059	1.007	0.908	0.972	0.997	0.960	0.958	0.927	0.940	0.947
7 D135	1.108	0.912	0.834	0.778	0.750	0.753	0.781	0.750	0.767	0.765	0.731	0.768
5 d135	1.319	1.240	1.141	1.093	0.921	1.095	1.023	1.068	1.043	0.957	1.037	1.009
P_{D123}	2.404	2.218	2.241	2.258	2.011	2.014	2.324	2.006	1.996	1.996	2.029	2.022
P_{D12}	1.014	0.991	1.042	0.924	0.842	0.843	1.049	0.839	0.840	0.843	0.824	0.823

The accuracies depend strongly on the number of compartments and initial condition strategy (M1–M5), but do not differ much with respect to modeling assumptions of possible effects of Ara-C considered in M6–M12. These values are even better when the standard schedule D135 is applied in the estimated and predicted cycles. Regarding the root mean squared errors for M1–M5, the results imply that one transition compartment and initial approach I3 are the best choice for the structural model and hence serve as a starting point to analyze different PD effects of Ara-C. As mentioned in the previous section, the number of transition compartments determine the MMT of the

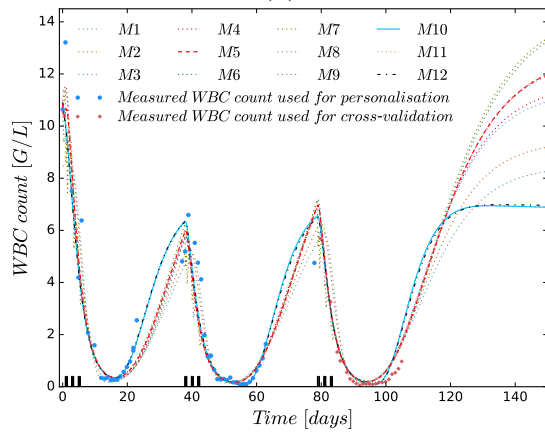
differentiating progenitor cells. Comparing the MMT s resulting from the population approach for M1 to M3, we achieve a slight decrease from 154 h to 144 h to 128 h by using the corrected formula $MMT = n/k_{tr}$ [45] instead of the original formula $MMT = (n+1)/k_{tr}$ [52]. During the administration of cytostatic drugs it is known that the cells are encouraged to rapidly differentiate such that a MMT of 128 h is reasonable. Furthermore, the MMT value from one transition compartment is closest to a previously published corrected MMT value of 106.4 [45, 53]. Studies with healthy volunteers reported MMT s of 153.6 h and 165.6 h [45]. But these values are difficult to compare as chemotherapy can speed up proliferation and differentiation. With this knowledge and the accuracy values of table 7.6 we decide to fix the number of transition compartments to one. The original MMT formula from [52] would result in 180 h, 193 h and 256 h. By using M5 as the reference model and analyzing different hypotheses of Ara-C's PD effect in M6-M12, all models can describe the clinical data equally well. Goodness-of-fit plots in figure 7.8a–b and 7.13 visually support the good match between model predictions and measured WBC counts (respectively observed vs. calculated t_{rec} values) around the nadir and a wider spread of large WBC counts. To analyze the reliability of the PMs to predict the WBC dynamics in subsequent CCs, Figures 7.8c–d indicate the involved model uncertainty from parameter uncertainty by means of Monte Carlo simulations. The model uncertainty is derived from 1000 randomly chosen parameter sets sampled from the variance-covariance matrix resulting from the individual parameter estimation problem (4.11). The information from one CC and no available prior knowledge leads to a high uncertainty. The uncertainty reduces when more WBC counts are present, and the prediction accuracy for consecutive CCs and myelosuppression increases. Examining the accuracy of the PMs for each patient separately, the WBC counts around the nadir are explained well by all models for fixed Ara-C schedules (either D135 or D123), as shown in figures 7.7a–d for two exemplary patients and in figures 7.14 and 7.16 for the other 12 patients with at least two consecutive CCs.



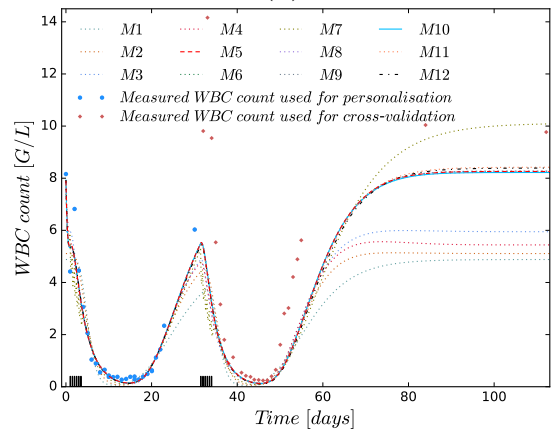
(a)



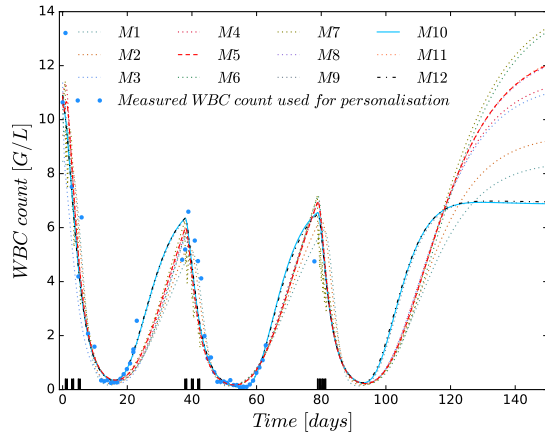
(b)



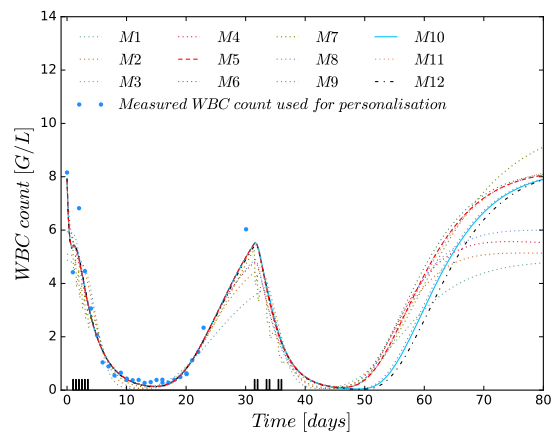
(c)



(d)



(e)



(f)

Figure 7.7: **Comparison of personalized models based on M1-M12 and white blood cell data.** Patient with three D135 cycles (left) and patient P_{D123} with two D123 cycles (right), as indicated on the x-axis. The personalized models (PMs) exemplify reproducibility (first row), predictability (second row) and simulation of a different schedule in prediction than estimation (third row). **(a)** Reproducibility: all 12 PMs based on M1–M12 are able to explain the measured white blood cell (WBC) counts. **(b)** As in (a), all PMs explain the measured WBC counts well, particularly around the nadirs. **(c)** Cross-validated prediction: all PMs explain the WBC counts well, also in the predicted third cycle. **(d)** As in (c), here with a slightly too slow predicted recovery time in the second cycle for all models. **(e)** Varied Ara-C schedule: prediction of D123 in the third cycle for a PM based on two D135 cycles shows faster WBC recovery for M9, M10, and M12. **(f)** Prediction of D135 in the second cycle for a PM based on one D123 cycle shows slower WBC recovery times for M9, M10, and M12.

Regarding the estimated parameter values, we only determine a slight change of the estimated fixed-effects parameter values for B, k_{tr} and slope, the inter-individual variability for all four parameters and the residual error between models M3 and M10 whereas the estimated fixed-effects parameter value for slope significantly decreases when a second PD term is introduced (see table 7.11).

Prediction & Cross-Validation/Accuracy of PMs with altered Ara-C schedule

The PMs are then used to predict (simulate) and cross-validate WBC counts for the last CC of 14 patients for whom at least two consecutive CCs are available. Additionally, we calculate predicted t_{rec} values from our 42 PMs applying D123 and D135 schedules and compare the descriptive statistics with published average t_{rec} values from a subset of data (367 CCs of 208 AML patients, no G-CSF support) of the AMLSG 07-04 trial in which the schedules D123 and D135 after 7+3 regimen are analyzed [20]. The published AMLSG 07-04 [20] trial does not provide WBC counts to obtain new PMs, therefore we use the median of observed t_{rec} values for D123 and D135 Ara-C schedules. In the interest of a fair comparison (i.e., to avoid comparison with the value 0) we exclude five (d135: 1 and D135: 4) out of 42 PMs for which at least one out of the 42 predictions (M1–M12 with either D123 or D135) result in no WBC counts below the threshold value. This can occur as we personalize the models for a specific treatment plan, e.g. D135. Afterwards we apply a different treatment plan to the PMs, i.e. D123, which may result in a reduced cytotoxic effect. Not each out of the 42 predictions result in a nadir value below 1 G/L. Further, we predict t_{rec} values for two Ara-C schedules in which a constant administration of Ara-C throughout days 1-5, with either 100 mg/m² per day or 400 mg/m² per day was given. These schedules, together with D135, have been clinically analyzed for 1088 AML patients (median 52, 568 male) by Mayer *et al.* [10], and the superiority of D135 with respect to disease-free survival rates and remaining in continuous CR after four years has been shown but no t_{rec} values were reported. Finally,

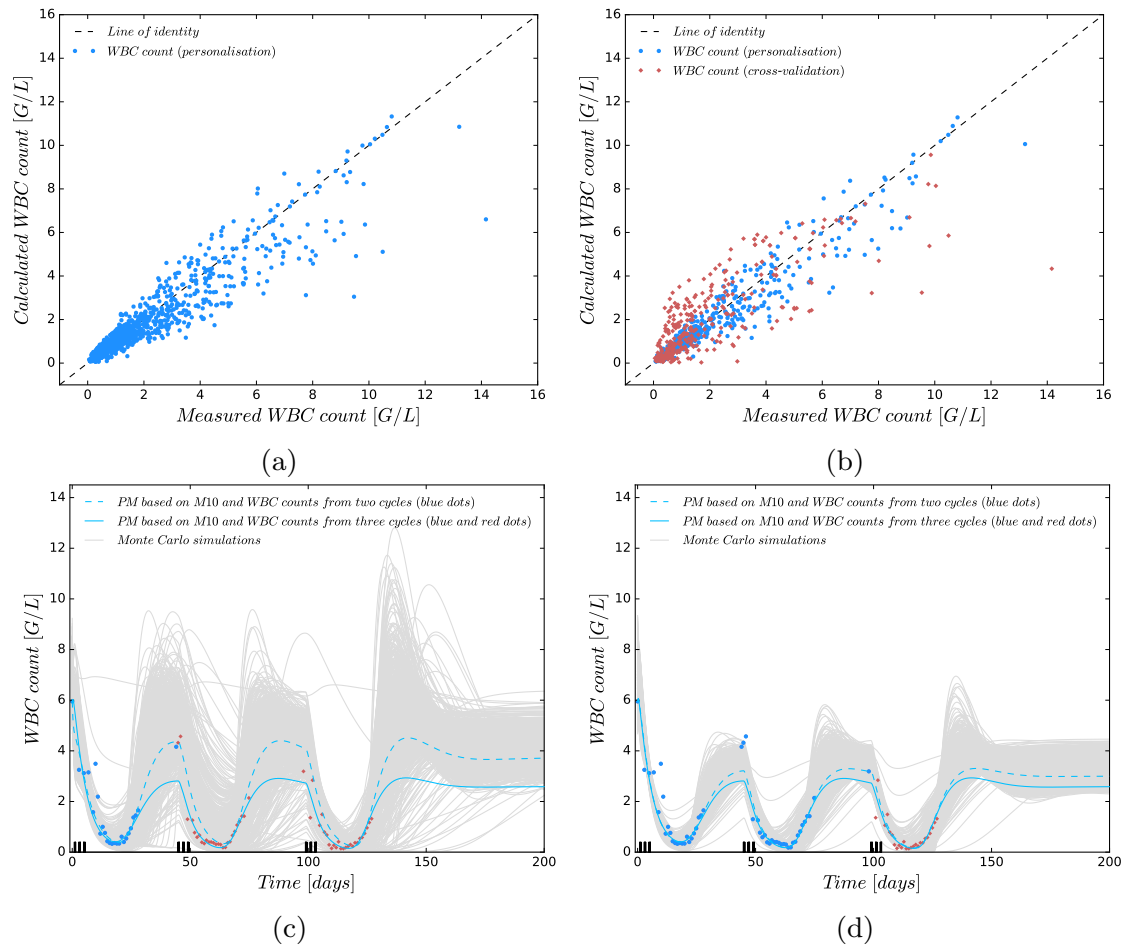


Figure 7.8: **Visualization of predictive accuracies of personalized models (PMs).** **(a)** Goodness-of-fit plot for M10. Shown are measured versus calculated white blood cell (WBC) counts. Models were personalized using complete data sets of one to three cycles from 23 patients. The measured counts around the nadir coincide well ($RMSE=0.740$) with the calculated WBC counts. **(b)** As (a), but cross-validated: WBC counts from the last cycle of patients were not used for personalization, but compared to predictions ($RMSE=0.927$). The plot shows cross-validated WBC counts from the last cycle in red, others in blue. The plots are prototypical for M1–M12. **(c)** PMs based on M10 and either personalization with WBC counts from one or from all three cycles. 1000 Monte Carlo simulations after personalization with WBC counts from one cycle were used to indicate the propagated probability density function. **(d)** As (c), but using WBC counts from the first two cycles for personalization. More measurements lead to higher prediction accuracy. The uncertainty tube tightens and the predicted trajectory gets closer to the solution that used all available WBC counts.

we analyze the effect of the inter-individual PK variability on the t_{rec} values derived by the models M3 and M10 (with I1). We apply schedules D123 and D135 with fixed population parameter values for B , slope, k_{tr} , and γ and perform 500 simulations each with randomly chosen values from constructed IIV for the PK parameters clearance CL and central volume V_C .

All experiments are performed to analyze the 12 proposed models with respect to WBC count and t_{rec} predictability.

As we are interested to differentiate between the distinctive model hypothesis, we apply different chemotherapy schedules to the PMs and analyze their dynamical behavior, especially the WBC recovery. Figures 7.7e–f show two cases where D135 is used for personalization and D123 for prediction (and vice versa). Here, M9, M10, and M12 have a faster (slower) hematological recovery for D123 (D135). All three models assume that the proliferation speed γ depends on the Ara-C concentration. This modeling assumption is visualized in a different way for M5, M10 and M12 in figures 7.9 - 7.11.

In figures 7.9, for an exemplary patient, defined as I, the personalization results in different model parameter values for M1–M12. Figure 7.10 shows another example. For M5 and M10 shown above, the PMs are characterized by the following estimated model parameters:

Model	B	k_{tr}	γ	slope	$x_{pr}(0)$	$x_{tr}(0)$	$x_{ma}(0)$
M5	3.32589	0.124924	1.19429	13.0743	67.1581	86.1515	6.63146
M10	3.33717	0.129158	1.16475	13.6057	66.0178	79.3855	6.66219

The values are quite close to another. Hence, the differences in figure 7.9a are mainly due to different modeling assumptions. For the assumed impact of Ara-C concentration on the proliferation rate exponent in M10, the death rate F is reduced on days 1 and 3, figure 7.9c. At day 5, Ara-C is administered when $x_{ma} < B$, indicated by a white background in figure 7.9c. This leads to a higher absolute value of the feedback term and hence to an increased death rate compared to M5. The increased death rate at day 5 compensates the decreased ones at day 1 and 3, leading to almost identical dynamics for M5 D135 and M10 D135 in 7.9a. For the D123 schedule, figure 7.9d shows the reduced death rate F on all (grey) treatment days 1,2 and 3. As a result, the PM based on M10 recovers faster than the PM based on M5.

Figure 7.10 is organized as figure 7.9, but the PMs were calculated for a different set of WBC counts from an exemplary patient defined as II. Here, the initial WBC count $x_{ma}(t_0)$ is below the baseline WBC count value B (hence and in contrast to figures 7.9c–d we start in a white, not grey, area). Thus, for identical model parameters the death rates of M10 would be increased for the D135 treatment and no compensation as in figure 7.9 would occur. The estimated model parameters are:

Model	B	k_{tr}	γ	slope	$x_{pr}(0)$	$x_{tr}(0)$	$x_{ma}(0)$
M5	4.33160	0.156974	0.482914	7.85156	47.5211	29.6839	3.83573
M10	4.35574	0.160689	0.471371	1.61711	37.9152	28.4292	3.81437

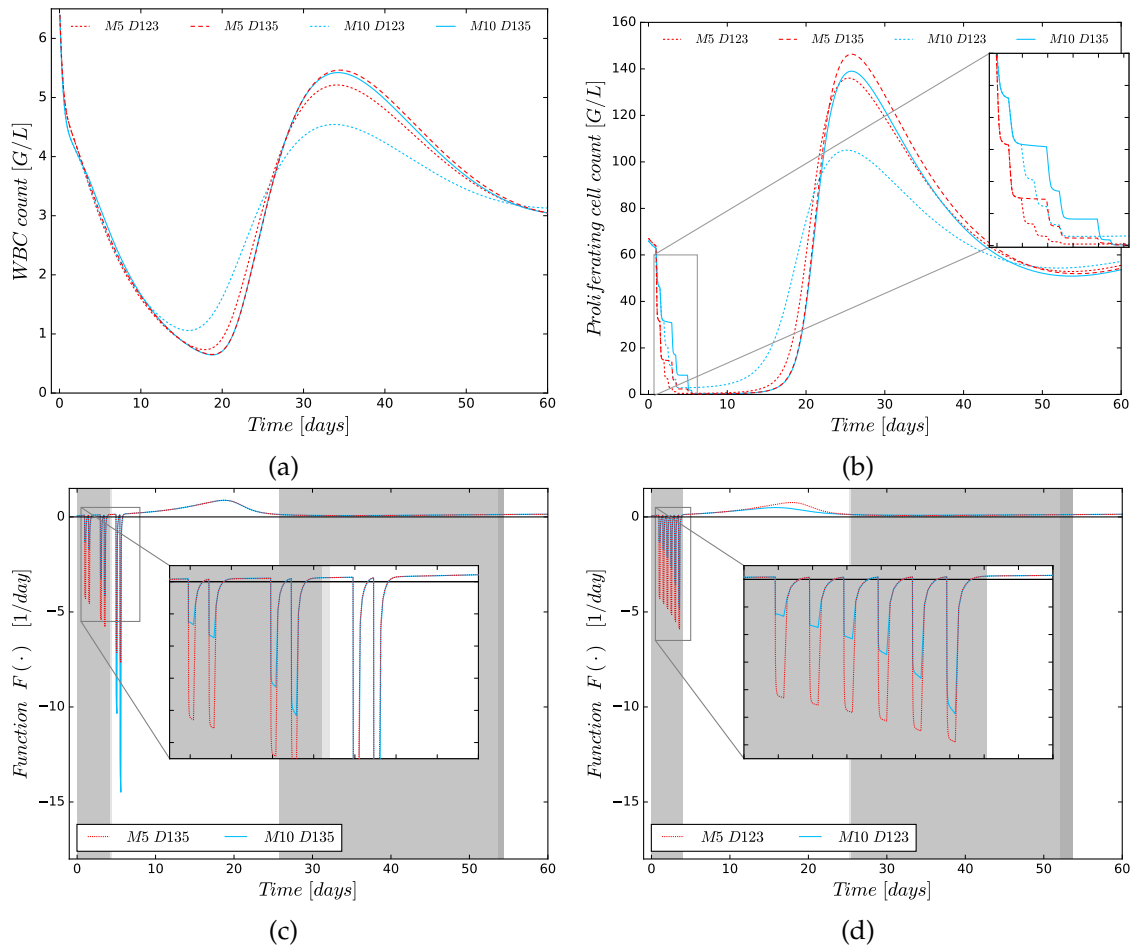


Figure 7.9: **Comparing personalized models M5 and M10 for D123 and D135 schedules (exemplary patient I).** (a) Exemplary prediction of D123 and D135 schedules based on the gold-standard M5 and the promising extension M10. The D135 predictions are similar, the D123 predictions differ. (b) As (a), but proliferating cells x_{pr} are shown. The proliferating cell count of the personalized model (PM) based on M10 D123 recovers fastest, followed by M5 D123. For both D135 schedules the recovery takes longer. (c) Proliferation rate F for (a). Grey indicates at what times the white blood cell (WBC) count is above the baseline WBC count ($x_{ma} \geq B$), resulting in reduced feedback. Compared to M5, the death rate for M10 is decreased at days 1 and 3, and increased at day 5. (d) As in (c), but for the D123 schedules. Compared to M5, the death rate for M10 is decreased at days 1, 2, and 3. This explains why M10 resulted in a faster WBC recovery compared to M5.

Obviously, the model parameter slope is reduced significantly for M10. As can be seen in figure 7.10c this leads to a similar situation as in figure 7.9c, with a reduced death rate on day 1, and an increased death rate on days 3 and 5. As a result, M5 D135

and M10 D135 in figure 7.10a are almost identical.

The death rates for the D123 schedule are reduced compared to the D135 schedule, as shown in Figures 7.10c–d. As in Figures 7.9c–d, the reduction is more significant for the M10 model, which leads to the faster recovery of proliferating cells in figure 7.10b and hence faster recovery of WBC counts in figure 7.10a. Figures 7.9 and 7.10 show the two possible scenarios for the start of a chemotherapy, either $x_{\text{ma}}(t_0) \geq B$ or $x_{\text{ma}}(t_0) < B$. In both the WBC counts decrease after day 1 of the treatment. This decrease leads to increased feedback terms $(B/x_{\text{ma}})^{\gamma}$ and hence to increased death rates. Therefore, administering Ara-C on days 1, 3, 5 instead of days 1, 2, 3 kills more healthy progenitor WBC. In M10 this important effect is stronger than in the gold-standard model M5.

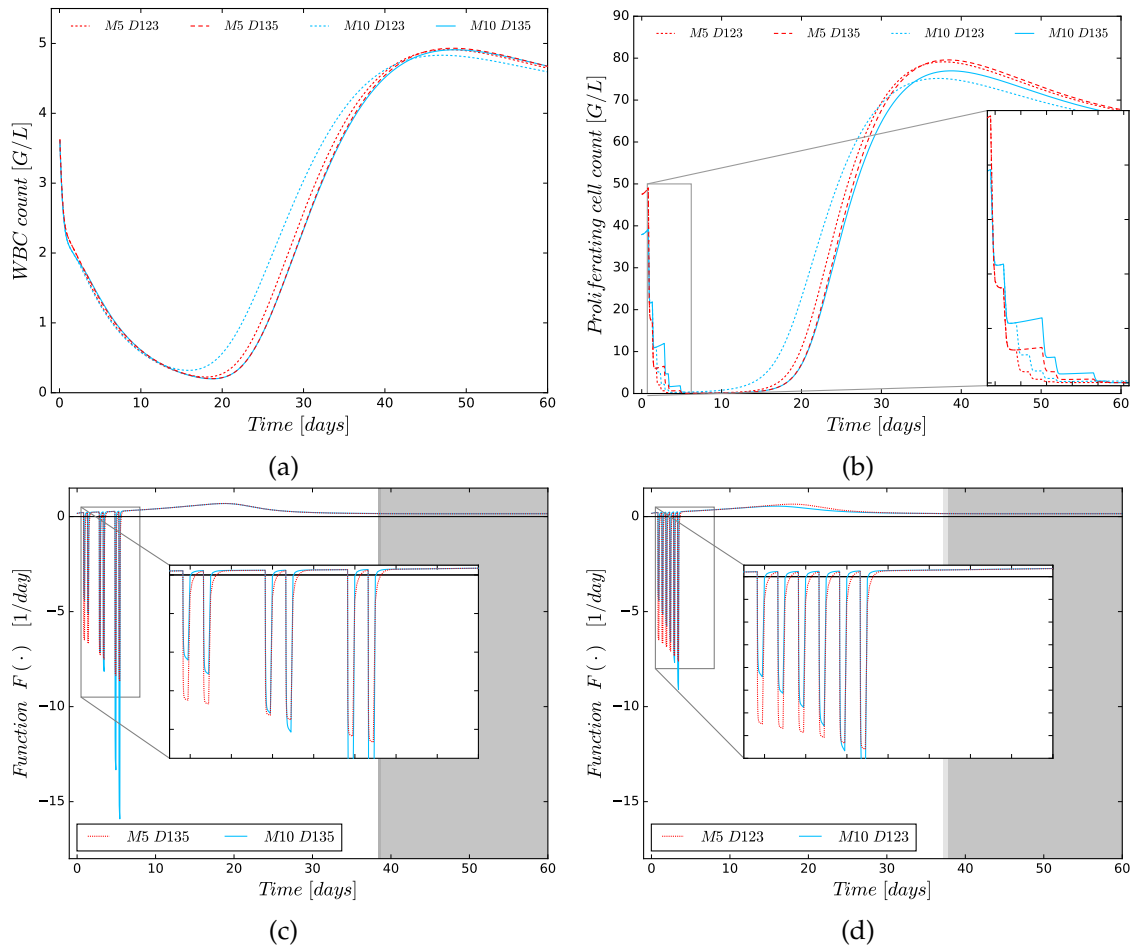


Figure 7.10: Comparing personalized models M5 and M10 for D123 and D135 schedules (exemplary patient II).

Figure 7.11 is organized as figure 7.9 and based on the same set of WBC counts, but comparing M10 and M12. The estimated model parameters are

Model	B	k_{tr}	γ	slope	$x_{pr}(0)$	$x_{tr}(0)$	$x_{ma}(0)$
M5	3.32589	0.124924	1.19429	13.0743	67.1581	86.1515	6.63146
M10	3.33717	0.129158	1.16475	13.6057	66.0178	79.3855	6.66219
M12	3.50825	0.127320	1.22611	10.0560	69.1946	80.0315	6.64934

Model M10 assumes a feedback term $(B/x_{ma})^{\gamma S(x_1)}$ for the proliferation rate F , while M12 assumes $(B_{bm}/(0.01 * x_{pr} + 0.99 * x_{tr}))^{\gamma S(x_1)}$. Administration of Ara-C leads to a reduction of WBC progenitor cells, compare figure 7.11b. With a time delay of a few days this reduction then leads to a reduction of WBC counts as well, see figure 7.11a. Using WBC progenitor cells in the feedback term in M12 thus magnifies the effect described in figures 7.9 and 7.10. For the D135 schedule this is compensated by a reduced estimated slope value. For D123, the death rates of M12 are increased in the peaks, but the proliferation rate is slightly higher. As can be seen in figure 7.11b, the M12 WBC progenitor cells recover faster, although they are below the M10 cell count at day 5.

It is shown that the negative proliferation rate F of M10 and M12 compared to M5 has an altered dynamical behavior during chemotherapy due to the increased γ value from the PD effect achieving a faster WBC recovery for D123 schedules. For this accelerated feedback relationship between WBCs and G-CSF biological interpretations are given in the discussion.

In conclusion, the comparison of WBC recovery times between D123 and D135 treatments is a suitable criterium for model discrimination.

The next study is performed to compare the calculated t_{rec} values from M1-M12 with clinically collected values to figure out which of the models coincide with clinical findings. We use 444 PMs (using M1–M12 and clinical data from 37 cycles with schedules D135, d135, D123 and D12) to predict the outcome of D135 and D123 schedules. The median values of the predicted t_{rec} are compared to the values from a subset of data (108 with D135 and 259 with D123 schedules) from the AMLSG 07-04 trial [20]. M9, M10, and M12 result in roughly 4 days faster t_{rec} for D123 compared to D135, similar to the clinical result from the literature and in contrast to the 1 day difference of M5 (compare table 7.7).

The individual results are qualitatively confirmed by the predicted t_{rec} values from the population approach (see table 7.11). The estimated parameters are approximately in the same range as published values which considered neutrophils and not leukocytes [55, 74]. This is true for B and its IIV. A comprehensive discussion of k_{tr} and the related MMT was already given previously. The parameter slope cannot be compared as we present the first study with high-dose Ara-C. The estimated γ value is roughly two to three times higher compared to published values for the reason that we only use one transition compartment. The γ values for M2, containing three transition compartments, are in the same range then published values. The models from Henrich *et al.* and Mangas-Sanjuan *et al.* are not further considered, as both models simplified to the Friberg model after parameter estimation. For the model from Henrich *et al.*, the estimated population parameter value f_{tr} is 0.96, supporting the visual assessment that the patients' nadirs are not decreasing during the CCs and underlying the clinical finding that single injections of Ara-C compared to treatments with carboplatinum, busulfan,

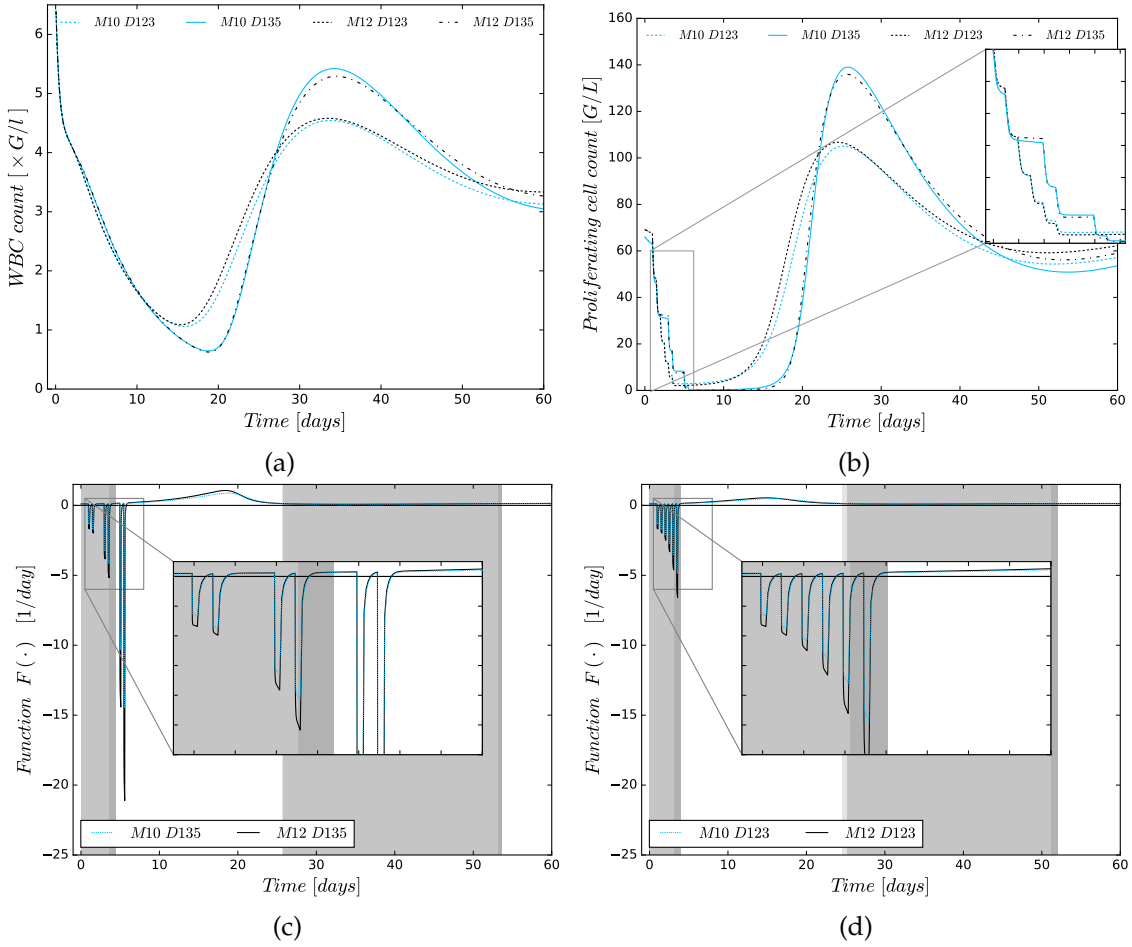


Figure 7.11: Comparing personalized models M10 and M12 for D123 and D135 schedules (exemplary patient I).

bis-chloronitrosourea and/or total body irradiation are less cytotoxic to HSCs leading more rarely to long term BM injury [198]. The estimated parameter values $k_{cycle} = 0.0009$ and $F_{prol} = 0.941$ of the model from Mangas-Sanjuan *et al.* yield a non-existing stem cell cycle. A possible reason for the non-identifiability of the parameters might be the limited schedule variation. The authors state that a vast variation of schedules has to be available for parameter identification [54]. The model from Stiehl *et al.* provide the highest model accuracy with respect to the final objective function value, but exhibit disagreeing WBC recovery times and large relative standard errors (see 7.8). Therefore we do not consider this model in our further studies.

We analyze the three compartment model from Stiehl *et al.* [48] in which, except for the last compartment, each compartment contains parameters for the fraction of self-renewal (a_1, a_2) and for differentiation (p_1, p_2). Similar to the general mathematical model (3.17) the PD effect E is applied to the proliferating cells c_1 , complementing

Table 7.7: Double cross-validation with clinical data from two independent clinical trials. Shown are the median, standard deviation, minimum and maximum (in brackets) of t_{rec} , the *leukopenia time* t_{leu} (the number of days with white blood cell count ≤ 1 G/L) and *nadir* for D123 and D135 schedules. The first two rows show values from two independent clinical studies that serve as a comparison. The second part of the table shows prediction results. Predictions were calculated with personalized models (PMs) from our clinical data with underlying mathematical models M1–M12. Model M5 explained well the outcome of schedule D135, but showed a significant mismatch of more than three days for schedule D123. The predictions using the extended model M10 were better for schedule D123.

		t_{rec}		$t_{\text{rec}}^{\text{D135-D123}}$		t_{leu}		t_{leu}		t_{leu}		t_{leu}			
		D123		D135		D123		D135		D123		D135			
Clinical Data		19.3	± 1.0	23.1	± 2.9	–	–	11.5	± 3.5	12.5	± 4.7	0.3	± 0.0	0.3	± 0.2
$n^{\text{D123}} = 2, n^{\text{D135}} = 23$		(18.6	20.1)	(14.1	27.1)	–	–	(9.1	14.0)	(5.0	20.0)	(0.24	0.27)	(0.1	0.8)
Subdata (AMLSG 07-04) $n^{\text{D123}} = 259, n^{\text{D135}} = 108$		18.0	–	22.0	–	–	–	–	–	–	–	–	–	–	–
Model	Group	D123		D135		D123		D135		D123		D135			
M1	37 PMs	21.9	± 3.7	22.6	± 3.7	0.7	± 0.2	13.3	± 4.5	13.3	± 4.6	0.2	± 0.2	0.2	± 0.2
		(16.0	34.8)	(17.0	35.6)	(0.3	1.0)	(7.5	28.3)	(7.5	28.5)	(0.0	0.6)	(0.0	0.6)
M2	37 PMs	22.2	± 3.5	22.6	± 3.5	0.5	0.2	13.3	± 4.2	13.4	± 4.2	0.3	± 0.2	0.3	± 0.2
		(16.4	33.3)	(17.4	33.8)	(0.2	1.0)	(7.5	26.2)	(7.6	26.4)	(0.1	0.6)	(0.1	0.6)
M3	37 PMs	22.3	± 2.7	23.2	± 2.7	0.9	0.1	13.2	± 3.7	14.1	± 3.6	0.4	± 0.2	0.4	± 0.2
		(17.1	30.7)	(18.2	31.7)	(0.8	1.3)	(7.2	23.3)	(8.3	23.9)	(0.1	0.8)	(0.1	0.8)
M4	37 PMs	22.4	± 2.8	23.3	± 2.7	0.9	0.1	13.2	± 3.7	14.1	± 3.6	0.4	± 0.2	0.4	± 0.2
		(17.0	30.9)	(18.1	31.9)	(0.8	1.2)	(8.5	23.5)	(9.4	24.1)	(0.1	0.8)	(0.1	0.7)
M5	37 PMs	22.4	± 3.1	23.3	± 3.0	0.9	0.2	12.7	± 4.0	13.5	± 4.0	0.3	± 0.2	0.4	± 0.2
		(16.8	32.5)	(18.0	33.5)	(0.1	1.2)	(6.6	25.5)	(7.6	26.1)	(0.1	0.9)	(0.1	0.9)
M6	37 PMs	22.6	± 3.4	22.8	± 3.3	0.2	0.2	13.2	± 4.0	13.2	± 4.0	0.4	± 0.2	0.4	± 0.2
		(14.5	32.0)	(15.3	32.4)	(0.0	0.8)	(4.6	25.0)	(4.7	24.9)	(0.1	0.9)	(0.1	0.9)
M7	37 PMs	22.5	± 2.7	23.0	± 2.7	0.5	0.2	12.8	± 4.3	13.2	± 4.7	0.3	± 0.4	0.3	± 0.4
		(17.8	31.0)	(18.4	31.8)	(0.0	1.1)	(0.0	23.6)	(0.0	23.9)	(0.1	2.7)	(0.0	0.9)
M8	37 PMs	21.7	± 2.7	22.6	± 2.6	0.9	0.1	12.6	± 4.0	13.5	± 3.9	0.3	± 0.2	0.4	± 0.2
		(16.7	29.4)	(17.9	30.5)	(0.6	1.3)	(6.5	22.1)	(7.3	22.7)	(0.1	0.8)	(0.1	0.7)
M9	37 PMs	20.1	± 2.7	23.7	± 2.6	3.1	0.9	10.5	± 4.0	14.7	± 3.6	0.4	± 0.2	0.3	± 0.2
		(16.0	28.9)	(18.6	31.6)	(0.8	5.2)	(3.4	21.7)	(7.3	23.9)	(0.1	0.9)	(0.0	0.7)
M10	37 PMs	20.3	± 3.2	24.2	± 3.2	3.5	1.0	11.6	± 4.4	15.2	± 3.9	0.4	± 0.2	0.3	± 0.2
		(15.4	32.4)	(18.9	35.7)	(0.9	5.8)	(1.6	25.5)	(7.6	28.4)	(0.1	1.0)	(0.0	0.7)
M11	37 PMs	22.3	± 3.0	23.2	± 2.9	0.9	0.1	12.7	± 4.1	13.5	± 4.0	0.3	± 0.2	0.4	± 0.2
		(16.7	32.6)	(17.9	33.7)	(0.7	1.2)	(6.5	25.6)	(7.6	26.2)	(0.1	0.8)	(0.1	0.7)
M12	37 PMs	20.4	± 3.3	24.0	± 3.4	4.0	1.2	11.9	± 4.4	15.4	± 3.9	0.4	± 0.2	0.2	± 0.2
		(15.6	32.9)	(18.7	36.4)	(2.0	8.2)	(3.1	26.0)	(8.4	29.1)	(0.1	0.9)	(0.0	0.6)

Table 7.8: Objectives (final objective function values from FOCEi method (OBJ), population predicted t_{rec}^{123} and t_{rec}^{135} values), parameter and coefficient of variation (CV) estimates with relative standard errors (RSE) from nonlinear mixed-effects modeling of model from Stiehl *et al.* [48].

Stiehl2018[48]	
Objectives	
t_{rec}^{123}	25.16
t_{rec}^{135}	25.68
Final OBJ	-399.89
Fixed Effects (RSE%)	
a_1	0.5929(13)
a_2	0.0003(89)
p_1	1.9880(80)
p_2	0.1971 (8)
k	0.0337(75)
slope	0.9270(74)
IIV CV%(RSE%)	
a_1	1.8 (176)
a_2	32.4(47222)
p_1	44.4 (195)
p_2	28.7 (136)
k	32.1 (19)
slope	33.4 (60)
Residual Error (CV%)	
Proportional	0.106(5)

the state equation of c_1 by the term $-Ea_1s(t)p_1c_1$. As it is not exactly known at which maturation step the ability of self-renewal gets lost, the values of the fractions of self-renewal a_i , $i = 1, \dots, n_{tr}$ can help specifying the step. As we only consider one transition compartment it turns out that almost only the stem cells perform self-renewal as the fixed effect parameter value of a_2 is close to zero. After the chemotherapy, the cells in the transition compartment draw their whole ability on differentiation such that the **WBC** recovery is speeded up and homeostasis is reached again as soon as possible. Due to the deviation of the recovery times with clinical findings and the large relative standard errors, we do not use the model for further investigations.

The simulation study analyzing the effect of the **PK** variability on the resulting recovery times of schedules D123 and D135 for models M3 and M10 (with I1) reveals that model M10 is more sensitive to different high-dose **Ara-C** treatment schedules compared to model M3 despite the high inter-individual **PK** variability. This is verified in figure 7.12 presenting boxplots of 500 simulated t_{rec} values for both models and schedules with constructed **IIV** on the **PK**.

Discussion

High-density **WBC** counts from 23 **AML** patients are collected and used to personalize 12 mathematical models and analyze their prediction accuracy with respect to different modeling hypotheses and treatment schedules. The high prediction accuracies of the **PMs**, especially around the nadir, confirm previous claims [199, 200] that the general approach of in-silico studies can be used for clinical decision support. As clinical decision support we understand tools which help physicians to monitor and predict **WBC** dynamics and the duration and grade of myelosuppression. In combination with clinical expertise on the impact of schedules on relapse probabilities and their small scope determining the start of the next cycle due to subjective experience and the patients fitness, this might have an important clinical impact via altered treatment schedules which might eventually result in decreased depth and duration of myelosuppression.

Current drawbacks are the high model uncertainty, if insufficient information is available. This makes precise and reliable predictions difficult (compare figures 7.8c–d). Furthermore, the lack of leukemic cell dynamics and the validation of the **PMs** based on one specific chemotherapy schedule might lead to not appropriate models concerning an optimization of **Ara-C** dosage.

Comparing the estimated parameter values with published values, the estimated baseline value for the **WBCs** is within the normal human **WBC** range of 4.5 – 10 *G/L* but reduced by 2 *G/L* compared to published baseline values for the Friberg model being in the range of 7 to 7.8 *G/L* [52]. The **MMT** of 128 h for M3 using the corrected formula [45] is reasonable and fits into the range of previously published values [201]. The estimated γ values are roughly two to three times higher compared to published values for the reason that we only use one transition compartment. The γ values for M2, containing three transition compartments, are in the same range then published values. The decrease of the slope parameter value from one to two **PD** effects occurs as the effect of **Ara-C** is distributed on two different sites of action. During the parameter estimation,

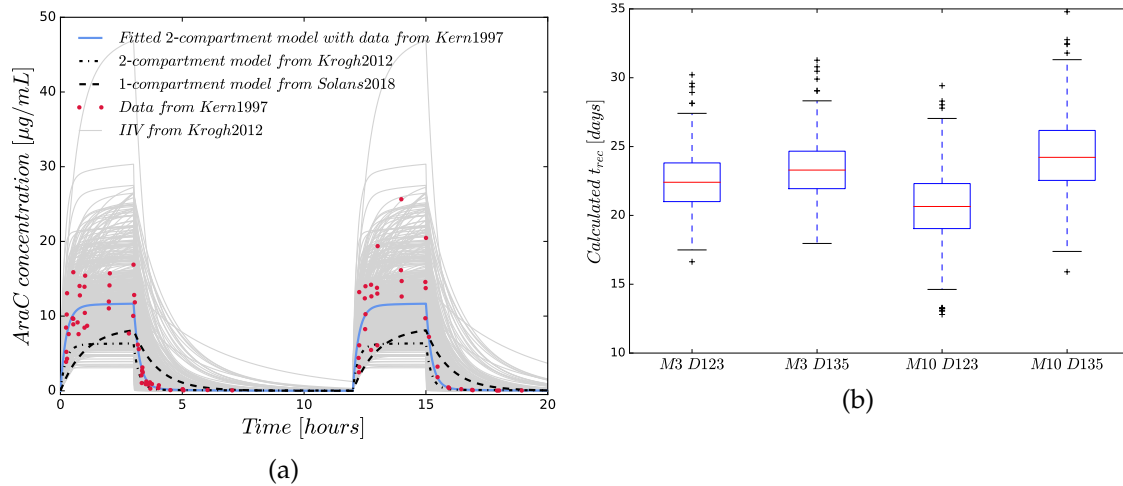


Figure 7.12: **Simulation study analyzing the sensitivity of model M5 and M10 on interindividual variability (IIV) of the pharmacokinetic(s) (PK) when schedules D123 and D135 are applied.** (a) As figure 3.7, but with 500 simulations of our fitted two-compartment PK model with interindividual variability on the clearance and the central volume.

(b) Recovery times (t_{rec}) from 500 simulations each of models M3 and M10 (with I1) applying schedules D123 and D135 with inter-individual variability given as coefficient of variation (CV) on PK parameters clearance (45%) and central volume (70%). Red lines within the boxes are the medians, the upper and lower box limits are the first (Q1) and third quartiles (Q3) of the data. The lower whiskers will extend to the first t_{rec} values greater than the first quartiles minus the 1.5-times the interquartile ranges (IQR) ($Q1 - 1.5 \times IQR$). Equivalently, the upper whiskers will extend to last t_{rec} values less than $Q3 + 1.5 \times IQR$. Beyond the whiskers, data are considered as outliers and are plotted as individual points (+). The simulation study revealed that model M10 was more sensitive to different high-dose Ara-C treatment schedules compared to model M3 despite the high inter-individual PK variability.

we observed for some CCs correlations (> 0.9) between γ and k_{tr} and between γ and slope. But these correlations have no influence on the parameter identifiability. Further, it is shown that under certain assumptions, which we fulfill ($k_{prol} = k_{tr}$), the Friberg model is structurally globally identifiable [201]. In future studies, we propose to use global design measures from [202] to provide treatment schedules reducing global parameter sensitivity and undesired parameter correlation.

We show that an analysis based on a fixed chemotherapy schedule cannot discriminate between different modeling hypotheses. The agglomerative nature of the mathematical models leads to a choice of model parameters that is not only personalized to the patient, but also to the applied schedule. Therefore, we use different schedules for personalization and prediction to overcome this problem and to allow discrimination of the models. This approach allows us to distinguish between the modeling hypotheses

Table 7.9: **Comparison of model predictions for low-dose treatment schedules.** As in table 7.7, predicted *nadir* values for different treatment schedules are shown, based on underlying mathematical models M1–M12. Shown are the values of median, standard deviation, minimum and maximum (in brackets) for two low-dose schedules. Both assume a continuous infusion throughout days 1 to 5, with either $100 \text{ mg}/\text{m}^2$ or $400 \text{ mg}/\text{m}^2$ Ara-C per day. No clinical observations are available to compare these predictions, but they give additional insight on the possibility to discriminate models M1–M12 and a general trend showing that for $100 \text{ mg}/\text{m}^2$ per day despite of M7-M9 almost all nadir values are above $1 \text{ G}/\text{L}$. The nadir values for the low-dose infusion with $400 \text{ mg}/\text{m}^2$ Ara-C per day are in the same range compared to the results of the high-dose schedules (Two further personalized cycles were excluded because for some models no recovery after chemotherapy was observed). The simulated nadirs above $1 \text{ G}/\text{L}$ for the low-dose schedule ($100 \text{ mg}/\text{m}^2$) reflect the lower toxic effects represented by required hospitalization due to fever and neutropenia and platelet transfusions compared to the low-dose ($400 \text{ mg}/\text{m}^2$) and high-dose schedules explored in [10]. As M7-M9 are not able to reflect the lower toxic effects through higher nadir values, the simulation study serves as an indicator that the secondary effect of Ara-C may not be an Ara-C induced reduction of the transition rate.

Model	Group	nadir			
		D1-5 100		D1-5 400	
M1	35 PMs	1.6	± 0.8	0.3	± 0.2
		(0.0	3.6)	(0.0	0.8)
M2	35 PMs	1.7	± 0.8	0.3	± 0.2
		(0.5	3.7)	(0.1	1.0)
M3	35 PMs	1.8	± 0.9	0.4	± 0.2
		(0.8	4.3)	(0.2	1.1)
M4	35 PMs	1.7	± 1.0	0.4	± 0.2
		(0.8	4.9)	(0.2	1.1)
M5	35 PMs	1.7	± 1.1	0.4	± 0.2
		(0.7	5.5)	(0.2	1.0)
M6	35 PMs	1.5	± 1.1	0.4	± 0.3
		(0.9	5.9)	(0.2	1.2)
M7	35 PMs	0.5	± 0.5	0.1	± 0.3
		(0.1	3.4)	(0.0	1.0)
M8	35 PMs	0.1	± 0.1	0.1	± 0.1
		(0.0	0.4)	(0.0	0.4)
M9	35 PMs	0.7	± 0.4	0.2	± 0.1
		(0.1	1.6)	(0.0	0.5)
M10	35 PMs	2.1	± 1.3	0.6	± 0.4
		(0.6	5.8)	(0.1	1.8)
M11	35 PMs	1.6	± 1.1	0.4	± 0.2
		(0.9	5.5)	(0.2	1.0)
M12	35 PMs	2.4	± 1.2	0.7	± 0.5
		(0.8	5.8)	(0.1	2.1)

Table 7.10: Model constants, patient-specific constants, and units of model parameters.

Constant	Unit	Value
Ara-C rate elimination k_{10}	1/day	98.64
Ara-C rate distribution k_{12}	1/day	2.69
Ara-C rate distribution k_{21}	1/day	1.29
Molecular Mass MM_{AraC}	g/mol	243.217
Volume of central compartment V_c	L	37.33
Death rate k_{ma}	1/day	2.3765
Patient-Specific	Unit	Range
BSA	m^2	[1.61, 2.07]
Infusion duration	day	3/24
Ara-C dosage	g/ m^2	[1, 3]
Model parameter	Unit	
k_{tr}	Transition rate	1/day
γ	Feedback exponent	–
slope	Pharmacodynamics	L/ μmol
B	Baseline WBC count	$10^9/L$
$x_{pr}(0)$	Initial value	$10^9/L$
$x_{tr}(0)$	n_{tr} initial values	$10^9/L$
$x_{ma}(0)$	Initial value	$10^9/L$

The values are used to obtain personalized mathematical models. The constants are determined from published data [92] and applied to all patients. To shorten notation we also use $c_V = \frac{1}{V_c MM_{AraC}}$. The patient-specific infusion times and dosages that define a treatment schedule are modified for simulation and optimization of different schedules. The range shows minimum and maximum values of all considered data in the clinical study.

implemented in models M5–M12 and enables us to find the suitable model assumption considered in M9, M10, and M12. In our opinion this procedure should be routinely applied, preferably using high density WBC counts for different schedules in the same patients. As an alternative to such a tedious clinical study we suggest to use average t_{rec} values as a discrimination criterion for competing models.

Comparing the t_{rec} values for D123 and D135 treatments from the PMs with our clinical data and the AMLSG 07-04 trial in table 7.7 and 7.9 implies, that model M10 (based on Ockam’s razor in comparison to M9 and M12) is the best candidate among M1–M12 for future work on the simulation and optimization of intermediate to high-dose Ara-C treatment schedules.

The 1 day shift in t_{rec} values between our clinical data and the AMLSG 07-04 trial

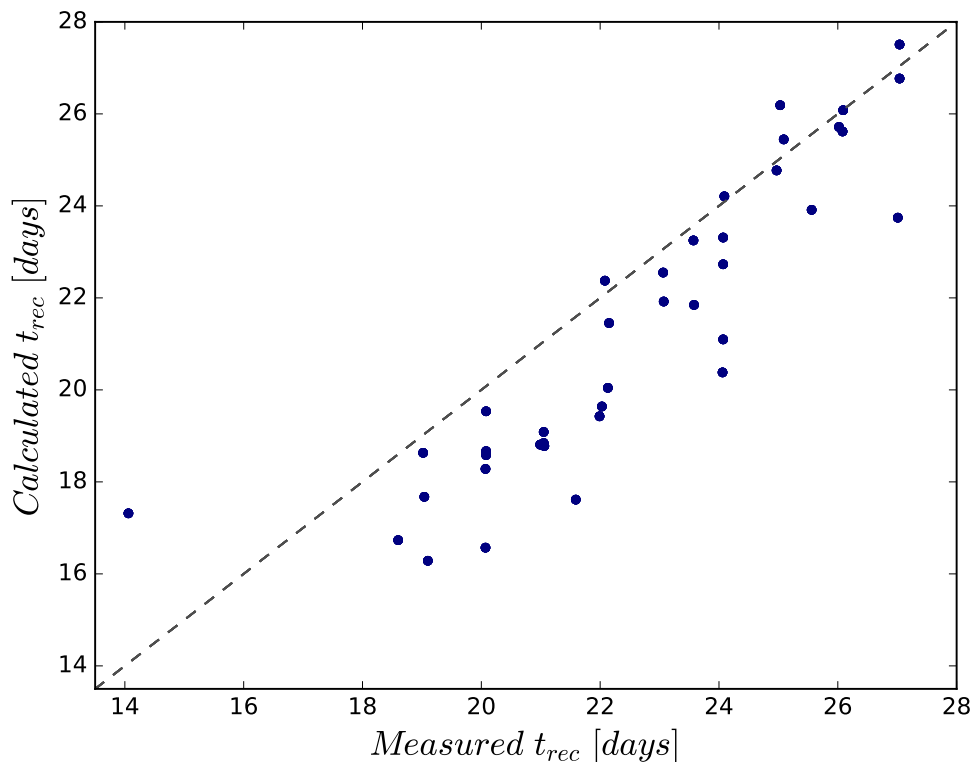


Figure 7.13: **Goodness-of-fit plot for all but three (because of white blood cell counts greater 1) measured and calculated t_{rec} values for M10 after model personalization for each consolidation cycle.** The 39 measured t_{rec} values are slightly higher due to the coarser measurement grid.

can be explained by the age difference between patients in our clinical data (median 62 and 57 years for D123 and D135, respectively) and the subdata of the AMLSG 07-04 trial (median of all patients in the trial 49 years) and a related statistical analysis: Jaramillo *et al.* [20] found in a multivariable analysis a significantly longer **WBC** recovery for older patients (hazard ratio of a 10-year age difference, 0.89; $P = 0.001$) [20] and a significantly shorter **WBC** recovery for patients receiving D123 compared to the reference group D135 (hazard ratio, 1.94; $P < 0.0001$) [20] which coincides well with our findings.

Regarding the **PK** model, no published compartment models for high-dose **Ara-C** are available. Comparing our model with published low-dose **Ara-C** models, we show that the published models do not reach the measured maximum **Ara-C** concentrations from high-dose schedules (see figure 3.7) so that we rely on our derived model. As we logarithmize the collected **Ara-C** concentrations, lower values become more important during parameter estimation such that our fitted **PK** model slightly underpredicts the

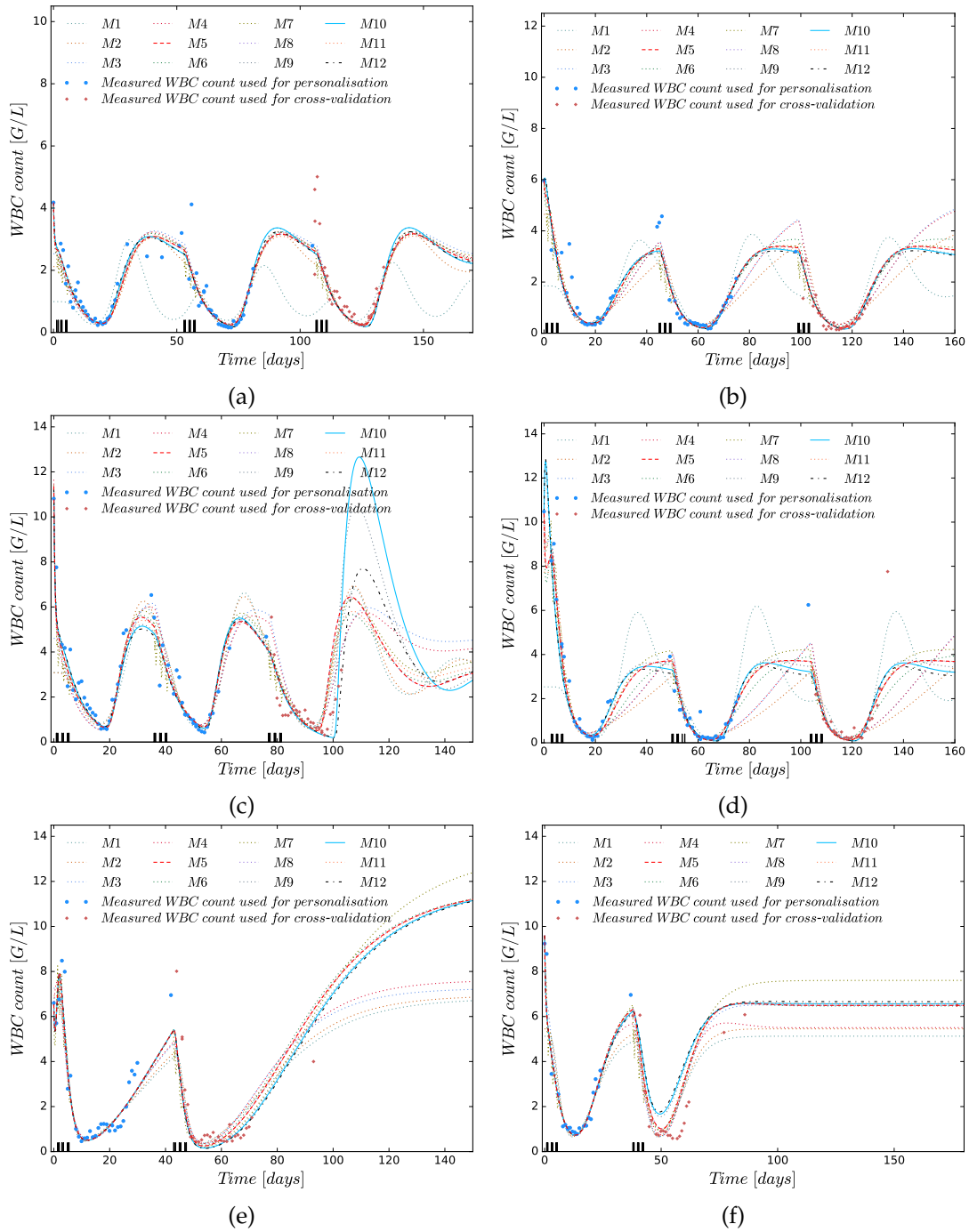
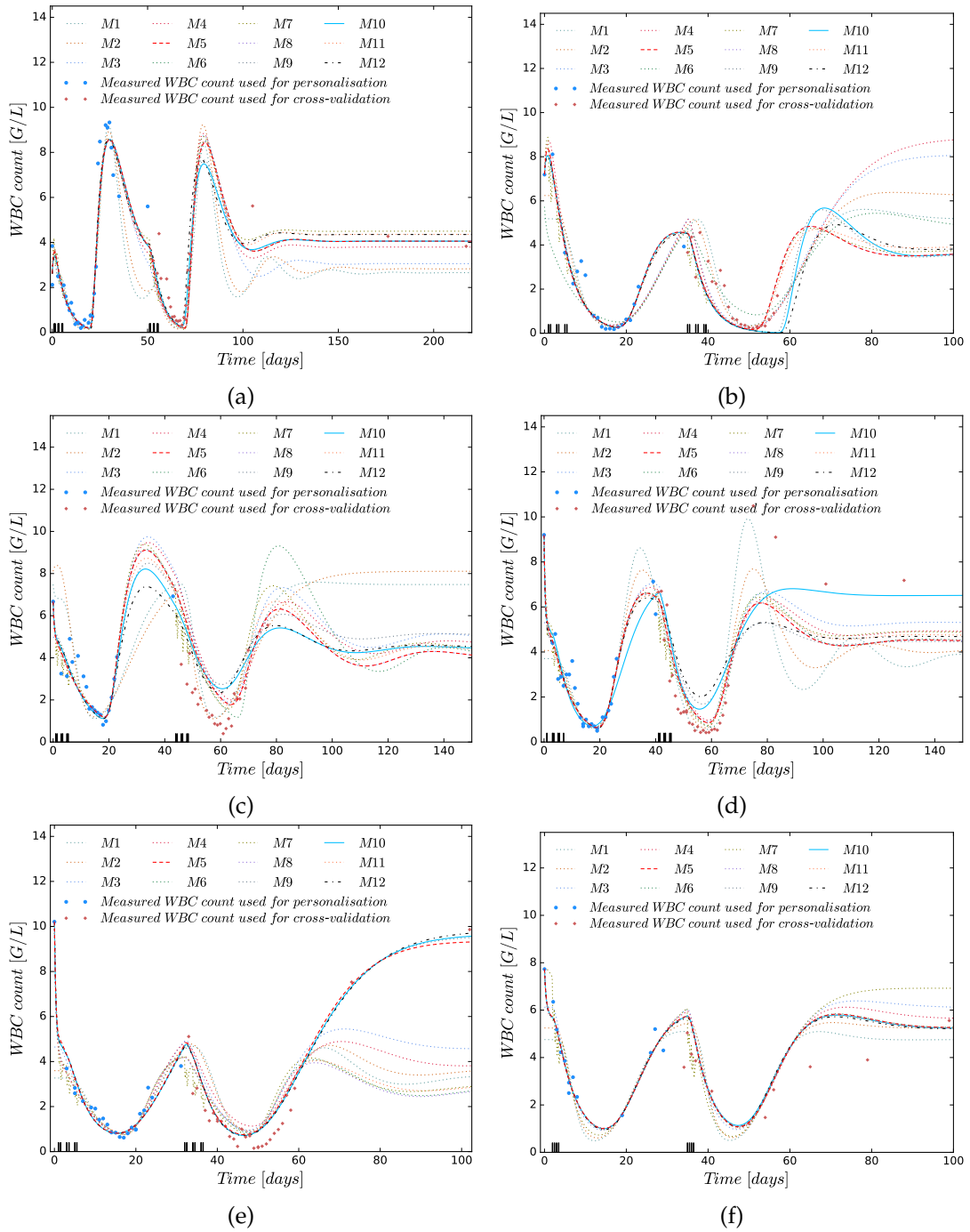


Figure 7.14: Cross-validation of predicted white blood cell (WBC) counts from personalized models M1-M12 and measured WBC counts for six patients treated with D135.



highest Ara-C concentrations (see figure 3.7). Nevertheless, our model achieves higher values compared to the models from [76] and [94] providing a more reasonable PK behavior of Ara-C. We estimate a smaller central volume leading to a reduced clearance

Figure 7.16: Cross-validation of predicted white blood cell (WBC) counts from personalized models (PMs) M1-M12 and measured WBC counts for five patients (a)-(e) treated with d135 and one patient (f) treated with D12. The PMs provide good predictions for patient (a) and (f) but show mismatches in recovery times and nadir values for patients (b)-(e).

Table 7.11: Objectives (final objective function values from FOCEi method (OBJ), population predicted t_{rec}^{123} and t_{rec}^{135} values), parameter and coefficient of variation (CV) estimates with relative standard errors (RSE) from nonlinear mixed-effects modeling of models M3 and M10 with initial condition approach I1.

	M3	M10 (with I1)
Objectives		
t_{rec}^{123}	22.09	20.35
t_{rec}^{135}	22.98	23.96
Final OBJ	-353.94	-348.49
Fixed Effects (RSE%)		
B	5.3248 (6)	5.1939 (9)
k_{tr}	0.18694(5)	0.19383(4)
γ	0.48587(9)	0.46885(5)
slope	8.5915 (9)	5.5101 (7)
inter-individual Variability CV%(RSE%)		
B	35.2(11)	34.9(10)
k_{tr}	21.0(17)	21.7(16)
γ	32.4(24)	36.6(23)
slope	38.9(16)	34.3(14)
Residual Error (CV%)		
Proportional	0.109(9)	0.109(10)

activity derived from an almost equivalently estimated elimination rate constant value (6.2). The distribution rate constants differ by a factor of 2 to 2.5 and the peripheral volume by a factor of almost 10. Future PK studies for high-dose Ara-C can be used for model verification or updating our model parameters. In a simulation study we analyze the influence of constructed PK variability on the WBC recovery time for models M5 and M10. We show that model M10 is more sensitive to varied PK dynamics and reflects clinical findings more accurately, i.e. that the standard and dense treatment plans result in significantly different WBC recovery times. M5 is not able to match the clinical results. A critical part of the study is the constructed IIV. In Krogh *et al.*[76] IIV was analyzed for low-dose Ara-C schedules. We use the published values as exemplary IIV values within our simulation study. Obviously, the results should be treated with care as IIV is related to the underlying study, treatment, model and population and thus cannot be applied to other studies in general. However, the IIV impacts only a small part of our

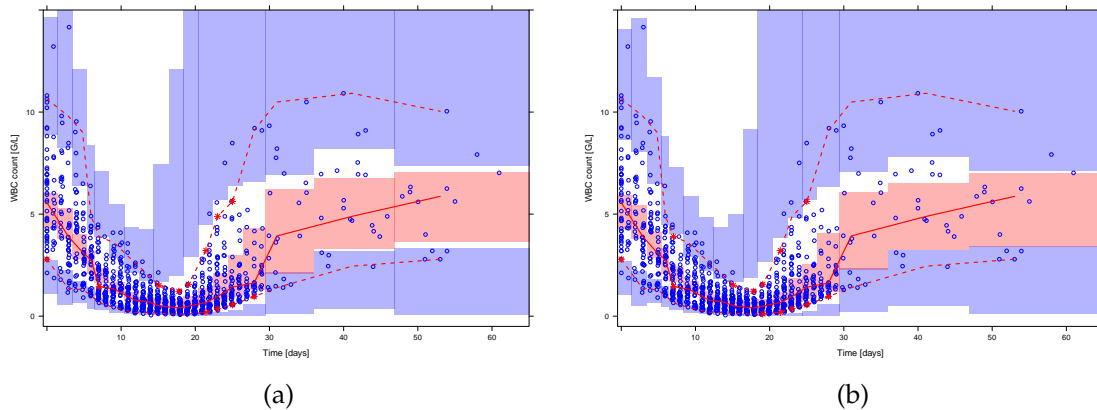


Figure 7.17: Generated **visual predictive checks**, derived by 1000 simulations, for leukocytes [G/L] versus time [$days$] starting with the first measurement before dosing for model M3 (a) and M10 (with I1) (b). Blue circles are the measured white blood cell (WBC) counts of 23 acute myeloid leukemia patients described in section 7.1.1. One measurement was taken at timepoint 88.98 [days] with the value 7.18 [G/L] which is not shown in the visual predictive checks (VPCs). Red lines show the median (solid) and 5th and 95th percentiles (dashed) of measurements. The shaded areas represent the 95% confidence intervals around the 5th (blue), 50th (red) and 95th (blue) simulated percentiles of the model predictions. Regarding the VPCs, model M3 and M10 have an almost equivalent prediction accuracy. The 50% percentiles of measurements and model predictions perfectly overlap, thus supporting our individually based results from 7.6. The same applies to the start of the 5% and 95% percentiles until the nadir. After the nadir the 5% and 95% percentiles of the model predictions recover slightly faster/slower compared to the measurements. At day 30 the percentiles of measurements and model predictions coincide again.

sensitivity analysis and we do not expect qualitative changes for updated IIV values.

7.1.2 PK/PD model with cytarabine and lenograstim (Data Ulm)

Secondary pharmacodynamic effect of Ara-C

To validate the proposed secondary PD effect of Ara-C on γ [181] for a larger variety of Ara-C treatment schedules, we first concentrate on a subset of data without exogenous G-CSF administration. We perform parameter estimations for three models (standard Ara-C myelosuppression model and two extensions with a secondary PD effect). The objective function values (least squares fitting term) and the estimated parameter values are shown in table 7.12.

Table 7.12: Results of parameter estimations for three different pharmacokinetic(s)/pharmacodynamic(s) models without (Q14AraC) and with (Q14 γ AraC) a secondary pharmacodynamic(s) effect of Ara-C on the proliferation term γ and with an additional parameter to estimate this effect (Q14 $\hat{\gamma}$ AraC). Shown are final objective function values, root mean squared error (RMSE), parameter estimates of fixed effects, interindividual variability as a coefficient of variation (CV%) with relative standard errors (RSEs) in brackets and proportional additive residual errors.

Model	Q14AraC	Q14 γ AraC	Q14 $\hat{\gamma}$ AraC
Objective value	102.313	74.417	27.751
RMSE	1.079467	-	1.074160
Fixed Effects (RSE%)			
B	5.42(4)	5.05(6)	5.31(5)
k_{tr}	0.177(3)	0.1768(3)	0.175(3)
slope	9.19(6)	6.16(7)	7.68(8)
γ	0.659(4)	0.689(4)	0.676(4)
slopeG	0 FIXED	1 FIXED	0.470(12)
Interindividual Variability CV% (RSE%)			
B	32.7(15)	30.2(14)	31.8(16)
k_{tr}	13.3(14)	13.7(20)	13.8(17)
slope	35.6(17)	31.8(11)	33.3(16)
γ	17.7(20)	15(29)	16.1(25)
Residual Error (RSE%)			
Proportional additive error	0.171(11)	0.166(11)	0.162(11)

The estimated fixed-effects parameter values for B , k_{tr} and γ and the IIV for all parameters are in the same range for all models. The estimated fixed-effects parameter value for slope significantly decrease when a second PD term is introduced. With slopeG as a degree of freedom, its value is 0.47. IIV on slopeG is also tested with an objective function reduction from 27.751 to 13.795, but with a high IIV and standard error, we neglected IIV on slopeG. The model fit improves (the objective function decreased) from the standard model to those with a secondary PD effect.

Modeling exogenous G-CSF

The effect of lenograstim on WBC counts is visually assessed by the cyclewise WBC dynamics after CT. Figure 7.18 shows that patients who received lenograstim had a rapid increase of WBC counts during WBC recovery. Figure 7.19 shows the VPCs derived from the final model after parameter estimation highlighting that patients who received lenograstim had a rapid increase of WBC counts during WBC recovery (compare the measurements in (a) and (b) after nadir). Further, the figure underlines the good match between model and clinical data capturing the rapid increase of WBC counts during WBC recovery for patients receiving lenograstim. The model slightly overpredicts the 50th and 97.5th percentiles for patients who did not receive lenograstim. The evaluation of model fitting via the medians of the individual mean absolute error (MAE) and RMSE values in table 7.13 reveal that the extended myelosuppression model with a subcutaneous absorption model and two transit compartments describe the clinical data best. The first column in table 7.14 shows the estimated model parameters. During model development we investigate the individual parameter estimates grouped by the lenograstim administration. The boxplots of the four parameters in figure 7.20 highlight that k_{tr} and γ are significantly increased in the model without consideration of an absorption model for patients who received lenograstim administrations. After extending the model with the subcutaneous absorption model and two transit compartments the parameter values of γ are almost equal between the two groups whereas the k_{tr} values only approached to a small degree. Values of slope were higher and the WBC steady state values were slightly lower in the group of lenograstim administrations. The VPCs in figure 7.19 underline the good match between model and clinical data. Also the rapid increase of WBC counts during WBC recovery is captured with a slight overprediction of the 50% and 97.5% percentiles before reaching steady state.

Table 7.13: **Medians of individual mean absolute error (MAE) and root mean squared error (RMSE) with standard deviations in parenthesis for different myelosuppression models with and without consideration of lenograstim.** The consideration of lenograstim (Leno) describe via a single pathway absorption model iteratively increases the model fits by the inclusion of additional transit compartments (Transit) until the best fit is achieved with two transit compartments.

Model	noLeno	noTransit	oneTransit	twoTransit	threeTransit
#Transit	–	0	1	2	3
Leno	no	yes	yes	yes	yes
MAE	0.842(3.22)	0.812(3.34)	0.802(3.31)	0.797(3.31)	0.806(3.30)
RMSE	0.918(0.84)	0.901(0.86)	0.896(0.86)	0.893(0.86)	0.898(0.86)

Modeling leukemic blasts

The PK/PD model is fitted to the clinical data with and without consideration of the leukemic cell lineage. The estimated parameter values are presented in the second and

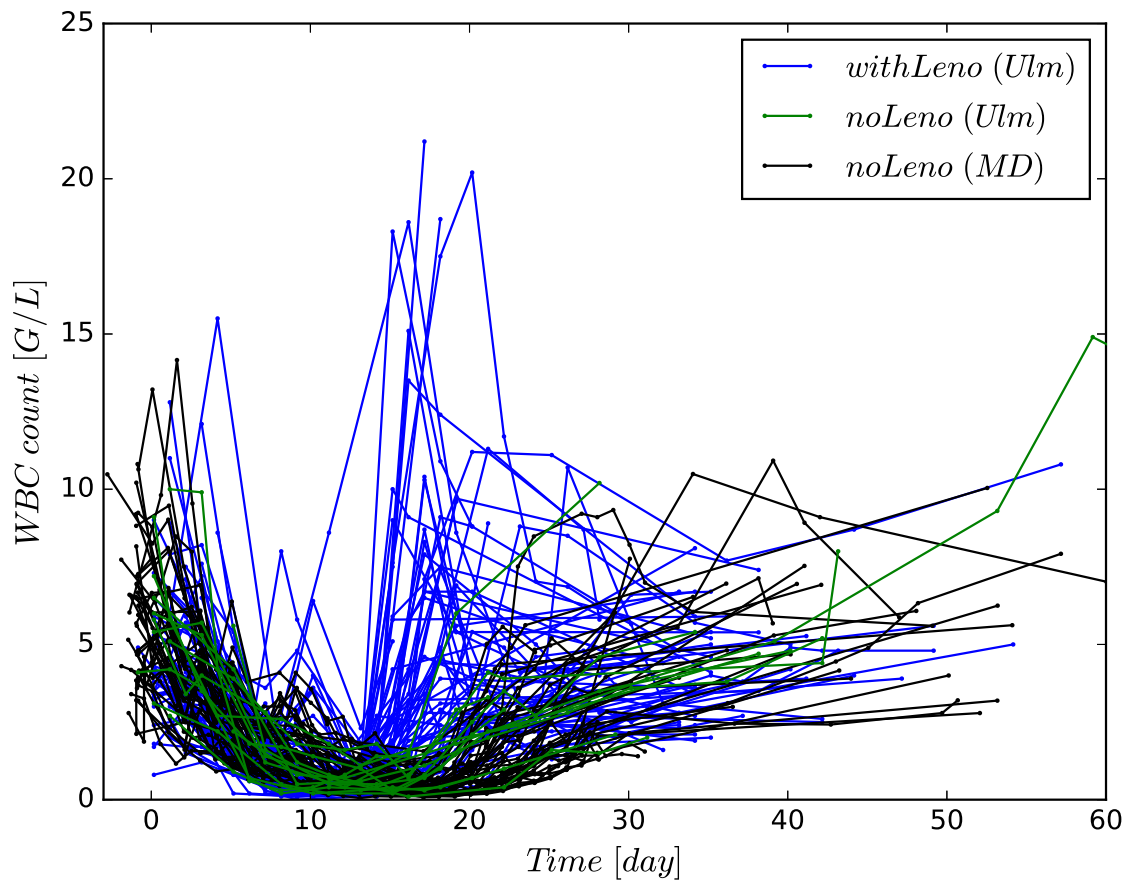


Figure 7.18: Cyclewise measured white blood cell (WBC) counts from two datasets with different colors for the datasets and lenograstim administration (blue: with Leno (Ulm), green: no Leno (Ulm), black: no Leno (MD)). At time point 0 first Ara-C infusion starts. Cycles in which lenograstim is administered show a rapid WBC increase during WBC recovery.

third column of table 7.14. The leukemic blast lineage only has a minor effect on the estimated parameter values with an increase of the slope parameter and the variance of the exponential error model.

The model performance of describing the clinically observed circulating WBC counts and relative blast counts in the BM is shown as VPCs in figure 7.21. The median of observed WBC counts coincides with the median of calculated WBC counts and falls within or close to its 95% prediction interval (blue area). The 2.5th percentile of the model shows an underestimation in the first CC and the 97.5th model percentile shows overestimations in all CCs. Considering the VPC of the blasts, the 95% prediction intervals of the 50th and 97.5th percentiles indicate that the model assumes a faster increase of blasts during the three CCs compared to the almost constant (2.5th and 50th

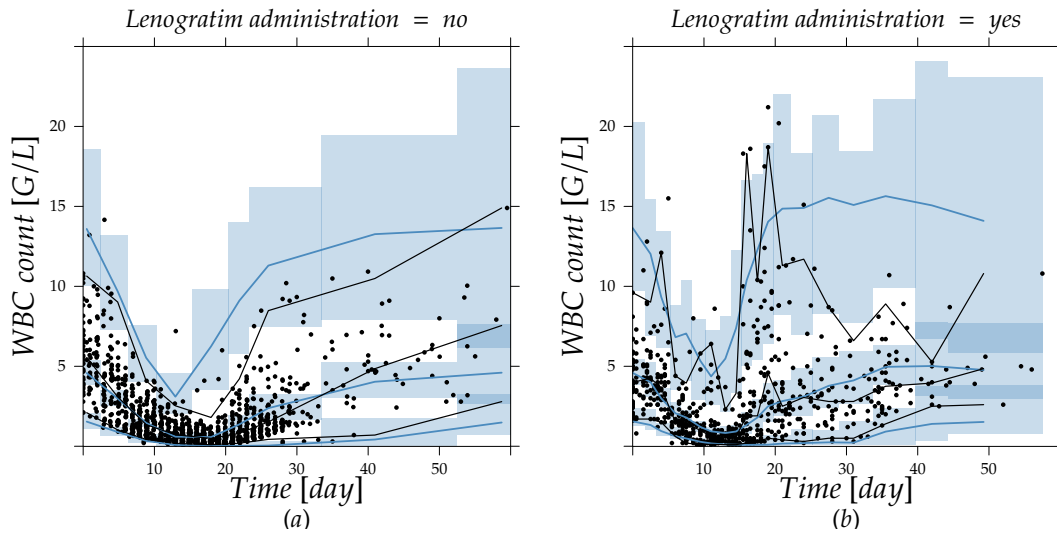


Figure 7.19: Generated visual predictive checks stratified by lenograstim administration and derived by 1000 simulations with the final parameter estimates from the myelosuppression model with two transit compartments (fourth column of table 7.13), for circulating white blood cells (WBCs) (G/L) versus time (day). Black dots are the measured WBC counts. Black and blue lines show the median and 2.5th and 97.5th percentiles of measurements and model predictions, respectively. The shaded areas represent the 95% confidence intervals around the 2.5th, 50th and 97.5th percentiles of the model predictions.

percentiles) and decreasing (97.5th percentile) dynamics observed within the patients.

Figure 7.22 shows the influence of G-CSF administrations (yes or no) and of varied G-CSF steady states on the WBC recovery. Ara-C without lenograstim administration results in a longer recovery time and a slightly lower WBC count before the start of the second and third CC. As a further consequence, the number of leukemic blasts in the BM was higher and increase more over time, than to the leukemic blast count when the actual treatment schedule of lenograstim is conducted. A different G-CSF steady state affects the recovery time, where lower steady-state values provoke an overproduction of WBC counts, leading to a higher value than the WBC steady state.

We investigate the out-of-sample prediction performance of the final model with its extension to lenograstim and leukemic blasts and analyze the potential of different treatment schedules derived by mathematical optimization.

Parameter estimation results for the data subset (compared to figure 5.1) are shown in table 7.14. Compared to the in-sample parameter estimates, the values of B , k_{tr} , slope and γ are almost equal to the values derived from the whole dataset and the values of k_a and x_{I1}^0 are slightly decreased, respectively increased. The prediction performance is visualized as a goodness-of-fit plot in figure 7.23. Both in-sample and out-of-sample,

Table 7.14: **Results of parameter estimations for different pharmacokinetic(s)/pharmacodynamic(s) models and datasets.** Shown are residuals (objective value), parameter estimates of fixed effects, interindividual variability as a coefficient of variation (CV%) and exponential (exp.) residual errors as variance with relative standard errors (RSEs) in brackets for in-sample and out-of-sample (without measurements of the last consolidation cycle).

Dataset	in-sample		out-of-sample	
	cyclewise	patientwise	patientwise	patientwise
Blasts	no	no	yes	yes
# patients	67	44	44	24
Fixed Effects (RSE%)				
B	4.67(6)	4.67(7)	4.85(8)	4.50(11)
k_{tr}	0.196(10)	0.236(3)	0.218(6)	0.224(7)
slope	10.1(3)	7.94(11)	8.53(8)	8.95(7)
γ	0.701(4)	0.651(4)	0.680(6)	0.679(7)
k_a	3.16(3)	3.15(26)	3.20(21)	2.828(31)
x_{t1}^0	–	–	0.029(28)	0.0434(19)
Interindividual Variability CV% (RSE%)				
B	39.6(8)	40.9(12)	49.3(14)	47.2(16)
k_{tr}	19.3(10)	14.3(22)	25.2(21)	25.4(20)
slope	42.1(13)	55.8(17)	11.8(24)	17.9(21)
γ	19.8(10)	19.7(16)	21.2(15)	23.3(26)
k_a	103.3(16)	95.1(28)	58.6(34)	119.6(22)
x_{blasts}^0	–	–	67.9(23)	24.0(101)
Residual Error (RSE%)				
Exp. error	0.152(9)	0.284(8)	0.315(8)	0.250(10)

the values are centered around the line of identity. No systematic error is apparent, only a slight overprediction of small [WBC](#) counts.

Global sensitivity analysis

A global sensitivity analysis is conducted to identify the impact of each parameter, respectively constant, on the variability of two model outputs [203]. The model outputs of interest are the leukemic cells in the [BM](#) (x_{t1}) at the end of a [CC](#) and the nadir of circulating [WBCs](#) similar to the two objective function terms in the optimization problem (7.24). The sensitivity analysis is performed in R (version 3.6.1) using the packages *mrg-solve* (version 0.10.0) for solving the [ODE](#) system (6.10) and *sensitivity* (version 1.17.0, *sobolmartinez* function) for the global sensitivity analysis. The function *sobolmartinez* implements the Monte Carlo estimation of the Sobol' indices for both first order and total indices for each parameter using correlation coefficient-based formulas. These are called the Martinez estimators. The Sobol method is based on the decomposition of the

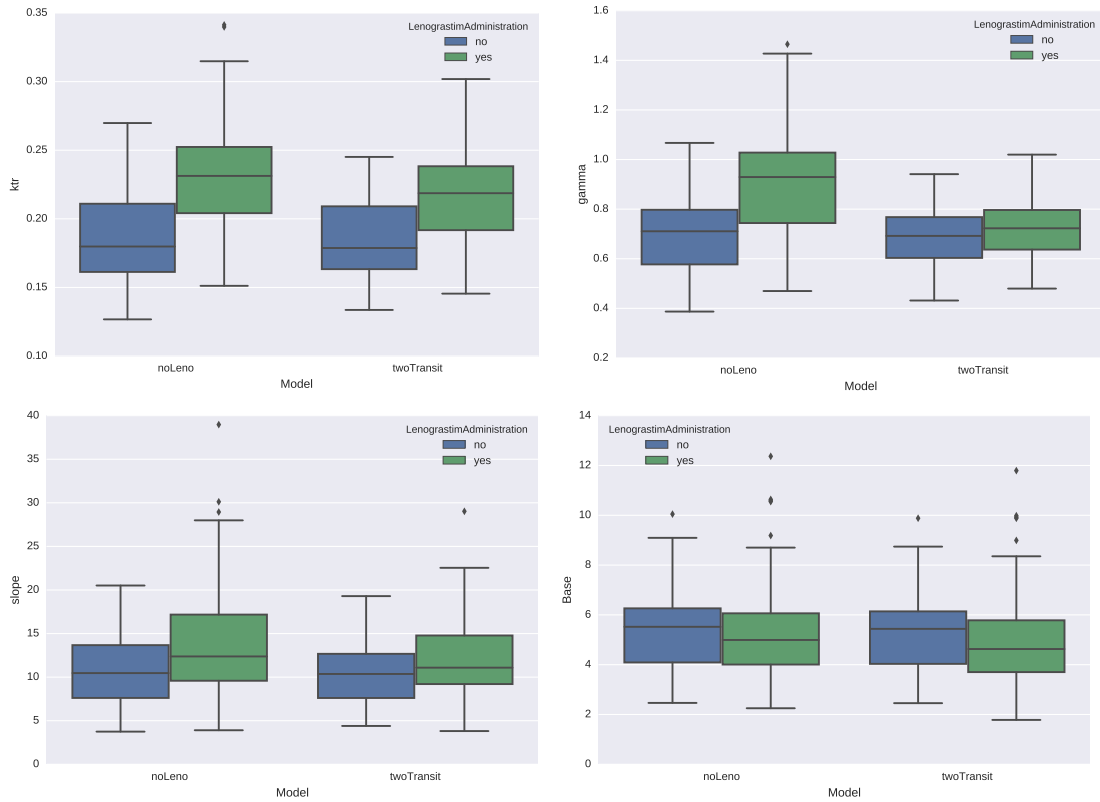


Figure 7.20: **Boxplots of final parameter values of k_{tr} , γ , slope and B grouped by lenograstim administrations for models *noLeno* and *twoTransit* (see table 7.13).**

model output variance into fractional contributions from effects of single parameters considering no interaction between parameters (first order/main effect) or an interaction between two (second-order), more or all (total effect) parameters. The theoretical background can be found in the tutorial [203] and references therein. The experimental setup is chosen as follows. One **CC** is defined with **Ara-C** schedule D123 for an exemplary patient with a **BSA** of 1.8 m^2 and six $263 \mu\text{g}$ daily subcutaneous lenograstim administrations starting at day 9. Two datasets with 3800 (2 times 19 [number of variables] times 100) sets of parameters are generated with uniformly chosen parameter samples from a 0.5-fold decrease to a 1.5 fold increase in the nominal parameter values. The contribution of each parameter to the variability in the two model outputs is presented in 7.24. The leukemic cells in the **BM** as well as the nadir of circulating **WBCs** are influenced by the elimination constant k_{10} , the volume of the central compartment V and the pharmacodynamic effect slope. The leukemic cells in the **BM** are further influenced by the fraction constant a_1 determining the fraction of daughter cells staying at the current differentiation stage and the stem cell proliferation p_1 . The nadir of circulating **WBCs** is additionally affected by B (Base), k_{tr} , γ and k_{ma} . The global sensitivity analysis reveals that the **WBC** nadir is mostly influenced by the hematopoietic parameters which we

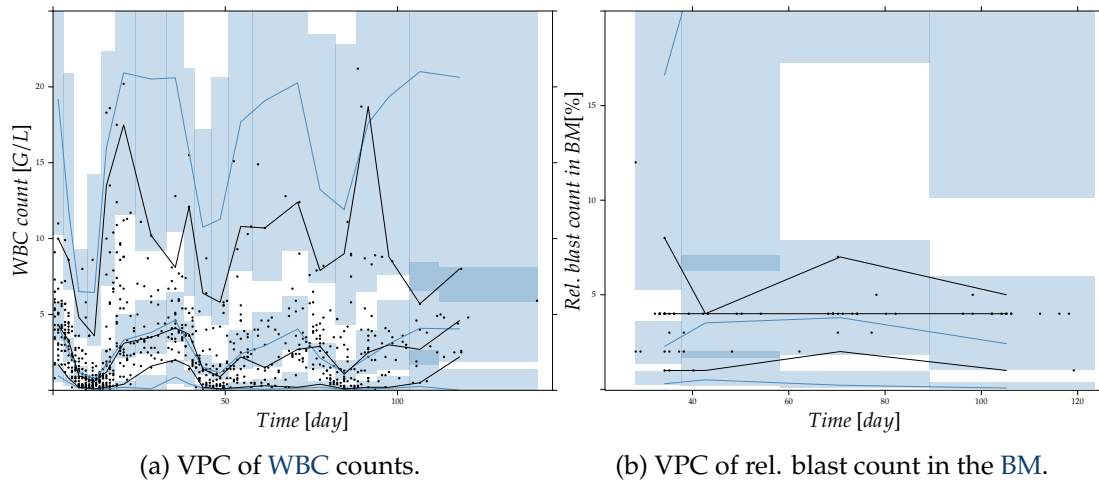


Figure 7.21: **Generated visual predictive checks, derived by 1000 simulations, for circulating white blood cells (WBCs) [G/L] and relative (rel.) blast counts in the bone marrow (BM) [%] versus time [day]. Black dots are the measured WBC counts, respectively rel. blast counts in the BM. Black and blue lines show the median and 2.5th and 97.5th percentiles of measurements and model predictions, respectively. The shaded areas represent the 95% confidence intervals around the 2.5th, 50th and 97.5th percentiles of the model predictions.**

individually determined during parameter estimation and therefore we achieve good accuracies in predicting the nadir of the last CCs (c.f. 7.23). We determine the dynamics of the leukemic cells in the BM and circulating blood via the estimation of the initial value of the leukemic cell count in the BM. The sensitivity analysis shows that a_1 and p_1 has a larger impact compared to the initial value but the current data availability does not allow to estimate those parameters such that we fix them to published values.

Discussion

The development, fitting, validation, and analysis of the PK/PD model is performed in an iterative way starting with the modification of the myelosuppression model provided by Quartino and colleagues [53] to Ara-C and to the subcutaneous administration of lenograstim and completed with the incorporation of the leukemic blast lineage. Several parameter estimations are performed to fit and validate the models. An analysis of the estimated model parameters in table 7.14 shows that the fixed effects and IIVs are in the same ranges in all the numerical studies, indicating that the general model behavior is maintained despite model extensions. Equivalent to the results in [53], our model predictions reveal an overprediction of the 50th and 97.5th percentiles for patients who do not receive lenograstim (c.f. figure 7.19). During model development, we examine two other models [48, 112]. Both models also show discrepancies in predicting the 97.5th percentile for the model from [112] and the 50th percentile for the model from

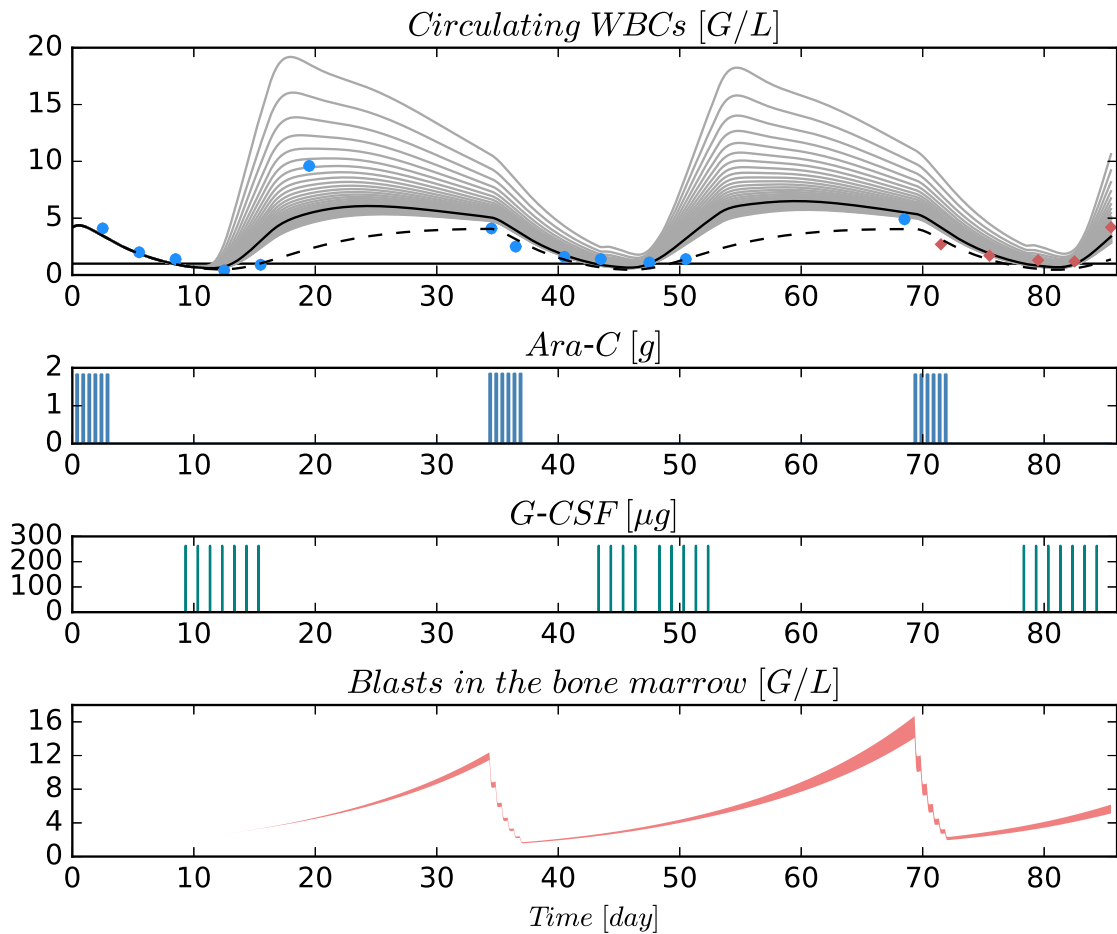


Figure 7.22: **Simulated white blood cell (WBC) dynamics (solid black line) of the final model fitted to observed WBC counts of the first two consolidation cycles (blue dots), and the Ara-C and lenograstim treatment schedules of one exemplary patient are shown.** The last cycle is used for model prediction and out-of-sample comparison. Simulated WBC dynamics for no lenograstim (dotted black line) and for different granulocyte-colony stimulating factor (G-CSF) steady state values (from 20% to 140% of used value) are shown (solid gray lines). No lenograstim administration prolongs WBC recovery time and lower/higher G-CSF steady state values shortens/prolongs WBC recovery. Moreover, no lenograstim administration results in a slightly larger leukemic blast count (the red area indicates the difference when compared to the actual treatment schedule shown in the third row).

[48]. This line of research is not further investigated. The values of B are within the normal human WBC range of 4–10 G/L and coincide with the values estimated in [181] and with the neutrophil base value from Quartino *et al.* [53], assuming that the relative amount of neutrophils ranges between 60–70%. Compared to published WBC baseline

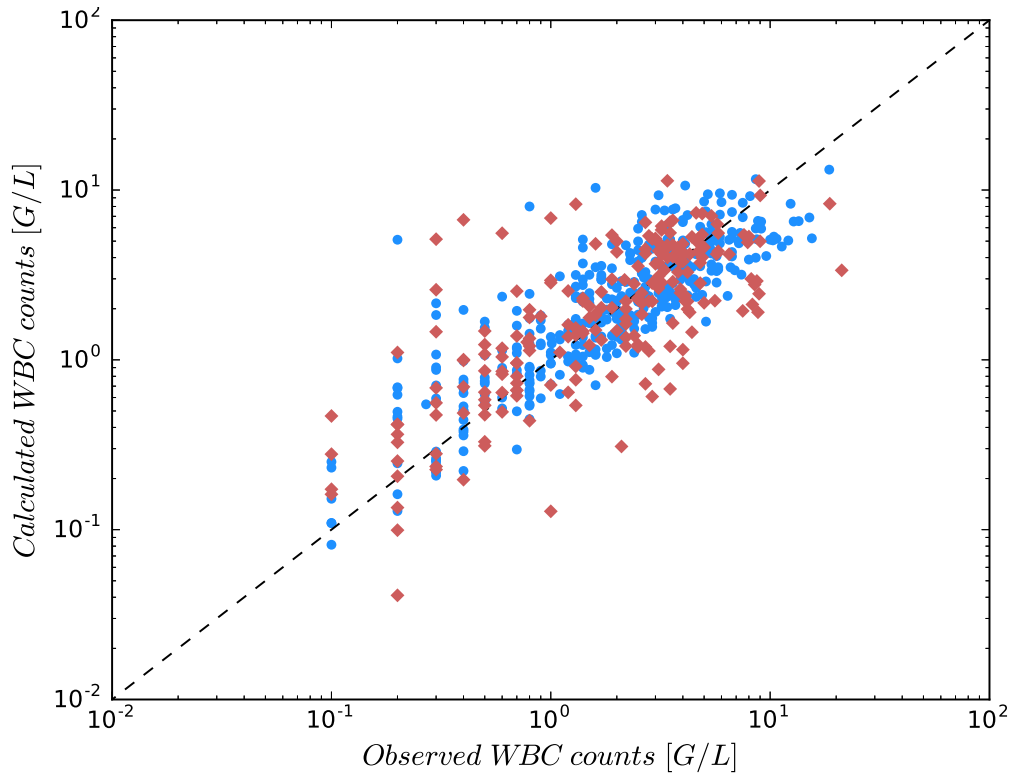


Figure 7.23: **Goodness-of-fit plot visualizing observed versus individually calculated white blood cell (WBC) counts for 24 patients.** Models are cross validated using out-of-sample (from the last consolidation cycle (CC)) WBC measurements (blue circles). Red cubes show in-sample WBC measurements from the remaining first CCs.

values for the model by Friberg *et al.* ranging between 7 and 7.8 G/L [52], our values are 2 – 3 G/L lower. The MMTs of 102-122 hours are reasonable and fit into the range of previously published values [201]. The value of γ is larger compared to the model of Quartino *et al.* [53], which might be due to the dense treatment schedules. The residual error doubles from the cyclewise to patientwise management of the data, assuming that interoccasional variabilities, which are not the focus of this work and as a consequence not modeled, might be one of the reasons for an increased model-reality mismatch. This mismatch is further increased with the consideration of relative blast counts in the third column of table 7.14 introducing an additional source of error.

We visualize the parameter estimates separately for cycles in which lenograstim is administered or not to analyze the influence of lenograstim on the parameter estimates. Figure 7.20 shows that the steady state value of WBC is lower for patients receiving lenograstim, indicating that the demand of exogenous G-CSF might be related to the patients' WBC steady states. In comparison to the estimated values of γ which are almost equal between the two groups after modeling the lenograstim administration, the transport rate k_{tr} is still increased for the patients who received lenograstim although

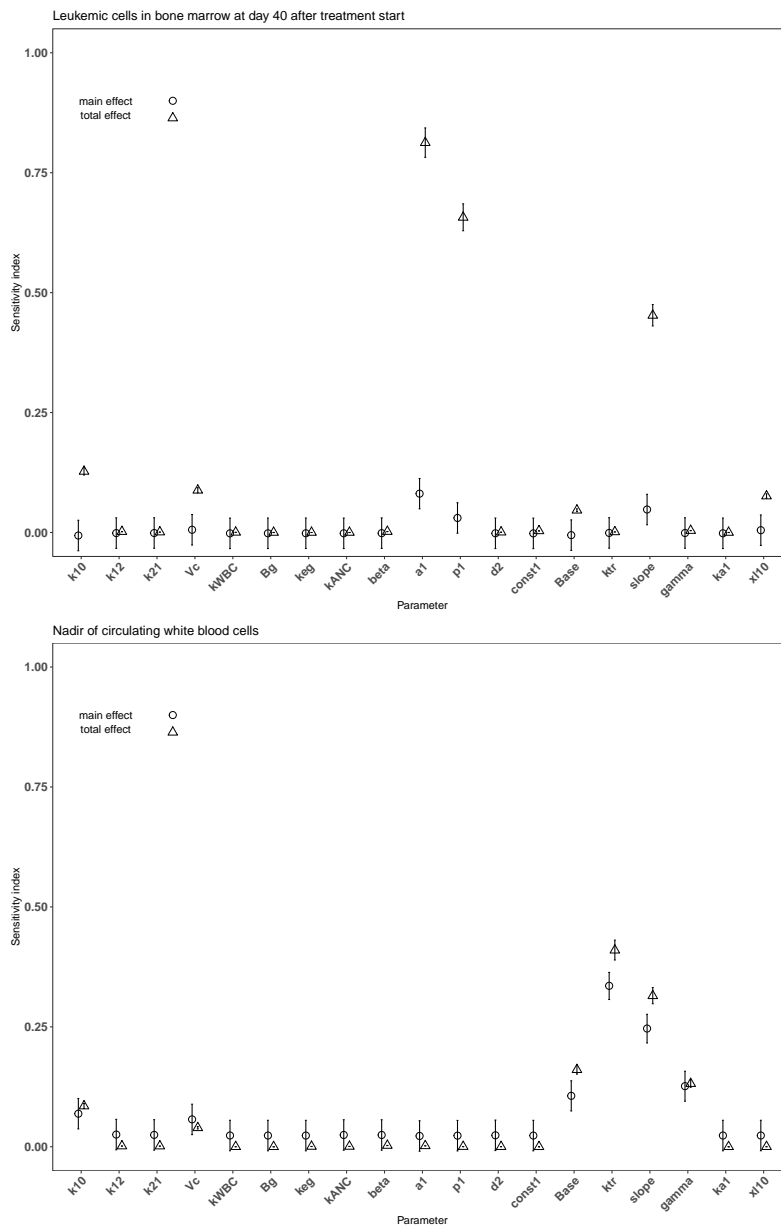


Figure 7.24: **Global sensitivity analysis for the constants and parameters listed in table 6.4.** Model outputs of interest were the amount of leukemic cells in the bone marrow at day 40 after treatment start and the nadir of circulating white blood cells.

exogenous **G-CSF** already influenced proliferation and maturation via the feedback term (x_g/B_g). We suspect that the higher values agglomerate biological phenomena that are not correctly described or fully covered by the current model. Nevertheless, the model exhibits the same behavior as in clinical trials with pegfilgrastim [20], i.e., a prolonged

WBC recovery time of several days without G-CSF, compared to figure 7.22.

The model has several constant parameters that are fixed to published values. As only WBC and relative BM blast counts are observed, this is necessary to avoid overfitting and obtain a good predictive accuracy. However, the interpretation of parameter values can now be misleading, as incorrect constants and modeling are usually compensated by parameter values. A better data situation with additional G-CSF and Ara-C concentration measurements would allow to identify further parameters. In addition to the global sensitivity analysis, in which we investigate the key parameters having the largest impact on two clinically relevant model outputs, a structural sensitivity analysis [204–206] would help to systematically investigate identifiability of parameters assuming additional biomarker measurements.

The VPC in figure 7.21 reveals that the model of leukemic blasts is able to describe trends respectively overpredicts the measurements with its exponential behavior, leading to a purely leukemic steady state after 4.6 month being in the reported interval for remission before relapses occurred [186]. This conservative model behavior is chosen to study the impact of different treatment schedules on the increase of leukemic cells and might not exactly represent the patients actual leukemic blast dynamics. Therefore, the presented treatment optimization results have to be considered with care and further investigations and efforts have to be undertaken to develop more advanced and reliable models for bringing optimized treatment schedules to clinics. As the number of leukemic blasts in our model will eventually converge to a purely leukemic steady state, we can only compare short-term impacts of treatment schedules on leukemic blasts and hence relapse probabilities. In the future, additional modeling assumptions could be considered, e.g., stable steady states of coexistence between leukemic and healthy cells achieved via the inclusion of the leukemic blasts' steady state value in the zero-order production term of endogenous G-CSF or a threshold value of leukemic blasts below which the immune system could avoid a relapse for good. Modeling minimal residual disease (MRD), proposed by multiple recent studies as a strong prognostic marker for relapse in AML [207–210] might also be a promising alternative to leukemic blasts. In the current study, no MRD information is available such that we concentrate on a model describing the relative blast count measurements. In the current study we focus on dynamic deterministic models but the low number of BM measurements might force future model development to stochastic or survival analysis approaches as it was previously done by [211] in their proposed stochastic MRD model.

In the previous section, secondary PD effect of Ara-C are analyzed and an empirical model extension through a second PD effect on the feedback term γ is proposed. During model development, we tested a parameterized PD effect. However, the evaluation criteria (such as the RMSE or a cross-validation in which the model is fitted to standard schedules and validated on dense schedules) shows only a minor benefit resulting from the consideration of Ara-C's possible secondary effects. For this reason and without any concentration-time profiles of Ara-C we decide to neglect a secondary PD effect of Ara-C. An additional simplification is made. We use the plasma concentration of Ara-C for the PD effect although the side of action is within the BM and it is shown that Ara-C

plasma concentration is not the best predictor for BM and intracellular Ara-C activity [212, 213]. To obtain a physiologically-based PK and PD model of Ara-C including secondary effects, further studies have to be performed to analyze the mechanisms and metabolism of high-dosage Ara-C [42] and its impact on dense treatment schedules. A first physiologically-based PK model is already presented in 1973 by Dedrick et al. and serves as a starting point [214].

7.1.3 PK/PD model with 6MP and MTX (Data Erlangen)

Table 7.15 shows RMSE values, MAE values, and final objective function values for four different parameter estimations. Here, we compare the usage of different PK/PD models and estimation based on either WBC counts or ANCs. First, the explicit consideration of MTX only has a minimal/non-significant effect on the model accuracy, so we fix it to the ratio 2.5:1 between 6MP and MTX. Second, our results show that the use of the PK model of [111] increases the sensitivity of the PD effect and the model accuracy compared to the 6MP PK model of [112]. Third, ANC measurements result in higher accuracy than do WBC measurements.

Table 7.15: **Results of parameter estimations for different models.** Shown are model characteristics (data based on absolute neutrophil count (ANC) or white blood cell (WBC) count and pharmacokinetic(s) (PK) models for 6-mercaptopurine (6MP) and methotrexate (MTX)), median and standard deviation in parentheses of individual root mean squared error (RMSE), mean absolute error (MAE), and final objective function values (FinalOBJ). Medians and final objective function values are rounded off to four and the standard deviations in parentheses to three significant figures.

	Model 1	Model 2	Model 3	Model 3
Data	ANC	ANC	ANC	WBC
PK 6MP	Jayachandra	Jayachandra	Hawwa	Hawwa
PK MTX	Panetta	-	-	-
MAE	1.068 (1.65)	1.045 (1.92)	0.9571 (4.31)	1.315 (2.92)
RMSE	1.033 (0.492)	1.022 (0.539)	0.9783 (0.678)	1.147 (0.579)
FinalOBJ	7003	7094	6550	9746*

*Objective value is not comparable to first three values due to different dataset

Parameter estimation

Figure 7.26 shows the comparisons of observed clinical and simulated ANCs derived from the final PK/PD model (6.14) after parameter estimation for three exemplary chosen patients presented in rows 1,3 and 5. For each patient, the individual 6MP [mg] dosing protocol is presented in rows 2, 4 and 6, indicating dose changes for efficacy adjustments. The model simulations represent the clinical ANCs quite well in the average

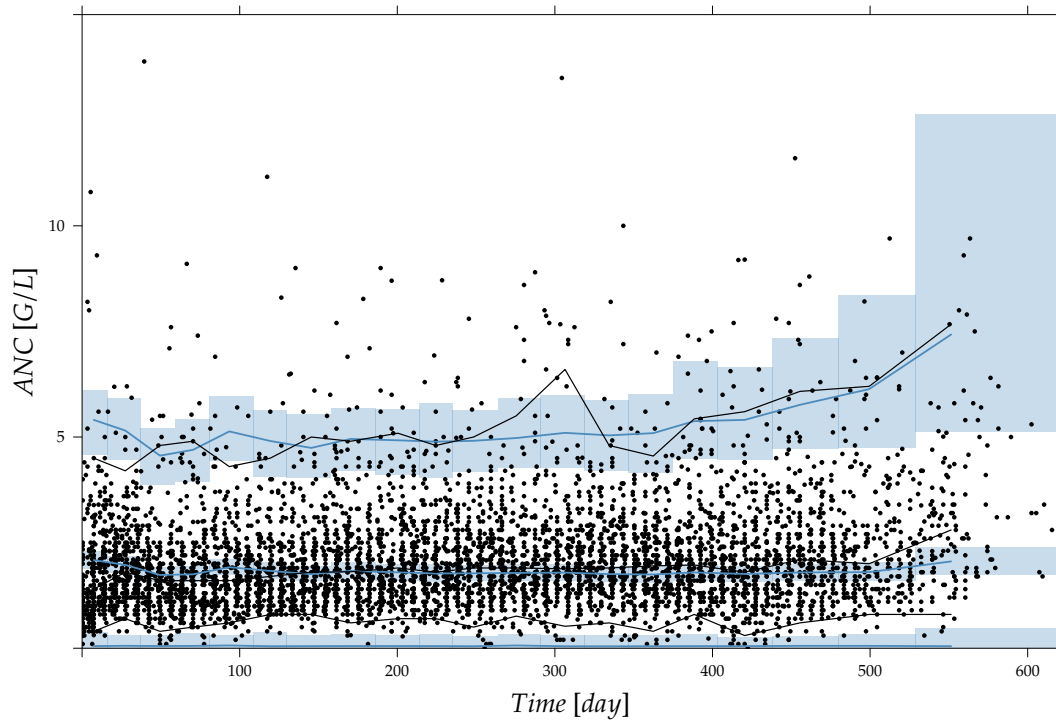


Figure 7.25: **Generated visual predictive check, derived by 1000 simulations with the final parameter estimates from the first column of table 7.17, for circulating absolute neutrophil counts (ANCs) (G/L) versus time (days).** Black dots are the measured ANCs. Black and blue lines show the median and 2.5th and 97.5th percentiles of measurements and model predictions, respectively. The shaded areas represent the 95% confidence intervals around the 2.5th, 50th and 97.5th percentiles of the model predictions. Two ANC outliers (19.9 and 17.8) at time points 285.42 and 340.42 days are not shown.

and capture trends toward larger or smaller ANC values. However, they do not oscillate as strongly as the measured values. Persistent oscillations of neutrophils often occur in chemotherapy-treated hematopoietic diseases inducing cyclic myelosuppression (see [215] and references therein). Several other reasons are responsible for the observed ANC oscillations such as aberrant hematopoiesis, chemotherapeutic dose adaptations, infections or measurement errors. This exemplary behavior is representative of the entire data set of 116 patients. The VPC plot in figure 7.25 shows the good agreement of model response and measurements for the median (solid line) and 97.5th percentile (dashed line) with a slight underprediction of the model for low ANC values. The 95% confidence interval of the model simulation median is very thin, indicative of high prediction accuracy. The fixed effect estimate for the ANC steady state is slightly higher than the target range limit of 2 G/L. The estimated transition rate of 0.148 results in a

Table 7.16: **Results of parameter estimations of the final model using all (in-sample) or 70% (out-of-sample) of the absolute neutrophil count (ANC) values.** Shown are parameter estimates of fixed effects, interindividual variability as coefficient of variation ($\omega/100$), proportional additive error as variance, and median errors of the parameter estimations rounded off to three significant figures. For the mean absolute and root mean squared errors all ANC measurements are used. Relative standard errors are shown in parentheses rounded off to one significant figure.

Data	In-sample	Out-of-sample
Fixed effect parameters		
B	2.34 (1)	2.06 (0.1)
k_{tr}	0.148 (0.4)	0.146 (0.2)
slope	0.242 (0.2)	0.103 (0.2)
γ	0.769 (0.1)	0.866 (0.2)
Interindividual variability as coefficients of variation		
B	23.1 (20)	27.5 (10)
k_{tr}	16.5 (30)	7.19 (3)
slope	44.9 (5)	67.8 (1)
γ	10.7 (0.5)	16.5 (0.4)
Proportional additive error	0.226 (2)	0.226 (FIXED)
Parameter estimation errors		
Mean absolute error	0.957 (4)	1.47 (500)
Root mean squared error	0.978 (0.7)	1.21 (7)

MMT ($MMT = n_{tr}/k_{tr}$) of 487 hours (20.3 days) [45]. The IIV and residual error are within reasonable ranges.

Out-of-sample validation

The reliability of the final population PK/PD model is tested via out-of-sample cross-validation. For each patient, the first 70% of ANC measurements are used for parameter estimation and the final 30% are used to evaluate the model predictions. Model accuracy and predictability were evaluated using the RMSE and the MAE.

The goodness-of-fit plot in figure 7.27 shows the results of out-of-sample cross-validation. It reflects reasonable model accuracy for fitted and predicted ANC measurements with spreading around the line of identity because the model is not able (and not intended) to hit the lower and upper peaks of the measurements. The values of estimated model parameters both for the in-sample and out-of-sample calculations are shown in table 7.17. The values of all four parameters coincide well, with a slightly reduced slope and increased k_{tr} value for the estimates based on 70% of the ANC. The IIV for the slope is significantly larger. To evaluate the model accuracy, we calculate the median and standard deviation of the individual MAE and RMSE values, showing the expected decrease in accuracy for out-of-sample predictions.

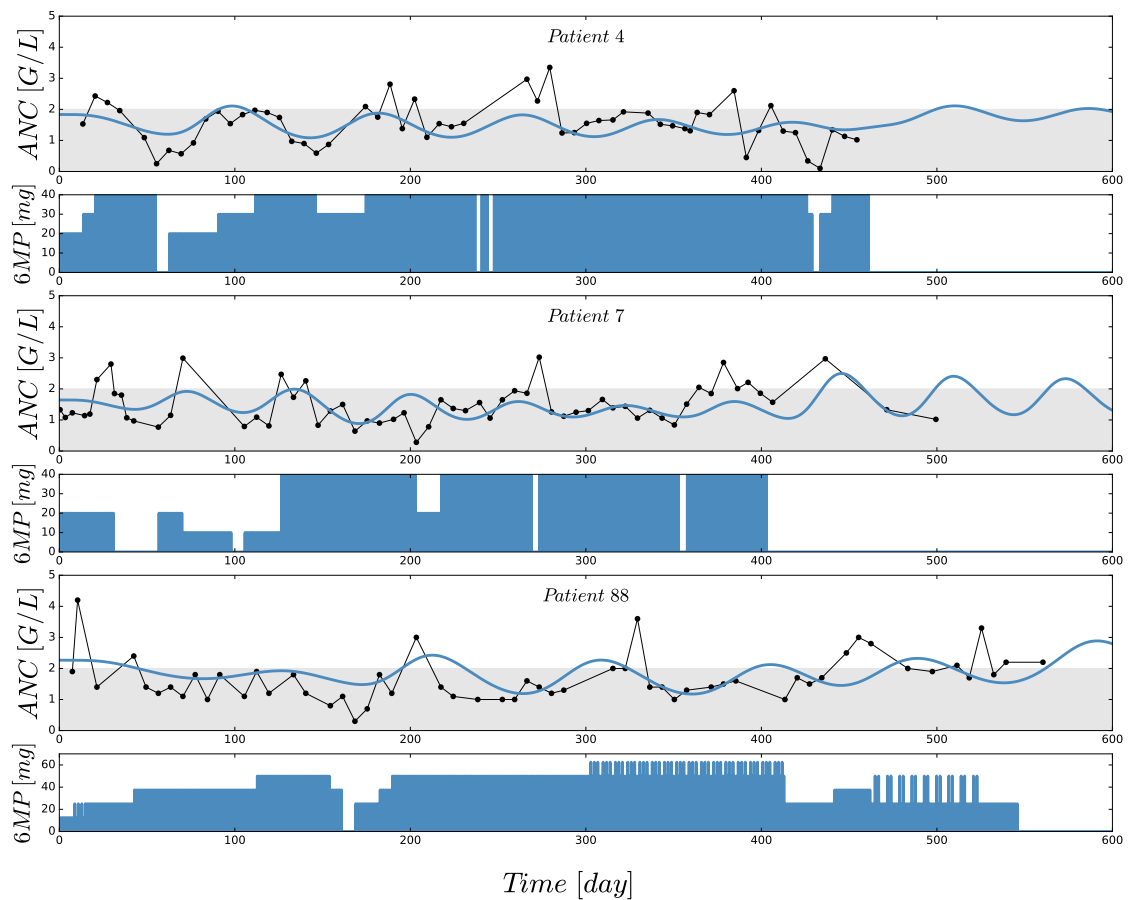


Figure 7.26: Exemplary comparisons of observed (black) absolute neutrophil counts (ANCs) and simulation results (blue), based on the newly proposed mathematical model and a nonlinear mixed-effects parameter estimation. In addition to a visual match between values and quite well captured trends (compared with the indicators in table 7.15) one can clearly see oscillations of ANCs in both the observed and simulated data.

Discussion

Mathematical model

We develop and fit a population PK/PD model to assess the ANC dynamics during 6MP/MTX treatment, get a better understanding of dose adjustments, and identify solutions to the challenges that arise throughout MT. During the model development process we also fit the model to WBC measurements. The resulting MAE and RMSE values are worse compared to the values resulting from ANC measurements. This is probably due to the fact that WBCs comprise different cell lineages, with additional

Table 7.17: **Results of parameter estimations of the final model using all (in-sample) or 70% (out-of-sample) of the absolute neutrophil count values.** Shown are parameter estimates of fixed effects, interindividual variability, and median errors of the parameter estimations. Relative standard errors are shown in parentheses.

Data	In-sample	Out-of-sample
Fixed effect parameters		
Base	2.16 (0.1)	2.19 (2.0)
k_{tr}	0.145 (0.2)	0.175 (0.4)
slope	0.0397 (0.7)	0.0282 (0.7)
γ	0.809 (0.5)	0.836 (0.1)
Interindividual variability as coefficients of variation		
Base	30.3 (6.70)	27.3 (7.4)
k_{tr}	12.5 (20.5)	9.9 (8.7)
slope	11.9 (11.4)	65.1 (6.5)
γ	12.8 (12.9)	10.7 (1.0)
Proportional additive error	0.245 (5.70)	0.245 (FIXED)
Parameter estimation errors		
Mean absolute error	1.029 (5.21)	1.430 (401.33)
Root mean squared error	1.014 (0.75)	1.196 (6.51)

physiological effects that are not accounted for in the mathematical model. In future studies, the current model might be extended to further cell lineages. The models brought forth by [82, 216] might serve as a basis and drive the modeling process from a semi-mechanistic approach toward a more mechanistic one.

In addition to using a population estimation approach and applying it to ANC instead of WBC, two modifications brought forth by [177] have shown to yield better results. First, the 6MP PK model of [112] is replaced by that of [111]. The first order kinetics in the PK model of [111] compared to the Michaelis–Menten terms in the PK model of [112] results in more significant concentration changes with altered drug amounts consequently in a more sensitive PD effect. Second, the MTX PK model is completely omitted as the constant ratio of administered 6MP and MTX prevents a differentiation of separate PD effects. Further studies with measurements of drug concentrations, metabolites and clinical effects as cell counts would push forward the development of a mathematical model additionally including the PK of MTX to provide two distinct PD effects and to account for varying ratios of 6MP to MTX. For the currently available data, our new model, which indirectly agglomerates the effects of 6MP and MTX, appears to be a good choice (compare for table 7.15).

Model parameter estimates

Looking at the resulting model parameter estimates listed in table 7.17, the question arises as to how these values relate to known biological properties of hematopoiesis

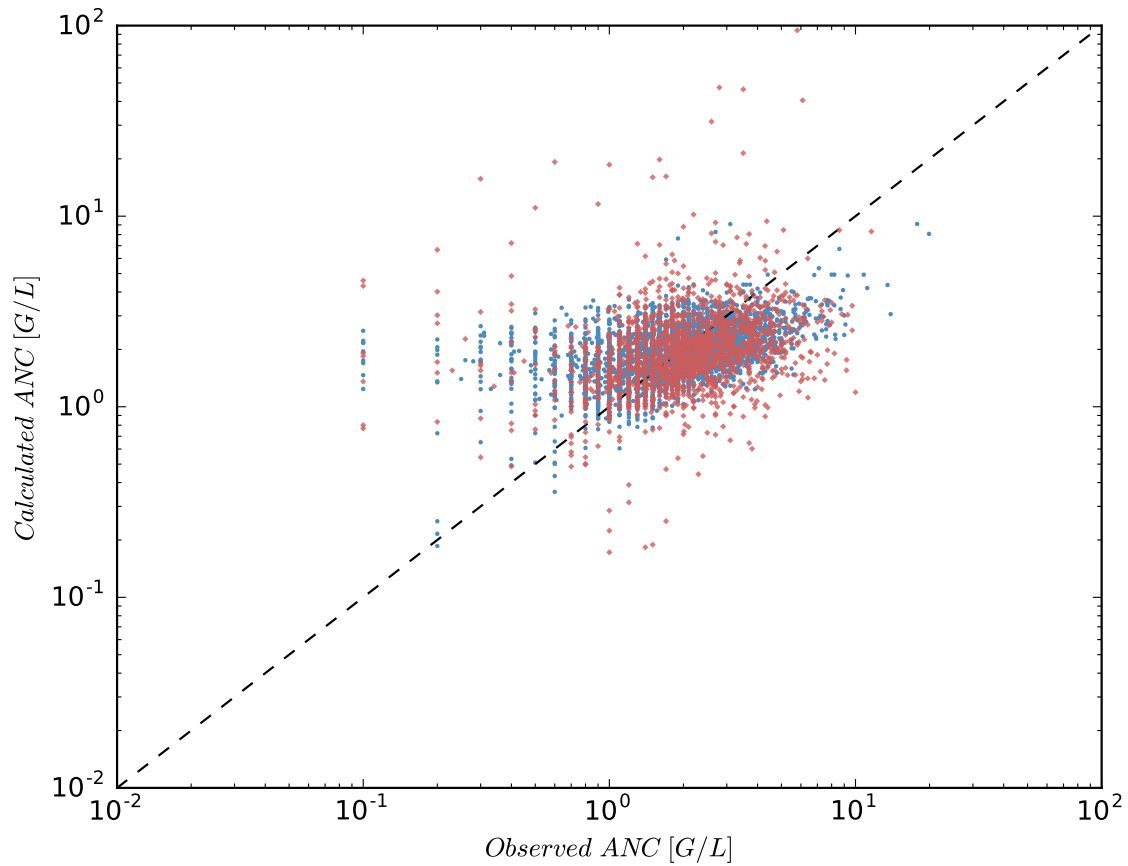


Figure 7.27: **Goodness-of-fit plot depicting observed versus individually calculated absolute neutrophil counts (ANCs) for 116 patients.** Blue markers show in-sample ANCs (first 70% of observed ANCs) used for parameter estimation. Models were cross-validated using 30% out-of-sample observed ANCs (red).

and myelosuppression and to other values from the literature. The estimated ANC steady state value B is below the normal ANC range for children, but still higher than the desired ANC range of 0.5–2 G/L. Without treatment, the model-based ANCs would increase to normal patient-specific steady states. Thus, low ANC values are induced via MT or some of the aforementioned external events.

The estimated fixed-effects parameter value of the transition rate $k_{tr} = 0.148$ is comparable with the published mean value ($\bar{k}_{tr} = 0.1431$) obtained from eight pediatric ALL patients from Riley Hospital for Children in Indianapolis [112]. For better interpretability, the transition rate parameter k_{tr} can be transformed to the MMT (n_{tr}/k_{tr}) of the neutrophils. The estimated MMT in our study, as well as the MMT from Jayachandran *et al.*, are extremely high and do not coincide with biological findings of 3.9 days obtained by [14]. This mismatch is a large disadvantage of the model as it fails to comply with biological properties, leading to falsely characterized physiological

mechanisms and thus reduced model reliability. Jayachandran *et al.* did not discuss this issue, but a similar observation was made by Craig and colleagues (2016) who determined an estimated proliferation time of 26 days [51]. In their work, the authors further presented model modifications to obtain a more realistic maturation time of 3.9 days. For this value we have performed two parameter estimations with either B as a parameter or fixed to 5 resulting in promising dynamics but worse RMSE and MAE values. In future studies, the falsely determined MMT and possible model limitations for continuous low-dose treatments should be further investigated.

The feedback parameter (γ) is significantly higher compared with published values [52], indicating a stronger feedback mechanism during the daily chemotherapy over a long period. This is the first time estimated slope values of the linear PD function from the PK model of [111] are presented; thus there are no available comparisons.

7.2 Optimal treatment schedules for acute leukemia

In the following we present optimal treatment schedules for the CT for AML and for the MT for ALL. In the next three sections, the three validated PK/PD models from the previous sections are used to calculate the optimal schedules.

7.2.1 Influence of treatment starts on leukopenia

After verifying the predictability performance of the PMs in section 7.1.1, we perform a simulation study in which we demonstrate a further possible application of the PMs in planning the start of consecutive CCs. We analyze the impact of the treatment timing on the individual nadir values. For each of the 14 patients, for whom at least two consecutive CCs were available, the nadir of the last CC are compared to 20 simulated nadirs. These nadirs result from simulations using the patient's PMs (second row of table 7.6) in which the timing of the last CC is varied daily with the maximal starting variation of 10 days earlier or later. Similar to previous simulation studies dealing with varying and shortening cycle duration and finding the optimal number and timing of G-CSF administrations to reduce myelosuppression [64, 65, 68], we analyze the impact of different treatment starts of the last CCs with respect to obtained nadir values.

Results

A comparison to the clinically observed nadir values indicate a large potential for clinical improvement, i.e., a higher nadir value due to a shifted treatment start (see figure 7.28a). 7.28b exemplarily shows the WBC dynamics for different treatment timings. Earlier (later) starts resulted in sequentially higher (lower) nadir values.

7.2.2 Consolidation therapy schedules for AML derived by optimizations

We use the individual models of 14 patients from section 7.1.2 for whom relative blast counts are available in the last CC for a mathematical optimization of the treatment

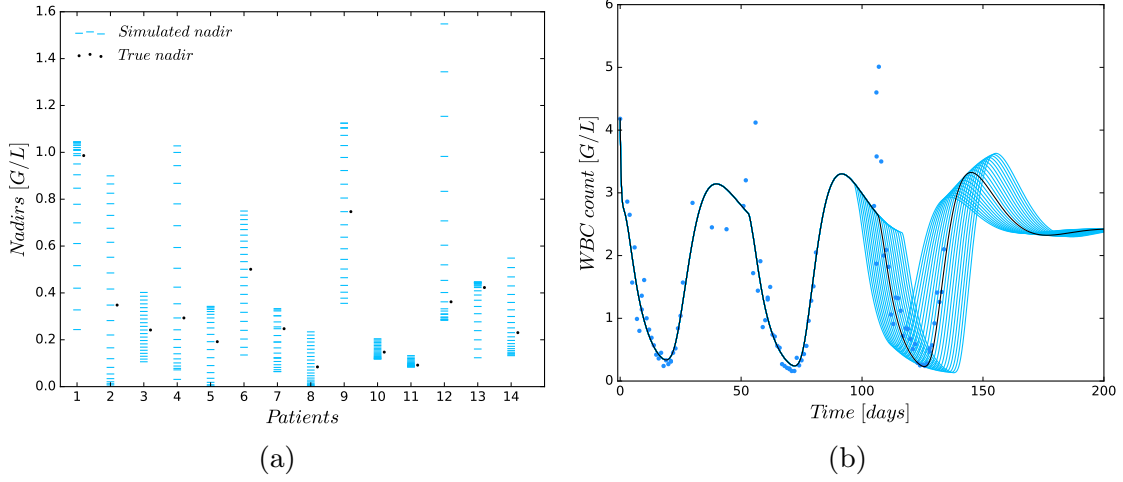


Figure 7.28: **Analyzing the influence of treatment timing on nadir values.** (a) Simulation study in which 20 simulated nadirs were compared with the true nadir of the last consolidation cycle (CC) for the 14 patients who have more than one CC. The simulated nadirs were computed by using the patient's personalized model (second row of table 7.6) and varying the start of the last CC daily with the maximal starting variation of 10 days earlier or later. (b) Exemplary variation of the CC start for one patient. An earlier (later) start results in a larger (lower) nadir.

schedules of the last CC. We compare clinically important indicators such as nadir values and relative blast counts in the BM to the measured values. Optimizing the treatment schedule for patient $i \in \{1, \dots, 14\}$ is formulated as a minimization problem

$$\min_{x^i(t), u_c^i(t), u_l^i(t)} \text{Obj}^i \quad (7.24a)$$

$$\text{s.t. } \dot{x}^i(t) = f(x(t), \theta^i, u_c^i(t), u_l^i(t)) \quad (7.24b)$$

$$x(t_0^i) = x_0^i, \quad (7.24c)$$

$$u_c^i(t) \in [0, 2000] \quad (7.24d)$$

$$u_l^i(t) \in [0, 236] \quad (7.24e)$$

on the individual time horizon t_0^i to t_f^i with $f(\cdot)$ the mathematical model (6.10) from the previous section, $\theta^i = (B^i, k_{tr}^i, \text{slope}^i, \gamma^i, p_1^i)$ the empirical Bayes estimate resulting from the model fit to the measurements from all but the last CC, x_0^i the initial values of the ODE system at time point t_0^i , $u_c^i(t)$ and $u_l^i(t)$ the control functions of Ara-C and lenograstim determining the administration schedule after optimization and

$$\text{Obj}^i = \alpha_1 x_{11}^i(t_f^i) + \alpha_2 \int_{t_0^i}^{t_f^i} \frac{1}{x_{ma}^i(t)} dt + \alpha_3 \int_{t_0^i}^{t_f^i} u_c^i(t) dt + \alpha_4 \int_{t_0^i}^{t_f^i} u_l^i(t) dt$$

the objective function consisting of four terms. The first term denotes the number of leukemic cells in the BM at time t_f^i representing the disease status at the end of the consolidation treatment. The second term reflects the health condition of the patient during treatment (heavily penalizing small WBC counts). The last two terms model the costs via the amount of totally administered Ara-C and lenograstim, respectively. Scalar weights $\alpha_1, \dots, \alpha_4$ allow the weighting of these terms according to personalized, clinical, and ethical preferences. Values of the weights were chosen by initial guesses and α_1 was iteratively adapted until the clinically relevant optimization outcomes, meaning $h_{blasts}(t_f^i) < 5\%$ and $\min(x_{ma}(t)) > 1$, are met. The final values for the α_i are presented in table 7.18.

All optimization results are calculated for a time period starting 10 days before the start of the actual Ara-C treatment of the last CC (t_0^i) and ending with the time point of the patient's conducted BM puncture (t_f^i). This time horizon is chosen to compare the optimized values with the measured relative blast counts in the BM. The initial conditions $x(t_0^i)$ are derived from the individual models. We define a hourly time grid for model evaluation and for Ara-C infusions in which Ara-C infusions can be optimized within the first 20 days. The control grid for Ara-C is restricted to the first 20 days so that no Ara-C infusions are placed at the end of the time horizon. Lenograstim administrations are defined as 0.0007 day injections on the hourly grid once a day at 8 a.m. The upper limit of hourly Ara-C infusions is chosen to be 2 g per hour, being the recommended maximum amount of a high-dose treatment schedule for a patient under 60 years with a BSA of 2 m² which should not be exceeded [19]. As mentioned in the introduction, intermediate Ara-C dosage is administered to elderly patients but in our previous study [181] a 64 year old patient was treated with D12 such that we decide to define the upper limit of 2 g per hour as a further degree of freedom during optimization. The upper limit of lenograstim administrations is chosen to be 263 μ g equivalently to the actual daily administered dose amount. The infinite-dimensional optimal control problem (7.24) is solved by a direct collocation approach (simultaneous approach) in which the control functions and the differential states are simultaneously discretized by low order polynomials [166]. The resulting finite-dimensional optimization problem is large scale due to the introduction of additional optimization variables and constraints, but highly structured such that tailored iterative procedures can be applied to numerically calculate local optimal solutions.

Results

Using the final model and the individual parameter estimates for 14 patients from above, we calculate optimized individual treatment schedules. Optimal refers to a numerical local optimization of (7.24) in the last CC. From the solutions, we extract the WBC nadir values and final time relative blast counts in the BM. A comparison to the observed values in figure 7.30 shows that the optimized treatment schedules of Ara-C and lenograstim achieve an increase in nadir values for each patient (in median 4.2-fold higher values), although relative BM blast counts are comparable to the observed ones

Table 7.18: Final values of the multiobjective optimization problem weights.

Patient	α_1	α_2	α_3	α_4
1	.9	3.	0.001	0.007
2	.8	1.	0.0001	0.007
3	1.8	.8	0.0001	0.007
4	1.	2.	0.001	0.007
5	.35	1.	0.0001	0.007
6	1.	1.	0.0001	0.007
7	1.4	1.	0.0001	0.007
8	1.	1.	0.0001	0.007
9	1.	10.	0.0001	0.007
10	1.25	1.	0.001	0.007
11	1.	1.	0.001	0.007
12	.6	1.	0.0001	0.007
13	1.	1.	0.0001	0.007
14	.9	1.	0.001	0.007

and below the clinically important threshold of 5%. Not shown is that the median Ara-C amount was lower by approximately 60%. Three exemplary optimization results with detailed trajectories are shown in figure 7.29, and the results for all 14 patients can be found in the supplement material of [217]. While optimal timing and dosages of Ara-C and lenograstim are personalized and hence different for each considered patient, two qualitative patterns can be observed. In pattern A, an additional Ara-C administration period (and hence an additional CC) is introduced, and the administration order is Ara-C, lenograstim, Ara-C, lenograstim. In pattern B, the nadir is increased compared to the clinical treatment schedule with the administration order lenograstim, Ara-C, lenograstim. The amount of Ara-C is usually considerably reduced. Figure 7.29 shows examples for patterns A (middle, right) and B (left). Over all of the considered case studies, pattern A arises 9 times and pattern B 5 times.

Discussion

The optimized individual treatments derived by solving problem (7.24) rely on the mathematical model (6.10). Application of the results to the real world is thus always under the assumption that the model and a personalized parameter estimation capture reality sufficiently well. This model-reality mismatch is amplified when optimized results are calculated. It is well known that optimization tends to exploit modeling errors as the ones discussed above. Thus, all interpretations should be considered very carefully and should be mainly seen as an incentive for clinical trials to validate the conjectures derived from simulations.

On the positive side, the developed model showed a good prediction accuracy for a variety of different treatment schedules despite the large number of constants and

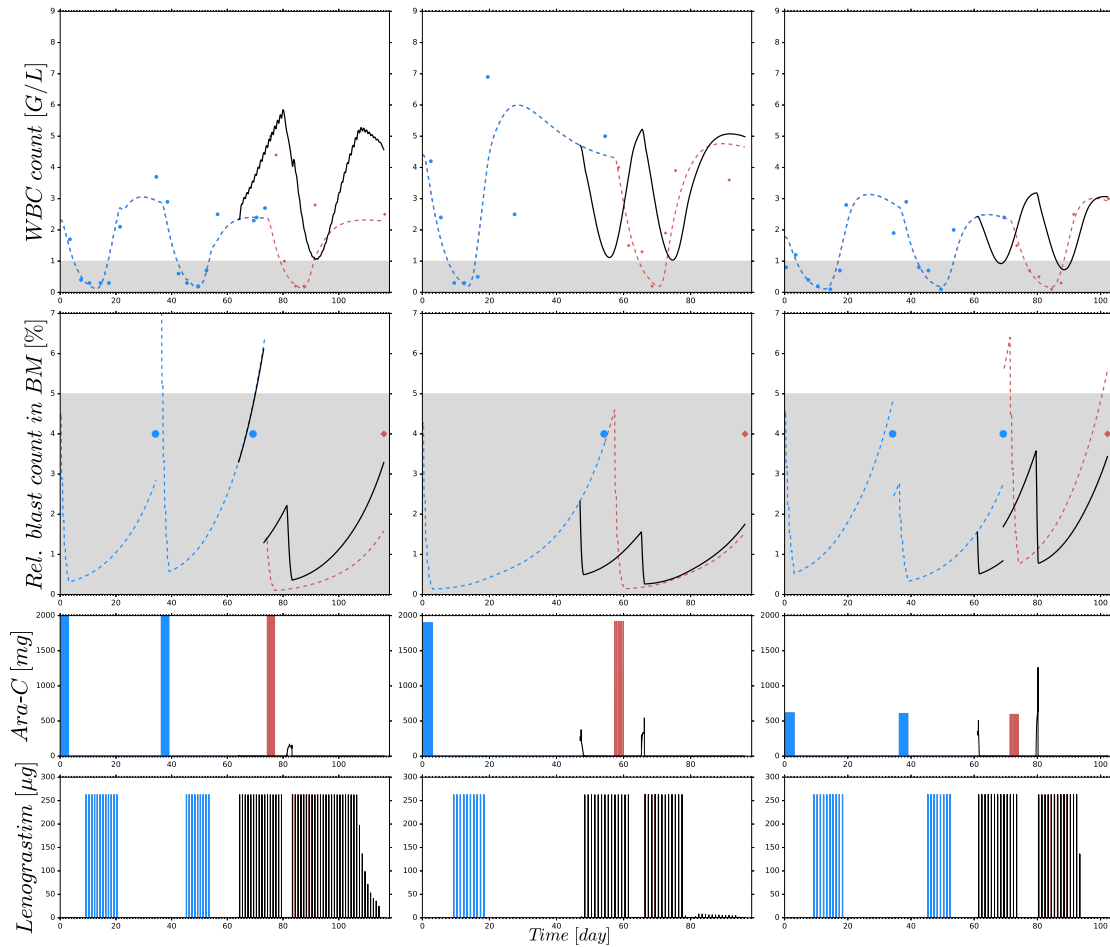


Figure 7.29: Detailed optimization results for Patients 1, 2, and 3, respectively (same order as in figure 7.30). The treatment schedules of Ara-C and lenograstim in the last consolidation cycle (CC) are optimized (black) and compared with the clinically applied treatment schedules (red). Shown are white blood cell (WBC) counts and relative blast counts in the bone marrow (BM) (dotted lines) resulting from individual models. Personalization is performed using in-sample measurements (blue dots) and clinical treatment schedules (blue lines) from all but the last CC. The optimized schedules and the affected dynamics of WBC (solid black lines) qualitatively differ for each patient. In (a), one later low-dose treatment and in (b), two intermediate-dose Ara-C treatments result in higher nadir values compared to the measured values (red dots). In (c), the daily lenograstim administrations before and after the postponed Ara-C treatment do not prevent a fall of WBCs below 1 G/L. Discontinuities in the dynamics of the relative (rel.) blast counts in the BM occur due to possible cyclewise cellularity changes in the measurement function (6.12).

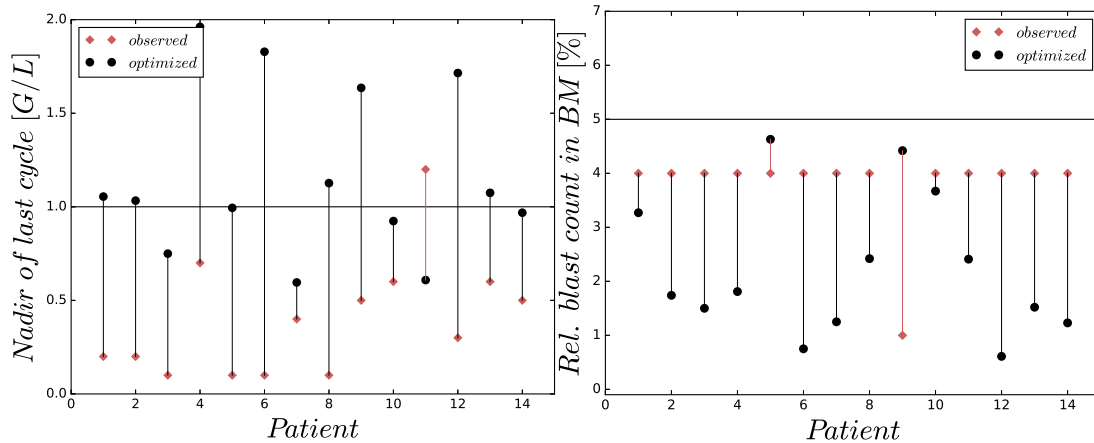


Figure 7.30: Comparison between clinical (observed) and optimized treatments with respect to white blood cell (WBC) count nadirs (left) and relative (rel.) blast counts in the bone marrow (BM) (right) for 14 patients. The nadirs are significantly higher, often even above the leukopenia threshold, while the corresponding relative BM blasts are maintained in the same range as the observed values and below the clinically important threshold of 5%.

missing concentration measurements of *Ara-C* and *G-CSF*. This could not only become a basis for individual decision support, but allows for the first time to quantify the potential of optimized treatment schedules in terms of nadir values, blast counts, and overall chemotherapy usage. We see the value of a more than 4-times increased nadir as a strong motivation to continue research in model-based treatment planning, even if the current personalized mathematical models might not yet be a perfect match to the situation of the patient for whom the data were observed.

Additionally, the approach allows to apply a variety of methods from mathematical optimization to get closer to clinical practice. Our deterministic optimization approach is very sensitive with respect to model parameters and the choice of scalar weights within the objective function. Stochastic optimization techniques result in optimized schedules that are more robust against modeling and parameter uncertainties [218]. The consideration of combinatorial constraints restricting the administration of *Ara-C* and lenograstim to plausible schedules would increase the applicability of the optimized schedules in clinical practice. Multi-objective optimization can provide Pareto fronts with respect to key performance indicators (high WBC, low blasts, low costs, low treatment time, ...) as already indicated in this study. The optimized treatment schedules demonstrated that a 60% (median) reduction in the amount of *Ara-C* and daily administrations of lenograstim could lead to higher nadir values compared to the clinical schedules (see figure 7.30a). The efficacy of the optimized treatment schedules was evaluated by comparing the optimized and measured relative blast counts in the BM at the end of the last CCs (c.f. figure 7.30b). The first clinical impact of the exploration of the optimized treatment schedules was the proposed administration of lenograstim

before the start of *Ara-C* treatments, similar to the FLAG protocol [219], as a prevention to mitigate myelosuppression and increase leukemic blast death. For all 14 patients, lenograstim accomplished an increase in *WBC* count before *Ara-C* treatment, leading to moderate myelosuppression compared to the conducted treatment schedules (see figure 7.30). In the clinical trial from which the dataset was provided [21], lenograstim administration was started nine days after *Ara-C* treatment, reducing the *WBC* recovery time but not necessarily achieving nadir values above 1 *G/L*. As we consider the amount of lenograstim within the objective function, we assess the times that have the smallest or largest impact either on *WBC* recovery or leukemic blast apoptosis. We also performed calculations with a modified objective function without consideration of *WBC* count and lenograstim costs ($\alpha_2 = \alpha_4 = 0$). The optimized treatment schedules still result in the administration of lenograstim every day. This indicates that exogenous *G-CSF* has a beneficial influence on the eradication of leukemic blasts. In our model and setting, lenograstim administration not only reduced *WBC* recovery times but also the leukemic blast counts (c.f. figure 7.22). This coincides with clinical findings [220]. However, the contrary assumption also exists: exogenous *G-CSF* may lead to an increased leukemic blast count. Until now, no evidence is given which claim holds, and in general, no clinical trial with long-term follow-up has shown an increase in mortality or relapse rate if *G-CSF* was administered [221, 222]. As the optimized treatment schedules propose daily administration of lenograstim, the change from subcutaneous injections to continuous intravenous infusions might be worth considering. However, it was shown that the subcutaneous administration of *G-CSF* (filgrastim) results in lower peaks but more prolonged and stable levels of *G-CSF* compared with intravenous administration [23].

Considering short-term effects under the assumption of rapidly evolving leukemic blasts, our results indicate that two *CCs* with reduced doses of *Ara-C* can achieve the same outcome as that achieved by one *CC*, with the benefit of increased *WBC* nadir values. This pattern emerged in 9 out of 12 cases and coincides with published results for docetaxel-induced neutropenia [223]. This result gives a partial answer to the question of Schlenk regarding whether four cycles of *CT* are the best treatment choice [224]. The developed mathematical model and optimization approach might help in the future to determine an optimal treatment schedule for the whole consolidation phase.

7.2.3 Maintenance therapy schedules for ALL derived by simulations

Method

We compare individual simulated minimal, median, and maximal *ANCs* resulting from the application of different dosing protocols (*MT* dosage over time). The choice of the different protocols described in table 7.19 are based on clinical procedures (AIEOP-BFM 2009 with EudraCT number 2007-004270-43, NOPHO-ALL 2008-003235-20, and UKALL 2010-020924-22). In particular, we seek to investigate the relationship between an increased total amount of chemotherapy (higher dosage) and plausibly reduced *ANC* in the *in silico* simulations. Throughout, we use the fitted models (estimated model

parameters) from section 7.1.3 and only vary the chemotherapy dosage. The simulated ANC values are obtained from the individual actual measurement time points.

Table 7.19: **Different dosing protocols for our *in silico* simulation study.** Identical protocols for the administration of 6-mercaptopurine (6MP) for ClinicalData and FittedModels with a median of the patient-individual average daily dosages of 43.15 ± 10.5 mg/m² (minimum 15.8 mg/m², maximum 72.9 mg/m²).

Nr	Description	Short
1	Collected clinical data	(ClinicalData)
2	Fitted model based on patient's actual dosing	(FittedModels)
3	Daily 6MP administration of 25 mg/m ² (50% of AIEOP dosis)	(25 mg/m ²)
4	Daily 6MP administration of 50 mg/m ² (AIEOP dosis)	(50 mg/m ²)
5	Daily 6MP administration of 75 mg/m ² (NOPHO/UK dosis)	(75 mg/m ²)
6	Daily 6MP administration of 100 mg/m ² (200% of AIEOP dosis)	(100 mg/m ²)

Results

Figure 7.31 shows boxplot results for an *in silico* simulation study based on the 6 different treatment protocols (including the real clinical data) from table 7.19. We want to stress three main observations.

First, a comparison of the first two entries of the three boxplots confirms an already known result. The PMs can reproduce the clinical ANC data on average quite well, with the exception of extreme values quantitatively confirming the observation made in figure 7.26. Given the similarity of simulated and observed median values, we continue with an objective comparison only of the simulated results (protocols 2–6).

Second, a comparison of the protocols 3–6 (25, 50, 75, and 100 mg/m² BSA 6MP) shows a significant and linear dosage-effect relationship with respect to the total amount of 6MP administered, which is, of course, proportional to the daily dose. All (minimal, median and maximal) ANC values decrease linearly, when daily dosing is increased linearly.

Third, a comparison of protocol 2 (the simulation of the real treatment) and protocols 3 and 4 (which give lower and upper bounds on the total amount of administered 6MP in protocol 2, respectively) show that the median ANC value of protocol 2 is indeed bounded by the two other values, however, for significantly lower minimal and higher maximal ANC values. Figure 7.32 shows an exemplary comparison of protocols 2–6 for one patient, highlighting lower peak values and smaller drug-induced steady state values when the dosing is linearly increased from 25 mg/m² to 100 mg/m². The actual dosage administered to the patient (blue) ranges between the 25 mg/m² and 50 mg/m² protocols and resulted in similar ANC dynamics. At approximately day 240, the actual dosing was stopped for a short period, inducing stronger ANC oscillations in the subsequent treatment period and revealing a significant impact of the dosing regimen on the ANCs. This observation is even stronger regarding the proliferating cells as well as

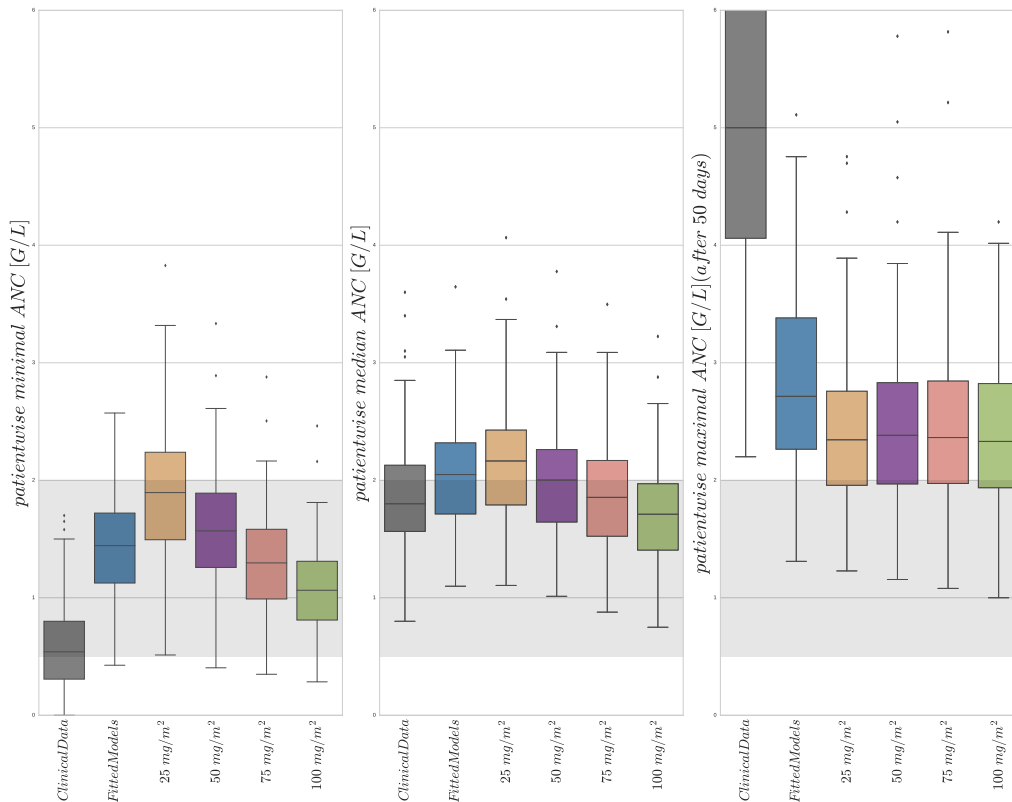


Figure 7.31: **Boxplots of minimal, median, and maximal (from left to right) individual ANCs for all 116 patients.** Shown are values for the 6 different protocols from table 7.19, observed for the first column and simulated for protocols 2–6. The target range (0.5-2.0 G/L) of the NOPHO/UK treatment protocol is shown as the gray background. Horizontal lines within the boxes are the medians, the upper and lower box limits are the first and third quartiles of the data, respectively. The whiskers indicate an even larger confidence region of these quartiles plus/minus 1.5-times the interquartile range. Beyond the whiskers, data are considered as outliers and are plotted as individual points. For the columns representing 25 mg/m² to 100 mg/m², the total amount of 6-mercaptopurine administered is increasing. The median average individual daily doses actually administered for protocols 1 and 2 were 43.15 ± 10.5 mg/m².

cells in the first transit compartment. Similar plots for all 116 patients are provided in the supplemental data of [225].

Discussion

The newly developed mathematical model enables us to perform a virtual comparison of different treatment protocols. The boxplots in figure 7.31 show several interesting results.

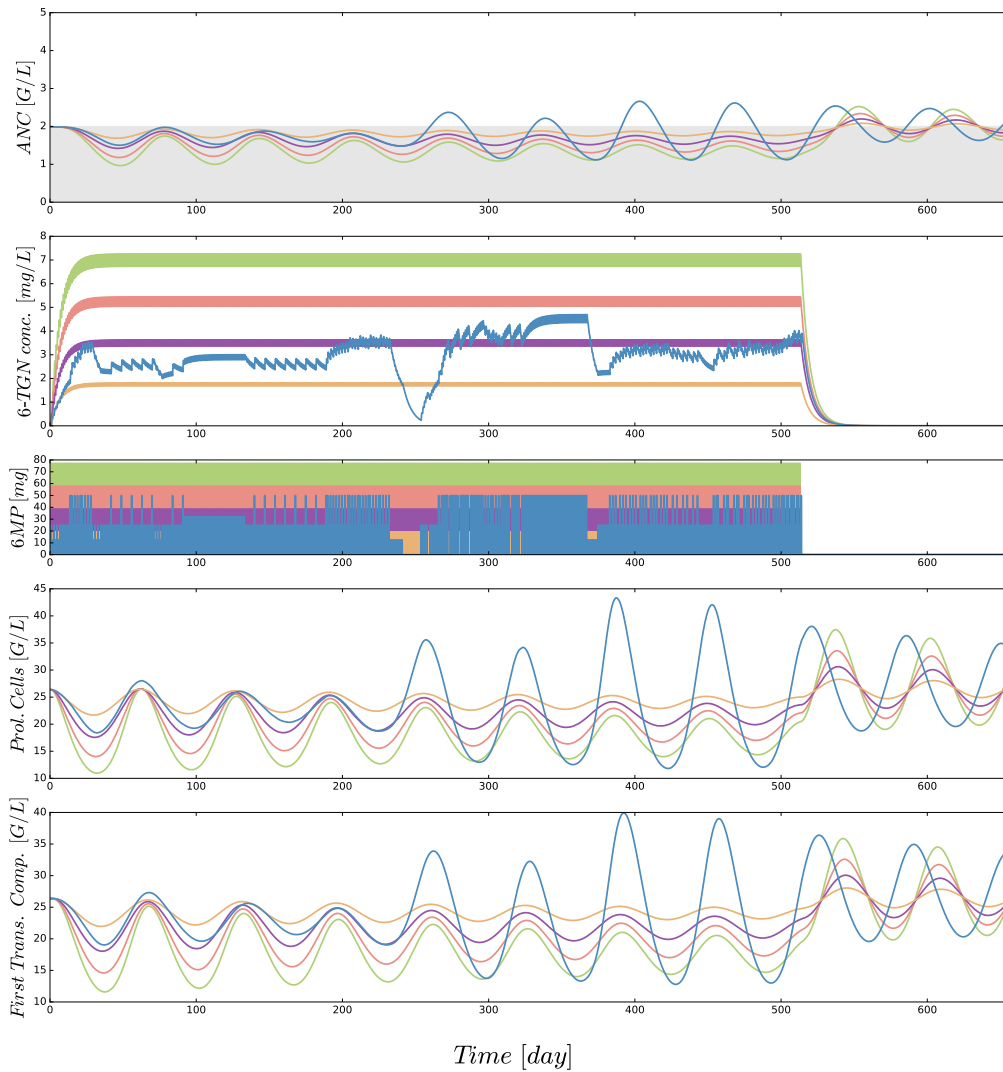


Figure 7.32: **Simulated trajectories for 5 different protocols from table 7.19 and an exemplary patient.** Colors of the trajectories are identical to those used in figure 7.31. The linear increase in dosing from 25 mg/m^2 to 100 mg/m^2 forces the absolute neutrophil counts (ANCs) to lower peak values and a smaller drug-induced steady state value at the end of treatment. The actual dosage administered to the patient (blue) ranged between the 25 mg/m^2 and 50 mg/m^2 protocols and resulted in similar ANC dynamics. At approximately day 240, the actual dosing was stopped for a short period, inducing stronger ANC oscillations in the subsequent treatment period. This observation is even stronger regarding the proliferating cells as well as cells in the first transit compartment. Interestingly, these oscillations also continued for some time after the end of treatment.

First, the median and standard deviation of actual ANC measurements are very accurately matched by the simulation using the estimated parameters (compare the first two entries in the middle boxplot of figure 7.31). Concerning the patientwise observed and simulated minimal and maximal ANC values, the model demonstrates a corresponding weakened chemotherapy-induced myelosuppression, respectively overproduction of ANCs compared to the high measured variability. This variability is biologically and clinically very plausible due to the aforementioned external events and uncertainties, although periods of severe infections were already excluded. The reproducibility of the median and avoidance of over-fitting of the extreme values are in our opinion good properties of a mathematical model. Given this good correspondence between cross-validated data and simulations, we feel encouraged to compare simulations of different treatment protocols as specified in table 7.19. Note, however, that generalizations of mathematical models personalized for data from one protocol to another have to be considered with extreme care (compare the discussion for acute myeloid leukemia models by [181]). Further, we want to highlight that the current model is not intended to describe the ANC extrema such that the results of the simulation study have to be treated with caution. The results shall serve as a preliminary assessment of the dose-effect relationship which has to be confirmed in future studies. The relationship might be stronger compared to the current model predictions and demonstrated by the clinical data in figure 7.32. The impact of model variations on the outcome of simulation studies is usually significant. We have tested the value of fixing the k_{tr} parameter to represent a biologically plausible MMT of 3.9 days. This decreases the model accuracy (which is why the results are not included here), but still leads qualitatively to the same subsequent effects.

Second, an approximately linear decrease in minimal, median and maximal values can be observed as the dosage increased linearly from 25 mg/m² to 100 mg/m² with a slightly reduced decrease of the maximal ANC values. Again, this linear dose-effect relationship seems biologically plausible. For most of the simulations such as those shown in figure 7.32, the maximal ANC value decreases. However, for other simulations (see online supplement of [225]) stronger myelosuppression led to identical maximal ANC values. This effect is due to a feedback mechanism that may lead to increased proliferation for reduced ANC which leads to larger ANC values after some delay.

Third, a tendency for higher oscillations for treatments with pauses and changes in dosage is seen in a comparison of the simulated actual treatment protocol 2 and the constant administrations of protocols 3 and 4, which uses lower/higher total amounts of 6MP. Again, an example of this can be seen in figure 7.32. We believe that in the future adapted dosing schedules might take advantage of the chemotherapy-induced oscillations for an optimized dosing regimen. In the CT of AML it is shown *in silico* that the timing of the treatment start can have a beneficial influence on the reduction of myelosuppression [181]. However, high dose chemotherapy administered every three to four weeks provokes stronger periodic oscillations compared to the daily oral dosing which makes it more challenging to identify and capture the oscillations. For high dosage, previously a multi-compartment hematopoietic model was analyzed regarding Hopf

bifurcation and an explicit analytical expression for the bifurcation point was provided depending on model parameters [215]. Oscillations of various blood cell populations have been observed in clinical data and partly investigated for different hematological disorders [226, 227]. The exact mechanisms and interaction between 1) stem cell cycling, 2) hematological disorder, and 3) drug exposure are still not fully understood. In our case, for all 116 patients *in silico* simulations show that the oscillations are damped (in 84 cases into a steady state) once the chemotherapy is stopped, albeit with long time ranges of up to one year (see supplemental data of [225] for examples). Therefore, we assume that the oscillations in the ANC_s observed in our simulations can be attributed to the influence of chemotherapy on the nonlinear dynamics of hematopoiesis. The connection between *model-intrinsic* and *chemotherapy-induced* oscillations should be assessed in detail in future studies. A stability analysis [37] of the steady state could be performed (e.g., similar to [228] and [73]) to assess the theoretical properties of the model and relate them to the physiological behavior of neutrophils.

7.3 Feedback optimal control algorithm for the Lotka-Volterra fishing problem

In this section we apply algorithm 2 to the Lotka-Volterra fishing benchmark problem demonstrating the performance of the algorithm and separately analyze optimal finite support designs.

The Lotka-Volterra example is chosen as a well studied dynamic system representing the relation between two competing populations. The model can be modified analyzing disease spreading in an epidemiological context [229] or technological forecasting of stock markets [230] such that the model combines medical, biological and economical interests. The optimal control and OED problem of the Lotka-Volterra fishing example are introduced and described in the following.

The goal of the optimal control problem is an optimal fishing strategy $u^*(t)$ that brings the prey $x_1(t)$ and predator $x_2(t)$ populations into a steady state (7.25d), by penalizing deviations from the steady state over the whole time horizon $[t_0, t_f]$. The optimal control problem of type (4.8) is

$$\min_{x(t), u(t)} x_3(t_f) \quad (7.25a)$$

$$\text{s.t. } \dot{x}_1(t) = p_1 x_1(t) - p_2 x_1(t) x_2(t) - c_0 x_1(t) u(t), \quad (7.25b)$$

$$\dot{x}_2(t) = -p_3 x_2(t) + p_4 x_1(t) x_2(t) - c_1 x_2(t) u(t), \quad (7.25c)$$

$$\dot{x}_3(t) = (x_1(t) - 1)^2 + (x_2(t) - 1)^2, \quad (7.25d)$$

$$x(t_0) = x_0, \quad (7.25e)$$

$$u(t) \in [0, 1]. \quad (7.25f)$$

The Lotka-Volterra OED problem is of type (4.35) and defined as

$$\min_{x(t), G(t), F_d(t_i), w^1, w^2} \text{trace}(F_d^{-1}(t_f)) \quad (7.26a)$$

$$\text{s.t. } \dot{x}_1(t) = p_1 x_1(t) - p_2 x_1(t) x_2(t), \quad (7.26b)$$

$$\dot{x}_2(t) = -p_3 x_2(t) + p_4 x_1(t) x_2(t), \quad (7.26c)$$

$$\dot{G}_{11}(t) = f_{x11} G_{11}(t) + f_{x12} G_{21}(t) + f_{p11}, \quad (7.26d)$$

$$\dot{G}_{12}(t) = f_{x11} G_{12}(t) + f_{x12} G_{22}(t) + f_{p12}, \quad (7.26e)$$

$$\dot{G}_{13}(t) = f_{x11} G_{13}(t) + f_{x12} G_{23}(t), \quad (7.26f)$$

$$\dot{G}_{14}(t) = f_{x11} G_{14}(t) + f_{x12} G_{24}(t), \quad (7.26g)$$

$$\dot{G}_{21}(t) = f_{x21} G_{11}(t) + f_{x22} G_{21}(t), \quad (7.26h)$$

$$\dot{G}_{22}(t) = f_{x21} G_{12}(t) + f_{x22} G_{22}(t), \quad (7.26i)$$

$$\dot{G}_{23}(t) = f_{x21} G_{13}(t) + f_{x22} G_{23}(t) + f_{p23}, \quad (7.26j)$$

$$\dot{G}_{24}(t) = f_{x21} G_{14}(t) + f_{x22} G_{24}(t) + f_{p24}, \quad (7.26k)$$

$$F_{11}(t_i) = F_{11}(t_{i-1}) + w_i^1 G_{11}^2(t_i) + w_i^2 G_{21}^2(t_i), \quad (7.26l)$$

$$F_{12}(t_i) = F_{12}(t_{i-1}) + w_i^1 G_{11}(t_i) G_{12}(t_i) + w_i^2 G_{21}(t_i) G_{22}(t_i), \quad (7.26m)$$

$$F_{13}(t_i) = F_{13}(t_{i-1}) + w_i^1 G_{11}(t_i) G_{13}(t_i) + w_i^2 G_{21}(t_i) G_{23}(t_i), \quad (7.26n)$$

$$F_{14}(t_i) = F_{14}(t_{i-1}) + w_i^1 G_{11}(t_i) G_{14}(t_i) + w_i^2 G_{21}(t_i) G_{24}(t_i), \quad (7.26o)$$

$$F_{22}(t_i) = F_{22}(t_{i-1}) + w_i^1 G_{12}^2(t_i) + w_i^2 G_{22}^2(t_i), \quad (7.26p)$$

$$F_{23}(t_i) = F_{23}(t_{i-1}) + w_i^1 G_{12}(t_i) G_{13}(t_i) + w_i^2 G_{22}(t_i) G_{23}(t_i), \quad (7.26q)$$

$$F_{24}(t_i) = F_{24}(t_{i-1}) + w_i^1 G_{12}(t_i) G_{14}(t_i) + w_i^2 G_{22}(t_i) G_{24}(t_i), \quad (7.26r)$$

$$F_{33}(t_i) = F_{33}(t_{i-1}) + w_i^1 G_{13}^2(t_i) + w_i^2 G_{23}^2(t_i), \quad (7.26s)$$

$$F_{34}(t_i) = F_{34}(t_{i-1}) + w_i^1 G_{13}(t_i) G_{14}(t_i) + w_i^2 G_{23}(t_i) G_{24}(t_i), \quad (7.26t)$$

$$F_{44}(t_i) = F_{44}(t_{i-1}) + w_i^1 G_{14}^2(t_i) + w_i^2 G_{24}^2(t_i), \quad (7.26u)$$

$$x(t_0) = x_0, \quad (7.26v)$$

$$F_{ij}(t_0) = 0 \quad i, j \in \{1, 2, 3, 4\} \text{ and } i \leq j, \quad (7.26w)$$

$$G_{ij}(t_0) = 0 \quad i \in \{1, 2\}, j \in \{1, 2, 3, 4\}, \quad (7.26x)$$

$$\sum_{i=0}^N w_i^\omega \leq 1 \quad \omega \in \{1, 2\}, \quad (7.26y)$$

$$w_i^\omega \in [0, 1] \quad (7.26z)$$

on the time grid $t \in [t_0, t_f]$ with

$$f_{x11} = \partial f_1(t)/\partial x_1 = p_1 - p_2 x_2, \quad (7.27a)$$

$$f_{x12} = -p_2 x_1, \quad (7.27b)$$

$$f_{x21} = p_4 x_2, \quad (7.27c)$$

$$f_{x22} = p_4 x_1 - p_3, \quad (7.27d)$$

$$f_{p11} = \partial f_1(t)/\partial p_1 = x_1, \quad (7.27e)$$

$$f_{p12} = -x_1 x_2, \quad (7.27f)$$

$$f_{p23} = -x_2, \quad (7.27g)$$

$$f_{p24} = x_1 x_2. \quad (7.27h)$$

The solution of problem (7.26) provides an optimal sampling design minimizing the uncertainties of the parameters p_1, p_2, p_3 and p_4 . The right upper entries of the FIM are considered as differential states in the optimization problem instead of all matrix entries due to symmetry properties of the FIM. Explicit values of the time horizon, the initial states, the parameters and the constants chosen for the numerical computations are given in the next subsection.

Software and experimental settings

Algorithm 2 is implemented as a prototype in the open-source software tool CasADi [178]. We used the version 3.1.0 together with Python 2.7.6. The finite-dimensional nonlinear programs resulting from discretizing the optimal control problem (4.8) and OEDs problem (4.35) are solved with IPOPT [231]. The parameter estimation problems are solved by a GN algorithm using IPOPT. The derivatives needed for the optimization problems and their robustifications are efficiently generated within CasADi using automatic differentiation, [178]. In subsection 7.3 the system of ODEs is solved using the in-house fixed-step explicit Runge-Kutta integrator and a single shooting method with a stepsize of 0.15. For the first state and parameter estimation problem on the time interval $[0,15]$ the initial guess is $p = (p_1, p_2, p_3, p_4, x_1(0), x_2(0))^T = (1.5, 1.5, 1.5, 1.5, 0.0, 0.0)$. We assume that both states $h_1(t_i) = x_1(t_i)$ and $h_2(t_i) = x_2(t_i)$ can be measured and that no fishing is permitted on $t \in [0, 15]$. The pseudo-measurements are derived from a simulation with the true parameters plus a measurement error $\varepsilon_i \sim \mathcal{N}\left(\begin{pmatrix} 0 \\ 0 \end{pmatrix}, \begin{pmatrix} 0.03^2 & 0 \\ 0 & 0.03^2 \end{pmatrix}\right)$ according to equation (4.9). For the OED problems only the uncertainty of the parameters is considered.

For the analysis of finite support designs in subsection 7.3 the ODE system is solved with CVODES from the SUNDIALS suite [174] and a multiple shooting method with stepsize $h(= 12/500)$. The continuous version of the OED problem (7.26) is computed on the time grid $[0,12]$ with $p = (p_1, p_2, p_3, p_4) = (1, 1, 1, 1)$. In both examples the discretization of the optimization variable $u(t)$ coincides with the time grid of the ODE problem.

Three versions of Algorithm FOCOed applied to the Lotka-Volterra fishing problem

We apply three versions of algorithm 2 to the control problem (7.25a) to stress the relevance of optimal measurement time points and the influence of parameter uncertainty during optimization.

- *with_OED*. This is algorithm 2, i.e., using measurement time points from non-robust OED.
- *without_OED*. The OED problem in step 2 of algorithm 2 is omitted, and an equidistant time grid is used for measurements.
- *with_r_OED*. The optimal control problem in step 1 and the OED problem in step 2 of algorithm 2 are replaced with their robust counterparts as described in section 6.3.

In the following, the experimental setting is described independently of the chosen version of algorithm 2. The experiment is performed on the time interval $[0,30]$. From 0 to 15 a first state and parameter estimation with seven measurements, initial guesses $p_{ini} = (1.5, 1.5, 1.5, 1.5, 0.0., 0.0)^T$ is performed. From time point $t = 15$, algorithm 2 is performed with the estimated parameter values \hat{p} , the state values $\hat{x}(15) = (\hat{x}_1(15), \hat{x}_2(15))^T$ and the objective function $\phi(\cdot) = \text{trace}(F^{-1}(t_f))$ of the optimization problem (4.35).

For a quantitative statement the three versions of algorithm 2 are repeated 50 times with the normally distributed measurement error ε_i used for the generation of pseudo-measurements. The averaged estimated parameter values and the corresponding uncertainties after $t = 15$ and $t = 30$ are presented in table 7.20 for the three different algorithm versions *with_r_OED*, *with_OED* and *without_OED*. The first column shows the objective function value of the optimal control problem (7.25) solved on $t \in [15, 30]$ with the true parameter values and the initial state values $x(15) = (1.25847, 0.473369, 0)^T$ as the reference solution. The last row additionally presents the averaged objective function values of the three algorithm versions and the last three columns contain the relative uncertainty and objective function value improvements between the three algorithm versions.

First of all, table 7.20 indicates that the three versions of algorithm 2 provide estimated parameters next to the true parameter values but the results qualitatively differ by means of the resulting parameter uncertainties and the optimal control objective function values. The use of measurement time points from OEDs (*with_OED*) compared to equidistant time points (*without_OED*) improves the parameter uncertainty by 15 % after $t = 15$ and by 34 % after $t = 30$ on average. The robustification of the optimal control and OED problems (*with_r_OED*) results in an improvement of the parameter uncertainties compared to version *without_OED* of 15 % after $t = 15$ and of 36 % after $t = 30$ on average and compared to the non-robust version *with_OED* of 0.26 % after $t = 15$ and of 2.52 % after $t = 30$ on average. The objective function of the optimal control problem is reduced by approximately 8 %, respectively 10 %, using version *with_r_OED* or version

with_OED compared to version *without_OED*. The robustification of algorithm 2 has a minor averaged improvement of 0.41 %.

at t = 15											
	OC	with_r_OED (A)			with_OED (B)		without_OED (C)		I_{AC}	I_{BC}	I_{AB}
	value	value	$\sigma^2(\times 10^{-3})$	value	$\sigma^2(\times 10^{-3})$	value	$\sigma^2(\times 10^{-3})$				
p_1	1.000	1.0074	0.3377	0.9925	0.3300	1.0293	0.5090	33.65	35.17	-2.33	
p_2	1.000	1.0085	0.5540	0.9954	0.5404	1.0267	0.5313	-4.27	-1.71	-2.52	
p_3	1.000	0.9935	0.5861	1.0073	0.6063	0.9758	0.6139	4.53	1.24	3.33	
p_4	1.000	0.9959	0.6466	1.0053	0.6635	0.9762	0.8780	26.36	24.43	2.55	
at t = 30											
		with_r_OED (A)		with_OED (B)		without_OED (C)		I_{AC}	I_{BC}	I_{AB}	
	value	value	σ^2	value	σ^2	value	σ^2				
p_1	1.000	1.0066	0.2414	0.9974	0.2418	1.0082	0.4214	42.71	42.62	0.17	
p_2	1.000	1.0065	0.3639	1.0004	0.3706	1.0069	0.4624	21.30	19.85	1.81	
p_3	1.000	0.9936	0.3472	1.0029	0.3582	0.9924	0.5068	31.49	29.32	3.07	
p_4	1.000	0.9958	0.3575	1.0014	0.3764	0.9937	0.6837	47.71	44.95	5.02	
M_{LV}	0.714		0.724		0.727		0.790	9.62	7.97	0.41	

Table 7.20: Averaged estimated parameter values with their uncertainties and the objective function value ($M_{LV} = x_3(30)$) after 50 runs of the optimal control problem (7.25) solved with three versions of algorithm 2 (*with_r_OED* (A), *with_OED* (B), *without_OED* (C)). $I_{ij}(\%)$ is the relative uncertainty and objective value improvement after $t = 15$ and $t = 30$ of column i compared to column j . Column OC contains the true parameter values with which the optimal control problem (7.25) is solved on $t \in [15, 30]$ and the resulting objective function value.

Figure 7.33 shows exemplary the solution of the Lotka-Volterra fishing problem computed with the three versions *with_r_OED*, *with_OED* and *without_OED* of algorithm 2.

Analyzing finite support designs of optimal experimental design problems

In this section, we demonstrate the theoretical result of lemma 6.3.3 on the Lotka-Volterra optimal experimental design problem.

The optimal solution $w^{1*}(t)$ and $w^{2*}(t)$ of the OED problem are plotted in figure 7.34 together with the information gain matrices

$$\Pi^1(t) = F^{-1}(t) \begin{pmatrix} G_{11}^2 & G_{11} G_{12} & G_{11} G_{13} & G_{11} G_{14} \\ G_{11} G_{12} & G_{12}^2 & G_{12} G_{13} & G_{12} G_{14} \\ G_{11} G_{13} & G_{12} G_{13} & G_{13}^2 & G_{13} G_{14} \\ G_{11} G_{14} & G_{12} G_{14} & G_{13} G_{14} & G_{14}^2 \end{pmatrix} F^{-1}(t)$$

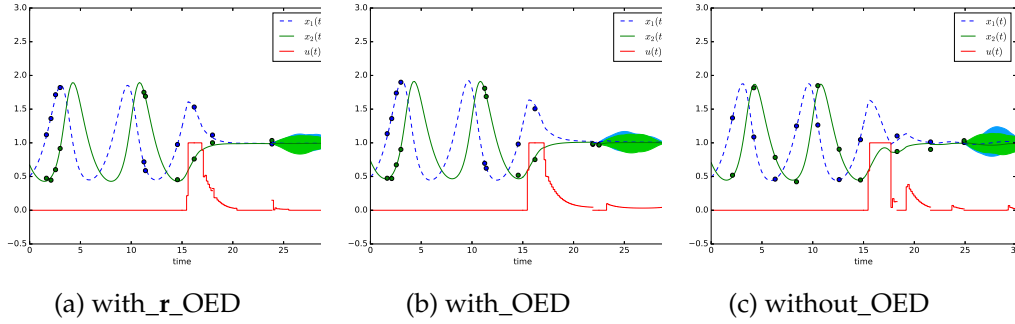


Figure 7.33: **Visualization of three versions (*with_r_OED*, *with_OED* and *without_OED*) of the feedback optimal control Algorithm 2 applied to the Lotka-Volterra fishing example.** The algorithm is performed on the time interval $[15,30]$. On the time interval $[0,15]$ seven measurements are taken for a state and parameter estimation. The estimated parameters with the corresponding uncertainties and initial states serve as input for the algorithm. In figure 7.33a the robust version and in figure 7.33b the non-robust version of Algorithm 2 is used with measurement time points from OEDs. Figure 7.33c presents the solution of algorithm 2 with measurements taken on an equidistant time grid. After the last measurement time point uncertainty tubes are computed by 100 simulations with parameter values sampled from a normal distribution with the estimated parameters as mean $\hat{p} = [0.982, 0.990, 1.015, 1.023]$ and variance $\Sigma_{\hat{p}} = \text{diag}(0.000214, 0.000321, 0.000347, 0.000351)$ in figure 7.33a, $\hat{p} = [1.014, 0.998, 0.981, 0.977]$ and variance $\Sigma_{\hat{p}} = \text{diag}(0.000231, 0.000325, 0.000319, 0.000334)$ in figure 7.33b and $\hat{p} = [1.031, 1.047, 0.977, 0.978]$ and $\Sigma_{\hat{p}} = \text{diag}(0.000413, 0.000470, 0.000463, 0.000636)$ in figure 7.33c.

and

$$\Pi^2(t) = F^{-1}(t) \begin{pmatrix} G_{21}^2 & G_{21} G_{22} & G_{21} G_{23} & G_{21} G_{24} \\ G_{21} G_{22} & G_{22}^2 & G_{22} G_{23} & G_{22} G_{24} \\ G_{21} G_{23} & G_{22} G_{23} & G_{23}^2 & G_{23} G_{24} \\ G_{21} G_{24} & G_{22} G_{24} & G_{23} G_{24} & G_{24}^2 \end{pmatrix} F^{-1}(t).$$

The Lagrange multipliers are also shown as horizontal lines in figure 7.34a and figure 7.34b. Both figures visualize the result of lemma 6.3.3 such that the touching of the information gains' maxima is equivalent to a singular arc of the sampling decisions $w^1(t)$ and $w^2(t)$.

Discussion

The measurement time points have a large impact on the uncertainty of the model parameters and consequently an impact on the optimal control solution, even if the optimizing control does not excite the system dynamics. The quantitative study of

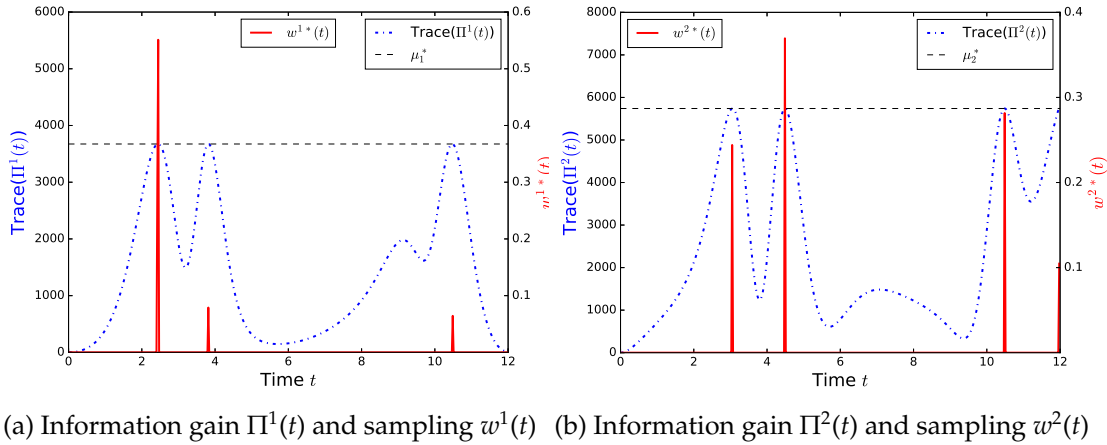


Figure 7.34: Visual relation between the trace of the information gain matrices $\Pi^1(t), \Pi^2(t)$, the Lagrange multipliers μ_1^*, μ_2^* and the optimized sampling decisions $w^{1*}(t), w^{2*}(t)$ of the Lotka-Volterra optimal experimental design problem.

subsection 7.3, which is summarized in table 7.20, significantly shows that the optimal measurement time points taken from non-robust and robust OEDs lead to an averaged uncertainty improvement of 34 %, respectively 36 %, compared to equidistantly taken measurements. The qualitatively different measuring positions are visualized in figure 7.33. The measurement time points of the OEDs are placed at the beginning and at the end of the time interval $[0,15]$ in which a first state and parameter estimation is performed. During the optimal control phase starting from $t = 15$ the non-robust and robust OEDs suggest measuring once, respectively twice, at the steep descent/ascent of the populations on the interval $[15,20]$ where a larger information content is expected compared to the equidistant time points next to the trajectories' steady state. The heterogeneity in the improvement of the parameters' uncertainties results in the used objective function trace($F^{-1}(t_f)$) with which the averaged parameter uncertainty is minimized and not each uncertainty separately. This leads to slightly increased uncertainties of parameter p_2 after $t = 15$ by the use of OED. A different scalar function $\phi(\cdot)$ such as the determinant or the largest eigenvalue of the information matrix might prevent this problem but this analysis is not part of the work. Besides this minor increase the estimated parameter values are closer to the true values using OEDs in comparison to equidistant measurement time points. The uncertainty tubes in figure 7.33 give an indication that the reduced uncertainty of the parameters from Algorithm 2 has an indirect positive influence on the state uncertainty leading to tighter uncertainty tubes. The visual indication is strengthened by the last row of table 7.20 presenting the optimal control objective function value of the reference solution and the averaged values resulting from the three different versions (*with_r_OED*, *with_OED* and *without_OED*) of algorithm 2. The reduced parameter uncertainties obtained from non-robust and robust OEDs lead to a 8 %, respectively 10 %, objective function value

compared to the version *without_OED* with measurements taken on equidistant time points.

Lemma 6.3.3 is visualized for the Lotka-Volterra *OED* benchmark problem in figures 7.34a and 7.34b. Whenever the Lagrange multiplier μ^* is equal to the value of the information gain matrix, the sampling decision variable $w^*(t)$ is between 0 and 1.

7.4 Fisher's method for population parameter estimations

In this section, to our best knowledge, we apply for the first time Newton's and Fisher's method to parameter estimation problems for two specific *NLME* models. We present these results to highlight that it is worthwhile to use tailored optimization algorithms for parameter estimation of *NLME* models, meaning Fisher's method for the Hessian approximation. This section serves as a starting point for further investigations in future projects for this direction of research. We develop a prototype of the *FO* algorithm with the Fisher's method of scoring to compare the method with current standard solvers such as *NONMEM* in which a *BFGS* method is implemented. In a first attempt, we perform numerical tests and present objective function values per iteration but we do not calculate and compare computational costs and do not present any theoretical findings. Convergence rates of the different methods are known and can be found in [169]. The aim is to test the performance of the Fisher's method regarding objective function value reductions per iteration for two examples to get a first impression on the convergence rate of the Fisher's method as the method highly depends on the classification of the observed problem to a large or low residual problem [126, 169]. Additionally, we test a different quasi Newton's method and Fisher's method together with the Levenberg-Marquardt (*LM*) method [232]. In the discussion, we will briefly address some theoretical aspects which might be of interest for the consideration of Fisher's method in pharmacometric *NLME* parameter estimation problems.

Instead of using cheap update formulas as *BFGS*-updates for the Hessian of the likelihood used in *NONMEM*, *Pumas* or *nlmixr* or the exact Hessian, which is in most *PK/PD* analysis with large datasets computationally intractable, we believe in Gauss-Newton for nonlinear regression and Fisher's method of scoring [233] for mixed-effects models.

The *FIM* is used in experimental design problems for *NLME* models but within parameter estimation problems for these kind of models the *FIM* is not considered at all. This is incomprehensible as the usage of the *FIM* as Hessian might have some advantages with respect to a probably faster convergence compared to quasi-Newton methods, better statistical properties (algorithm only converges to local minima with identifiable parameters not affected by measurement error/variability), and in most cases the *FIM* is used for quantifying parameter uncertainties after parameter estimation anyway. Regarding a sequential/online approach for parameter estimation and optimal experimental design, the usage of the *FIM* in both optimization problems reduces the preparation phase of each *OED* problem and the parameter estimation problems might converge faster compared to the usage of low-rank Hessian approximations.

Methods

Theophylline example

For testing the different algorithmic methods, we use the theophylline dataset and the proposed **NLME** model from [136]. The publicly available dataset consists of 120 concentration measurements, 10 each, from 12 subjects following an oral administration of 320 mg theophylline, a drug for respiratory diseases. The measurements are visualized in figure 7.36(a). The concentration time profiles are modelled by an one compartment PK model with first order absorption (see section 7.35).

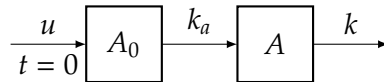


Figure 7.35: **One compartment PK model with first order absorption.**

The one compartment PK model with first order absorption is described as an **IVP**

$$\begin{aligned} \dot{A}_0(t) &= -k_a A_0(t), & A_0(0) &= 320, \\ \dot{A}(t) &= k_a A_0(t) - k_e A(t), & A(0) &= 0 \end{aligned}$$

with its analytical solution $C(t) = \frac{320}{V} \frac{k_a}{k_a - k_e} (e^{-k_e t} - e^{-k_a t})$ and the measurement function $h(t) = C(t) = \frac{A(t)}{V}$. Parameters of interest are the volume of distribution V of the central compartment and first order rate constants of the absorption k_a and elimination k_e . **IV** is described by not correlated normally distributed random effects η with mean zero and covariance matrix Ω :

$$\begin{aligned} k_a &= \theta_1 e^{\eta_1}, & V &= \theta_2 e^{\eta_2}, & k &= \theta_3 e^{\eta_3} \\ \eta &= (\eta_1, \eta_2, \eta_3)^T \sim \mathcal{N}(0, \Omega) & \text{with } \Omega &= \begin{pmatrix} \omega_{11}^2 & 0 & 0 \\ 0 & \omega_{22}^2 & 0 \\ 0 & 0 & \omega_{33}^2 \end{pmatrix}. \end{aligned}$$

A proportional error model

$$F = C(t) + C(t) \varepsilon$$

with $\varepsilon \sim \mathcal{N}(0, \sigma_1^2)$ was assumed. The starting values for parameter estimation are $\theta = (1, 20, .1)$, $\omega_{ii}^2 = 0.1, i = 1, 2, 3$ and $\sigma_1^2 = 0.1$. For the computations we reimplement the **FO** method as a prototype in CasADi. For the Fisher's method we use the population **FIM** presented in section 4.2.3 which is passed as the Hessian to IPOPT. We also test the **LM** method in which we iteratively increase the influence of the diagonal matrix from 0.0 to 1. with a 0.01 stepsize. We design two parameter estimation scenarios with the difference in either estimating or fixing σ_1^2 .

AML example

We also apply the Fisher's method to the [AML](#) example from section 7.1.1 with the publicly available cyclewise dataset from section 5.1. We perform a parameter estimation using the first 21 [CCs](#). Using the whole dataset results in numerical difficulties during estimation such that we concentrate on the half dataset. We use an additive error model, the [PK/PD](#) model M3 with the initial value approach I1 (steady state approach). The steady state of leukocytes B , the transition rate k_{tr} , the feedback term γ , and the [PD](#) effect slope are defined as parameters and [IIV](#) is assumed as log-normally distributed for all four parameters. The starting values for the parameters are $(B, \gamma, k_{tr}, \text{slope}) = (10, 0.4, 0.17, 3.4)$, $\omega_{ii}^2 = 0.1, i = 1, 2, 3, 4$ and $\sigma_1^2 = 0.1$.

Results

Theophylline example

The figures 7.36(a) and (b) visually demonstrate that all algorithms converge to the same minimum. In both scenarios, the Newton's method needs the lowest number of iterations for convergence. The Fisher's method shows a smooth decrease in each iteration compared to the mixture of flat and steep areas derived by the [BFGS](#) methods. Further, the Fisher's method behaves similar to the [BFGS](#) methods when σ_1^2 is estimated, whereas with fixed σ_1^2 the Fisher's method has a similar decrease in the first iterations compared to the Newton method but after the third iteration Newton's method outperforms the other methods.

AML example

Figure 7.37 shows that the algorithms converge to the same minimum with respect to the objective function value and the first Newton iteration underperforms compared to the other methods. After the third iteration, the situation changes and the fast decreasing of [NONMEM](#)'s algorithm becomes flatten and underperforms compared to the other methods.

Discussion

We compare different methods for solving population parameter estimation problems with [FO](#) approximation illustrated by two examples differing in their model complexity (linear vs. nonlinear [ODE](#) system) and number of measurements. The two practice-oriented examples demonstrate that Fisher's method is an alternative to currently used low rank Hessian approximation methods and the computationally expensive Newton's method. Similar or even steeper descent steps per iterations are achieved by Fisher's method compared to the [BFGS](#) approximations. Regarding convergence, Fisher's method needs several more iterations close to the solution revealing numerical difficulties which have to be analyzed in future studies. Additionally, it is known that the performance of Fisher's method strongly depends on the properties of the

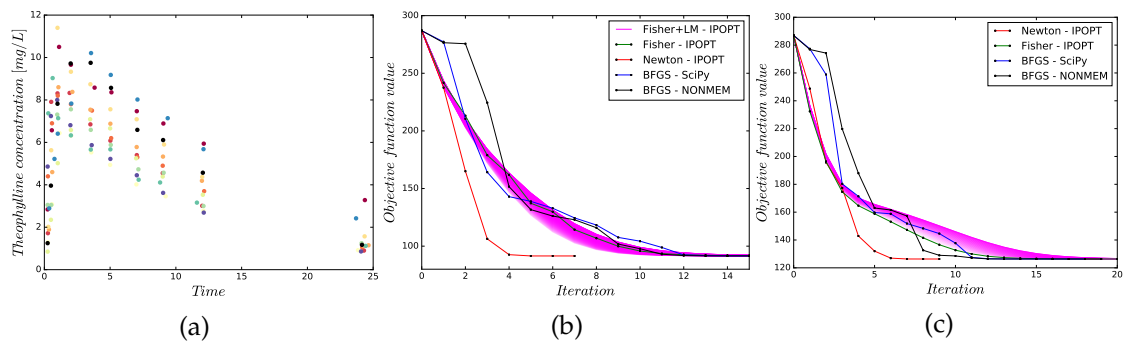


Figure 7.36: **Dataset and objective function values per iteration.** (a) Visualization of the theophylline dataset with 120 (10 per subjects) theophylline concentration measurements from 12 subjects.

(b) Objective function values per iteration for the example with estimating σ_1^2 and applying Fisher's method with and without Levenberg-Marquardt (LM) method, Newton method and Broyden, Fletcher, Goldfarb, and Shanno (BFGS) methods. The number of iterations until convergence were 7 (Newton), 32 (Fisher), 20 (NONMEM), 23 (SciPy) and on average 47 (min:30, max:64) for Fisher with LM. The influence of the diagonal matrix in the LM method increases iteratively from 0. to 1. with a 0.01 stepsize visually represented via a reduced transparency of the line color.

(c) As (b) but without estimating σ_1^2 . The number of iterations until convergence are 9 (Newton), 36 (Fisher), 19 (NONMEM), 18 (SciPy) and on average 42 (min:36, max:49) for Fisher with LM.

underlying parameter estimation problem being a zero/low or large residual problem. We expect that population parameter estimation problems with FO approximation and heterogeneous data fit into large residual problems as one set of parameters must explain the various time profiles. The situation changes and the large residual problem might become a low residual problem as soon as the FOCE with and without interaction approximations will be considered. The impact of the LM method is additionally analyzed for both scenarios concluding that the method can result in steeper descent steps (compare for figure 7.36(b)) but also in worst steps (see figure 7.36 (c)). In [169], Theorem 10.2.5 states that "a LM algorithm may still be slowly locally convergent on large residual or very nonlinear problems" which should be kept in mind for using the method.

Summarizing, further numerical tests and theoretical analysis have to be performed for evaluating if Fisher's method is a good trade-of between additional computational expense and a faster convergence rate with only converging to minima not effected by measurement errors compared to low-rank Hessian approximations. Bock's κ analysis [168] might help to get a better understanding and an a priori classification of the parameter estimation problem into a low or large residual problem.

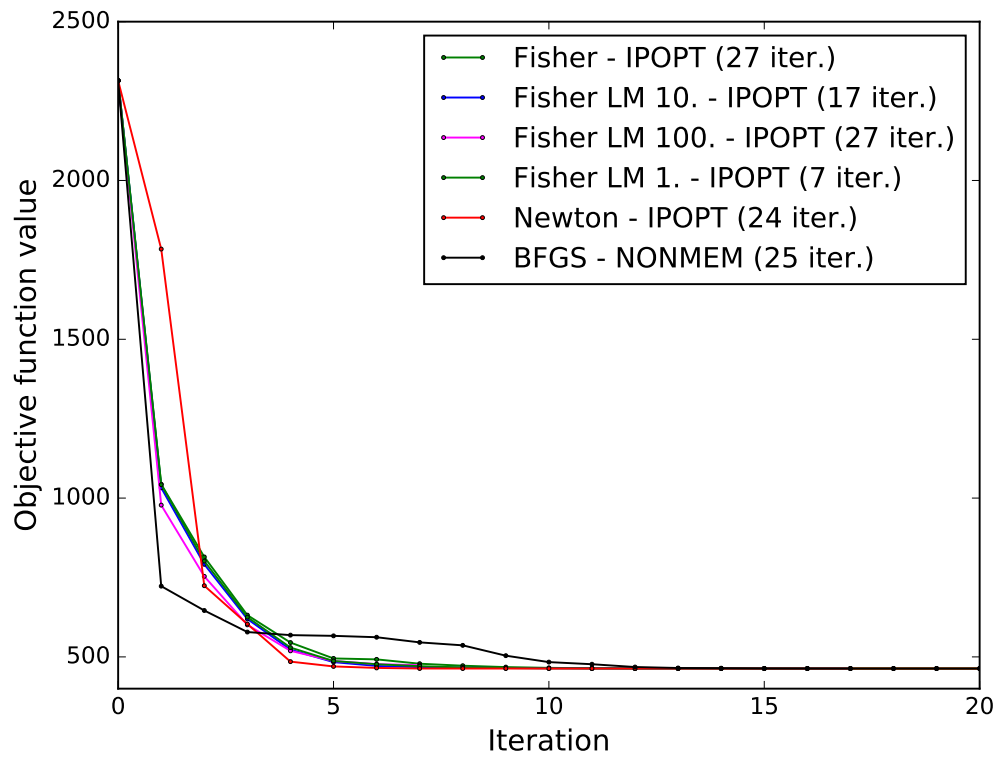


Figure 7.37: Objective function values per iteration derived by different optimization methods for the parameter estimation problem using the half acute myeloid leukemia dataset from section 7.1.1.

Part IV

Summary & future perspectives

Summary

In this thesis, we have developed semi-mechanistic population PK/PD models for the CT of AML patients and the MT of childhood ALL patients. We have fitted the models to clinical data and we have used those models to investigate clinically relevant aspects with simulation and optimization studies. In addition, we have proposed a framework for feedback optimal control with measurement time points computed from OED problems and have evaluated the benefit of Fisher's method for the first order approximated parameter estimation problem for NLME models.

Summarizing, we extended the gold-standard model for myelosuppression in pharmacometrics [52] to the most important component in AML CT [19, 91], Ara-C, and showed that one modeling assumption was important for a faster WBC count recovery for D123 schedules. In three extended models (M9, M10, and M12) we assumed that the Ara-C concentration has a direct impact on the proliferation term γ . Independent from the underlying physiological process, the dense treatment schedule D123 profits more than the standard plan D135 from the induced dynamics with respect to WBC recovery times. Future G-CSF concentration measurements for AML patients during consolidation cycles of D123 and D135 treatments and a comparison of our extended models with Quartino's [53] integrated G-CSF-myelosuppression model or more sophisticated models from quantitative systems pharmacology [65] may shed light on these generated hypotheses.

Next, we developed a second PK/PD model for the consolidation phase of AML patients treated with Ara-C and additionally lenograstim, based on Quartino's myelosuppression model considering endogenous G-CSF. Similar to our previous work, no G-CSF concentration measurements were available. In comparison to the firstly presented model, this model contains not only the dynamics of WBCs but also of leukemic cells and G-CSF concentrations. The consideration of leukemic cells enables an improved understanding of the interaction between WBCs and leukemic blasts and the evaluation of different treatment schedules on remission and leukopenia. The developed model and the results from the computational approach to optimize the administration of Ara-C and lenograstim with respect to clinically important outcomes are further steps toward providing personalized medicine and decision-support tools for physicians [234].

In the context of pediatric ALL, we presented a novel population PK/PD model describing myelosuppression for ALL maintenance therapy among children who received 6MP and MTX. A comparison with alternative modeling approaches and using WBC counts instead of ANCs showed the benefit of this model. We could show a linear dose-effect relationship superimposed with fluctuations of varying magnitude. Mathematical simulations and more mechanistic modeling approaches will allow to improve the understanding of intrinsic and extrinsic influence factors on the aberrant hematopoiesis and chemotherapy-induced myelosuppression of pediatric ALL patients. Therefore, the monitoring of individual PK profiles and a subsequent analysis of the PK/PD relationship are mandatory next steps for a better dose-effect correlation.

Regarding algorithmic contributions, we present a novel framework for feedback optimal control with measurement time points for parameter estimations computed from OED problems. It is based on a decoupled approach to dual control. The algorithm provides a reduction of parameter uncertainties while applying an optimal control strategy when measurement time points are used from OEDs compared to heuristically chosen equidistant measurement time points for parameter estimations. We also investigated a robustified version of the algorithm. Furthermore, a theoretical insight about the solution of the OED problem is given. Therefore Pontryagin's Maximum Principle is applied to the OED problem when the sum of optimization variables is constrained by one and a connection is drawn between the trace of the information gain matrix and the Lagrange multipliers for a discrete optimal design. The algorithmic and theoretical results are demonstrated on the *Lotka-Volterra fishing* benchmark problem.

Finally, we investigated Fisher's method in the context of parameter estimation for NLME models. For two numerical examples (theophylline and AML), differing in their problem size and nonlinearity, we applied Fisher's method to the FO approximated parameter estimation problems and compared the method with other solving methods. Similar or even steeper descent steps per iteration were achieved by Fisher's method compared to the BFGS approximations but further studies have to be performed to analyze the method of choice for parameter estimation of NLME models.

Future perspectives

In the following, we give several future perspectives worthwhile to investigate in follow-up studies.

In the context of AML, the models could be extended for the application in induction therapy with its anthracycline- and Ara-C-based 7+3 schedule, such that individualized schedules can be proposed at the start of chemotherapy treatment and not after induction therapy. Moreover, during induction therapy the increase of leukemic blasts and their response to the treatment can be analyzed leading to identifiable and thus more individualized mathematical models predicting the long term remission more precisely. Based on a prospective study with adequate biomarker information, the development of a mechanistic model for Ara-C, G-CSF, WBCs and leukemic cells might be a next step to better understand the PD effects of standard and dense high-dose Ara-C treatments. Modeling MRD, proposed by multiple recent studies as a strong prognostic marker for relapse in AML [207–210], might also be a promising alternative to leukemic blasts. Further, the deterministic optimization results could be extended with a comprehensive comparison of different optimization approaches and formulations addressing robustification, stochasticity, multiple objective functions and mixed integer aspects in constraints and controls (see [235]) for the actual application of the optimized schedules in clinical practice.

Mathematical modeling in the field of childhood ALL is a very promising and also a crucial field of research as there currently exist only four publications about PK/PD models for the MT aiming at explaining the variability of the PK and PD and

their related treatment efficacy and toxicity. Current daily oral administration and the collection of blood samples from children are two factors which make the modeling efforts demanding. In our work, we already addressed and highlighted important clinical aspects which still need further investigation. Follow-up analysis and studies are needed to investigate the

- impact of treatment breaks
- model-intrinsic and chemotherapy-induced oscillations
- impact of G-CSF administrations
- dynamics of leukemic blasts, respectively MRD
- differentiation of PD effect of 6MP and MTX

Our work also revealed different issues with regard to the mathematical model, e.g. a high MMT which does not coincide with physiologically plausible values. For a more mechanistic representation the PK models of 6MP and MTX should be extended with an additional compartment representing the concentration within the BM as it is the side of action for both drugs. The model and data show oscillations which might be beneficial for advanced treatment, but the relation between PK/PD and the chemotherapy-induced oscillations needs further investigation for a profound explanation. An interesting modeling approach for short- and long-term PD effects might be the introduction of two separate cell lines describing acute and chronic therapy-induced myelosuppression. The interested reader is referred to [236] for such kind of a model applied to oxaliplatin-induced peripheral neuropathy. Additionally, further cell lines for other hematopoietic cells and leukemic blasts or MRD as surrogate could be introduced. Based on our simulation study and further advanced models, optimization problems can be formulated to compute individually optimized treatment schedules.

Regarding algorithmic and numerical investigations, we believe that real time optimization might find its way to the computation of chemotherapy schedules for leukemia patients as soon as fast measurement devices are available for updating the mathematical models. In this context, online methods such as Moving Horizon or Kalman Filter have to be developed for the different NLME parameter estimation methods with efficient update formulas for real-time feasibility. Further investigations regarding the application and benefits of the Fisher's method might also be of great value for the PK/PD community and ultimately the patients, as PK/PD models are primarily developed to continuously assess and improve their therapy and medical condition.

Bibliography

1. Juliusson, G. & Hough, R. Leukemia. *Progress in Tumor Research* **43**, 87–100 (2016).
2. Watts, J. & Nimer, S. Recent advances in the understanding and treatment of acute myeloid leukemia. *F1000Research* **7** (2018).
3. Van der Graaf, P. H. & Benson, N. Systems pharmacology: bridging systems biology and pharmacokinetics-pharmacodynamics (PKPD) in drug discovery and development. *Pharmaceutical research* **28**, 1460–1464 (2011).
4. Mager, D. E., Kimko, H. H., *et al.* *Systems pharmacology and pharmacodynamics* (Springer, 2016).
5. Trame, M. N., Riggs, M., Biliouris, K., Marathe, D., Mettetal, J., Post, T. M., Rizk, M. L., Visser, S. A. & Musante, C. J. Perspective on the State of Pharmacometrics and Systems Pharmacology Integration. *CPT: Pharmacometrics & Systems Pharmacology* **7**, 617–620 (2018).
6. Bonate, P. L. & Steimer, J.-L. *Pharmacokinetic-pharmacodynamic modeling and simulation* (Springer, New York, 2011).
7. Upton, R. & Mould, D. Basic concepts in population modeling, simulation, and Model-Based drug development: Part 3—Introduction to pharmacodynamic modeling methods. *CPT: Pharmacometrics & Systems Pharmacology* **3**, 1–16 (2014).
8. US Food and Drug Administration. Guidance for industry: population pharmacokinetics. <<https://www.fda.gov/media/128793/download>> (1999).
9. Brown, S. A., Kovatchev, B. P., Raghinaru, D., Lum, J. W., Buckingham, B. A., Kudva, Y. C., Laffel, L. M., Levy, C. J., Pinsker, J. E., Wadwa, R. P., *et al.* Six-Month Randomized, Multicenter Trial of Closed-Loop Control in Type 1 Diabetes. *New England Journal of Medicine* (2019).
10. Mayer, R. J., Davis, R. B., Schiffer, C. A., Berg, D. T., Powell, B. L., Schulman, P, Omura, G. A., Moore, J. O., McIntyre, O. R. & Frei, E. Intensive postremission chemotherapy in adults with acute myeloid leukemia. Cancer and Leukemia Group B. *New England Journal of Medicine* **331**, 896–903 (1994).
11. Sun, W., Malvar, J., Sposto, R., Verma, A., Wilkes, J. J., Dennis, R., Heym, K., Laetsch, T. W., Widener, M., Rheingold, S. R., *et al.* Outcome of children with multiply relapsed B-cell acute lymphoblastic leukemia: a therapeutic advances in childhood leukemia & lymphoma study. *Leukemia* **32**, 2316 (2018).

12. Hoffbrand, A. V., Higgs, D. R., Keeling, D. M. & Mehta, A. B. *Postgraduate Haematology* 5. (Blackwell Publishing Ltd, Massachusetts, 2005).
13. Lichtman, M. A., Beutler, E., Kipps, T. J., Seligsohn, U., Kaushansky, K. & Prchal, J. T. *Williams hematology* (McGraw-Hill New York, 2006).
14. Hearn, T., Haurie, C. & Mackey, M. C. Cyclical neutropenia and the peripheral control of white blood cell production. *Journal of Theoretical Biology* **192**, 167–181 (1998).
15. Ackermann, M., Liebhaber, S., Klusmann, J.-H. & Lachmann, N. Lost in translation: pluripotent stem cell-derived hematopoiesis. *EMBO molecular medicine* **7**, 1388–1402 (2015).
16. Davis, A. S., Viera, A. J. & Mead, M. D. Leukemia: An overview for primary care. *Am Fam Physician* **89**, 731–738 (2014).
17. Elias, H., Schinke, C, Bhattacharyya, S., Will, B., Verma, A & Steidl, U. Stem cell origin of myelodysplastic syndromes. *Oncogene* **33**, 5139 (2014).
18. Terwilliger, T & Abdul-Hay, M. Acute lymphoblastic leukemia: a comprehensive review and 2017 update. *Blood Cancer Journal* **7**, e577–e577 (2017).
19. Döhner, H. *et al.* Diagnosis and management of AML in adults: 2017 ELN recommendations from an international expert panel. *Blood* **129**, 424–447 (2017).
20. Jaramillo, S, Benner, A, Krauter, J, Martin, H, Kindler, T, Bentz, M, Salih, H., Held, G, Köhne, C., Götze, K, *et al.* Condensed versus standard schedule of high-dose cytarabine consolidation therapy with pegfilgrastim growth factor support in acute myeloid leukemia. *Blood Cancer Journal* **7**, e564 (2017).
21. Schlenk, R. F., Weber, D., Herr, W., Wulf, G., Salih, H. R., Derigs, H. G., Kuendgen, A., Ringhoffer, M., Hertenstein, B., Martens, U. M., *et al.* Randomized phase-II trial evaluating induction therapy with idarubicin and etoposide plus sequential or concurrent azacitidine and maintenance therapy with azacitidine. *Leukemia* (2019).
22. Malka, R., Wolach, B., Gavrieli, R., Shochat, E. & Rom-Kedar, V. Evidence for bistable bacteria-neutrophil interaction and its clinical implications. *Journal of Clinical Investigation* **122**, 3002–3011 (2012).
23. Paul, M., Ram, R., Kugler, E., Farbman, L., Peck, A., Leibovici, L., Lahav, M., Yeshurun, M., Shpilberg, O., Herscovici, C., *et al.* Subcutaneous versus intravenous granulocyte colony stimulating factor for the treatment of neutropenia in hospitalized hemato-oncological patients: randomized controlled trial. *American Journal of Hematology* **89**, 243–248 (2014).
24. Welte, K., Gahrilove, J., Bronchud, M. H., Platzer, E. & Morstyn, G. Filgrastim (r-metHuG-CSF): the first 10 years. *Blood* **88**, 1907–1929 (1996).
25. Klastersky, J., De Naurois, J, Rolston, K., Rapoport, B, Maschmeyer, G., Aapro, M. & Herrstedt, J. Management of febrile neutropaenia: ESMO clinical practice guidelines. *Annals of Oncology* **27**, v111–v118 (2016).

26. Bolis, S., Cocorocchio, E., Corti, C., Ferreri, A. J., Frungillo, N., Grillo, G., Omodeo, E. S., Tedeschi, L. & Zilioli, V. R. Clinical implications, safety, efficacy of recombinant human Granulocyte Colony-Stimulating Factors and pegylated equivalent. *Epidemiology, Biostatistics and Public Health* **10** (2013).
27. Stein, E. M., Walter, R. B., Erba, H. P., Fathi, A. T., Advani, A. S., Lancet, J. E., Ravandi, F., Kovacs, T., DeAngelo, D. J., Bixby, D., *et al.* A phase 1 trial of vadastuximab talirine as monotherapy in patients with CD33-positive acute myeloid leukemia. *Blood* **131**, 387–396 (2018).
28. Hunger, S. P. & Mullighan, C. G. Acute lymphoblastic leukemia in children. *The New England Journal of Medicine* **373**, 1541–1552 (2015).
29. Balis, F. M., Holcenberg, J. S., Poplack, D. G., Ge, J., Sather, H. N., Murphy, R. F., Ames, M. M., Waskerwitz, M. J., Tubergen, D. G., Zimm, S., *et al.* Pharmacokinetics and pharmacodynamics of oral methotrexate and mercaptopurine in children with lower risk acute lymphoblastic leukemia: a joint children’s cancer group and pediatric oncology branch study. *Blood* **92**, 3569–3577 (1998).
30. Schmiegelow, K., Nielsen, S. N., Frandsen, T. L. & Nersting, J. Mercaptopurine/methotrexate maintenance therapy of childhood acute lymphoblastic leukemia: clinical facts and fiction. *Journal of Pediatric Hematology/Oncology* **36**, 503 (2014).
31. Newman, J., Anderson, W. & Whitfield, D. *Multidisciplinary Sensitivity Derivatives Using Complex Variables* tech. rep. MSSU-COE-ERC-98-08 (Mississippi State University, 1998).
32. Guenter, B. in *ACM SIGGRAPH 2007 papers* 108–es (2007).
33. Griewank, A. & Walther, A. *Evaluating Derivatives* Second (SIAM, 2008).
34. Gerdt, M. *Optimal Control of Ordinary Differential Equations and Differential-Algebraic Equations* (Habilitation, University of Bayreuth, 2006).
35. Kelley, W. G. & Peterson, A. C. *The theory of differential equations: classical and qualitative* (Springer Science & Business Media, 2010).
36. Hale, J. K. in *Analytic theory of differential equations* 9–22 (Springer, 1971).
37. Edelstein-Keshet, L. *Mathematical Models in Biology* (SIAM, Philadelphia, 2005).
38. Schiesser, W. E. *Differential Equation Analysis in Biomedical Science and Engineering: Ordinary Differential Equation Applications with R* (John Wiley & Sons, 2014).
39. Carson, E. & Cobelli, C. *Modelling methodology for physiology and medicine* (Newnes, 2013).
40. Gabrielsson, J. & Weiner, D. *Pharmacokinetic and pharmacodynamic data analysis: concepts and applications* (CRC Press, 2001).
41. Derendorf, G. & Schäfer, S. *Pharmakokinetik kompakt* (Wissenschaftliche Verlagsgesellschaft Stuttgart, 2011).

42. Li, Z., Guo, J.-R., Chen, Q.-Q., Wang, C.-Y., Zhang, W.-J., Yao, M.-C. & Zhang, W. Exploring the antitumor mechanism of high-dose cytarabine through the metabolic perturbations of ribonucleotide and deoxyribonucleotide in human promyelocytic leukemia HL-60 cells. *Molecules* **22**, 499 (2017).
43. Felmler, M., Morris, M. & Mager, D. Mechanism-based pharmacodynamic modeling. *Methods in molecular biology (Clifton, NJ)* **929**, 583–600 (2012).
44. Sun, Y.-N. & Jusko, W. J. Transit compartments versus gamma distribution function to model signal transduction processes in pharmacodynamics. *Journal of Pharmaceutical Sciences* **87**, 732–737 (1998).
45. DeSouza, D. C., Craig, M., Cassidy, T., Li, J., Nekka, F., Bélair, J. & Humphries, A. R. Transit and lifespan in neutrophil production: implications for drug intervention. *Journal of Pharmacokinetics and Pharmacodynamics* **45**, 59–77 (2018).
46. Manesso, E., Teles, J., Bryder, D. & Peterson, C. Dynamical modelling of haematopoiesis: an integrated view over the system in homeostasis and under perturbation. *Journal of The Royal Society Interface* **10**, 20120817 (2013).
47. Marciniak-Czochra, A., Stiehl, T., Ho, A. D., Jäger, W. & Wagner, W. Modeling of asymmetric cell division in hematopoietic stem cells—regulation of self-renewal is essential for efficient repopulation. *Stem cells and development* **18**, 377–386 (2009).
48. Stiehl, T., Ho, A. D. & Marciniak-Czochra, A. Mathematical modeling of the impact of cytokine response of acute myeloid leukemia cells on patient prognosis. *Scientific Reports* **8**, 2809 (2018).
49. Østby, I., Rusten, L. S., Kvalheim, G. & Grøttum, P. A mathematical model for reconstitution of granulopoiesis after high dose chemotherapy with autologous stem cell transplantation. *Journal of mathematical biology* **47**, 101–136 (2003).
50. Engel, C., Scholz, M. & Loeffler, M. A computational model of human granulopoiesis to simulate the hematotoxic effects of multicycle polychemotherapy. *Blood* **104**, 2323–2331 (2004).
51. Craig, M., Humphries, A. R. & Mackey, M. C. A mathematical model of granulopoiesis incorporating the negative feedback dynamics and kinetics of g-csf/neutrophil binding and internalization. *Bulletin of Mathematical Biology* **78**, 2304–2357 (2016).
52. Friberg, L., Henningson, A., Maas, H., Nguyen, L. & Karlsson, M. Model of chemotherapy-induced myelosuppression with parameter consistency across drugs. *Journal of Clinical Oncology* **20**, 4713–4721 (2002).
53. Quartino, A. L., Karlsson, M. O., Lindman, H. & Friberg, L. E. Characterization of endogenous G-CSF and the inverse correlation to chemotherapy-induced neutropenia in patients with breast cancer using population modeling. *Pharmaceutical Research* **31**, 3390–3403 (2014).

54. Mangas-Sanjuan, V., Buil-Bruna, N., Garrido, M. J., Soto, E. & Trocóniz, I. F. Semimechanistic cell-cycle type-based pharmacokinetic/pharmacodynamic model of chemotherapy-induced neutropenic effects of diflomotecan under different dosing schedules. *Journal of Pharmacology and Experimental Therapeutics* **354**, 55–64 (2015).
55. Henrich, A., Joerger, M., Kraff, S., Jaehde, U., Huisinga, W., Kloft, C. & Parra-Guillen, Z. P. Semimechanistic bone marrow exhaustion pharmacokinetic/pharmacodynamic model for chemotherapy-induced cumulative neutropenia. *Journal of Pharmacology and Experimental Therapeutics* **362**, 347–358 (2017).
56. Afenya, E. Acute leukemia and chemotherapy: a modeling viewpoint. *Mathematical Biosciences* **138**, 79–100 (1996).
57. Pefani, E., Panoskaltsis, N., Mantalaris, A., Georgiadis, M. C. & Pistikopoulos, E. N. Chemotherapy drug scheduling for the induction treatment of patients with acute myeloid leukemia. *IEEE Transactions on Biomedical Engineering* **61**, 2049–2056 (2014).
58. Fuentes-Garí, M., Misener, R., Georgiadis, M. C., Kostoglou, M., Panoskaltsis, N., Mantalaris, A. & Pistikopoulos, E. N. Selecting a differential equation cell cycle model for simulating leukemia treatment. *Industrial & Engineering Chemistry Research* **54**, 8847–8859 (2015).
59. Afenya, E. K., Ouifki, R., Camara, B. I. & Mundle, S. D. Mathematical modeling of bone marrow–peripheral blood dynamics in the disease state based on current emerging paradigms, part I. *Mathematical Biosciences* **274**, 83–93 (2016).
60. Afenya, E. K., Ouifki, R. & Mundle, S. D. Mathematical modeling of bone marrow–peripheral blood dynamics in the disease state based on current emerging paradigms, part II. *Journal of Theoretical Biology* **460**, 37–55 (2019).
61. Clairambault, J. Modelling physiological and pharmacological control on cell proliferation to optimise cancer treatments. *Mathematical Modelling of Natural Phenomena* **4**, 12–67 (2009).
62. Wang, W. *et al.* Reduced hematopoietic stem cell frequency predicts outcome in acute myeloid leukemia. *Haematologica* **102**, 1567–1577 (2017).
63. Shochat, E. & Rom-Kedar, V. Novel strategies for granulocyte colony-stimulating factor treatment of severe prolonged neutropenia suggested by mathematical modeling. *Clinical Cancer Research* **14**, 6354–6363 (2008).
64. Vainas, O, Ariad, S, Amir, O, Mermershtain, W, Vainstein, V, Kleiman, M, Inbar, O, Ben-Av, R, Mukherjee, A, Chan, S, *et al.* Personalising docetaxel and G-CSF schedules in cancer patients by a clinically validated computational model. *British journal of cancer* **107**, 814 (2012).

65. Craig, M., Humphries, A. R., Nekka, F., Bélair, J., Li, J. & Mackey, M. C. Neutrophil dynamics during concurrent chemotherapy and G-CSF administration: mathematical modelling guides dose optimisation to minimise neutropenia. *Journal of theoretical biology* **385**, 77–89 (2015).
66. Brekkan, A., Lopez-Lazaro, L., Yngman, G., Plan, E. L., Acharya, C., Hooker, A. C., Kankanwadi, S. & Karlsson, M. O. A Population Pharmacokinetic-Pharmacodynamic Model of Pegfilgrastim. *AAPS Journal* **20**, 91 (2018).
67. Melhem, M., Delor, I., Pérez-Ruixo, J. J., Harrold, J., Chow, A., Wu, L. & Jacqmin, P. Pharmacokinetic–pharmacodynamic modelling of neutrophil response to G-CSF in healthy subjects and patients with chemotherapy-induced neutropenia. *British Journal of Clinical Pharmacology* **84**, 911–925 (2018).
68. Scholz, M, Engel, C & Loeffler, M. Modelling human granulopoiesis under polychemotherapy with G-CSF support. *Journal of mathematical biology* **50**, 397–439 (2005).
69. Scholz, M., Schirm, S., Wetzler, M., Engel, C. & Loeffler, M. Pharmacokinetic and-dynamic modelling of G-CSF derivatives in humans. *Theoretical Biology and Medical Modelling* **9**, 32 (2012).
70. Schirm, S., Engel, C., Loibl, S., Loeffler, M. & Scholz, M. Model-based optimization of G-CSF treatment during cytotoxic chemotherapy. *Journal of Cancer Research and Clinical Oncology* **144**, 343–358 (2018).
71. Craig, M. Towards Quantitative Systems Pharmacology Models of Chemotherapy-Induced Neutropenia. *CPT: Pharmacometrics & Systems Pharmacology* (2017).
72. Fornari, C., O'Connor, L. O., Yates, J. W., Cheung, S. A., Jodrell, D. I., Mettetal, J. T. & Collins, T. A. Understanding Hematological Toxicities Using Mathematical Modeling. *Clinical Pharmacology & Therapeutics* (2018).
73. Tetschke, M., Lilienthal, P., Pottgiesser, T., Fischer, T., Schalk, E. & Sager, S. Mathematical Modeling of RBC Count Dynamics after Blood Loss. *Processes* **6**, 157–185 (2018).
74. Kloft, C., Wallin, J., Henningsson, A., Chatelut, E. & Karlsson, M. O. Population pharmacokinetic-pharmacodynamic model for neutropenia with patient subgroup identification: comparison across anticancer drugs. *Clinical Cancer Research* **12**, 5481–5490 (2006).
75. Quartino, A. *Pharmacometric Models for Improved Prediction of Myelosuppression and Treatment Response in Oncology* PhD thesis (Acta Universitatis Upsaliensis, 2011).
76. Krogh-Madsen, M., Bender, B., Jensen, M. K., Nielsen, O. J., Friberg, L. E. & Honoré, P. H. Population pharmacokinetics of cytarabine, etoposide, and daunorubicin in the treatment for acute myeloid leukemia. *Cancer Chemotherapy and Pharmacology* **69**, 1155–1163 (2012).

77. Pefani, E., Panoskaltsis, N., Mantalaris, A., Georgiadis, M. C. & Pistikopoulos, E. N. Design of optimal patient-specific chemotherapy protocols for the treatment of acute myeloid leukemia (AML). *Computers and Chemical Engineering* **57**, 187–195 (2013).
78. Nock, V. *Pharmacometric modelling of processes in the haematopoietic system and blood* PhD thesis (Freie Universität Berlin, 2013).
79. Rinke, K., Jost, F., Findeisen, R., Fischer, T., Bartsch, R., Schalk, E & Sager, S. *Parameter estimation for leukocyte dynamics after chemotherapy* in *Proceedings of the Foundations of Systems Biology in Engineering (FOSBE) Conference* **49** (Elsevier, 2016), 44–49.
80. Savic, R. M., Jonker, D. M., Kerbusch, T. & Karlsson, M. O. Implementation of a transit compartment model for describing drug absorption in pharmacokinetic studies. *Journal of Pharmacokinetics and Pharmacodynamics* **34**, 711–726 (2007).
81. Brown, G., Hughes, P. J., Michell, R. H., Rolink, A. G. & Ceredig, R. The sequential determination model of hematopoiesis. *Trends in immunology* **28**, 442–448 (2007).
82. Quartino, A., Friberg, L. & Karlsson, M. A simultaneous analysis of the time-course of leukocytes and neutrophils following docetaxel administration using a semi-mechanistic myelosuppression model. *Investigational new Drugs* **30**, 833–845 (2012).
83. Minami, H., Sasaki, Y., Saijo, N., Ohtsu, T., Fujii, H., Igarashi, T. & Itoh, K. Indirect-response model for the time course of leukopenia with anticancer drugs. *Clinical Pharmacology and Therapeutics* **64**, 511–521 (1998).
84. Derendorf, H. & Meibohm, B. Modeling of pharmacokinetic/pharmacodynamic (PK/PD) relationships: concepts and perspectives. *Pharmaceutical Research* **16**, 176–185 (1999).
85. Hing, J., Perez-Ruixo, J., Stuyckens, K., Soto-Matos, A., Lopez-Lazaro, L & Zannikos, P. Mechanism-based pharmacokinetic/pharmacodynamic meta-analysis of trabectedin (ET-743, Yondelis) induced neutropenia. *Clinical Pharmacology & Therapeutics* **83**, 130–143 (2008).
86. Takatani, H., Soda, H., Fukuda, M., Watanabe, M., Kinoshita, A., Nakamura, T. & Oka, M. Levels of recombinant human granulocyte colony-stimulating factor in serum are inversely correlated with circulating neutrophil counts. *Antimicrobial Agents and Chemotherapy* **40**, 988–991 (1996).
87. Roberts, A. W. G-CSF: a key regulator of neutrophil production, but that's not all! *Growth factors* **23**, 33–41 (2005).
88. Hareng, L. & Hartung, T. Induction and regulation of endogenous granulocyte colony-stimulating factor formation. *Biological chemistry* **383**, 1501–1517 (2002).

89. Reisbach, G., Kamp, T., Welzl, G., Giez, C., Abedinpour, F., Lodri, A., Kaboth, W., Dörmer, P. & Nerl, C. Regulated plasma levels of colony-stimulating factors, interleukin-6 and interleukin-10 in patients with acute leukaemia and non-Hodgkin's lymphoma undergoing cytoreductive chemotherapy. *British journal of haematology* **92**, 907–912 (1996).
90. Stiehl, T. & Marciniak-Czochra, A. Mathematical modeling of leukemogenesis and cancer stem cell dynamics. *Mathematical Modelling of Natural Phenomena* **7**, 166–202 (2012).
91. Löwenberg, B. *et al.* Cytarabine dose for acute myeloid leukemia. *The New England Journal of Medicine* **364**, 1027–36 (2011).
92. Kern, W., Schleyer, E., Unterhalt, M., Wörmann, B., Büchner, T. & Hiddemann, W. High antileukemic activity of sequential high dose cytosine arabinoside and mitoxantrone in patients with refractory acute leukemias. *Cancer* **79**, 59–68 (1997).
93. Burk, M., Heyll, A., Arning, M., Volmer, M., Fartash, K. & Schneider, W. Pharmacokinetics of high-dose cytarabine and its deamination product-A reappraisal. *Leukemia & lymphoma* **27**, 321–327 (1997).
94. Solans, B. P., Fleury, A., Freiwald, M., Fritsch, H., Haug, K. & Trocóniz, I. F. Population Pharmacokinetics of Volasertib Administered in Patients with Acute Myeloid Leukaemia as a Single Agent or in Combination with Cytarabine. *Clinical Pharmacokinetics* **57**, 379–392 (2018).
95. Cros, E., Jordheim, L., Dumontet, C. & Galmarini, C. M. Problems related to resistance to cytarabine in acute myeloid leukemia. *Leukemia & lymphoma* **45**, 1123–1132 (2004).
96. Hiddemann, W. Cytosine arabinoside in the treatment of acute myeloid leukemia: the role and place of high-dose regimens. *Annals of hematology* **62**, 119–128 (1991).
97. Herold, N. *et al.* Targeting SAMHD1 with the Vpx protein to improve cytarabine therapy for hematological malignancies. *Journal of Natural Medicines* **23**, 256–263 (2017).
98. Plunkett, W., Liliemark, J. O., Adams, T. M., Nowak, B., Estey, E., Kantarjian, H. & Keating, M. J. Saturation of 1- β -D-arabinofuranosylcytosine 5-triphosphate accumulation in leukemia cells during high-dose 1- β -D-arabinofuranosylcytosine therapy. *Cancer Research* **47**, 3005–3011 (1987).
99. Capizzi, R., White, J. C., Powell, B. & Perrino, F. *Effect of dose on the pharmacokinetic and pharmacodynamic effects of cytarabine.* in *Seminars in hematology* **28** (1991), 54–69.
100. Wang, B., Ludden, T. M., Cheung, E. N., Schwab, G. G. & Roskos, L. K. Population pharmacokinetic–pharmacodynamic modeling of filgrastim (r-metHuG-CSF) in healthy volunteers. *Journal of Pharmacokinetics and Pharmacodynamics* **28**, 321–342 (2001).

101. Wiczling, P., Lowe, P., Pigeolet, E., Lüdicke, F., Balsler, S. & Krzyzanski, W. Population pharmacokinetic modelling of filgrastim in healthy adults following intravenous and subcutaneous administrations. *Clinical Pharmacokinetics* **48**, 817–826 (2009).
102. Krzyzanski, W., Wiczling, P., Lowe, P., Pigeolet, E., Fink, M., Berghout, A. & Balsler, S. Population modeling of filgrastim PK-PD in healthy adults following intravenous and subcutaneous administrations. *Journal of Clinical Pharmacology* **50**, 101S–112S (2010).
103. Foley, C. & Mackey, M. C. Mathematical model for G-CSF administration after chemotherapy. *Journal of Theoretical Biology* **257**, 27–44 (2009).
104. Roskos, L. K., Lum, P., Lockbaum, P., Schwab, G. & Yang, B.-B. Pharmacokinetic/pharmacodynamic modeling of pegfilgrastim in healthy subjects. *Journal of Clinical Pharmacology* **46**, 747–757 (2006).
105. Yang, B.-B. & Kido, A. Pharmacokinetics and pharmacodynamics of pegfilgrastim. *Clinical Pharmacokinetics* **50**, 295–306 (2011).
106. Hayashi, N., Kinoshita, H., Yukawa, E. & Higuchi, S. Pharmacokinetic and pharmacodynamic analysis of subcutaneous recombinant human granulocyte colony stimulating factor (lenograstim) administration. *Journal of Clinical Pharmacology* **39**, 583–592 (1999).
107. Akizuki, S., Mizorogi, F., Inoue, T., Sudo, K & Ohnishi, A. Pharmacokinetics and adverse events following 5-day repeated administration of lenograstim, a recombinant human granulocyte colony-stimulating factor, in healthy subjects. *Bone Marrow Transplantation* **26**, 939 (2000).
108. Hayashi, N., Aso, H., Higashida, M., Kinoshita, H., Ohdo, S., Yukawa, E. & Higuchi, S. Estimation of RHG-CSF absorption kinetics after subcutaneous administration using a modified Wagner–Nelson method with a nonlinear elimination model. *European Journal of Pharmaceutical Sciences* **13**, 151–158 (2001).
109. Ria, R., Gasparre, T., Mangialardi, G, Bruno, A, Iodice, G, Vacca, A & Dammacco, F. Comparison between filgrastim and lenograstim plus chemotherapy for mobilization of PBPCs. *Bone Marrow Transplantation* **45**, 277 (2010).
110. Kagan, L. Pharmacokinetic modeling of the subcutaneous absorption of therapeutic proteins. *Drug Metabolism and Disposition* **42**, 1890–1905 (2014).
111. Hawwa, A. F., Collier, P. S., Millership, J. S., McCarthy, A., Dempsey, S., Cairns, C. & McElnay, J. C. Population pharmacokinetic and pharmacogenetic analysis of 6-mercaptopurine in paediatric patients with acute lymphoblastic leukaemia. *British Journal of Clinical Pharmacology* **66**, 826–837 (2008).
112. Jayachandran, D., Rundell, A. E., Hannemann, R. E., Vik, T. A. & Ramkrishna, D. Optimal chemotherapy for leukemia: a model-based strategy for individualized treatment. *PloS One* **9**, e109623 (2014).

113. Jayachandran, D., Laínez-Aguirre, J., Rundell, A., Vik, T., Hannemann, R., Reklaitis, G. & Ramkrishna, D. Model-based individualized treatment of chemotherapeutics: Bayesian population modeling and dose optimization. *PLoS One* **10**, e0133244 (2015).
114. Schmiegelow, K., Schröder, H, Gustafsson, G., Kristinsson, J., Glomstein, A., Salmi, T. & Wranne, L. Risk of relapse in childhood acute lymphoblastic leukemia is related to RBC methotrexate and mercaptopurine metabolites during maintenance chemotherapy. Nordic Society for Pediatric Hematology and Oncology. *Journal of Clinical Oncology* **13**, 345–351 (1995).
115. Zimm, S., Collins, J. M., Riccardi, R., O'Neill, D., Narang, P. K., Chabner, B. & Poplack, D. G. Variable bioavailability of oral mercaptopurine: is maintenance chemotherapy in acute lymphoblastic leukemia being optimally delivered? *The New England Journal of Medicine* **308**, 1005–1009 (1983).
116. Arndt, C. A., Balis, F. M., McCully, C. L., Jeffries, S. L., Doherty, K., Murphy, R. & Poplack, D. G. Bioavailability of low-dose vs high-dose 6-mercaptopurine. *Clinical Pharmacology & Therapeutics* **43**, 588–591 (1988).
117. Panetta, J., Yanishevski, Y., Pui, C.-H., Sandlund, J. T., Rubnitz, J., Rivera, G. K., Ribeiro, R., Evans, W. E. & Relling, M. V. A mathematical model of in vivo methotrexate accumulation in acute lymphoblastic leukemia. *Cancer Chemotherapy and Pharmacology* **50**, 419–428 (2002).
118. Panetta, J. C., Sparreboom, A., Pui, C.-H., Relling, M. V. & Evans, W. E. Modeling mechanisms of in vivo variability in methotrexate accumulation and folate pathway inhibition in acute lymphoblastic leukemia cells. *PLoS Computational Biology* **6**, e1001019 (2010).
119. Nagulu, M., Kiran, V. U., Nalini, Y, Reddy, Y. N. & Krishna, D. R. Population pharmacokinetics of methotrexate in Indian cancer patients. *Asian Pacific Journal of Cancer Prevention* **11**, 403–407. ISSN: 1513-7368 (2010).
120. Rühls, H., Becker, A., Drescher, A., Panetta, J. C., Pui, C.-H., Relling, M. V. & Jaehde, U. Population PK/PD model of homocysteine concentrations after high-dose methotrexate treatment in patients with acute lymphoblastic leukemia. *PLoS One* **7**, e46015 (2012).
121. Korell, J., Stamp, L. K., Barclay, M. L., Dalrymple, J. M., Drake, J., Zhang, M. & Duffull, S. B. A population pharmacokinetic model for low-dose methotrexate and its polyglutamated metabolites in red blood cells. *Clinical Pharmacokinetics* **52**, 475–485 (2013).
122. Hui, K. H., Chu, H. M., Fong, P. S., Cheng, W. T. F. & Lam, T. N. Population pharmacokinetic study and individual dose adjustments of high-dose methotrexate in chinese pediatric patients with acute lymphoblastic leukemia or osteosarcoma. *The Journal of Clinical Pharmacology* **59**, 566–577 (2019).

123. Godfrey, C, Sweeney, K, Miller, K, Hamilton, R & Kremer, J. The population pharmacokinetics of long-term methotrexate in rheumatoid arthritis. *British Journal of Clinical Pharmacology* **46**, 369–376 (1998).
124. Du Bois, D. A formula to estimate the approximate surface area if height and weight be known. *Nutrition* **5**, 303–313 (1989).
125. Pinkerton, C., Welshman, S., Dempsey, S., Bridges, J. & Glasgow, J. Absorption of methotrexate under standardized conditions in children with acute lymphoblastic leukaemia. *British Journal of Cancer* **42**, 613 (1980).
126. Nocedal, J. & Wright, S. *Numerical Optimization* Second. ISBN 0-387-30303-0 (hardcover) (Springer Verlag, Berlin Heidelberg New York, 2006).
127. Ulbrich, M. & Ulbrich, S. *Nichtlineare Optimierung* (Birkhäuser, Basel, 2012).
128. Walter, E. & Pronzato, L. *Identification of Parametric Models* (Springer, London, Berlin, Heidelberg, 1997).
129. Körkel, S. *Numerische Methoden für Optimale Versuchsplanungsprobleme bei nicht-linearen DAE-Modellen* PhD thesis (Universität Heidelberg, Heidelberg, 2002). <<http://www.koerkel.de>>.
130. Bock, H. G., Körkel, S. & Schlöder, J. P. in *Model Based Parameter Estimation: Theory and Applications* (eds Bock, H. G., Carraro, T., Jäger, W., Körkel, S., Rannacher, R. & Schlöder, J. P.) 1–30 (Springer, Heidelberg, 2013). ISBN: 978-3-642-30367-8.
131. Pinheiro, J. & Bates, D. *Mixed-effects models in S and S-PLUS* (Springer Science & Business Media, 2006).
132. Demidenko, E. *Mixed models: theory and applications with R* (John Wiley & Sons, New Jersey, 2013).
133. Beal, S. L. 1. Population pharmacokinetic data and parameter estimation based on their first two statistical moments. *Drug Metabolism Reviews* **15**, 173–193 (1984).
134. Lindstrom, M. J. & Bates, D. M. Nonlinear mixed effects models for repeated measures data. *Biometrics*, 673–687 (1990).
135. Wang, Y. Derivation of various NONMEM estimation methods. *Journal of Pharmacokinetics and Pharmacodynamics* **34**, 575–593 (2007).
136. Kim, M.-G., Yim, D.-S. & Bae, K.-S. R-based reproduction of the estimation process hidden behind NONMEM® Part 1: first-order approximation method. *Translational and Clinical Pharmacology* **23**, 1–7 (2015).
137. Bae, K.-S. & Yim, D.-S. R-based reproduction of the estimation process hidden behind NONMEM® Part 2: First-order conditional estimation. *Translational and Clinical Pharmacology* **24**, 161–168 (2016).
138. Solms, A. M. *Integrating nonlinear mixed effects and physiologically-based modeling approaches for the analysis of repeated measurement studies* doctoralthesis (Universität Potsdam, 2017), x, 141.

139. Mould, D. & Upton, R. N. Basic concepts in population modeling, simulation, and model-based drug development—part 2: introduction to pharmacokinetic modeling methods. *CPT: Pharmacometrics & Systems Pharmacology* **2**, 1–14 (2013).
140. Demidenko, E. *Mixed models: theory and applications* (John Wiley & Sons, 2004).
141. Beal, S., Sheiner, L., Boeckmann, A. & Bauer, R. NONMEM user's guides (1989–2009). *Icon Development Solutions, Ellicott City, MD* (2009).
142. Aoki, Y., Nordgren, R. & Hooker, A. C. Preconditioning of nonlinear mixed effects models for stabilisation of variance-covariance matrix computations. *The AAPS Journal* **18**, 505–518 (2016).
143. Bauer, R. J. NONMEM Tutorial Part I: Description of Commands and Options, with Simple Examples of Population Analysis. *CPT: pharmacometrics & Systems Pharmacology* (2019).
144. Sager, S. Sampling Decisions in Optimum Experimental Design in the Light of Pontryagin's Maximum Principle. *SIAM Journal on Control and Optimization* **51**, 3181–3207 (2013).
145. Pukelsheim, F. *Optimal Design of Experiments* ISBN 978-0-898716-04-7 (SIAM, 2006).
146. Gerdts, M. A variable time transformation method for mixed-integer optimal control problems. *Optimal Control Applications and Methods* **27**, 169–182 (2006).
147. Sager, S., Reinelt, G. & Bock, H. Direct Methods With Maximal Lower Bound for Mixed-Integer Optimal Control Problems. *Mathematical Programming* **118**, 109–149 (2009).
148. Gerdts, M. & Sager, S. in *Control and Optimization with Differential-Algebraic Constraints* (eds Biegler, L., Campbell, S. & Mehrmann, V.) 189–212 (SIAM, 2012). <<https://mathopt.de/PUBLICATIONS/Gerdts2012.pdf>>.
149. Retout, S., Duffull, S. & Mentré, F. Development and implementation of the population Fisher information matrix for the evaluation of population pharmacokinetic designs. *Computer Methods and Programs in Biomedicine* **65**, 141–151 (2001).
150. Retout, S. & Mentré, F. Further developments of the Fisher information matrix in nonlinear mixed effects models with evaluation in population pharmacokinetics. *Journal of Biopharmaceutical Statistics* **13**, 209–227 (2003).
151. Foracchia, M., Hooker, A., Vicini, P. & Ruggeri, A. POPED, a software for optimal experiment design in population kinetics. *Computer Methods and Programs in Biomedicine* **74**, 29–46 (2004).
152. Bazzoli, C., Retout, S. & Mentré, F. Design evaluation and optimisation in multiple response nonlinear mixed effect models: PFIM 3.0. *Computer Methods and Programs in Biomedicine* **98**, 55–65 (2010).
153. Nyberg, J., Ueckert, S., Strömberg, E. A., Hennig, S., Karlsson, M. O. & Hooker, A. C. PopED: an extended, parallelized, nonlinear mixed effects models optimal design tool. *Computer Methods and Programs in Biomedicine* **108**, 789–805 (2012).

154. Nyberg, J., Bazzoli, C., Ogungbenro, K., Aliev, A., Leonov, S., Duffull, S., Hooker, A. C. & Mentré, F. Methods and software tools for design evaluation in population pharmacokinetics–pharmacodynamics studies. *British Journal of Clinical Pharmacology* **79**, 6–17 (2015).
155. Dokoumetzidis, A. & Aarons, L. Bayesian optimal designs for pharmacokinetic models: sensitivity to uncertainty. *Journal of Biopharmaceutical Statistics* **17**, 851–867 (2007).
156. Dodds, M. G., Hooker, A. C. & Vicini, P. Robust population pharmacokinetic experiment design. *Journal of Pharmacokinetics and Pharmacodynamics* **32**, 33–64 (2005).
157. Strömberg, E. *Applied Adaptive Optimal Design and Novel Optimization Algorithms for Practical Use* PhD thesis (Acta Universitatis Upsaliensis, 2016).
158. Nyberg, J., Karlsson, M. O. & Hooker, A. C. Simultaneous optimal experimental design on dose and sample times. *Journal of Pharmacokinetics and Pharmacodynamics* **36**, 125 (2009).
159. Bellman, R. *Dynamic Programming* 6th. ISBN 0-486-42809-5 (paperback) (University Press, Princeton, N.J., 1957).
160. Pontryagin, L., Boltyanski, V., Gamkrelidze, R. & Miscenko, E. *The Mathematical Theory of Optimal Processes* (Wiley, Chichester, 1962).
161. Betts, J. *Practical Methods for Optimal Control Using Nonlinear Programming* (SIAM, Philadelphia, 2001).
162. Ioffe, A. & Tihomirov, V. *Theory of extremal problems* (North-Holland Publishing Co., Amsterdam, 1979).
163. Bryson, A. & Ho, Y.-C. *Applied Optimal Control* (Wiley, New York, 1975).
164. Cacace, S., Ferretti, R. & Rafiei, Z. in *Numerical Methods for Optimal Control Problems* 39–62 (Springer, 2018).
165. Vinter, R. State constrained optimal control problems with time delays. *Journal of Mathematical Analysis and Applications* **457**, 1696–1712 (2018).
166. Biegler, L. *Nonlinear Programming: Concepts, Algorithms, and Applications to Chemical Processes* (SIAM, 2010).
167. Albersmeyer, J. & Diehl, M. The Lifted Newton Method and its Application in Optimization. *SIAM Journal on Optimization* **20**, 1655–1684 (2010).
168. Bock, H. *Randwertproblemmethoden zur Parameteridentifizierung in Systemen nicht-linearer Differentialgleichungen* <<http://www.iwr.uni-heidelberg.de/groups/agbock/FILES/Bock1987.pdf>> (Universität Bonn, Bonn, 1987).
169. Dennis Jr, J. E. & Schnabel, R. B. *Numerical methods for unconstrained optimization and nonlinear equations* (Siam, 1996).
170. Fletcher, R. *Practical Methods of Optimization* Second. ISBN 0-471-49463-1 (paperback) (Wiley, Chichester, 1987).

171. Bertsekas, D. *Dynamic Programming and Optimal Control* (Athena Scientific, Belmont, MA, 1995).
172. Curtis, F. E., Mitchell, T. & Overton, M. L. A BFGS-SQP method for nonsmooth, nonconvex, constrained optimization and its evaluation using relative minimization profiles. *Optimization Methods and Software* **32**, 148–181 (2017).
173. Janka, D., Kirches, C., Sager, S. & Wächter, A. An SR1/BFGS SQP algorithm for nonconvex nonlinear programs with block-diagonal Hessian matrix. *Mathematical Programming Computation* **8**, 435–459 (2016).
174. Hindmarsh, A., Brown, P., Grant, K., Lee, S., Serban, R., Shumaker, D. & Woodward, C. SUNDIALS: Suite of Nonlinear and Differential/Algebraic Equation Solvers. *ACM Transactions on Mathematical Software* **31**, 363–396 (2005).
175. Wächter, A. *An Interior Point Algorithm for Large-Scale Nonlinear Optimization with Applications in Process Engineering* PhD thesis (Carnegie Mellon University, 2002). <<http://www.research.ibm.com/people/a/andreasw/papers/thesis.pdf>>.
176. Melicher, V., Haber, T. & Vanroose, W. Fast derivatives of likelihood functionals for ODE based models using adjoint-state method. *Computational Statistics* **32**, 1621–1643 (2017).
177. Le, T. T., Jost, F., Raupach, T., Zierk, J., Rauh, M., Suttorp, M., Stanulla, M., Metzler, M. & Sager, S. A mathematical model of white blood cell dynamics during maintenance therapy of childhood acute lymphoblastic leukemia. *Mathematical Medicine and Biology* **36**, 471–488 (Oct. 2018).
178. Andersson, J. *A General-Purpose Software Framework for Dynamic Optimization* PhD thesis (Arenberg Doctoral School, KU Leuven, Department of Electrical Engineering (ESAT/SCD) and Optimization in Engineering Center, Kasteelpark Arenberg 10, 3001-Heverlee, Belgium, 2013).
179. Jacqmin, P., Snoeck, E., Van Schaick, E. A., Gieschke, R., Pillai, P., Steimer, J. L. & Girard, P. Modelling response time profiles in the absence of drug concentrations: definition and performance evaluation of the K–PD model. *Journal of Pharmacokinetics and Pharmacodynamics* **34**, 57–85 (2007).
180. Perry, M., Doll, D. & Freter, C. *Chemotherapy source book* (Wolters Kluwer Health/Lippincott Williams & Wilkins, Philadelphia, 2012).
181. Jost, F., Schalk, E., Rinke, K., Fischer, T. & Sager, S. Mathematical models for cytarabine-derived myelosuppression in acute myeloid leukaemia. *PLoS One* **14**, e0204540 (2019).
182. Fernández-Varón, E. & Villamayor, L. Granulocyte and granulocyte macrophage colony-stimulating factors as therapy in human and veterinary medicine. *The Veterinary Journal* **174**, 33–41 (2007).
183. Bonnet, D. & Dick, J. E. Human acute myeloid leukemia is organized as a hierarchy that originates from a primitive hematopoietic cell. *Nature Medicine* **3**, 730 (1997).

184. Hope, K. J., Jin, L. & Dick, J. E. Acute myeloid leukemia originates from a hierarchy of leukemic stem cell classes that differ in self-renewal capacity. *Nature Immunology* **5**, 738 (2004).
185. Nobile, M. S., Vlachou, T., Spolaor, S., Bossi, D., Cazzaniga, P., Lanfranccone, L., Mauri, G., Pelicci, P. G. & Besozzi, D. Modeling cell proliferation in human acute myeloid leukemia xenografts. *Bioinformatics* (2019).
186. Cassileth, P. A., Harrington, D. P., Hines, J. D., Oken, M. M., Mazza, J. J., McGlave, P., Bennett, J. M. & O'Connell, M. J. Maintenance chemotherapy prolongs remission duration in adult acute nonlymphocytic leukemia. *Journal of Clinical Oncology* **6**, 583–587 (1988).
187. Pefani, E. *Modelling and optimisation based drug delivery systems for the treatment of Acute Myeloid Leukemia (AML)* PhD thesis (2013).
188. Nombela-Arrieta, C. & Manz, M. G. Quantification and three-dimensional microanatomical organization of the bone marrow. *Blood Advances* **1**, 407–416 (2017).
189. Hindorf, U., Lindqvist, M., Peterson, C., Söderkvist, P., Ström, M., Hjortswang, H., Pousette, A. & Almer, S. Pharmacogenetics during standardised initiation of thiopurine treatment in inflammatory bowel disease. *Gut* **55**, 1423–1431 (2006).
190. Houska, B., Ferreau, H. & Diehl, M. An Auto-Generated Real-Time Iteration Algorithm for Nonlinear MPC in the Microsecond Range. *Automatica* **47(10)**, 2279–2285 (2011).
191. Fedorov, V. & Malyutov, M. Optimal designs in regression problems. *Math. Operationsforschung and Statistik* **3**, 281–308 (1972).
192. La, H. C., Schlöder, J. P. & Bock, H. G. *Structure of Optimal Samples in Continuous Nonlinear Experimental Design for Parameter Estimation* in (2015).
193. Fedorov, V. *Theory of optimal experiments* (Academic Press, New York and London, 1972).
194. Boyd, S. & Vandenberghe, L. *Convex Optimization* (University Press, Cambridge, 2004).
195. Ben-Tal, A. & Nemirovski, A. Robust Convex Optimization. *Mathematics of Operations Research* **23**, 769–805 (1998).
196. Körkel, S., Kostina, E., Bock, H. & Schlöder, J. Numerical Methods for Optimal Control Problems in Design of Robust Optimal Experiments for Nonlinear Dynamic Processes. *Optimization Methods and Software* **19**, 327–338 (2004).
197. Diehl, M., Bock, H. & Kostina, E. An approximation technique for robust nonlinear optimization. *Mathematical Programming* **107**, 213–230 (2006).
198. Wang, Y., Probin, V. & Zhou, D. Cancer therapy-induced residual bone marrow injury: mechanisms of induction and implication for therapy. *Current cancer therapy reviews* **2**, 271–279 (2006).

199. Wallin, J. E., Friberg, L. E. & Karlsson, M. O. Model-Based Neutrophil-Guided Dose Adaptation in Chemotherapy: Evaluation of Predicted Outcome with Different Types and Amounts of Information. *Basic & Clinical Pharmacology & Toxicology* **106**, 234–242 (2010).
200. Netterberg, I., Nielsen, E. I., Friberg, L. E. & Karlsson, M. O. Model-based prediction of myelosuppression and recovery based on frequent neutrophil monitoring. *Cancer Chemotherapy and Pharmacology*, 1–11 (2017).
201. Evans, N. D., Cheung, S. A. & Yates, J. W. Structural identifiability for mathematical pharmacology: models of myelosuppression. *Journal of Pharmacokinetics and Pharmacodynamics* **45**, 79–90 (2018).
202. Schenkendorf, R., Xie, X., Rehbein, M., Scholl, S. & Krewer, U. The impact of global sensitivities and design measures in model-based optimal experimental design. *Processes* **6**, 27 (2018).
203. Zhang, X.-Y., Trame, M., Lesko, L. & Schmidt, S. Sobol sensitivity analysis: a tool to guide the development and evaluation of systems pharmacology models. *CPT: Pharmacometrics & Systems Pharmacology* **4**, 69–79 (2015).
204. Gutenkunst, R. N., Waterfall, J. J., Casey, F. P., Brown, K. S., Myers, C. R. & Sethna, J. P. Universally sloppy parameter sensitivities in systems biology models. *PLoS Computational Biology* **3**, e189 (2007).
205. Chiş, O., Banga, J. R. & Balsa-Canto, E. GenSSI: a software toolbox for structural identifiability analysis of biological models. *Bioinformatics* **27**, 2610–2611 (2011).
206. Villaverde, A. F., Tsiantis, N. & Banga, J. R. Full observability and estimation of unknown inputs, states and parameters of nonlinear biological models. *Journal of the Royal Society Interface* **16**, 20190043 (2019).
207. Zhu, H.-H., Zhang, X.-H., Qin, Y.-Z., Liu, D.-H., Jiang, H., Chen, H., Jiang, Q., Xu, L.-P., Lu, J., Han, W., *et al.* MRD-directed risk stratification treatment may improve outcomes of t (8; 21) AML in the first complete remission: results from the AML05 multicenter trial. *Blood* **121**, 4056–4062 (2013).
208. Rücker, F. G., Agrawal, M., Corbacioglu, A., Weber, D., Kapp-Schwoerer, S., Gaidzik, V. I., Jahn, N., Schroeder, T., Wattad, M., Lübbert, M., *et al.* Measurable residual disease monitoring in acute myeloid leukemia with t (8; 21)(q22; q22. 1): results from the AML Study Group. *Blood* **134**, 1608–1618 (2019).
209. Thol, F., Gabdoulline, R., Liebich, A., Klement, P., Schiller, J., Kandziora, C., Hambach, L., Stadler, M., Koenecke, C., Flintrop, M., *et al.* Measurable residual disease monitoring by NGS before allogeneic hematopoietic cell transplantation in AML. *Blood* **132**, 1703–1713 (2018).
210. Schuurhuis, G. J., Heuser, M., Freeman, S., Béné, M.-C., Buccisano, F., Cloos, J., Grimwade, D., Haferlach, T., Hills, R. K., Hourigan, C. S., *et al.* Minimal/measurable residual disease in AML: a consensus document from the European LeukemiaNet MRD Working Party. *Blood* **131**, 1275–1291 (2018).

211. Dinh, K., Jaksik, R., Corey, S. J. & Kimmel, M. Predicting Minimal Residual Disease in Acute Myeloid Leukemia through Stochastic Modeling of Clonality. *bioRxiv*, 790261 (2019).
212. Rustum, Y. M., Slocum, H. K., Wang, G., Bakshi, D., Kelly, E., Buscaglia, D., Wrzosek, C., Early, A. P. & Preisler, H. Relationship between plasma Ara-C and intracellular Ara-CTP pools under conditions of continuous infusion and high-dose Ara-C treatment. *Medical and Pediatric Oncology* **10**, 33–43 (1982).
213. Liliemark, J. O., Plunkett, W. & Dixon, D. O. Relationship of 1- β -D-arabinofuranosylcytosine in plasma to 1- β -D-arabinofuranosylcytosine 5'-triphosphate levels in leukemic cells during treatment with high-dose 1- β -D-arabinofuranosylcytosine. *Cancer Research* **45**, 5952–5957 (1985).
214. Dedrick, R. L., Forrester, D. D., Cannon, J. N., El Dareer, S. M. & Mellett, L. B. Pharmacokinetics of 1- β -D-arabinofuranosylcytosine (Ara-C) deamination in several species. *Biochemical Pharmacology* **22**, 2405–2417 (1973).
215. Knauer, F., Stiehl, T. & Marciniak-Czochra, A. Oscillations in a white blood cell production model with multiple differentiation stages. *Journal of Mathematical Biology*, 1–26 (2019).
216. Fornari, C., O'Connor, L. O., Pin, C., Smith, A., Yates, J. W., Amy Cheung, S., Jodrell, D. I., Mettetal, J. T. & Collins, T. A. Quantifying drug-induced bone marrow toxicity using a novel haematopoiesis systems pharmacology model. *CPT: Pharmacometrics & Systems Pharmacology* **8**, 858–868 (2019).
217. Jost, F., Schalk, E., Weber, D., Döhner, H., Fischer, T. & Sager, S. Model-based optimal AML consolidation treatment. *IEEE Transactions on Biomedical Engineering*. accepted. <<https://arxiv.org/abs/1911.08980>> (2020).
218. Ben-Tal, A., Boyd, S. & Nemirovski, A. Extending Scope of Robust Optimization: Comprehensive Robust Counterparts of Uncertain Problems. *Mathematical Programming* **107**, 63–89 (June 2006).
219. Montillo, M., Mirto, S., Petti, M. C., Latagliata, R., Magrin, S., Pinto, A., Zagonel, V., Mele, G., Tedeschi, A. & Ferrara, F. Fludarabine, cytarabine, and G-CSF (FLAG) for the treatment of poor risk acute myeloid leukemia. *American Journal of Hematology* **58**, 105–109 (1998).
220. Nomdedeu, M., Lara-Castillo, M. C., Etxabe, A., Cornet-Masana, J. M., Pratcorona, M., Díaz-Beyá, M., Calvo, X., Rozman, M., Costa, D., Esteve, J., *et al.* Treatment with G-CSF reduces acute myeloid leukemia blast viability in the presence of bone marrow stroma. *Cancer Cell International* **15**, 122 (2015).
221. Ohno, R. G-CSF in the treatment of acute myeloid leukemia: Is it safe? *Leukemia & Lymphoma* **11**, 15–19 (1993).
222. Poston, J. N. & Becker, P. S. Controversies Regarding Use of Myeloid Growth Factors in Leukemia. *Journal of the National Comprehensive Cancer Network* **15**, 1551–1557 (2017).

223. Patel, M., Palani, S., Chakravarty, A., Yang, J., Shyu, W. C. & Mettetal, J. T. Dose schedule optimization and the pharmacokinetic driver of neutropenia. *PloS One* **9**, e109892 (2014).
224. Schlenk, R. F. Is there justification for 4 cycles of consolidation therapy in AML? *Best Practice and Research: Clinical Haematology* **29**, 341–344 (2016).
225. Jost, F., Zierk, J., Le, T. T., Raupach, T., Zierk, J., Rauh, M., Suttorp, M., Stanulla, M., Metzler, M. & Sager, S. Model-based simulation of maintenance therapy of childhood acute lymphoblastic leukemia. *Frontiers in Physiology* **11**, 217 (2020).
226. Haurie, C., Dale, D. C. & Mackey, M. C. Cyclical neutropenia and other periodic hematological disorders: a review of mechanisms and mathematical models. *Blood* **92**, 2629–2640 (1998).
227. Colijn, C., Fowler, A. & Mackey, M. C. High frequency spikes in long period blood cell oscillations. *Journal of Mathematical Biology* **53**, 499–519 (2006).
228. Stiehl, T.-P. *Mathematical Modeling of Stem Cell Dynamics in Acute Leukemias* PhD thesis (Ruprecht-Karls-Universität Heidelberg, 2014).
229. Venturino, E. The influence of diseases on Lotka-Volterra systems. *IMA Preprint Series* **913** (1994).
230. Lee, S.-J., Lee, D.-J. & Oh, H.-S. Technological forecasting at the Korean stock market: a dynamic competition analysis using Lotka–Volterra model. *Technological Forecasting and Social Change* **72**, 1044–1057 (2005).
231. Wächter, A. & Biegler, L. On the Implementation of an Interior-Point Filter Line-Search Algorithm for Large-Scale Nonlinear Programming. *Mathematical Programming* **106**, 25–57 (2006).
232. Gavin, H. The Levenberg-Marquardt method for nonlinear least squares curve-fitting problems. *Department of Civil and Environmental Engineering, Duke University*, 1–15 (2011).
233. Osborne, M. R. Fisher’s method of scoring. *International Statistical Review/Revue Internationale de Statistique*, 99–117 (1992).
234. Sager, S. Optimization and Clinical Decision Support. *Optima*. *Optima* **104**, 1–8 (2018).
235. Lilienthal, P., Tetschke, M., Schalk, E., Fischer, T. & Sager, S. Optimized and Personalized Phlebotomy Schedules for Patients suffering from Polycythemia Vera. *Frontiers in Physiology*. accepted (2020).
236. Kobuchi, S., Shimizu, R., *et al.* Semi-Mechanism-Based Pharmacokinetic-Toxicodynamic Model of Oxaliplatin-Induced Acute and Chronic Neuropathy. *Pharmaceutics* **12**, 125 (2020).